#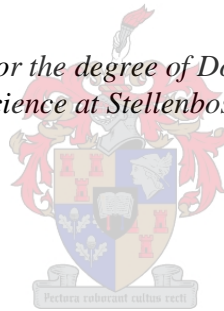 Exploring the antimalarial mechanism of action: Adsorption of diverse inhibitors to crystalline malaria pigment (haemozoin).

by
Ronel Müller

Dissertation presented for the degree of Doctor of Philosophy in the
Faculty of Science at Stellenbosch University

Supervisor: Dr Katherine A. de Villiers
Co-supervisor: Dr Stephen C. Pelly

March 2017

DECLARATION

By submitting this thesis electronically, I declare that the entirety of the work contained therein is my own, original work, that I am the sole author thereof (save to the extent explicitly otherwise stated), that reproduction and publication thereof by Stellenbosch University will not infringe any third party rights and that I have not previously in its entirety or in part submitted it for obtaining any qualification.

March 2017

ABSTRACT

The crystallization of free haem (ferriprotoporphyrin IX) into haemozoin within the parasitic food vacuole is a vital detoxification process in the life cycle of the malaria parasite. Quinoline antimalarial drugs achieve their mechanism of action by adsorbing onto the fastest growing face of haemozoin, which brings about inhibition of further crystal growth. Therefore, an in-depth study of the adsorption of quinoline antimalarial drugs and structurally related non-quinoline compounds to β-haematin (synthetic haemozoin) was undertaken in order to assess this hypothesis.

Adsorption of clinically-relevant quinoline drugs onto both the fastest and the second fastest growth faces of β-haematin was evaluated using molecular mechanics simulations. The adsorption geometries obtained were consistent with those previously reported in literature. When applying a multiple correlation that takes into account both the percentage speciation at pH 4.8 (pH in the food vacuole), as well as the adsorption onto both the fastest growing crystal faces, a significant linear correlation was found when comparing the calculated adsorption energies (E_{ads} (kcal.mol^{-1})) and the determined β-haematin growth inhibition activities (Lipid BHIC$_{50}$), where an R^2 value of 0.78 and a P value of 0.004 are found. This observation greatly supported the above mentioned hypothesis.

The study was further extended to evaluate the adsorption of a set of non-quinoline compounds onto the two fastest growing crystal faces. A new adsorption geometry was observed where the inhibitors were able to adsorb over two adjacent unit cells, thereby forming π-π interactions to two neighbouring porphyrin structures. This is the first time that this adsorption geometry has been observed. Therefore, following the successful synthesis of a small set of quinoline inhibitors, it was demonstrated that an improved adsorption and a

subsequent enhanced β-haematin growth inhibition activity is dependent on the formation of a larger number of intermolecular interactions between the inhibitor and the crystal surface.

Finally, by combining all compounds investigated (25 in total) and thereby evaluating a more comprehensive data set, an exponential relationship is found when comparing the calculated adsorption energy (E_{ads} (kcal.mol^{-1})) and the determined β-haematin growth inhibition activity (NP40 BHIC$_{50}$), when applying the multiple correlation equation, and upon considering both the percentage speciation at pH 4.8 as well as the adsorption onto both the fastest growing crystal faces. An R^2 value of 0.73 with a P value of <0.0001 are obtained.

These results add merit to the argument that antimalarial drugs adsorb onto β-haematin to inhibit further crystal growth. Moreover, by determining the necessary intermolecular interactions required for improved adsorption onto these crystal faces, this information could be applied in future drug development to rationally design novel and more active antimalarial drugs.

OPSOMMING

Die kristallisering van vrye heem (ysterprotoporfirien IX) na hemozoin binne in die parasitiese voedsel vakuool, is 'n belangrikke ontgiftigings proses in die lewenssiklus van die malaria parasiet. Kinolien anti-malaria geneesmiddelle verrig hul meganisme van aksie deur op die vinnigste groeiende kristalvlak van hemozoin te adsorbeer, wat dan lei tot die inhibisie van verdere kristal groei. Daarom, was 'n in-diepte studie van die adsorpsie van kinolien en strukturele verwante nie-kinolien verbindings op β-hematien (sintetiese hemozoin) uitegevoer, om dus hierdie hipotese te ondersoek.

Adsorpsie van klinies-relevante kinolien geneesmiddele op beide die vinnigste en die tweede vinnigste groei vlakke van β-hematien was geëvalueer deur gebruik te maak van molekulêre meganiese simulasies. Die adsorpsie geometrieë wat verkry was, is oorenstemmend met dié wat voorheen in die literatuur gepubliseer is. Met die toepassing van 'n meervoudige korrelasie wat beide die persentasie spesiasie by 'n pH van 4.8 (pH in die voedsel vakuool) sowel as die adsorpsie op beide die twee vinigste groeiende kristalvlakke in ag neem, was 'n beduidende liniêre verband tussen die berekende adsorpsie energieë (E_{ads} ($kcal.mol^{-1}$)) en die bepaalde β-hematien groei inhibisie aktiwiteite (Lipied $BHIC_{50}$) gevind, met 'n R^2 waarde van 0.78 en 'n P waarde van 0.004. Hierdie observasie ondersteun dus die bogenoemde hipotese.

Die studie was verder uitgebrei om die adsorpsie van 'n stel nie-kinolien verbindings op die twee vinnigste groeiende kristalvlakke te ondersoek. 'n Nuwe adsorpsie geometrie was waargeneem, waar die verbindings oor twee aanligende seleenhede adsorbeer, en waar die vorming van π-π interaksies na die twee aanliggende porfirien strukture bevorder word. Dit is die eerste keer dat hierdie adsorpsie geometrie waargeneem was. Daarom, gevolg deur die

sintese van 'n klein stel kinolien verbindings, was dit gedemonstreer dat verbeterde adsorpsie en dus ook 'n verbeterde β-hematien inhibisie aktiwiteit afhanklik is van die vorming van 'n vermeerderde aantal intermolekulêre interaksies tussen die verbinding en die kristaloppervlakte.

As 'n finale bydrae, deur al die verbindings wat ondersoek was saam te evalueer (25 in totaal) en gevolglik 'n meer voledige data stel te ondersoek, was 'n eksponensiële verhouding verkry wanneer die berekende adsorpsie energieë (E_{ads} (kcal.mol^{-1})) en die bepaalde β-hematien groei inhibisie aktiwiteite (NP40 BHIC$_{50}$) vergelyk was deur die meervoudige korrelasie toe te pas, en sodoende ook die persentasie spesiasie by 'n pH van 4.8 en die adsorpsie op beide die vinnigste groeiende kristalvlakke in ag te neem. 'n R^2 waarde van 0.73 met 'n P waarde van <0.0001 was verkry.

Hierdie resultate voeg meriete tot die argument dat anti-malaria geneesmiddelle adsorbeer op β-hematien wat lei tot die inhibisie van verdere kristal groei. Ook, deur die belangrikke intermolekulêre interaksies wat noodsaak is vir 'n verbeterde adsorpsie te identifiseer, kan hierdie inliging toegepas word in verdere geneesmiddel ontwikkeling, waar nuwe anti-malaria geneesmiddelle met verbeterde aktiwiteit rasioneel ontwerp kan word.

DEDICATION

To my mother,

Elizabeth Aletta Müller

ACKNOWLEDGEMENTS

Personal Acknowledgements

Upon embarking on this endeavour, I cannot but be thankful to my heavenly Father for realising my dream in completing this PhD. Thank you for providing me with a heart of joy and perseverance, and for carrying me through this journey.

I have to thank the two persons who have guided me throughout this project, and who have provided me with the opportunity to grow as an individual. **Dr Katherine A. de Villiers** and **Dr Steve C. Pelly**, you have been my wings during this time.

Furthermore, I would like to thank the two research groups, the group of medicinal and organic chemistry and the Stellenbosch haem team, who warmly welcomed my stay in the chemistry department. **Sharné**, **Chandré**, and **Dave**, thank you for keeping me sane.

A special thank goes to the de Beers staff, **Mubarick**, **Raymond**, **Aunty Mary**, and **Debbie**, for keeping the working environment tidy and organised and for always lending a helping hand. Without you, life would be much harder.

Lastly, to my family, **Elbie**, **Deon**, **Rudolf**, **Sumari**, **Oupa Koos**, and **Ouma Marie**, thank you for your love and support. I hope you are as excited as I am on beginning a new chapter.

CONFERENCE PROCEEDINGS AND PUBLICATIONS

Poster Presentations

Poster: R. Müller, K. A. de Villiers, A computational investigation towards understanding the mechanism of inhibition of β-haematin formation by quinoline antimalarials.

1. 13th International Symposium on Applied Bioinorganic Chemistry (ISABC), **2015**, Galway, Ireland.

2. South African Chemical Institute Inorganic Conference (SACI), **2015**, Grahamstown, South Africa.

3. South African Chemical Institute Young Chemist's Symposium (SACI), **2015**, Cape Town, South Africa.

Publications

1. Gildenhuys, J.; Sammy, C. J.; Müller, R.; Streltsov, V. A.; Le Roux, T.; Kuter, D.; de Villiers, K. A., Alkoxide coordination of iron(III) protoporphyrin IX by antimalarial quinoline methanols: a key interaction observed in the solid-state and solution. *Dalton Transactions* **2015**, 44, 16767-16777.

CHAPTER 1

MALARIA AND β-HAEMATIN

Malaria, one of the most prevalent diseases known to humanity, is a tropical disease which is spread by the *Anopheles* mosquito and is mainly caused by the protozoan parasite of the genus *Plasmodium*.[1] With more than 214 million people infected and with an estimated 438 000 deaths annually, malaria greatly contributes to both social and economic challenges.[2] The areas affected are the tropics, with the sub-Saharan African countries affected the worst. Pregnant women and children are more susceptible to this disease, where malaria is considered as one of the major causes of death for children under the age of 5 in affected African countries.[2]

In a comprehensive attempt to eradicate malaria, the World Health Organisation (WHO) reported a decrease of 37% in the annual amount of cases reported and a decrease of 60% in the annual mortality rate since the turn of the millennium.[2] This result has mainly been attributed to the mass distribution of insecticide treated mosquito nets, the intermittent chemoprevention treatment in pregnant women, and the chemo treatment of malaria cases.[3]

Current treatments involve artemisinin-based combination therapies (ACT) for the treatment of uncomplicated *Plasmodium falciparum* and uncomplicated *Plasmodium vivax* malaria.[3] In the rare case of non-chloroquine resistant uncomplicated *Plasmodium vivax* malaria, chloroquine (CQ) is still the recommended drug for treatment.

However, even with great progress made in combatting malaria, with the development of resistant strains towards current treatments (including ACTs in Thailand and Cambodia),[2] and

1

with the exact mechanism of action of these antimalarial drugs still unknown, malaria is still considered a threat to humanity. This thus emphasises the need for further research in understanding the mechanism of antimalarial drug action and thereby the development of new antimalarial drugs.

1.1 MALARIA: AN ACCOUNT OF THE DISEASE FROM DISCOVERY TO PRESENT

1.1.1 The extent of the malaria problem

Malaria is not a modern disease, as ancient manuscripts dating back as far as 3000 BC, found in ancient China, Egypt, Greece, and Italy, describe similar symptoms associated with this disease, where it was mainly observed in areas in close proximity to marshes and rivers.[4,5]

The earliest indication of malaria is found in ancient China and Egypt. The Chinese medical classic *Nei Ching* (ca. 2700 BC) describes the symptoms of the disease and the accompanied formation of an enlarged spleen.[4] It was believed that the symptoms of headaches, chills and fever were instigated by three demons. Each demon carried an object which was associated with these undesirable symptoms. It is said that one demon carried a hammer, one a vessel of water, and the last one, a stove.[4] In Egypt, more direct evidence of malaria was found. Here, mummies were discovered with enlarged spleens, and with modern technology available, malaria antigens were detected in the skin and lung samples of these historic ancestors (ca. 3200 and 1304 B.C.).[4] Additionally, various herbal treatments of the time, as well as the symptoms of the disease were well documented in an Egyptian medical papyrus, known as the Ebers Papyrus (ca. 1570 BC).[4]

More of these manuscripts, describing this fever-causing disease, were found in ancient communities of Greece and Rome. Even though the Greeks tended not to talk about their illnesses, both Plato and Hippocrates (ca. 400 BC) clearly described the symptoms of the disease referred to as the "burning disease", accompanied by the enlargement of the spleen.[5] This disease was mostly dominant in summer and in autumn. The first reference to malaria in Italy was described by Celsus (ca. 50 AD).[5] However, with the natural landscape of Italy not being optimal for the breeding of the mosquito, writings indicate that Rome was mostly affected by this disease during war periods. It became known as the "Roman fever" which later led to the Italian word *mal'aria*, meaning "bad air".[4]

Throughout Europe, other than seasonal outbreaks amongst the wetlands, the occurrence of malaria was mainly associated with travellers, merchants, and soldiers during war times. With no previous indication of malaria, it is believed that malaria was only introduced to the New World by European travellers, accompanied by the importation of goods and slaves.[4]

Finally, aside from herbal and folk medicine used for the treatment of malaria, it was not until the discovery of quinine (QN), extracted from the bark of the *Cinchona* tree, that a treatment was developed by more modern medicinal practices and was finally distributed commercially for the treatment of malaria.[6,7]

According to legend, this discovery originated when a native Indian remedy, named "fever bark", was introduced to the Countess of Chinchon during her stay in Peru in 1629, after which it became known as cinchona and Countess' powder.[6,7] Eleven years later she returned to Spain, where the treatment was introduced to, and widely spread across Europe. Almost 200 years later, in 1820, a French chemist, Pelletier, successfully extracted QN, the active

compound in the *Cinchona* tree bark for the use as the first antimalarial drug.[6] This drug became the main treatment against malaria for more than a century. However, as with most modern antimalarial drugs, this treatment had its shortcomings and was not active against all strains of malaria.

For the duration of World War II, the United States army suffered a tremendous loss of soldiers during the invasion of South East Asia, where this fired a new interest in finding active treatments against malaria.[6,7] Subsequently, increased funding was directed towards malaria research, which led to the development of more active treatments against this disease. It was at this stage, that Chloroquine (CQ), which was developed by Johann "Hans" Andersag in 1934, became used as the first-line treatment against malaria.[8]

In the 1950's, a campaign was initiated to stop the spread of malaria by eradicating the malaria mosquito with the excessive use of the insecticide, dichlorodiphenyltrichloroethane (DDT).[9] This limited the spread of malaria mainly to a large part of Africa. Unfortunately, not only did this colourless insecticide destroy the malaria mosquito, but it had a devastating environmental impact, destroying both plant and animal life in the areas affected. With the ban of the use of DDT in large parts of the globe in the 1970's, the spread of malaria resumed, again causing the deaths of millions worldwide.[10]

It was not until 1972 that artemisinin (AR) was extracted from 'qinghao', an ancient Chinese herbal remedy also known as *Artemisia annua*, or sweet wormwood.[4] AR was widely used throughout China by the 1980's, where artemisinin-based drugs, together with quinoline-based drugs form the foundation of modern antimalarial treatment.

_____

The breakthrough in the understanding of the cause of malaria was aided by the development of the microscope and with the progression of the idea that diseases are caused by microbes. In 1716, an Italian physician, Giovanni M. Lancisi, first observed black granules in the spleen of corpses.[4] However, it was only in 1847 that the German pathologist, Johann H. Meckel, associated this brown pigment found in the spleen, blood and liver of patients who had succumbed to malaria, with the cause of the disease. He referred to this brown pigment as haemozoin.[4,6] Even though his understanding that haemozoin is the cause of the disease was not entirely accurate, his observation created a new focal point in malaria research. Finally, this led to the finding in 1880, by a French pathologist, Charles L.A. Laveran, that this pigment was in fact accompanied by a parasite in the blood, which he referred to as *Oscillaria malariae*.[4,11] Laveran observed and clearly described four different forms of the parasite: crescents, spherical bodies with actively moving flagella, motionless spherical bodies which contained pigment, and smaller spherical bodies which also contained pigment.[11]

Today, with more research performed on the parasite, it is believed that these bodies that Laveran had described were indeed the different life stages of *Plasmodium falciparum* as it is known today. This greater understanding of the malaria parasite's life cycle was a remarkable discovery for scientists.

_____

1.1.2 The malaria parasite and its life cycle

The malaria parasite is carried by the *Anopheles* mosquito and is transferred to the human host during feeding.[12] The disease is caused by five different protozoa parasite types of the same genus: *Plasmodium falciparum*, *Plasmodium vivax*, *Plasmodium ovale*, *Plasmodium malariae*, and less common, *Plasmodium knowlesi*.[13] Even though *Plasmodium vivax* is the most widespread, *Plasmodium falciparum* is still the leading cause of malaria on the African continent and is considered the deadliest of the protozoa parasites.[3]

As the parasite's life cycle is highly complex, a large amount of research has been performed to better understand the different stages, as well as the proteins expressed during each of these stages.[14,15]

The parasite's life cycle progresses in three stages: a sexual stage in the mosquito and two asexual stages in the human host, the latter occurring in hepatocytes (liver cells) and erythrocytes (red blood cells), respectively (Figure 1).[12,14–16]
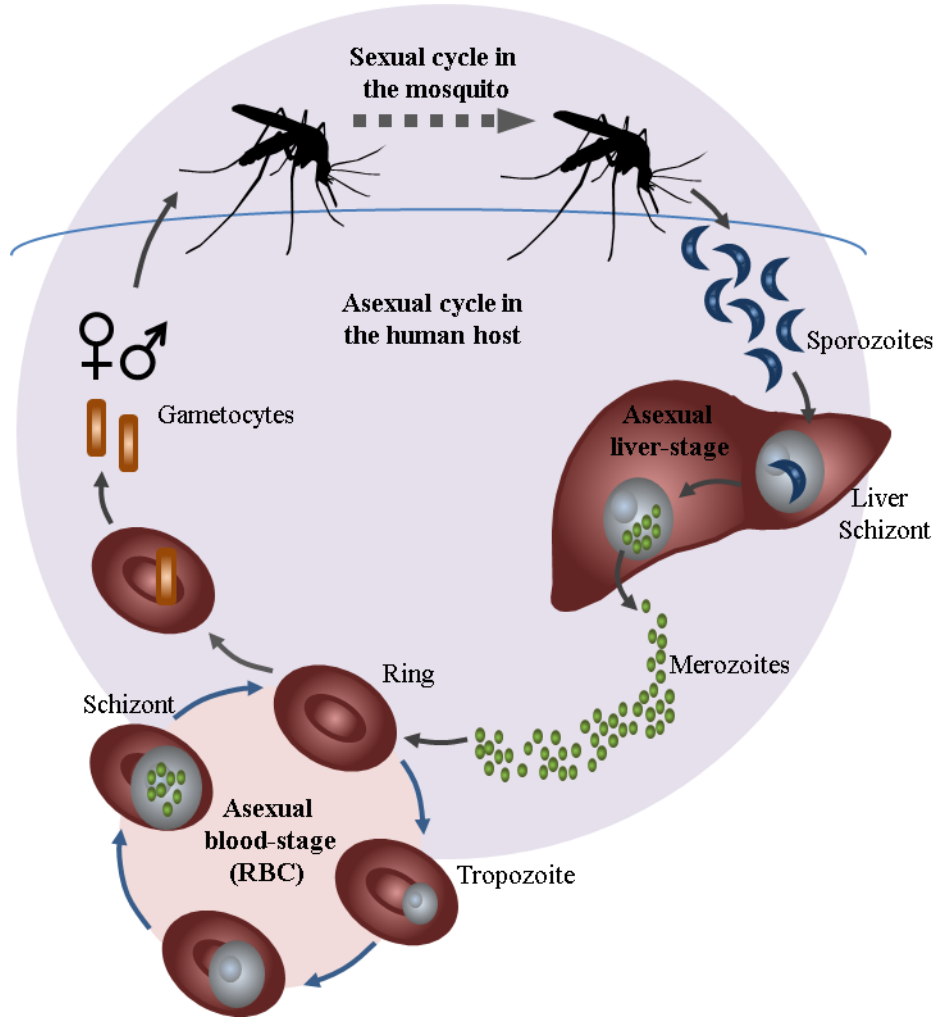
Figure 1: The life cycle of *Plasmodium falciparum*.

This image was created with information obtained from images published by Bautista[15]

and McNamara et al.[17]

The cycle is initiated when the parasite, in the form of sporozoites, is transmitted to the human in the saliva of the mosquito during feeding. These sporozoites then pass to the liver by means of the blood stream to initiate the asymptomatic liver stage, where they would invade the liver cells, named hepatocytes, and develop into schizonts. Within a period of 5-15 days, daughter parasites, called merozoites, are formed within the schizonts. Finally the schizonts will rupture and release the merozoites back into the blood stream.

The symptomatic blood stage is initiated when these merozoites invade the red blood cells (RBCs). At this stage of the life cycle, the human host will start to show symptoms and pathologic signs of malaria infection. The merozoites develop through ring, trophozoite and schizont forms. During the trophozoite form, the parasite modifies the host cell, allowing for the transportation of molecules in and out of the cell. Here, haemoglobin is digested as the main nutrient source within the parasite's food vacuole.[16] The trophozoite will finally develop into the schizont, where the schizont will again rupture and release new daughter merozoites to invade other red blood cells. A cycle in the blood stage typically lasts 48 hours.

Finally, some of these merozoites develop into dimorphic gametocytes, with a male to female ratio of 1:4.[14] These are ingested by the mosquito during feeding. Finally, the sexual reproduction stage is initiated, where further development of the parasites lead to the formation of new sporozoites. These then migrate into the mosquito's salivary glands, and are ready to infect another human host.

1.1.3 Haemoglobin degradation

Host haemoglobin is a major nutrient source for the malaria parasite, where it is broken down to provide valuable amino acids for parasite growth.[18] Even though the exact mechanism of haemoglobin digestion is still unknown, both cysteine and aspartic proteases have been isolated from the food vacuole, where these are believed to be vital enzymes in haemoglobin proteolysis.[16,19–24]

During the trophozoite stage in the red blood cell, an estimate of 25-80% of host haemoglobin is digested.[25–27] The parasite ingests the haemoglobin into the cytostome, where after it is pinched off into small vesicles (Figure 3).[28] These vesicles migrate into the food vacuole (digestive vacuole), where haemoglobin is digested at a low pH (4.8-5.2).[29] At this stage, the iron centre is oxidised, whereupon toxic free haem (ferriprotoporphyrin IX (Fe(III)PPIX)) (Figure 2), is released.[20] Finally, the toxic free haem is crystallised into an ordered non-toxic form, previously referred to as haemozoin.
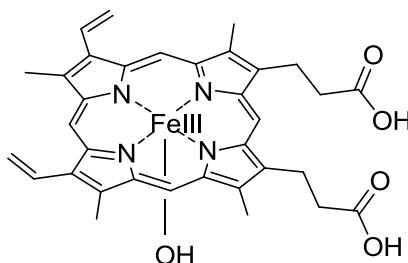
Figure 2: Free haem (ferriprotoporphyrin IX (Fe(III)PPIX))

This brown pigment (haemozoin) is characteristic of infected red blood cells. It is at this trophozoite stage that the disease becomes symptomatic, with the occurrence of aches, fever, and chills. This concurrence led to the previous incorrect understanding that the formation of haemozoin is the major cause of the disease.[4,6]

_____
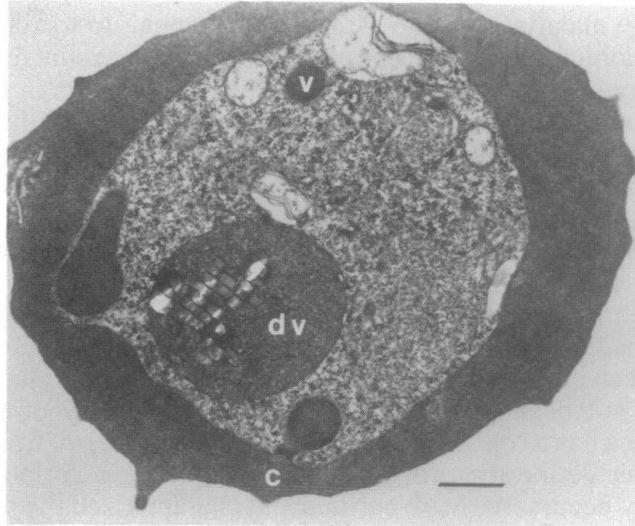
Figure 3: An electron micrograph of a whole parasitised erythrocyte collected by Goldberg *et al.*[19]

In this image the cytostome (c) is visible, as well as a haemoglobin containing vesicle (v) in the cytoplasm, which moves towards the digestive vacuole (dv). The haemozoin crystals are clearly visible inside the digestive vacuole as an ordered structure.

10

1.2 HAEMOZOIN AND β-HAEMATIN

1.2.1 Chemical composition of haemozoin and β-haematin

In 1987, Fitch and Kanjananggulpan were the first to report the chemical composition of haemozoin. The crystalline material was purified from infected mouse erythrocytes, where they found that it consists of ferriprotoporphyrin IX (Fe(III)PPIX).[30] A few years later, in 1991, Slater and co-workers were the first to show insight into the structural composition of haemozoin and β-haematin (synthetic haemozoin). They confirmed by means of elemental analysis, that haemozoin solely consists of Fe(III)PPIX and that it is chemically identical to β-haematin, which is subsequently known as synthetic heamozoin.[31]

By performing Fourier transform infrared spectroscopy studies, strong absorbance was observed between 1720 and 1650 cm^{-1}, which is consistent with C=O stretching vibrations (Figure 4).[31] It was suggested that similar to acetato[deuteroporphyrin IX dimethyl ester]iron(III), a ferric ion with a unidentate acetate coordination must be present, which would give rise to one of the C-O bonds having double-bond character. This argument was then further strengthened by means of extended X-ray adsorption fine structure spectroscopy (EXAFS) analysis,[31] where the obtained bond lengths were compared to that of a theoretical model.

From these findings, it was suggested, and assumed for many years thereafter, that haemozoin is a polymer, in which the molecules are linked through the propionate group of one ferriprotoporphyrin IX (Fe(III)PPIX) monomer coordinated to the Fe(III) centre of an adjacent one.[31]
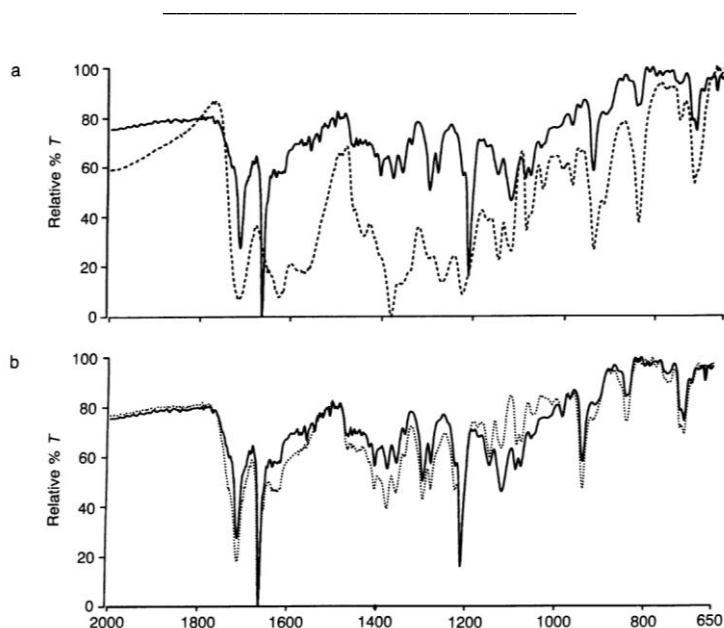
Figure 4: The FTIR spectra reported by Slater *et al.*[31]

*The FTIR spectrum of haemozoin (−) was compared to that of haematin (---) in **a**,*

*and β-haematin (···) in **b**.*

1.2.2 Proposed methods for β-haematin formation

In 1990, Goldberg *et al.* investigated the degradation of haemoglobin in *Plasmodium*

falciparum, where the haemozoin crystals were observed to line up along a single axis in the

food vacuole.[19] Resultantly, it was proposed that haemozoin formation is an ordered process,

which is most likely promoted by the paramagnetic properties of this structure. It was later

suggested by Slater *et al.,* that haemozoin growth might be catalysed by an enzyme that they

referred to as "haem polymerase".[32] Thereafter, it was believed for an extensive period of

time, that haemozoin is a polymer.

It was also proposed that haemozoin grows in the presence of histidine-rich proteins II and III

(HRPII and III), with it being an abundant protein in *Plasmodium falciparum*.[33,34] However,

_____

evidence has indicated that HRPII is exported from the parasite to the red blood cell, leaving only small amounts of the protein present in the food vacuole.[35,36] Furthermore, Noland *et al.* observed haemozoin formation in parasite clones in which HRPII and HRPIII were absent.[37] Therefore, these findings strongly suggest that HRPII and III might not play an important role in haemozoin formation.

Dorn *et al.* were the first to suggest that the process of haemozoin formation might be solely chemical in nature, after β-haematin (synthetic haemozoin) crystals were grown in an acidic buffer solution.[38] Since this discovery, β-haematin crystals have been grown from acidic acetate or phosphate buffer solutions, as well as organic solvents such as methanol, chloroform and acetonitrile.[38–40]

More recently, it is proposed that haemozoin growth might be promoted by neutral lipid bodies in the cell.[41–45] By using Nile red labelling and thin layer chromatography, Jackson *et al.* were able to isolate triacylglycerol (TAG) and diacylglycerol (DAG) neutral lipids from the parasitic food vacuole, where enhanced concentrations were isolated from more mature erythrocytes.[41] It was previously found that the accumulation of TAG is only observed in infected erythrocytes.[46–48] Pisciotta *et al.* observed the formation of haemozoin within neutral lipid bodies inside the food vacuole by means of transmission electron microscopy (TEM) (Figure 5), where it was suggested that these lipid bodies could also protect haem from peroxide degradation.[43]

_____
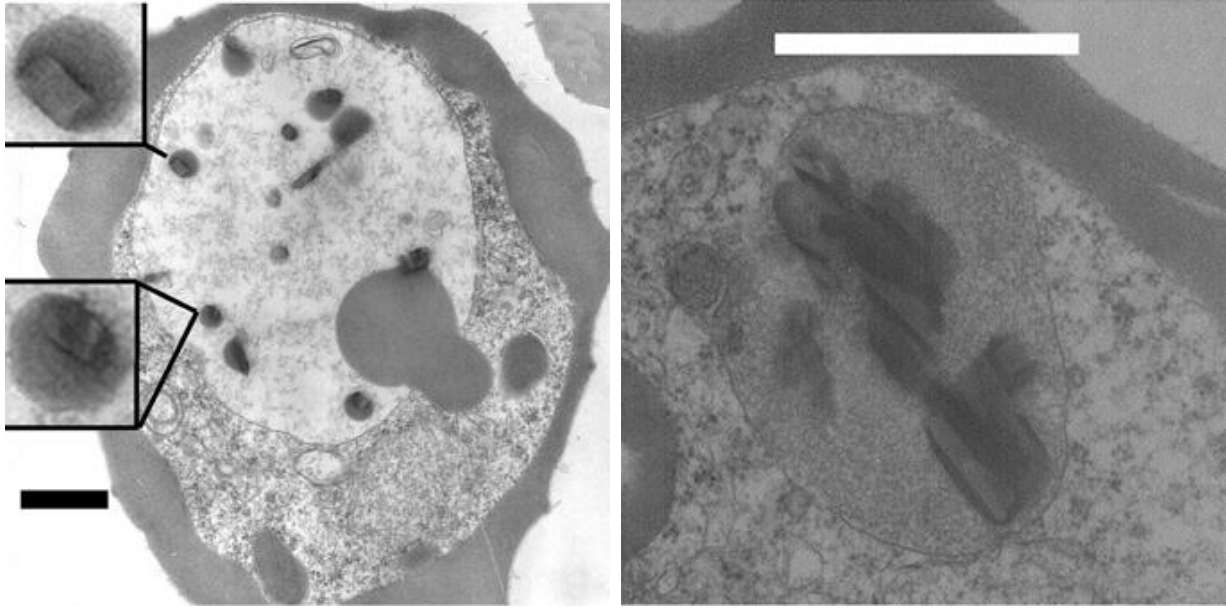
Figure 5: TEM images of the parasitic food vacuole collected by Pisciotta *et al.*[43]

A TEM image of early trophozoite stages, indicating the haemozoin crystals in the lipid bodies, is shown (left), as well as a TEM image of a mature trophozoites, containing larger haemozoin crystals (right). Scale bar, 1 μm.

With β-haematin crystals commonly obtained from acidic acetate or phosphate buffer solutions, improved β-haematin crystal growth was obtained *in vitro* at a water-octanol and pentanol-water interfaces, as well as in the presence of various neutral glycerol lipids.[44,49,50] Therefore, the current thinking is that the formation of haemozoin is a lipid-mediated process of biomineralisation.

In light of the latest findings that lipid bodies promote β-haematin growth, a new focus has turned to obtaining larger synthetic crystals. Furthermore, by being able to mimic haemozoin crystal growth outside of the infected food vacuole, more research could be performed to improve the current understanding on the mechanism of β-haematin growth.

14

_____

1.2.3 The β-haematin crystal structure

A landmark discovery came as somewhat of a surprise in 1997, when Bohle *et al.* obtained and refined the first crystal structure of β-haematin by means of high resolution powder X-ray diffraction, since at that time, β-haematin was still believed to be a polymer (Figure 6).[40,51]

In the study of Bohle *et al.*, infected late trophozoites and uninfected erythrocytes were isolated from the NF54 strain of *Plasmodium falciparum*, whereupon the samples were freeze-dried prior to obtaining the powder X-ray diffraction patterns thereof.[51] Synthetic β-haematin was prepared from haemin (ferriprotoporphyrin IX, with a chloride ligand). Finally, by comparing the crystallographic patterns, it was found that the haemozoin is crystalline *in situ* and that it crystallised with the same unit cell parameters as β-haematin. In other words, this material is not a polymer. The β-haematin monomer units were found to be linked through reciprocal Fe(III)-carboxylate bonds resulting in the formation of centrosymmetric dimers, which hydrogen bond to one another via the free propionic acid side chains (Figure 6). Furthermore, it was shown that the crystalline species found in the trophozoites have clear Bragg diffraction spikes.[51] This crystalline species was absent in the uninfected erythrocytes.

Pagola *et al.* further refined the obtained crystal structure of β-haematin by means of simulated annealing techniques.[40] From this study it was concluded that the β-haematin unit cell consists of a cyclic dimer pair (Figure 7). The observed Fe-O bond distance of 1.886 Å is in agreement with other high-spin ferric and ferrous complexes reported by Bominaar *et al*, where "picket-fence" (porphyrinato)(acetato)iron complexes, $[Fe^{II/III}(CH_3CO_2)(TPpivP)]^{-/0}$, were synthesised and fully characterised, followed by the determination of the crystal structures by means of X-ray diffraction.[52]
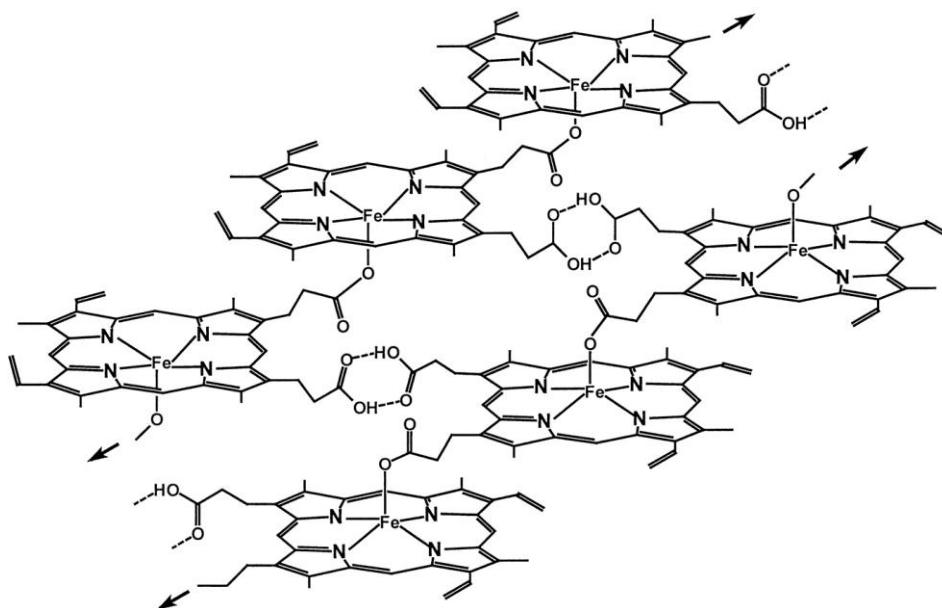
Figure 6: β-Haematin crystal growth as suggested by Bohle *et al*.[51]
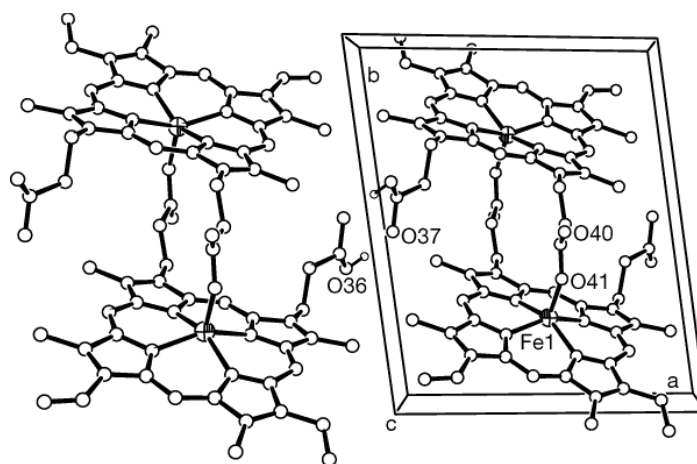
Figure 7: The β-haematin unit cell determined by Pagola *et al*.[40]

16

More recently, in 2013, Gildenhuys *et al.* (members of our research group) obtained the first single crystal data of β-haematin dimethyl sulfoxide solvate by means of single crystal X-ray diffraction.[53] This crystal was grown in the presence of chloroquine, where it was suggested that the inhibitor slowed the crystal growth in order to obtain a large enough single crystal. In this crystal structure, the free propionic acid functional groups were found to be hydrogen bonded to dimethyl sulfoxide molecules. However, their finding with regards to the porphyrin dimer coincided with that reported by Bohle *et al.*, which strengthened the argument that it most possibly represents the true crystal structure of β-haematin.

1.2.4 β-Haematin crystal growth morphology

With the initial crystal structure of β-haematin obtained, Buller *et al.* investigated the theoretical crystal growth morphology thereof, thus contributing in the understanding of β-haematin crystal growth.[54] The calculated crystal morphology was correlated to the scanning electron micrographs of natural haemozoin, where it is found to be similar in habit (external shape) and form (Figure 8).

By doing so, the crystal face attachment energies (E_{att} (kcal.mol^{-1})) were calculated, where E_{att} is the energy released upon the formation of a new layer. It is found that faces {100} and {010} had the highest calculated E_{att} energies, in which case they are expressed the most, and a larger crystal surface is observed in the morphology. Similarly, faces {001} and {011} were identified as the fastest growing faces, with the lowest calculated E_{att} energies. The latter are relatively small, and do not dominate the crystal morphology (Figure 27).

The crystal face attachment energies and the layer energies are calculated by means of molecular mechanical potential energy calculations, where this information is combined to

17

determine the crystal morphology based on Hartman-Perdok principles.[55–58] The face attachment energy is defined as the energy released per molecule when a new molecule is attached to the face, and determines the growth rate of the crystal. The layer energy is defined as the total energy released when a new layer is formed, and is an indication of the stability of the layer.[12] The morphological importance of a crystal face is inversely proportional to the growth rate and directly proportional to the stability of the crystal face. Therefore, the most stable crystal face with the slowest growth rate, would be expressed the most.[59]
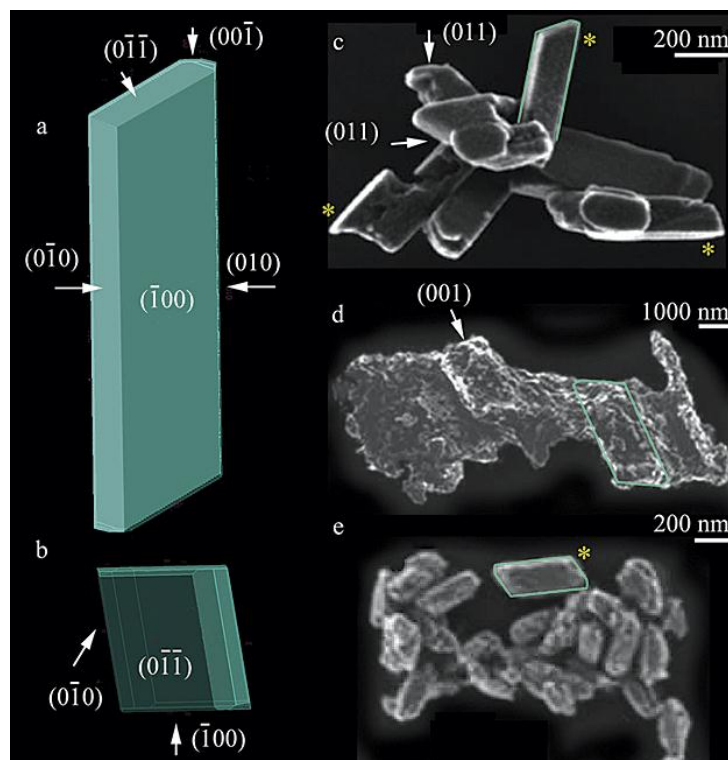
Figure 8: The theoretical growth morphology of β-haematin as proposed by Buller et al.[54]

The crystal structure is viewed perpendicular to the {100} face (a), and perpendicular to the {011} face (b), in which the crystal extends. The faces are correlated to scanning electron micrographs of natural haemozoin isolated form P. falciparum *(c),* S. mansoni *(d), and* H. columbae *(e).*

In order to grasp a greater understanding of the crystal growth morphology, Straasø *et al.* performed further high-resolution X-ray powder diffraction studies.[60] They have suggested that due to the enantio-facial symmetry of the porphyrin monomers and the disorder of the peripheral methyl and vinyl groups, four stereoisomers (Figure 9), of which two centrosymmetric (*cd$\bar{1}_1$* and *cd$\bar{1}_2$*) and two chiral enantiomers (*cd2(±)*), could occur in solution. However, the crystal structure reported by Pagola *et al.* only showed one of the centrosymmetric dimers (*cd$\bar{1}_1$*). In 2011, Marom *et al.* further reported the calculated structural parameters of each of the three stereoisomers (*cd$\bar{1}_1$, cd$\bar{1}_2$, and cd2*) by means of van der Waals (vdW)-corrected density functional theory (DFT) simulations.[61]
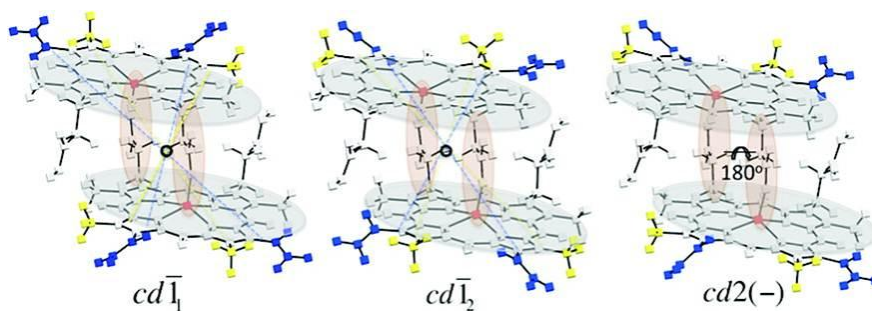
Figure 9: The stereoisomers of β-haematin found by Straasø *et al.*[60]

The two centrosymmetric dimers cd$\bar{1}_1$ (left) and cd$\bar{1}_2$ (centre), and the chiral dimers cd2(-)(right).

By understanding the crystal packing arrangement of β-haematin, it was further proposed that the free monomers are drawn to the crystal lattice by the interactions formed on the surface of the crystal. These include possible π-π interactions between the porphyrin rings, dispersion and van der Waals interactions to the methyl and vinyl groups, and hydrogen bonding to the free propionic acid groups.[60,61]

_____

The crystals obtained by Straasø *et al*. reportedly consist of a major and a minor phase, where the major phase is constructed of the more stable $cd\overline{1}_1$ dimers, and the minor phase of $cd\overline{1}_2$ dimers.[60] It is suggested that the *cd2(±)* dimers adsorb onto the outside of the formed crystal faces (Figure 10). Here, they would hinder adsorption of the $cd\overline{1}_1$ or $cd\overline{1}_2$ dimers onto the crystal face, which would impede further crystal growth. It is considered that this might be the reason why only relatively small haemozoin crystals were isolated until now, and a single crystal X-ray structure has not yet been obtained.
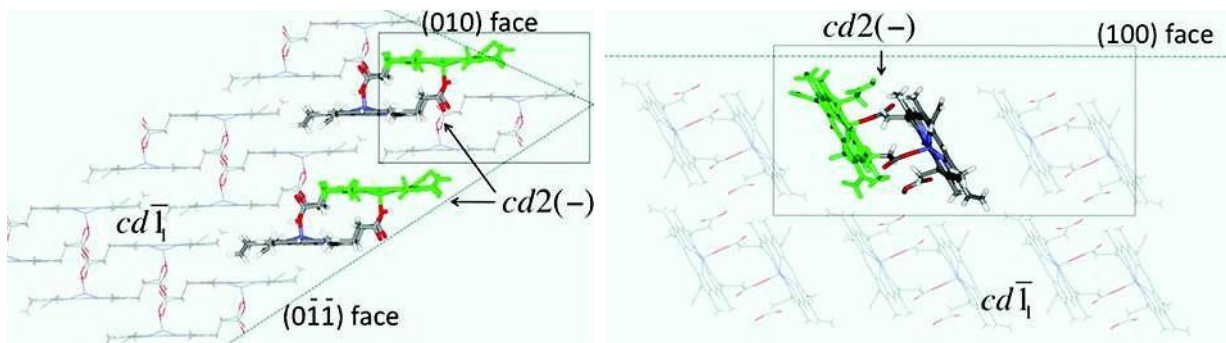
Figure 10: The packing arrangement of the major phase as proposed by Straasø *et al*.

showing face {010} and face {100}.[60]

The adsorption of the cd2(-) dimers is shown onto face {010} (left) and face {100} (right) of the major phase,

which comprises an ordered array of cd $\overline{1}_1$ dimers.

_____

1. 3 ANTIMALARIAL TREATMENTS

1.3.1 Current antimalarial treatment

Since the use of quinine as an extract of the *Cinchona* bark,[6] more antimalarial drugs have been developed and subsequently approved by the Food and Drug Administration (FDA) for the treatment of malaria. However, with the emergence of resistant strains against these drugs, the WHO has stipulated recommended guidelines for the treatment of malaria in order to achieve the optimal results in combatting this disease.

In general, a three day artemisinin-based combination therapy (ACT) is recommended,[62] where this comprises a combination treatment of more than one drug with different modes of action, with at least one of these drugs being an artemisinin (AR) derivative (Figure 11 and Figure 12). With the artemisinin derivatives having a rapid mode of action, it is combined with slow-clearing drugs to remove remaining parasites.[63] As a consequence of combination therapy, more than one mode of action is achieved, and the risk of the development of resistant strains is minimised. In combination with this treatment, a single dose of primaquine (PQ) is administered prior to the ACT treatment, to reduce transmissibility.[62]

Existing ACTs that are available for clinical use include arthemether (AM) and lumefantrine (LUM) (sold as Coartem®, distributed by Novartis),[64] artesunate (AS) and amodiaquine (AQ) (sold as Coarsucam™ or Artesunate/Amodiaquine Winthrop®, distributed by Sanofi-Aventis),[65] artesunate (AS) and mefloquine (MQ), (distributed by Cipla),[66] dihydroartemisinin (DHA) and piperaquine (PIP) (sold as Eurartesim®, distributed by Sigma-Tau),[67] or artesunate (AS) and sulfadoxine/pyrimethamine (SP).[62] In the cases of

21

uncomplicated *Plasmodium vivax*, *Plasmodium ovale*, *Plasmodium malariae*, and *Plasmodium knowlesi*, ACT or chloroquine (CQ) could be administered.[62]

It is recommended that if a patient tests positive for the human immunodeficiency virus (HIV) and is being treated with efavirenz or zidovudine, that artesunate (AS) and amodiaquine (AQ) are not administed, and if a patient is being treated with the antibiotic co-trimoxazole, that artesunate (AS) and sulfadoxine/pyrmethamine (SP) are not administered. The two main reasons for these recommendations are related to interference, which could reduce the efficacy of the drugs, and adverse drug interactions, which could affect the patient.[62]

Furthermore, within the first trimester of pregnancy, pregnant women are treated with a combination of quinine (QN) and clindamycin (CL), or chloroquine (CQ). For chemo preventative treatment in malaria regions, sulfadoxine-pyrmethamine (SP) is administered in the first and second trimester of pregnancy, and to infants under the age of 12 months. A combination of amodiaquine (AQ) and sulfadoxine-pyrmethamine (SP) is administered to children under the age of 6 years for chemo preventative treatment.[62]

Lumefantrine (LUM)

Sulfadoxine

Pyrimethamine
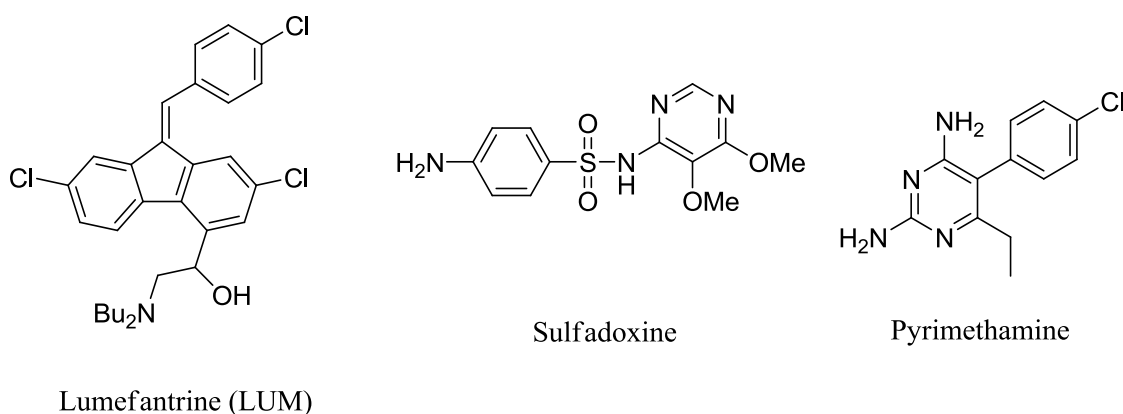
Figure 11: Co-drugs currently used for the treatment of malaria.

22

Artemisinin (AR)

Dihydroartemisinin (DHA)   Artemether (AM)

Artesunate (AS)

Chloroquine (CQ)   Amodiaquine (AQ)   Quinine (QN)

Primaquine (PQ)   (-)-Mefloquine (MQ)   (+)-Mefloquine (MQ)
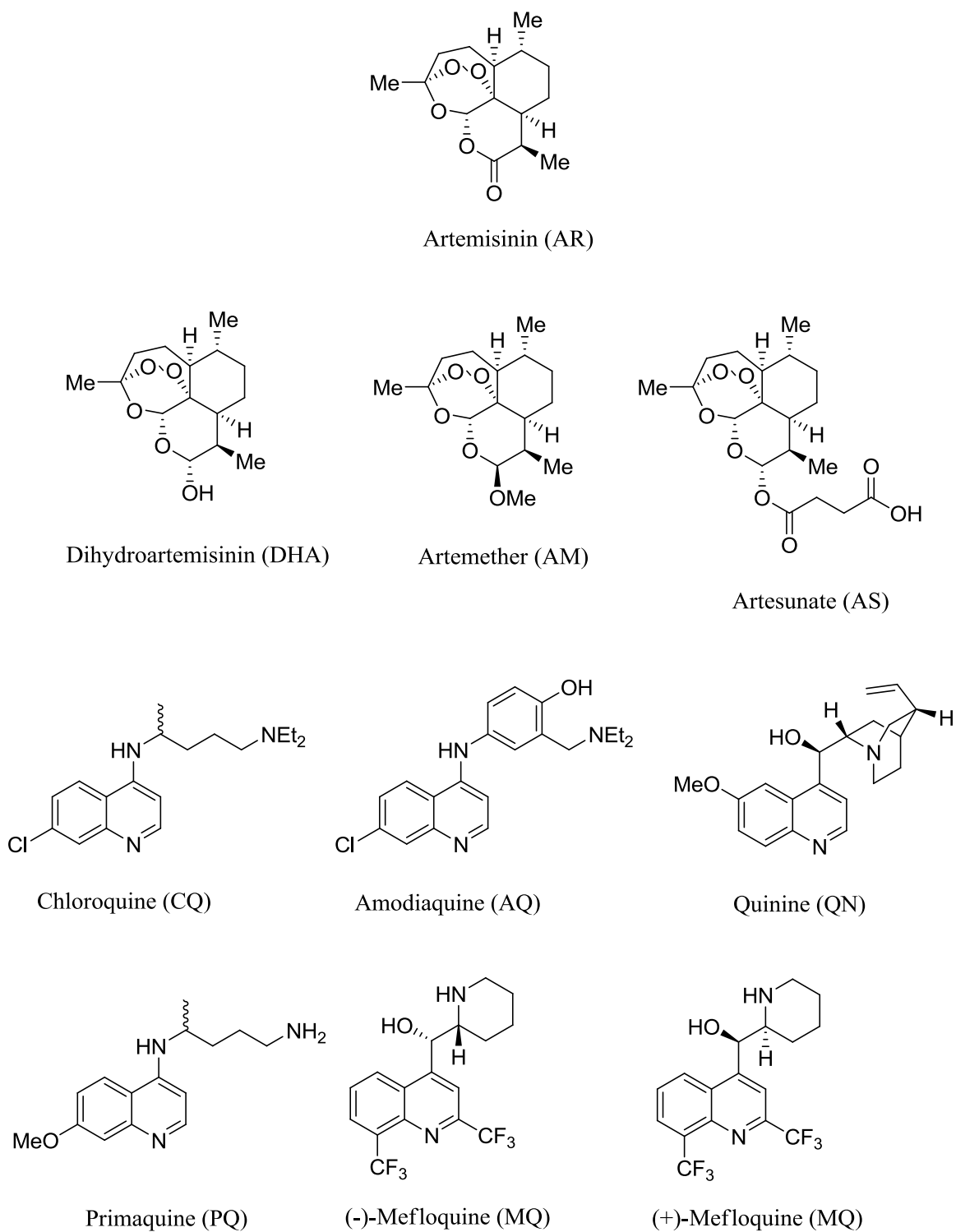
Figure 12: Artemisinin and quinoline-based drugs currently used for the treatment of malaria.

In July 2015, after 30 years of development by GlaxoSmithKline Biologicals, the world's first malaria vaccine, Mosquirix™, was approved by the European Union (EU) regulators.[68,69] However, with a reduction in malaria cases of only 36% in young children and 26% in infants, an advisory group to the World Health Organisation has recommended that the pilot study be undertaken with caution.[70] One of the main concerns is that the vaccine is ineffective if the recommended four doses are not administered.

Even with the vaccine not being as effective as initially anticipated, the pilot study continues with the hope of developing a more potent vaccine in time. To date, ACTs and chloroquine are still the recommended treatment for malaria, but with the rapid development of resistant strains,[2] the great need for the development of new antimalarial drugs still remains.

1.3.2 Current drug resistance and modes of action

Even though the exact mechanisms of antimalarial drug action are still unknown, a significant amount of research has been performed in understanding these modes of action. It is believed that drug resistance is mainly a result of incomplete clearance of the parasite from the patient's blood after treatment, as well as the ineffective administering of these treatments.[62] Moreover, the occurrence of co-drug resistance, where the resistance of one drug results in the resistance of more drugs of the same family, causes more drugs to be ineffective against new resistant strains of malaria.[62]

1.3.2.1 Quinoline-based drugs

Chloroquine and related quinoline drugs are primarily active in the blood stage of the parasite's life cycle, where they selectively penetrate the food vacuole. It is postulated that with the quinoline being a weak base, the drug could easily be protonated. One explanation is

that it crosses the food vacuolar membrane and concentrates within the acidic food vacuole where it is protonated, by means of a method known as pH trapping.[71,72]

Studies have shown that quinoline drugs might have two possible mechanisms of action. During the blood stage of the parasite's life cycle, host haemoglobin is digested and the iron centre is oxidised, whereupon the resulting toxic free haem, also known as ferriprotoporphyrin IX (Fe(III)PPIX), is released.[19] At this point, the toxic free haem is crystallised into a non-toxic form, known as malaria pigment or haemozoin. It is during this detoxification process that the presence of quinoline drugs brings about inhibition of haemozoin formation, which subsequently results in parasite death.[73] It has been suggested that the quinoline drugs might adsorb onto the haemozoin crystal surface, impeding further crystal growth.[54,73] Furthermore, crystal structures have been obtained of drug-haem complexes, indicating that the quinoline drugs complexes with the free haem, leaving a lower free haem concentration to crystallise into haemozoin.[74,75]

CQ resistance was slow to develop. With an elapsed time of 20 years, the first case of resistance was reported in the 1960's in Southeast Asia and South America, with another 20 year time period before resistance spread to East Africa.[76] In the late 1990's the *pfcrt* gene was linked to chloroquine resistance.[77–79] The mutant protein, the *Plasmodium falciparum* chloroquine resistance transporter (PfCRT), seems to alter the flux of CQ across the food vacuole membrane and thereby prevents the accumulation of the drug in the food vacuole, which renders the drug to be ineffective.[78]

_____

1.3.2.2 Artemisinin-based drugs

Artemisinin drugs are mostly active in the blood stage of the parasite, especially targeting membrane containing structures within the malaria infected cells, such as the plasma membrane, the food vacuolar membrane, the nuclear envelope, the endoplasmic reticulum, and the mitochondria membrane.[80] Studies have shown activity against trophozoites, rings, schizonts**,** and gametocytes. [81–83] However, exactly which of the stages in the life cycle is targeted most, is still under debate.[84]

Even with artemisinin-based drugs being most effective for malaria treatment, little is yet known about the mechanism of drug action. It is suggested that the interparasitic free haem or iron interacts to assist in the initial breaking of the endoperoxide bridge of the artemisinin drug, thereby releasing toxic free radicals to the surroundings.[85,86] It is believed that these free radicals might react with parasite cell constituents (in particular membranes), or that these free radicals again interact with haem to induce a more toxic form of haem, which results in parasite death.[86]

The occurrence of the world's first artemisinin resistance was reported in 2008 in western Cambodia.[87,88] Six years later, Ariey *et al.* were able to identify the K13-propeller polymorphism as a molecular marker of AR resistance from the ART-resistant F32-ART5 parasite line.[89] To date, more than 50 K13 mutant alleles have been identified, where each carries a single nucleotide polymorphism that changes the amino acids, and thus the biological structure and function in the "propeller region" of the gene.[87,90]

1.3.3 The development of new types of antimalarial drugs in an attempt to overcome drug resistance

Great success has been achieved with the development of bis-quinoline compounds, where two quinoline moieties are connected via a long alkyl chain. It was shown that the length of this linker chain affects the activity of the molecule.[91] Several bis-quinoline compounds with similar activities to that of CQ have been developed. However, these compounds were found to exhibit greater activity against CQ-sensitive strains, with prolonged duration of action.[92,93] Piperaquine and Hydroxypiperaquine are considered the most successful bis-quinolines to date, where these two compounds exhibited greater activity than CQ against both CQ-sensitive and CQ-resistant strains of malaria (Figure 13). Piperaquine is currently used in China as part of a short-course artemisinin-based combination treatment, trading as CV8®.[94] Also, with the growing sulfadoxine–pyrimethamine resistance in East and Southern Africa, it has been shown that dihydroartemisinin–piperaquine could be used as an alternative antimalarial treatment during pregnancy.[95]
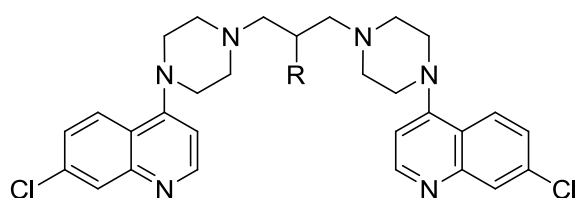
R = H, Piperaquine; R = OH, Hydroxypiperaquine

Figure 13: The chemical structures of Piperaquine and Hydroxypiperaquine

Owing to the great success of artemisinin-combination treatment in overcoming new resistant strains of the malaria parasite, a new research focus is set on developing hybrid antimalarial drugs, which could interact at more than one target site.

A more recent trend is the development of hybrid antimalarial drugs with vastly different pharmacophores.[96] In an attempt to overcome CQ-resistance, the molecular structure of CQ was combined with that of clinically available drugs which is able to inhibit the activity of the protein responsible for the emergence of CQ resistance, the *Plasmodium* transmembrane protein, PfCRT.[97] Two examples are the CQ combinations with Impramine,[98] and Artemizole,[99,100] where these hybrid drugs were found to be active against both CQ-sensitive and CQ-resistant strains (Figure 14).
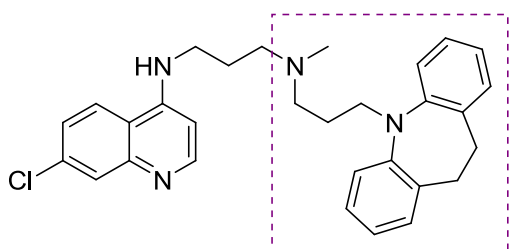
CQ-impramine hybrid drug   Impramine
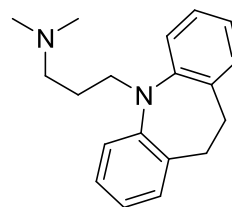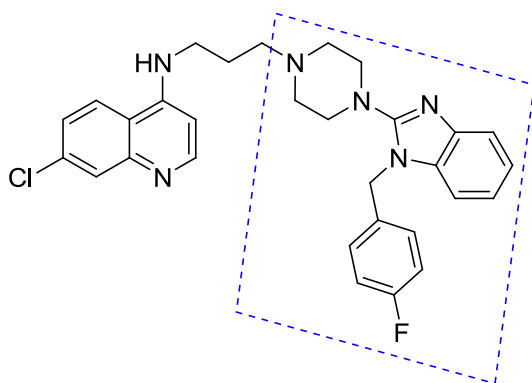
CQ-astemizole hybrid drug   Astemizole
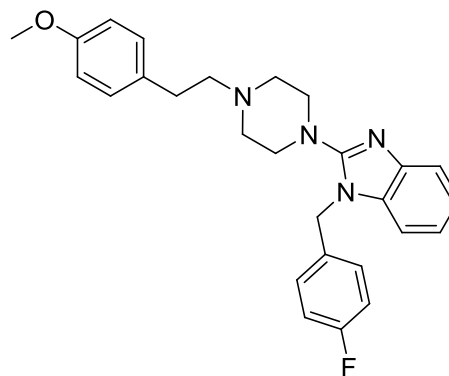
Figure 14: The CQ-containing hybrid compounds, and the chemical structures of Impramine and Astemizole.[98–100]

_____

In an attempt to promote dual mechanism of action, different classes of antimalarial drugs have also been combined. For instance, QN and MQ were combined with Artemether (AM) to obtain QN-AM and MQ-AM hybrids (Figure 15).[101,102] These compounds were found to be active *in vivo* (comparable to ART) against CQ-resistant strains, but no substantial evidence has been obtained with regards to the mechanisms of action.

QN-AM   MQ-AM
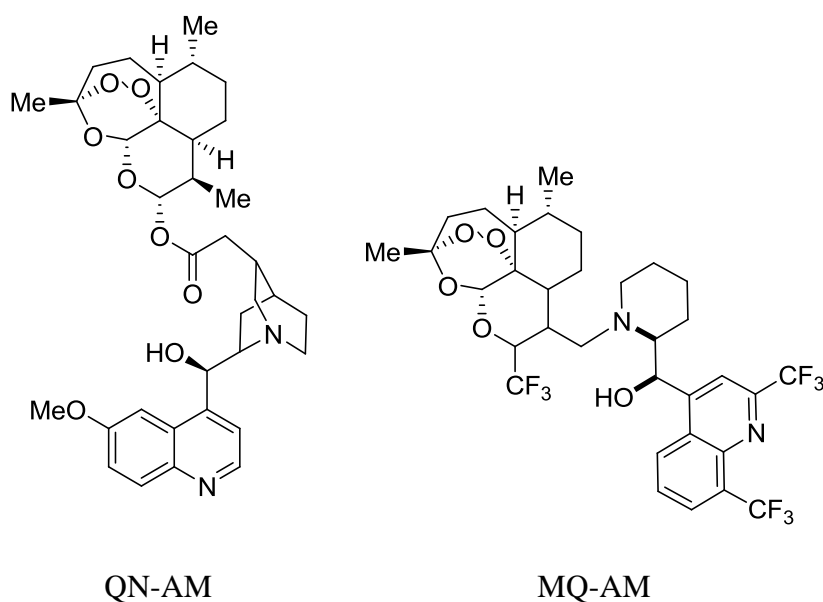
Figure 15: Artemether-containing hybrid compounds.[101,102]

1.3.4 Strategies and methods used in antimalarial drug discovery

Current methods used in modern drug discovery, include chemical alteration of existing drugs, whole-cell high throughput screening of drug libraries (HTS), and the development of new drugs based on structure-activity pharmacophore modelling.[103–105] In the latter case, a new scaffold would be preferable to currently-used scaffolds (such as quinoline) to which resistance is known. Of these three methods, especially since the exact modes of action of

antimalarial drugs are still unknown, the whole-cell HTS method is found to be the most promising in finding new lead compounds, where these compounds are already optimised with the required pharmacokinetic and pharmacodynamic properties in order to permeate cell membranes, as well as to interact at the desired target area.

However, with the exact mechanism of drug action still unknown, the rational optimisation of these newly identified lead compounds for the treatment of malaria, is still a challenge. This highlights the importance of gaining a greater understanding of the mechanism of antimalarial drug action, for future drug development.

Given their clinical success, quinoline antimalarial drugs have been the focus of numerous studies. There is substantial evidence that points to the mechanism of drug action of this class of compound, where inhibition of beta-haematin formation in vitro suggests inhibition of haemozoin formation in vivo. With the process of haemozoin formation being chemical in nature, it is considered an important drug target for further exploration..[106] Furthermore, the mechanism of chloroquine resistance is known to be distinctly separate from the mode of action, and thus haemozoin remains a valuable target against which new drugs could be developed to overcome this obstacle in the treatment of malaria. Therefore, the understanding of the mechanism of haemozoin formation and quinoline drug development are still considered as valid research focal points.

_____

1.4 β-HAEMATIN GROWTH AND INHIBITION BY QUINOLINE-BASED DRUGS

1.4.1 Physical evidence for β-haematin growth inhibition by quinoline drugs

With quinoline-based drugs being one of the main classes of drugs used in current ACT treatment, a significant amount of research has been performed to better understand their mechanism of action. As mentioned in Section 1.3.2.1, various studies have shown that these drugs inhibit haemozoin growth inside the parasitic food vacuole.

In 2007, Solomonov *et al.* performed a thorough study to investigate β-haematin crystal growth.[73] β-Haematin crystals were grown in two solvent systems, chloroform, and a methanol and dimethyl sulfoxide mixture, as well as in the presence of quinine and chloroquine. The resultant crystals were examined by transmission electron microscopy (TEM), grazing incidence X-ray diffraction (GIXD), electron diffraction (ED), synchrotron X-ray powder diffraction (XRPD), coherent grazing exit synchrotron X-ray scattering, micro-Raman spectroscopy, and infrared attenuated total reflectance (IR-ATR) spectroscopy. They found that the crystals grown in the presence of a drug, formed slower, and were cylindrically tapered at the edges (Figure 16). This indicated that the drugs most likely acted as inhibitors at the fastest-growing (least expressed) crystal faces, thereby inhibiting further crystal growth.
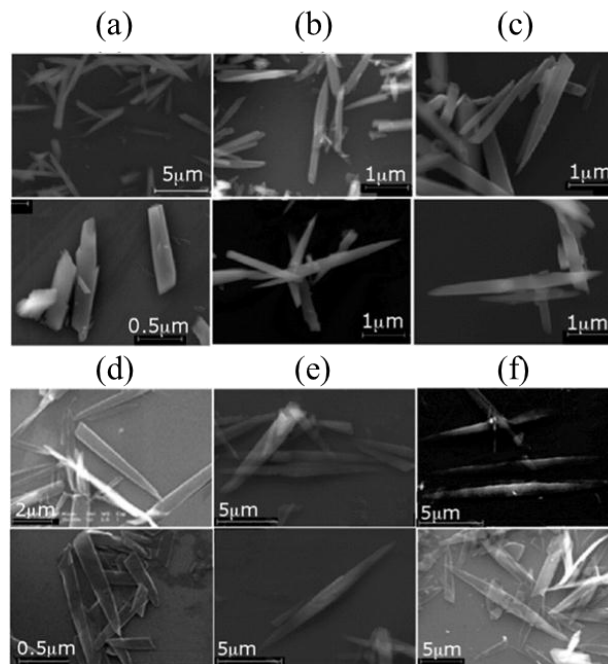
Figure 16: SEM images of β-haematin collected by Solomonov *et al*.[73]

The crystals were grown in methanol and dimethyl sulfoxide (a-c), and chloroform (d-f), where they were also

grown in the absence of drug (a and d),10% quinine (b and e), and 10% chloroquine (c and f).

In a more recent study, Olafson *et al.* investigated β-haematin growth by means of time-resolved *in situ* atomic force microscopy (AFM) (Figure 17).[49] A citric acid buffer-saturated solution of octanol, at pH 4.8, was used, since the crystals that were obtained from this solution best represented the morphology of haemozoin crystals extracted from *Plasmodium falciparum*. By observing a large crystal surface, a classical layer-by-layer growth was observed. For each layer that was formed, new layers formed on top of these, resulting in islands, with step-like edges. Upon nucleation of a new layer, it transformed from an initial isometric to an anisometric shape, where these new layers grew the fastest in the *c* direction (Figure 17 (a)).
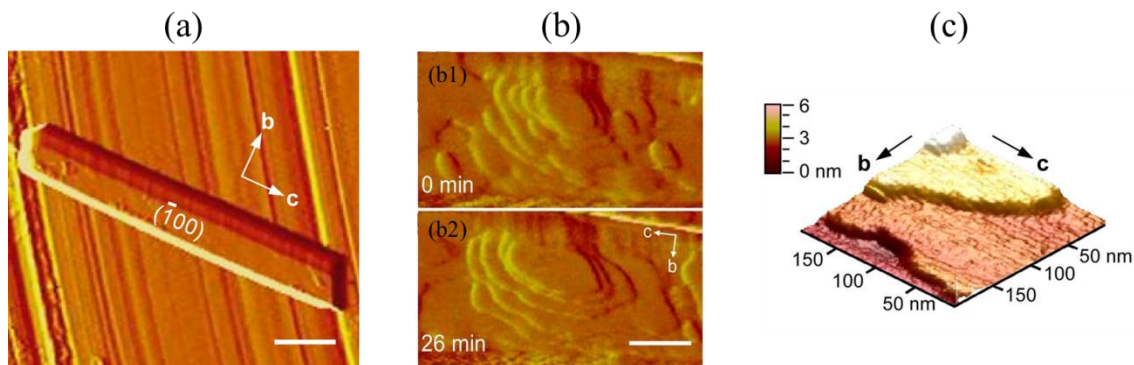
Figure 17: The AFM images of β-haematin crystals collected by Olafson *et al*.[49]

An AFM image is collected of a β-haematin crystal (a), viewed onto the largest face, face {100}, where the

b and c growth directions are indicated. The newly formed islands were monitored over time (b1 and b2). An

AFM 3D height image is also collected, showing the newly formed layers (c).

During this study, it was also noticed that new layers grew slower in the presence of chloroquine, with more uneven edges.

These physical findings reported by Solomonov *et al.* and Olafson *et al.*, greatly strengthened the idea that quinoline compounds inhibits β-haematin crystal growth. As mentioned in Section 1.3.2.1, it is believed that these drugs act by means of two modes of inhibition, one where the drug adsorbs onto the β-haematin crystal surface thereby preventing further crystal growth, and the second being the formation of a drug-haem complex. However, to what extent these two processes might compete with one another, has still not been conclusively resolved.

33

1.4.2 Inhibition by adsorption of the drug onto the crystal surface

One of the proposed mechanisms of drug inhibition is the adsorption of drugs onto the β-haematin crystal surface, whereby the growth sites are blocked and further crystal growth is inhibited. Even though no physical evidence for this argument, other than the slower β-haematin crystal growth in the presence of a quinoline drug, has been obtained, it is believed that this is the stronger competitor in β-haematin crystal growth inhibition.[34,107,108]

Webster *et al.* performed Resonance Raman Spectroscopy on haemozoin within the food vacuole of *Plasmodium falciparum* trophozoites.[109] Upon treating the infected cells with CQ, it was found that a number of bands commonly observed in the spectrum of haemozoin decreased in intensity, and were in some cases shifted. Strangely, the characteristic bands of CQ were absent. Therefore it was postulated that the quinoline moiety in CQ forms intermolecular π-π interactions to the porphyrin structures of haemozoin, thereby hindering further crystal growth.

Olafsen *et al.* strengthened this argument by visually investigating the β-haematin crystal layer and step growth at various concentrations of chloroquine drug over time.[49] Chloroquine concentrations of 0-2 μM were used, where a complete halt in layer formation was observed at 2 μM. It is argued that for a 1:1 chloroquine-haem complex to form, it would not be sufficient to totally stop layer formation at a 2 μM concentration, since there would still be a sufficient amount of free haem left to form new layers. However, this does not rule out the idea that complex formation might still occur.

Upon investigating the theoretical crystal morphology, Buller *et al.* further proposed how clinically-relevant antimalarial quinoline drugs might adsorb onto the fastest growing face of

the β-haematin crystal, at pH 4.8.[54] A Hartman-Perdok computational approach was used, using the Cerius2 software package, where the crystal morphology was optimised. The quinoline drugs structures were minimised using a universal force field, whereupon these were manually fitted to the crystal surface to obtain the maximum interaction, as judged visually. Only the monoprotic forms of the inhibitors were modelled, where the quinoline nitrogen atom of CQ would be neutral and the terminal amine nitrogen atom would be protonated. However, at pH 4.8, both the terminal and quinoline nitrogen atoms of CQ would in fact be protonated.[110]

Upon viewing the crystal surface of the fastest growing face (the one being expressed the least), large crevices are observed where these drugs could adsorb into (Figure 18). It is considered that possible π-π interactions could form between the quinoline moiety and the porphyrin structure, where additional hydrophobic interactions between the quinoline moiety and methyl groups on the porphyrin structure could form. Furthermore, by including a bridging water molecule, the formation of hydrogen bonding interactions between amine group on the side-chains of the inhibitors and the trapped water molecules, and then again between the water molecule and a carbonyl group on the crystal face, appear to strengthen the adsorption of the inhibitors onto the crystal face. For the adsorption of MQ onto the crystal face, it is proposed that with the large -CF_3 substituents, intermolecular C-F···H interactions form between the inhibitor and the vinyl hydrogen atoms on the porphyrin structure.[54]
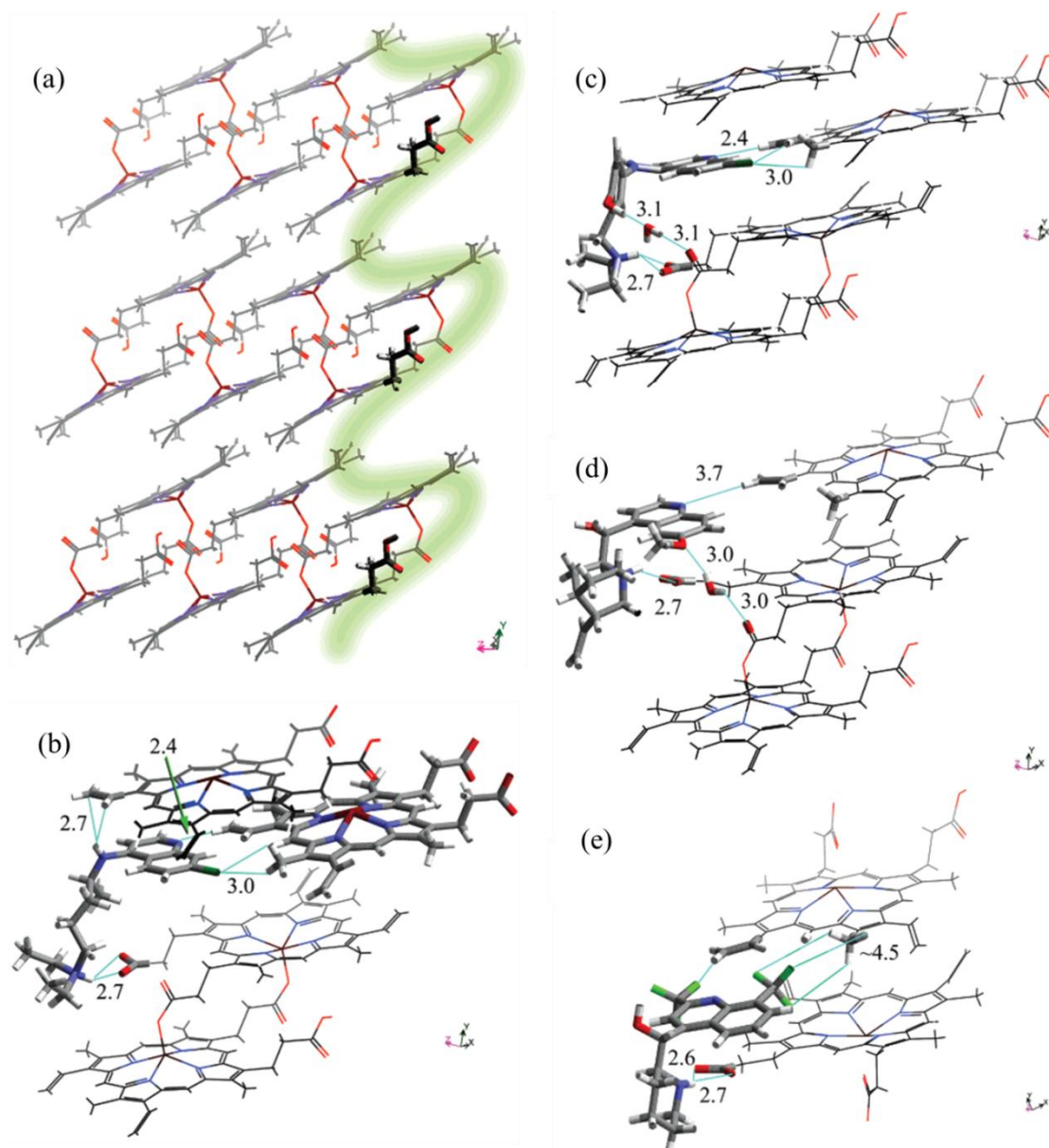
Figure 18: Molecular modelling results presented by Buller *et al.*[54]

The surface of the fastest growing face {001}, is shown (a), and the crevices are highlighted in green.

The proposed adsorption onto this face for chloroquine (b), amodiaquine (c), quinine (d), and mefloquine (e),

in the monoprotic form is shown, indicating the measured intermolecular interaction distances.

_____

Even though the molecular modelling results presented by Buller *et al.* were not investigated thoroughly by means of computational docking or adsorption methods, the study gave insight into how the quinoline antimalarial drugs might adsorb onto the β-haematin crystal surface, and which interactions might be important to promote adsorption.

Further research was performed by Dubar *et al.*,[111] where the mechanism of antimalarial drug action of ferroquine (FQ), a ferrocene-containing quinoline inhibitor, and analogues of ferroquine, were investigated (Figure 19). A similar computational approach has been used as discussed by Buller *et al.*, where the adsorbed geometries of the molecules onto the fastest growing crystal face {001}, and the largest crystal face {100}, were adjusted to fit that of CQ in the adsorbed state. The adsorbed geometries were minimised and the binding energies were calculated by means of density functional theory calculations (DFT).

Ferroquine (FQ)   Ruthenoquine (RQ)

Methylferroquine (Me-FQ)   Methylruthenoquine (Me-RQ)
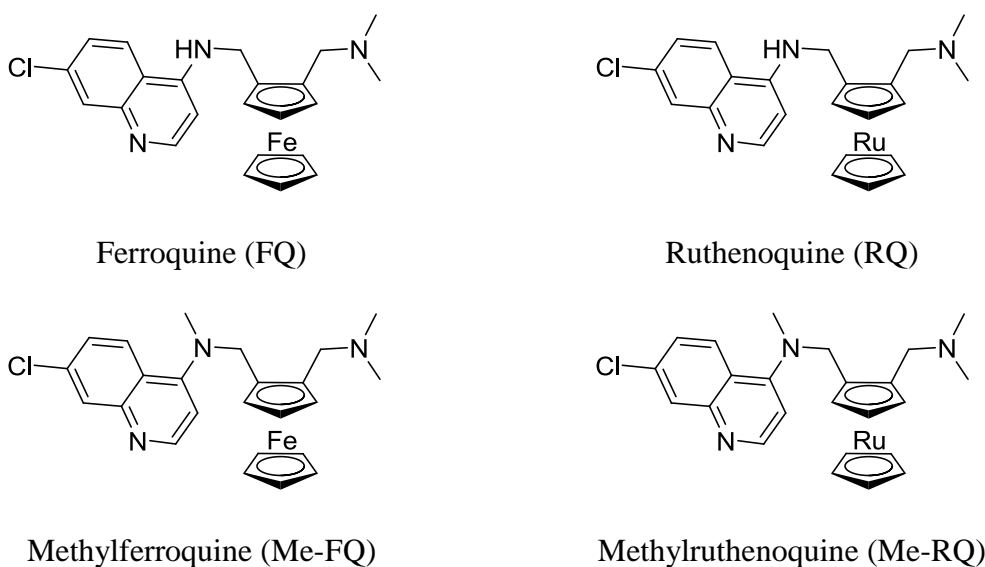
Figure 19: The ferrocene-containing quinoline inhibitors investigated by Dubar *et al.*[111]

For the adsorption onto the fastest growing crystal face, similar adsorption geometries were proposed as suggested by Buller *et al.*, where the formation of hydrophobic interactions between the quinoline moiety of the inhibitor and the methyl groups on the porphyrin structure is found (Figure 20). However, for the adsorption of FQ in the diprotic form onto the most expressed crystal face (Figure 21), hydrogen bonding interactions are observed between the amine hydrogen atoms on the side-chain of the inhibitor and free carbonyl groups on the crystal surface. The formation of additional hydrophobic interactions between the quinoline moiety of the inhibitor and methyl groups on the crystal surface was reported.[111]
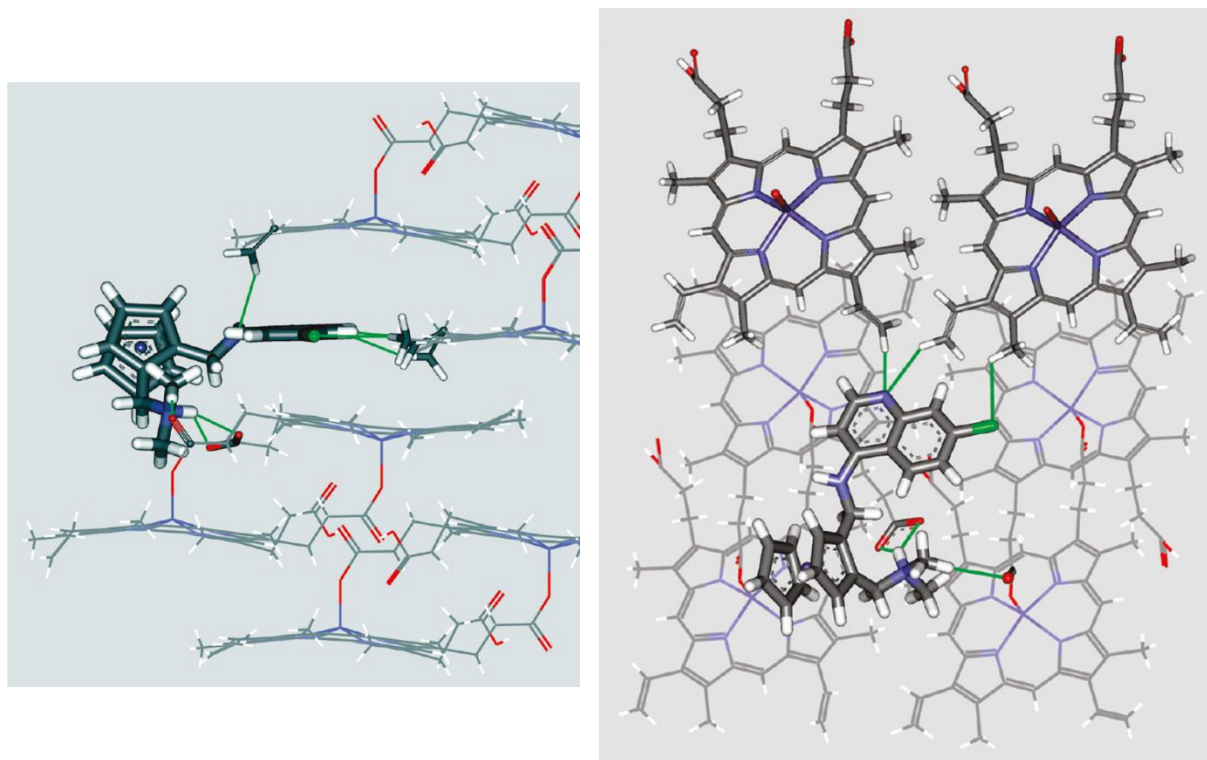
Figure 20: Adsorption of FQ onto face {001} as proposed by Dubar *et al.*[111]

The adsorption of FQ onto face {001} in the monoprotic form, as viewed from the side of the crystal face(left), and as viewed from the top of the crystal face (right), is shown. The intermolecular interactions that form are indicated by green lines.
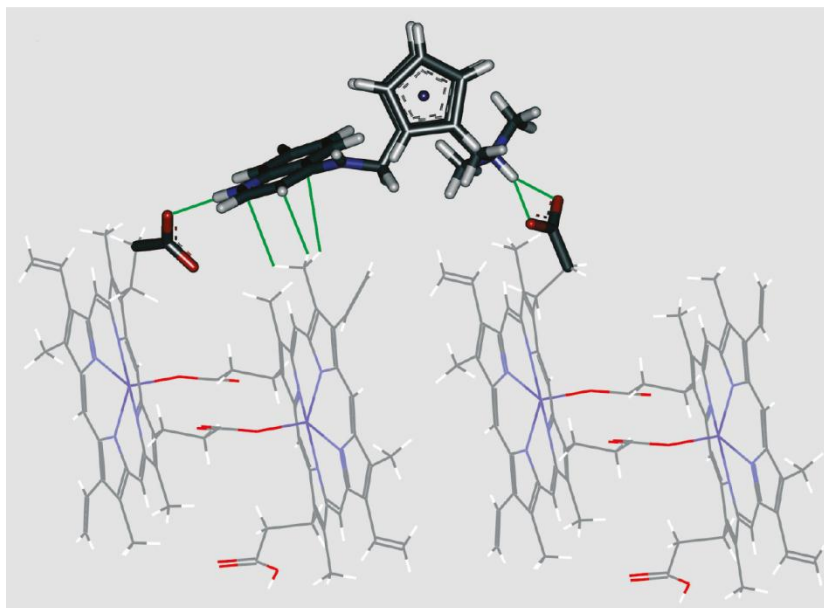
Figure 21: Adsorption of FQ onto face {100} as proposed by Dubar *et al.*[111]

The adsorption of FQ onto face {100} in the diprotic form, as viewed form the side of the crystal face is shown.

The intermolecular interactions that form are indicated by green lines.

It is believed that the formation of radicals might play a contributing part in the breakdown of the parasite membrane. FQ has been reported to form hydroxyl radicals from hydrogen peroxide commonly found in the parasitic food vacuole.[112] Therefore, by performing electron paramagnetic resonance (EPR) spin trapping experiments, Dubar *et al.* have shown that FQ and methylferroquine (Me-FQ) are able to generate hydroxyl radicals from hydrogen peroxide.[111] Furthermore, by performing ultrastructural studies, the breakdown of the parasite membrane is seen in the presence of these two compounds. As a result, it is believed that the formation of radicals might play a contributing part in the breakdown of the parasite membrane.   However, this observation is not seen for the ruthenium analogues, ruthenoquine (RQ) and methylruthenoquine (Me-RQ). Therefore, the mechanism of action by

39

adsorption onto the fastest growing crystal surface of β-haematin is still a viable mechanism of antimalarial drug action for these compounds.

A brief computational investigation of the adsorption of multiple artemisinin-based compounds onto β-haematin has been performed by Solomonov *et al.*[73] However, as the focus of this project is on investigating the mechanism of β-haematin growth inhibition by quinoline-based drugs, and with the mechanism of action of artemisinin drugs considered to be distinctly different to that of quinoline drugs, their findings will not be discussed here.

1.4.3 Complex formation

A competing argument to that of crystal inhibition by adsorption, is the formation of a drug-haem complex, and thereby the removal of free haem from the food vacuole cytoplasm of *Plasmodium falciparum*.

The idea of the drug binding to free haem was first introduced by Dorn *et al.*, where isothermal titration microcalorimetry (ITC) experiments were performed to measure the heats of dilution and mixing, by titrating haematin in a phosphate buffer with quinoline antimalarial drugs.[113] From this data, association constants (K_a values), enthalpy change ($\Delta H°$) and stoichiometry (n) were obtained. A good correlation between haematin polymerisation inhibition (common understanding at that time) and parasite growth inhibition for quinoline drug-containing blood schizonts were observed.

Another breakthrough occured in 2008, when de Villiers *et al.* from our lab determined the first crystal structure of the halofantrine-Fe(III)PPIX complex by means of single X-ray

diffraction, where the drug coordinates to the Fe(III)PPIX via its hydroxyl group in the side-chain. (Figure 22).[74]
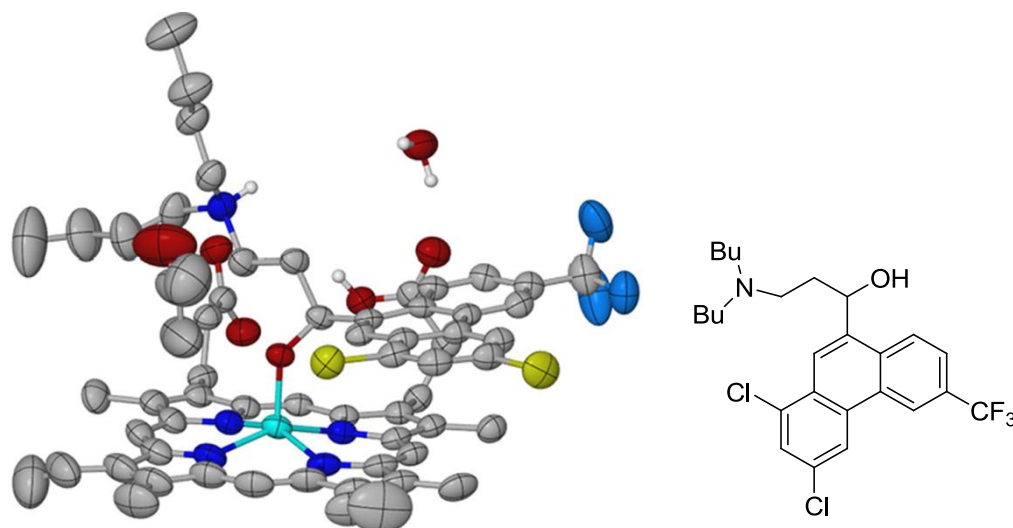
Figure 22: The chemical structure of halofantrine and the halofantrine-Fe(III)PPIX complex reported by de Villiers *et al.*[74]

The chemical structure of halofantrine (right) and the X-ray crystal structure of the halofantrine-Fe(III)PPIX complex (left) are shown. Only polar hydrogens are shown for clarity. The atom colours are as follow: C, grey; H, white; Cl, yellow; F, Prussian blue; Fe, cyan; N, blue; O, red.

The de Villiers research group continued their investigation on the complex formation, where they were able to obtain the crystal structures of a racemic *erytho* mefloquine-Fe(III)PPIX complex (Figure 23),[114] a quinine-Fe(III)PPIX and a quinidine-Fe(III)PPIX complex,[75] as well as validate the existence of these complexes in acetonitrile, by means of electrospray ionisation mass spectrometry (ESI-MS), extended X-ray adsorption fine structure (EXAFS), and UV-vis spectroscopy.[114] In each case the quinoline methanol compound is observed to coordinate to the Fe(III) centre via the deprotonated hydroxyl group.
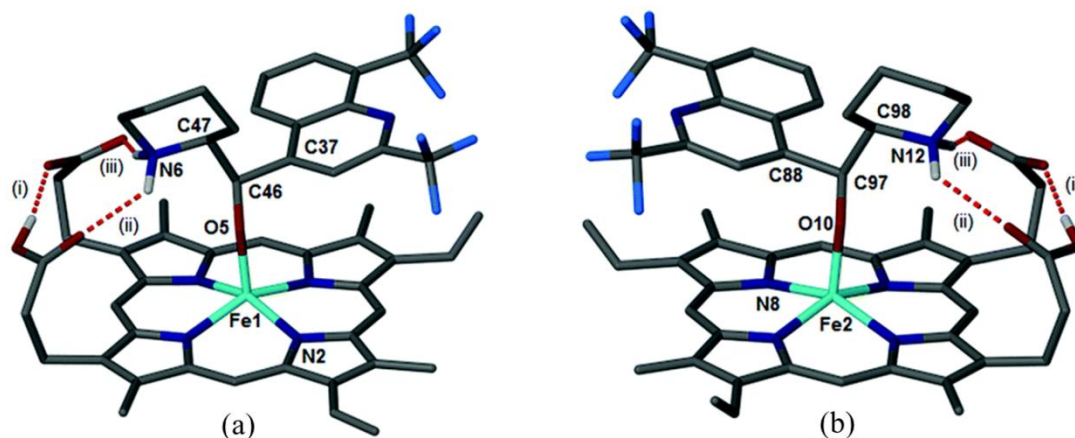
Figure 23: The two enantiomeric mefloquine-Fe(III)PPIX complexes reported by Gildenhuys *et al*.[114]

Showing the two mirrored enantiomers found in the racemic the erytho mefloquine-Fe(III)PPIX complex. Only

polar hydrogens are shown for clarity. The atom colours are as follow: C, grey; H, white; F, Prussian blue;

Fe, cyan; N, blue; O, red.

More recent in vitro studies performed within our research group, by S Fitzroy, has indicated that a decrease in the yield of β-haematin formation is observed at high drug concentrations. It was therefore suggested that adsorption onto β-haematin might be relevant at low drug concentrations, where complexation may be relevant at high drug concentrations.

Even though drug-complex formation might play a lesser role in β-haematin crystal growth inhibition at low drug concetrations, the concrete structural evidence obtained for the existence of these complexes could not be ignored. Therefore, this mechanism of inhibition is still considered relevant in the overall study of β-haematin crystal growth inhibition.

For the purposes of this study, complexation was not considered and the primary focus was set on β-haematin inhibition by adsorption of antimalarial drugs onto the crystal surface.

_____

1.4.4 β-Haematin growth inhibition assays

Determining the activity of antimalarial drugs is a vital process in identifying targeted drug treatments for the disease. Even though many assays have been developed for the *in vivo* activity testing against malaria, such as against D10 and NF54 strains, the development of assays for determining β-haematin growth inhibition is still a developing process.

Currently, three biomimetic assays are commonly used for determining the ability of compounds to bring about β-haematin growth inhibition, one in an acetate buffer (referred to as the acetate $BHIC_{50}$ assay)(Table 1),[115] and more recently, two in lipophilic detergent solutions, Tween 20,[116] and Nonident P-40 (NP40) (referred to as the NP40 $BHIC_{50}$ assay) (Table 1).[117,118] The development of these assays has been promoted by the earlier finding of Ncokazi *et al*., that pyridine acts as a ligand and coordinates with the Fe(III) atom in free haem.[107] The subsequent formation of a *bis*-pyridyl Fe (III)PPIX complex results in a colour change in the solution, which can be measured by means of UV-vis spectroscopy at 405 nm. This allows for the quantification of the amount of free haem left in solution after a fixed incubation time, in the presence of a β-haematin inhibitor.

With the understanding that β-haematin growth is promoted in the presence of neutral lipid bodies,[43] a modified assay was developed within our research group, for determining β-haematin growth inhibition in the presence of monopalmitoyl-*rac*-glycerol (MPG) (Table 1).[53] For this assay, the inhibitors were dissolved in a citric acid buffer solution (pH 4.8), after which it is incubated for 30 minutes at 37 °C. The haematin solution (synthetic haem dissolved in 0.1 M aqueous sodium hydroxide, which was diluted with a 1:9 acetone-methanol solvent), was premixed with the lipid solution (MPG lipid in the 1:9 acetone-methanol solvent). The haematin-lipid solution was carefully added to the surface of the

inhibitor-citrate buffer solution, after which the system was incubated at 37 °C for 8 hours. During this period of time, the inhibitor was allowed to interact with the free haematin, or the β-haematin that forms in solution. Therefore, upon the addition of a pyridine solution (2.0 M, pH 7.5) and 40% acetone), the amount of unreacted free haematin was detected by means of UV-vis spectroscopy at 405 nm, from which an IC_{50} dose-response curve was obtained. This assay was then further optimised to a medium throughput method performed in 96-well plates (referred to as the lipid $BHIC_{50}$ assay).[119]

Table 1: The three $BHIC_{50}$ assays used in this dissertation.

	Acetate $BHIC_{50}$ assay	NP40 $BHIC_{50}$ assay	Lipid $BHIC_{50}$ assay
Detergent or lipid	None	NP40-detergent	MPG lipid
Buffer	Acetate buffer	Acetate buffer	Citric acid
pH	5.0	4.9	4.8
Temperature	37°	37 °C	37 °C
Incubation time	18 hours	4 hours	8 hours

When the ability of the various assays to determine β-haematin growth inhibition was compared (Figure 24), the IC_{50} activity data of NP40 $BHIC_{50}$ assay compared well to that of the lipid $BHIC_{50}$ assay, with a significant linear correlation with an R^2 value of 0.93 and a P value of <0.05.[119] On the other hand, a non-significant linear correlation with and R^2 value of 0.68 was found when comparing the IC_{50} data of the acetate $BHIC_{50}$ assay to that of the lipid $BHIC_{50}$ assay.[119] A significant correlation was, however, observed between acetate $BHIC_{50}$ values and normalised antiplasmodial activity for a range of 4-aminoquinoline

compounds when taking into account pH trapping.[120] More recently, the determined IC_{50} values of the lipid $BHIC_{50}$ assay were also shown to be in good agreement with the IC_{50} activities determined against a CQ-sensitive strain of the malaria parasite, 3D7 (Figure 24). In the latter case, a linear correlation with an R^2 value of 0.91 and a P value of <0.05 was observed.[119] This finding was quite significant, seeing that for a biological assay, more factors need to be taken into account, such as the ability of the drug to cross cell membranes and to permeate into the cell.

These correlations were indicative that the newly developed lipid $BHIC_{50}$ assay, as well as the NP40 $BHIC_{50}$ assay, are more suitable to determine the abilities of compounds to bring about β-haematin growth inhibition. Importantly, given that these two biomimetic systems more closely align with the biological formation of β-haematin, they were prioritized in the current study where data was available.

For the purposes of this project, only the biomimetic assays were used and *in vivo* testing was not performed, as other factors would contribute to antiplasmodial activity. By performing a biomimetic assay, these external factors would be eliminated. Therefore, only β-haematin inhibition by means of the adsorption of antimalarial drugs onto the crystal surface could be explored.
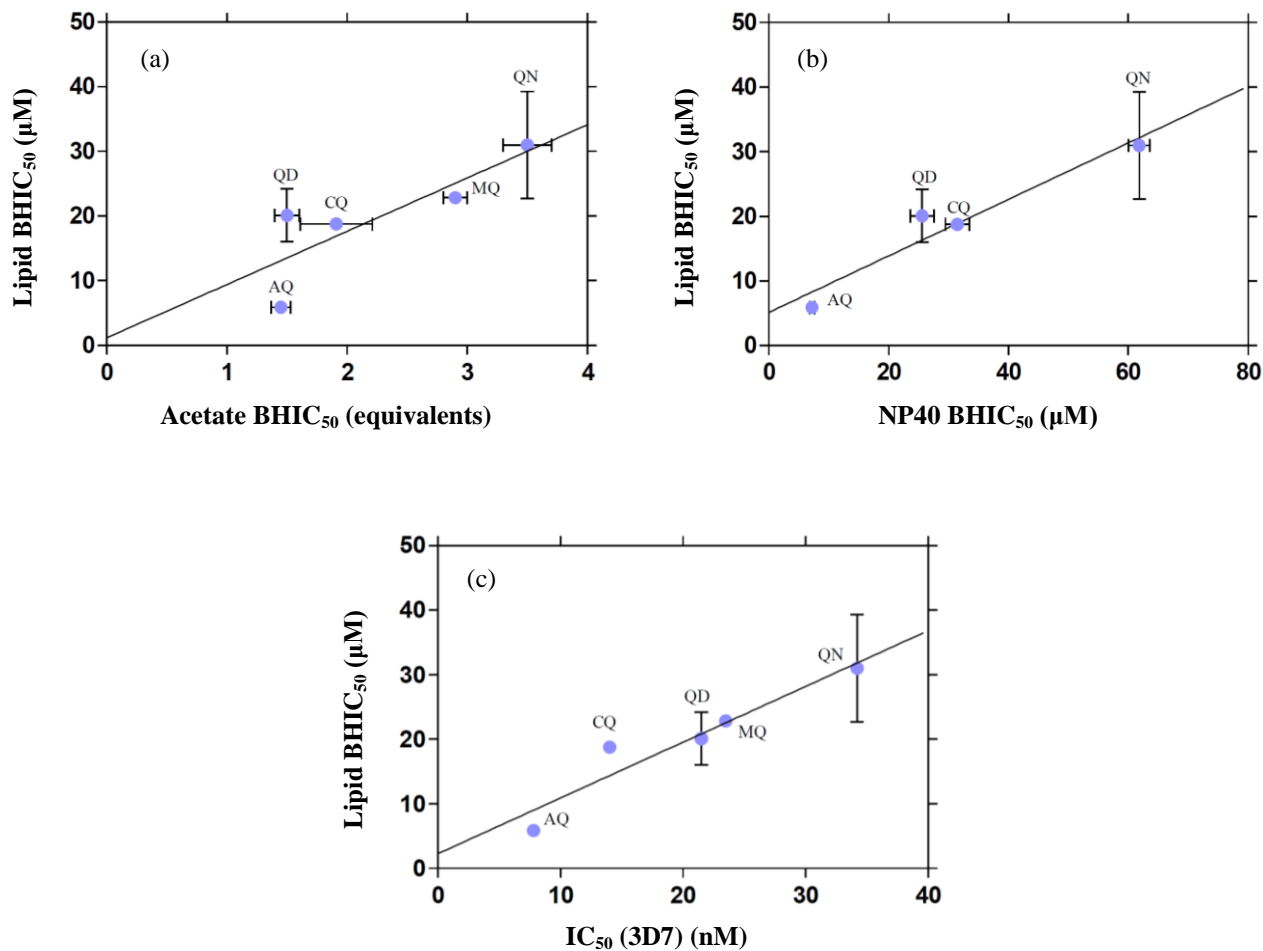
Figure 24: The Lipid BHIC$_{50}$ assay was compared to other assays by S. Fitzroy.[119]

The Lipid BHIC$_{50}$ assay was compared to the acetate BHIC$_{50}$ assay (a), the NP40 BHIC$_{50}$ assay (b), as well as

to the IC$_{50}$ activities against the 3D7 CQ-sensitive strain of the malaria parasite (c). Significant linear

correlations were found for comparing the lipid BHIC$_{50}$ activities with the NP40 BHIC$_{50}$ and the IC$_{50}$ (3D7)

activities, with R^2 values of 0.93 and 0.91 respectively, and P values of <0.05. A non-significant linear

correlation was found when comparing the lipid BHIC$_{50}$ activities against the acetate BHIC$_{50}$ activities, with an

R^2 value of 0.68.

_____

1.5 AIMS AND OBJECTIVES OF THIS PROJECT

In light of knowing the chemical and the structural composition of haemozoin and β-haematin, a new era of research has been sparked, with the focus on understanding the mechanism of β-haematin formation, as well as the inhibition thereof by antimalarial drugs. Furthermore, with growing support for the hypothesis that antimalarial drugs bring about β-haematin growth inhibition by adsorbing onto the crystal surface, and with the development of assays to determine the ability of antimalarial drugs to promote β-haematin growth inhibition, this information could be combined to evaluate the mechanism of β-haematin growth inhibition brought about by the adsorption of inhibitors onto the β-haematin crystal surface.

The main strategy for this project was to investigate the adsorption of quinoline inhibitors onto the two fastest growing β-haematin crystal faces, faces {001} and {011}, computationally, where a preferred target area could be identified. Moreover, structure-activity relationships could be investigated between the adsorption of known antimalarial drugs onto the β-haematin crystal surface and their determined β-haematin inhibition.

By gaining a greater understanding of the mechanism of antimalarial drug action, this research could be applied for future drug development, where this project fills an imperative role as part of a larger research strategy. Therefore, a significant contribution would be made in the fight against malaria.

In order to achieve the goals of this project, the objectives of this thesis were to:

1. Identify and optimise a computational protocol in order to evaluate the adsorption of small compounds onto the crystal surface computationally. For this, a small subset of quinoline compounds with existing activity data would be considered.

2. Evaluate the adsorption of clinically-relevant inhibitors onto the fastest and the second fastest growth face of β-haematin, and determine structure-activity relationships between the calculated adsorption energies and the determined β-haematin inhibition activities.

3. Extend the adsorption study to include a set of non-quinoline compounds that were synthesised by our collaborator's research group at the University of Cape Town. These compounds include a set of 2,4,5-triaryl substituted imidazole and benzamide inhibitors that were synthesised by Dr Kathryn Wicht,[121,122] and benzimidazole inhibitors that were synthesised by Fabrizio L'abbate, as part of their respective PhD projects.

4. Assess the theoretical computational model based on the information obtained from this study. The relevant molecules needed could either be synthesised or purchased, where after their β-haematin inhibition activities would be determined.

CHAPTER 2

THE ADSORPTION OF INHIBITORS ONTO β-HAEMATIN

For the first part of this project, a computational study was undertaken in order to gain a greater understanding of the mechanism of β-haematin growth inhibition by small molecule inhibiors. As mentioned earlier, we were not the first to consider this idea, as Buller *et al.* gave some insight as to how known antimalarial drugs might interact with the crystal surface (Section 1.4.2).[54] However, to date, no concrete computational investigation has been performed to strengthen their argument.

It is postulated that by investigating the adsorption of known antimalarial drugs onto β-haematin, some structure-activity correlations might be observed. The aim of the study was to determine whether a specific binding site is preferred and which molecular interactions are necessary for enhanced adsorption. Also, by considering the adsorption of these drugs onto multiple faces of the crystal, some insight might be gained as to why the two fastest growing faces, {001} and {011}, appear to be preferred over the others for inhibition, as observed by Solomonov *et al.* (Section 1.4.1).[73]

Furthermore, with a step-like formation of new layers onto the crystal surface observed by Olafson *et al.* (Section 1.4.1),[49] by investigating these newly formed "steps" and the adsorption of known antimalarial drugs thereon, a greater insight into the mechanism of β-haematin growth inhibition could be obtained.

2.1 PREPARING THE COMPUTATIONAL ENVIRONMENT

In order to proceed with the adsorption study, the computational environment had to be prepared, where the adsorption of inhibitors onto a large crystal surface would be investigated. Therefore, the more robust molecular mechanics simulations would be ideal for such a large computational system, as opposed to first principle calculations. The preparation of the computational environment would include finding an optimum force field and atomic charge method, determining which computational protocol would be suitable, as well as preparing and optimising the molecules that would be used.

For this study, the Accelrys Materials Studio software package was used, since a simulated annealing adsorption protocol was already available.[123] Although this software package is typically used to study the adsorption of molecular gasses or liquids onto substrates, it is considered that it could be used to investigate the adsorption of small organic molecules onto the β-haematin crystal surface. Moreover, the morphology protocol available in the Materials Studio suite could be used to investigate the crystal morphology, as well as prepare the crystal faces needed for the adsorption study.

By exploiting a thorough computational study, a visual insight would be obtained into how these inhibitors adsorb onto the crystal surface of β-haematin, and the adsorption energy (E_{ads}) would be calculated as the energy difference in the system before and after adsorption of the inhibitors.

This adsorption energy (E_{ads}) would take into account the substrate-inhibitor interaction energy, as well as the difference in the internal energy of the inhibitor. With the crystal being kept rigid during the simulation, a change in the internal energy would not be included in the

calculation. Therefore, E_{ads} is the difference in energy before adsorption (when the inhibitor and the crystal are separated) and after adsorption (when the inhibitor is adsorbed to the crystal). Equation 2.1 is an expression of E_{ads} :

$$E_{ads} = E_{final} - E_{initial}$$

$$= \left(E_{crystal+inhibitor}\right) - \left(E_{free\ crystal} + E_{free\ inhibitor}\right) \qquad (2.1)$$

In proceeding further, the computational environment that would best represent the molecular system (Figure 25), had to be determined and optimised. Following this, it was necessary to determine the crystal morphology in order to investigate the crystal faces. Finally, by investigating the adsorption of a subset of quinoline molecules that are similar in shape and size, adsorption trends would be more easily observed and the adsorption energies (E_{ads}) would be relatively similar and more easily comparable. The computational environment could be optimised with this subset of molecules, before investigating the adsorption of a more complex set of clinically-relevant antimalarial drugs.
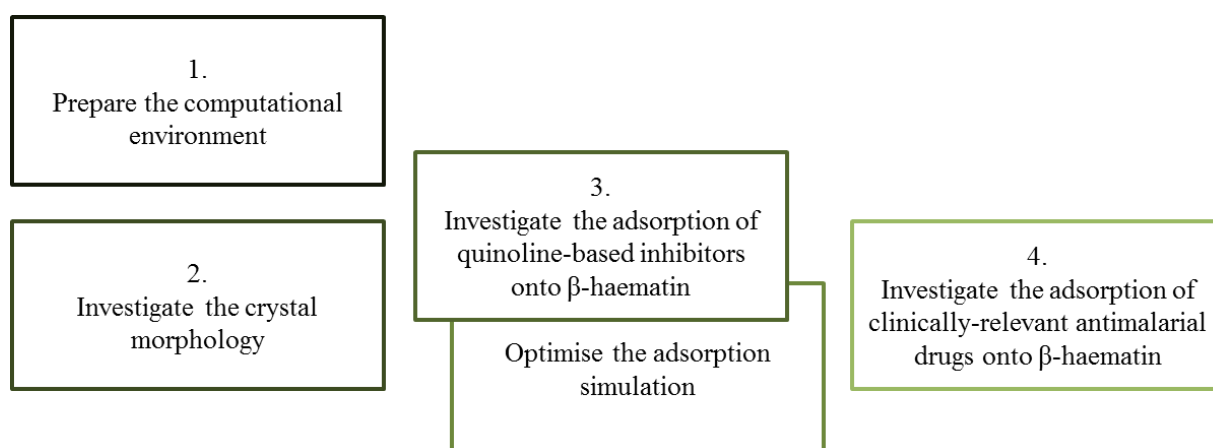
Figure 25: The computational strategy

_____

2.1.1. Optimising the force field

The first priority for this project was to choose a suitable force field that would represent all atoms within the computational system. While the CHARMM force field is normally deemed suitable for adsorption simulations,[124] it unfortunately does not account for the high-spin Fe(III) centre in the β-haematin porphyrin structure, and therefore it was not considered optimal for this study.

Given that the focus of the project was not the development of a new force field, but rather the application of an available package to provide insight to the research hypothesis, it was considered to optimise an existing force field in order to accommodate the high-spin Fe(III) centre. A more detailed discussion on the theory behind the computational techniques used, follows in Section 6.1.

The available force fields in Materials Studio, namely cvff,[125] deidring[126] and pcff,[127–130] were investigated. The cvff force field is optimised for simulations involving small organic molecules, where it is found to predict binding and conformational energies very well. In contrast, the deidring force field is rule-based, and found not to be ideal for determining geometries and crystal packing energies. The pcff force field is mainly optimised for polymers. Therefore, the cvff force field was chosen for this study, since the adsorption of small molecules would be investigated, where only the Fe(III) atom required additional parameterisation.

Munro *et al.* reported the optimisation of a force field for low-spin Fe(III)-porphyrin complexes,[131,132] and their procedure was utilised in the current study to optimise the cvff force field. For this purpose, the crystal structure of β-haematin,[40] as well as a training set of

_____

seven Fe(III)-containing porphyrin crystal structures was used, where these represented both the porphyrin, and the Fe(III)-O bond.[74,114,133–137]

In preparing each of these structures, the hydrogen atoms and double bonds were manually added in geometrically suitable locations. The structures were then minimised using the DMol^3 module in Materials Studio.[123] The minimisation was deemed adequate when the geometry of the minimised structure matched that of the original crystal structure when overlaying the two structures. The crystal structures were minimised by means of a density functional theory (DFT) calculation using the generalised gradient approximation (GGA, PW91),[138,139] and a double numerical basis set with polarisation (DNP),[140] as this combination gave the best results.

For the purposes of optimising the force field, the Forcefield viewer in Materials Studio was used to alter the cvff force field parameters, where the geometry optimisation protocol in the Forcite module was applied in order to evaluate the geometrical changes associated with the new parameters.[123]

In preparation for the geometry optimisation simulation, the molecules were charged using a charge equilibration approach (QEq),[141] and the atoms in the porphyrin structure were renamed and manually typed in order to obtain consistent results (Figure 26, Table 2), as well as to simplify the final output data. An iterative approach was used, where the force constant, K_0 (kcal.mol^{-1}.rad^2), was changed manually until the smallest root mean square deviations (rmsds) of bond lengths, R_0 (Å), bond angles, and torsion angles, T_0 (°), were obtained when comparing the geometries of the optimised structures, to that of the DFT minimised structures.

_____
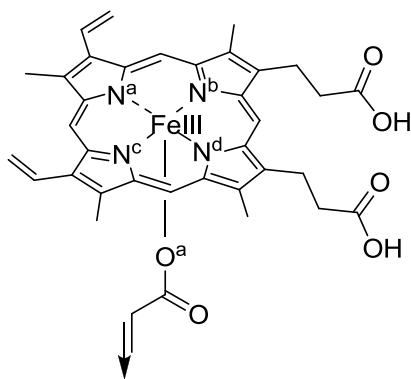
Figure 26: Atom numbering used for

the porphyrin structure

Table 2: The atom typing and numbering of the porphyrin structures used for the force field optimisation.

Atom typing	
N^a	n -nitrogen, SP2
N^b	np -nitrogen, SP2, aromatic
N^c	np -nitrogen, SP2, aromatic
N^d	n -nitrogen, SP2
Fe(III)	Fe3
O^a	o

In evaluating the altered force field, a scripting protocol was used to measure all the bonds and angles, as well as to simplify the overall simulation process. Upon completion, the measured values were exported, and processed in a pre-formulated Microsoft Office Excel document, where the final averages of each iteration were calculated automatically.

The final parameters were deemed optimum when for each structure, the final average bond angles obtained deviated by less than 1.5°, the bond lengths deviated by less than 0.015Å, and the torsion angles deviated by less than 4° from that of the DFT minimised structures (Table 3 and Table 4).[131] However, in some cases the standard deviation was greater than the allowed deviation. In such an occurrence, the measured values of the individual bonds or angles were also evaluated.

Table 3: Final force constants used in the optimised cvff force field, with the average optimised bond lengths and angles, as well as those calculated after the DFT optimisation.

	K^0 (kcal.mol^{-1}.rad^2)	Original DFT			Optimised cvff			Difference[*]
Bond stretch (Å)								
N-Fe	2200	2.1	±	0.01	2.1	±	0.01	0.001
O-Fe	300	1.9	±	0.1	1.9	±	0.1	0.001
Angle bend (•)								
C-N-Fe	150	126.2	±	0.9	127.4	±	0.9	1.2
C-O-Fe	150	126.1	±	2.3	126.6	±	1.8	0.5
N-Fe-O	150	102.5	±	2.3	102.2	±	0.9	0.3
N-Fe-N	480	87.3	±	0.6	87.9	±	2.2	0.6
N-Fe-N	480	154.9	±	1.8	155.5	±	0.5	0.6
Torsion angle bend (•)								
C-N-Fe-O	NA	81.9	±	5.6	81.6	±	5.6	0.3
C-N-Fe-O	NA	-81.9	±	5.6	-81.6	±	5.6	0.3
C-N-Fe-N	NA	174.9	±	3.6	175.0	±	3.9	0.1
C-N-Fe-N	NA	97.9	±	4.9	98.0	±	5.6	0.1
C-N-Fe-N	NA	20.3	±	4.3	20.1	±	5.7	0.3
C-N-Fe-N	NA	-20.3	±	4.3	-20.1	±	5.7	0.3
C-N-Fe-N	NA	-97.9	±	4.9	-98.0	±	5.6	0.1
C-N-Fe-N	NA	-174.9	±	3.6	-175.0	±	3.9	0.1

[*]*The calculated difference between the average values obtained after the geometry optimisation, by applying the optimised cvff force field, and the original values after the DFT optimisation.*

Table 4: Final averages obtained after a geometry optimisation of the eight crystal structures, when applying the optimised force field.

	XETXUP[40]	MQ-XETXUP[114]	QD-XETXUP[114]	QN-XETXUP[114]	FEWQON[133]	MPORFE10[134]	NADKOS[135]	SILKUT[137]
Bond stretch (Å)								
N-Fe	2.1 ± 0.01	2.1 ± 0.01	2.1 ± 0.01	2.1 ± 0.01	2.1 ± 0.01	2.1 ± 0.01	2.1 ± 0.01	2.1 ± 0.01
O-Fe	1.9	1.9	1.9	1.9	1.8	1.8	1.9	1.9
Angle bend (°)								
C-N-Fe	127.6 ± 1.0	127.6 ± 0.8	127.5 ± 0.6	127.4 ± 0.8	126.9 ± 1.2	127.6 ± 0.6	127.2 ± 1.2	127.6 ± 0.8
C-O-Fe	136.2	126.5	128.2	129.0	123.4	126.6	126.6	126.1
N-Fe-O	102.3 ± 2.6	102.2 ± 0.2	102.3 ± 0.5	102.2 ± 1.0	102.3 ± 0.6	102.2 ± 0.7	102.2 ± 0.7	102.2 ± 0.2
N-Fe-N	90.3 ± 6.2	87.4 ± 0.8	87.4 ± 0.5	87.4 ± 0.6	88.0 ± 1.5	87.5 ± 0.2	87.4 ± 0.5	87.4 ± 0.4
N-Fe-N	155.4 ± 0.1	155.5 ± 0.2	155.4 ± 0.4	155.5 ± 0.4	155.4 ± 0.8	155.7 ± 0.8	155.6 ± 1.3	155.6 ± 0.2
Torsion angle bend (°)								
C-N-Fe-O	81.8 ± 7.7	81.4 ± 5.2	80.7 ± 3.7	80.7 ± 4.2	81.6 ± 8.7	82.4 ± 3.6	81.9 ± 6.8	82.6 ± 5.0
C-N-Fe-O	-81.8 ± 7.7	-81.4 ± 5.2	-80.7 ± 3.7	-80.7 ± 4.2	-81.6 ± 8.7	-82.4 ± 3.6	-81.9 ± 6.8	-82.6 ± 5.0
C-N-Fe-N	174.9 ± 5.3	175.1 ± 3.4	176.1 ± 3.8	176.2 ± 2.6	172.8 ± 4.5	175.7 ± 3.2	173.8 ± 3.8	175.5 ± 4.9
C-N-Fe-N	98.2 ± 5.9	98.6 ± 5.1	99.3 ± 3.5	96.6 ± 7.9	98.4 ± 8.8	97.6 ± 3.0	98.1 ± 6.4	97.4 ± 4.2
C-N-Fe-N	20.2 ± 6.3	23.7 ± 4.2	21.3 ± 3.4	21.2 ± 3.8	20.5 ± 8.4	18.2 ± 4.1	20.0 ± 7.1	15.3 ± 4.6
C-N-Fe-N	-20.2 ± 6.3	-23.7 ± 4.2	-21.3 ± 3.4	-21.2 ± 3.8	-20.5 ± 8.4	-18.2 ± 4.1	-20.0 ± 7.1	-15.3 ± 4.6
C-N-Fe-N	-98.2 ± 5.9	-98.6 ± 5.1	-99.3 ± 3.5	-96.6 ± 7.9	-98.4 ± 8.8	-97.6 ± 3.0	-98.1 ± 6.4	-97.4 ± 4.2
C-N-Fe-N	-174.9 ± 5.3	-175.1 ± 3.4	-176.1 ± 3.8	-176.2 ± 2.6	-172.8 ± 4.5	-175.7 ± 3.2	-173.8 ± 3.8	-175.5 ± 4.9

_____

With an optimised force field in hand, that could accommodate the high-spin Fe(III) atom, it was used in molecular mechanics simulations for investigating the crystal morphology, as well as the adsorption of inhibitors onto the crystal faces.

This optimised force field was used throughout this project for all molecular mechanics simulations, where the molecules were charged using a charge equilibration approach (QEq).[141]

2.2 THE CRYSTAL MORPHOLOGY

2.2.1 Investigating the crystal morphology

Buller *et al.* and Straasø *et al.* gave some insight into the β-haematin crystal packing arrangement, as well as the crystal morphology (Section 1.2.4).[54,60] By having a three dimensional model of the β-haematin crystal, a greater understanding of the crystal growth, as well as of the step propagation observed by Olafson *et al.* could be obtained.[49]

A model of the β-haematin crystal was grown using the Morphology module within Materials Studio, by applying the parameterised cvff force field.[123] In order to evaluate the crystal face expression, the calculated crystal face attachment energies (E_{att} (kcal.mol^{-1})) for each face are compared to that of face {001}, where the values are also reported as a fraction of {001} (Table 5, Figure 27). The overall crystal morphology obtained agreed with that reported by Buller *et al*,[54] where it is found that the fastest growth would occur on face {001} and face {011}. The largest observed faces were found to be face {100} and face {010}.

The calculated E_{att} values are in good agreement with those reported by Buller *et al.*, where a universal force field was used.[54] The authors reported almost identical E_{att} values for face {100} and face {010}, which suggests that these faces should be expressed equally. However, this is contrary to the experimental crystal growth observed by Solomonov *et al.* and Olafson *et al.* (Section 1.4.1).[73]

Upon investigating the crystal morphology computationally, it is found that face {100} had the highest E_{att} value, which supports it being expressed the most. Therefore it is suggested that it would be expressed the most, followed by that of face {010}. Face {001} was found to

be the fastest growing face with the lowest E_{att}, with face {011} being the second-fastest growth face.

Growth in the *c* direction
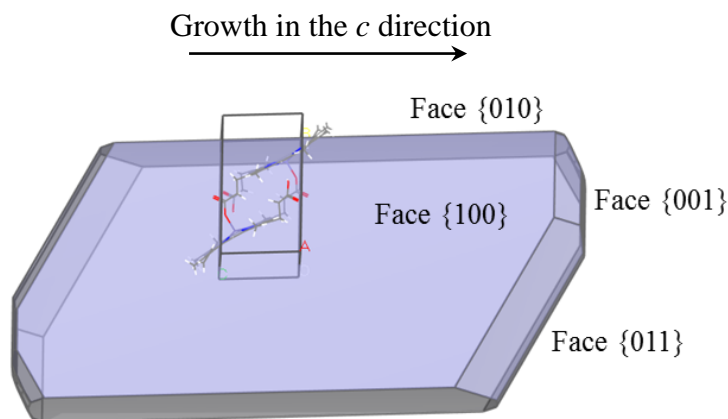
Figure 27: The calculated β-haematin crystal morphology.

The crystal morphology that was calculated using the Morphology tool in Materials Studio is shown.

The crystal faces expressed in the morphology were identified from most to least dominant as {100}, {010},

{011} and {001}, respectively. The orientation of the unit cell is indicated, with growth predicted primarily in

the c direction.

Table 5: Comparison of crystal face attachment energies calculated, and reported by Buller *et al*.[54]

	Buller *et al*.[54]		Calculated	
Face	**E_{att} (kcal.mol^{-1})**	**Fraction of {001}**	**E_{att} (kcal.mol^{-1})**	**Fraction of {001}**
{100}	-30.6	0.3	-14.26	0.2
{010}	-27.7	0.3	-32.7	0.5
{011}	-82.4	0.8	-58.3	0.8
{001}	-101.5	1	-71.9	1

By obtaining a greater understanding of the crystal morphology, the individual crystal surfaces were subsequently investigated, where the surface morphology of each of the faces was carefully examined.

_____

2.2.2 Surface morphology of the individual crystal faces

Upon analysing the crystal morphology of the largest crystal face, face {100}, no distinct crevices are observed (Figure 28). Free carboxylic acid side chains are present, which would normally form a hydrogen bonding interaction to an adjacent β-haematin dimer in the crystal phase. These might be possible sites for nucleation of a new layer onto the face, whereby haem or a β-haematin dimer could interact to form hydrogen bonding interactions, in order to promote further crystal growth onto this face.

Face {010} has a hydrophobic tile-like surface upon viewing the crystal surface from the top, where each of the porphyrins is slightly overlaid by an adjacent one (Figure 29). When viewed from the side, no hydrogen bonding sites are observed. It is possible that the flat porphyrin moiety of haem or β-haematin could be attracted to this surface to form π-π interactions to promote further crystal growth onto this face.
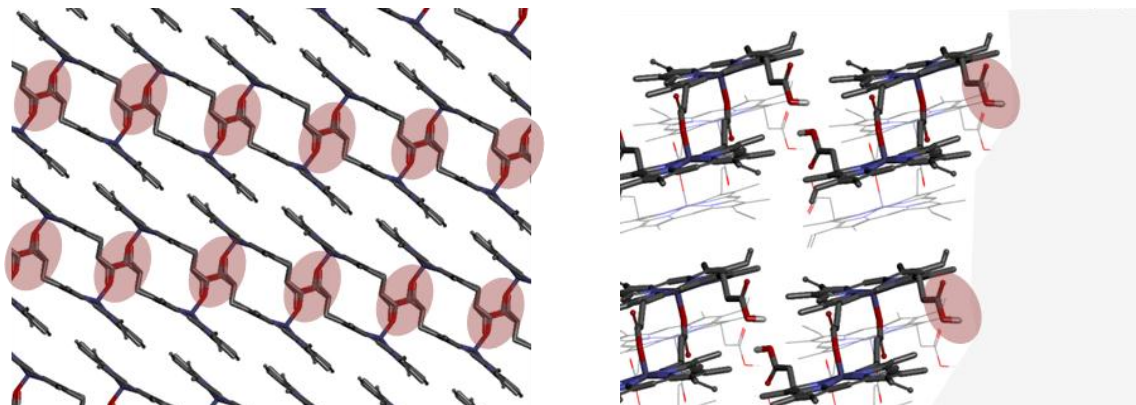
Figure 28: Face {100}

The crystal face viewed from the top (left), and viewed from the side (right).

Possible hydrogen bonding sites are indicated by ● .
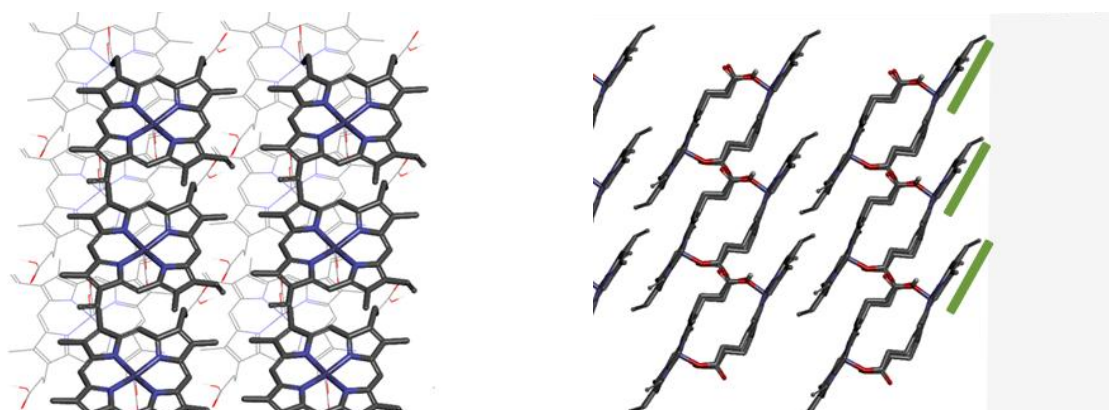
Figure 29: Face {010}

The crystal face viewed from the top (left), and viewed from the side (right).

Possible hydrophobic π-π interaction sites are indicated by ▬.

61

Face {011} could accommodate more intermolecular actions than the previously mentioned faces, where it has an overall step-like surface. By evaluating the overall surface in more detail, flat hydrophobic porphyrin surfaces are present for free haem or β-haematin to form π-π interactions to, as well as hydrophilic carbonyl groups and free carboxylic side chains that could participate in hydrogen bonding interactions (Figure 30).

The surface of face {001} is very similar to that of face {011}. By viewing face {001} from the side, areas for hydrophobic π-π interactions, as well as hydrophilic areas to form hydrogen bonding interactions are observed (Figure 31). However, when viewing this face from the top, a distinctive crevice is seen, wherein molecules could adsorb. The inside of this groove is hydrophobic in nature, where it is reasonable to expect that π-π interactions would be favoured to the porphyrin structure at the top, as well as to the one at bottom of this crevice. Just on the outside of this crevice, carbonyl groups and free carboxylic acid side chains are present at the surface, which could participate in the formation of hydrogen bonding interactions. Interestingly, this area on the outside of the crevice is similar in topology to the surface of face {011}.

It could be reasoned that, for instance, a β-haematin dimer would be able to adsorb onto both faces {001} and {011} in a similar geometry. However, with face {001} having a distinctive crevice where this molecule could adsorb into to form addition π-π interactions to, adsorption would most likely be favoured onto this face. Therefore, when the crystal expands in the *c* direction, growth would occur faster on face {001} than on face {011}.
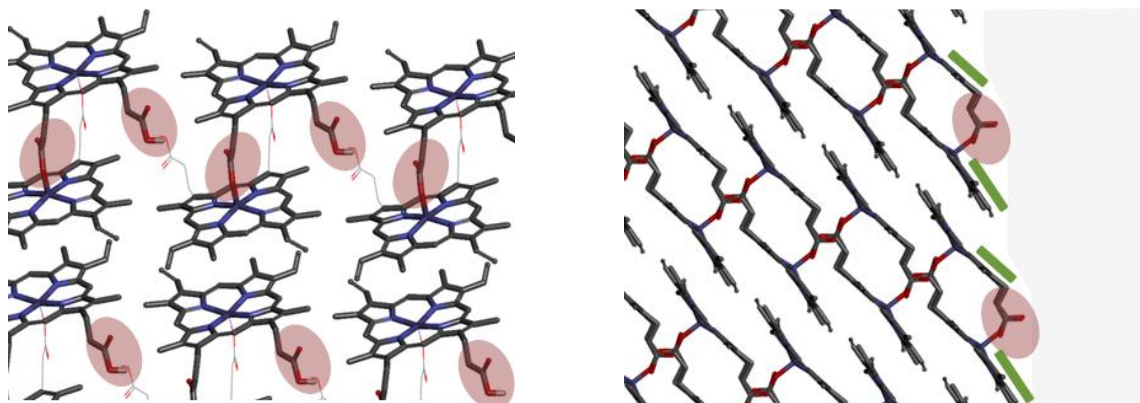
Figure 30: Face {011}

The crystal face viewed from the top (left), and viewed from the side (right).

Possible hydrogen bonding sites are indicated by ⬤ , and hydrophobic π-π interaction sites by ▬.

Only hydrogen bonding sites are shown in the image on the left.
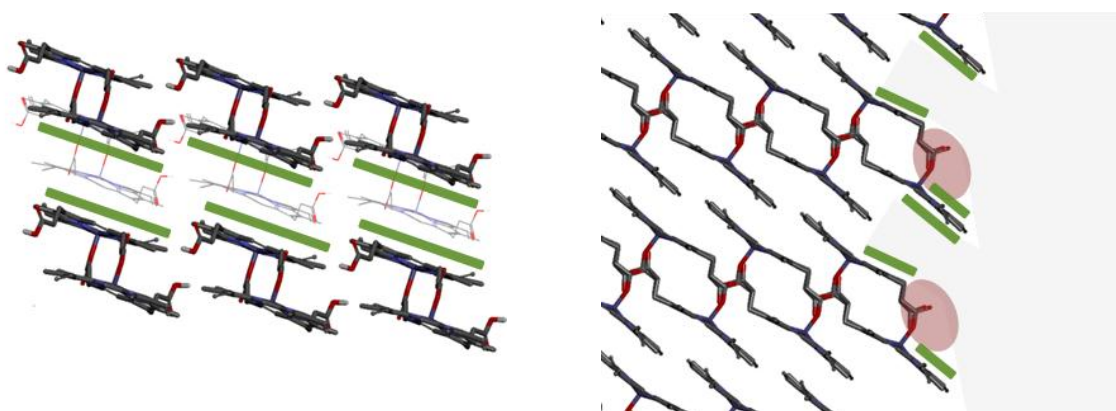
Figure 31: Face {001}

The crystal face viewed from the top (left), and viewed from the side (right).

Possible hydrogen bonding sites are indicated by ⬤ , and hydrophobic π-π interaction sites by ▬.

Only π-π interactions are shown in the image on the left.

_____

By comparing the interaction possibilities of the crystal faces, it is found that the larger faces might each only form one type of interaction. Face {100} could form hydrogen bonding interactions, and face {010} could form π-π interactions to promote the adsorption of other molecules, such as haem, β-haematin, or antimalarial drugs.

Faces {011} and {001} both allow for a greater amount of intermolecular interaction possibilities, which might explain why these two faces exhibit the fastest growth rates. Furthermore, with face {001} having a distinctive groove in which molecules could adsorb, it might give insight as to why this is considered to be the fastest growing face. This is also consistent with crystal growth theory, which predicts that inhibition is most likely at the fastest growing face.

If adsorption is favoured for haem or β-haematin onto these faces, the adsorption of antimalarial drugs would most likely also be favoured. This might give insight as to why β-haematin crystals grown in the presence of QN and CQ were cylindrically tapered at the edges, as observed by Solomonov *et al.*[73] (Section 1.4.1).

2.3 A BRIEF ADSORPTION INVESTIGATION.

Having explored the surface structure and the possible interaction sites on the four dominant crystal faces, the next consideration was to investigate the adsorption of clinically-relevant antimalarial drugs onto these surfaces, with the aim of identifying a possible target site on these surfaces. Based on the research performed by Solomonov *et al.*, as faces {001} and {011} are the fastest growing faces, these were considered of greater importance in the overall inhibition of β-haematin growth, as the inhibitors might preferentially adsorb onto these crystal faces.[73]

Initially, a subset of short-chain quinoline compounds, that are analogues of the antimalarial drug chloroquine, was investigated. In this way structure-activity relationships could be examined in greater depth, before proceeding to investigate the adsorption of clinically-relevant antimalarial drugs. Furthermore, as these compounds have similar structures, trends were anticipated in the adsorption study, which would ease the optimisation of the overall adsorption simulation.

2.3.1 The initial adsorption study

For the adsorption protocol, the Forcite module within Materials studio was used.[123] Here, the parameterised cvff force field, defined atom typing for the β-haematin crystal, and QEq charges were applied.

The quinoline inhibitors used in this study were synthesised and tested for β-haematin activity by Kaschula *et al.* and Nsumiwa *et al.* (Figure 32).[120,142] These inhibitors were ideal, since they are similar in shape and size, and the activity data is available.

R₁ = CH₃ (**KN3**), F (**KN4**), Br (**KN5**), Cl (**KN6**), CF₃ (**KN7**), NO₂ (**KN8**).
R₂ = H (**KN9**), CH₃ (**KN10**), CF₃ (**KN11**), Cl (**KN12**), CN (**KN13**), NO₂ (**KN14**).
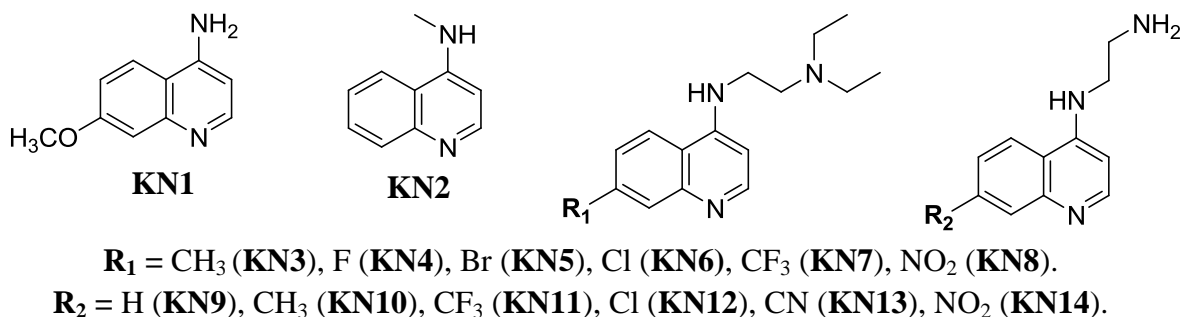
Figure 32: Quinoline-base inhibitors used for the initial adsorption study.

These inhibitors were reported by Kaschula et al. and Nsumiwa et al.[120,142]

Since the adsorption of these compounds onto the β-haematin crystal surface in the food vacuole at pH 4.8 was modelled, the speciation at this pH had to be accounted for. Therefore, the pK_a values and the percentage of each species at pH 4.8 were calculated using the Chem Axon Marvin Sketch software package (Table 6).[143] Experimental pK_a values were reported for compounds **KN3**-**8** by Kaschula *et al.*, however the calculated values was used for consistency in this study, since experimental pK_a values are not available for all the compounds.

Chapter 2 - The adsorption of inhibitors onto β-haematin

_____

Table 6: Calculated and experimental pK_a values, and speciation at pH 4.8.

	Quinoline nitrogen pK_a		Terminal amine pK_a[a]		% Diprotic
	Experimental[b]	Calculated[c]	Experimental[b]	Calculated[c]	Calculated[c]
KN1	−	0.00	−	8.64	100
KN2	−	0.32	−	8.19	100
KN3	8.12 ± 0.01	8.54	9.51 ± 0.01	9.43	100
KN4	7.62 ± 0.01	7.61	9.24 ± 0.01	9.42	100
KN5	7.93 ± 0.02	7.37	7.97 ± 0.05	9.42	100
KN6	7.56 ± 0.02	7.30	8.83 ± 0.01	9.42	100
KN7	7.50 ± 0.02	7.52	7.65 ± 0.03	9.42	100
KN8	6.28 ± 0.03	4.96	8.80 ± 0.02	9.40	55
KN9	−	8.54	−	9.62	100
KN10	−	7.52	−	9.62	100
KN11	−	7.30	−	9.62	100
KN12	−	5.86	−	9.62	92
KN13	−	8.15	−	9.62	100
KN14	−	4.96	−	9.62	59

[a] *The second pK$_a$ is that of the terminal amine, which is tertiary in **KN3-8** and primary in **KN9-14**.*

[b] *The experimental values were reported by Kaschula et al.*[120]

[c] *The pK$_a$ values and percentage speciation were calculated using Marvin Sketch.*[143]

For this subset of compounds, it is found that the calculated values correlate reasonably well with the experimental values. The calculated pK_a value for the quinoline nitrogen atom in compound **KN8**, with a nitro functional group in the 7-position of the quinoline, is considerably lower than the experimental value. However, as the experimental value is lower than those of the other related compounds, it is more likely that compound **KN8** is not 100% diprotic.

Most of the compounds were doubly protonated at pH 4.8, thus diprotic, where the quinoline nitrogen atom and the terminal amine functional groups on the side-chain are protonated. A small number of compounds, namely **KN8**, **KN12** and **KN14**, were also predicted to be

singly protonated, where the quinoline nitrogen atom is neutral. The electron density of the aromatic ring is decreased due to the electron-withdrawing effects of the more electron-negative substituents (cyano and nitro groups) on the ring, making the quinoline nitrogen atom less basic. Therefore, the adsorption of these monoprotic forms onto the β-haematin crystal surfaces was also investigated.

Different conformations of each quinoline compound were generated using the Generate conformers protocol in the Accelrys Discovery studio software package, where the lowest energy conformation was selected before proceeding with the adsorption simulation.[144] These were minimised by means of a geometry optimisation simulation in Materials studio, where the atoms were automatically typed as for the original cvff force field.

As per the adsorption protocol in Materials Studio, the crystal faces of interest were initially prepared by cleaving a slice of the crystal surface and growing it into a vacuum slab (Figure 33). The slice was selected in such a way that it contains all the possible interaction sites on the surface, as discussed in Section 2.2.2. Therefore, a square of 9 unit cells was chosen. Furthermore, it was important that the slice was thick enough so that all the crevices are seen, therefore it was chosen to be 3 unit cells thick. The vacuum slab was chosen with a thickness of 10 Å to allow the inhibitor to move and rotate freely. Finally, the atoms on the crystal surface were selected and identified as the adsorption target atoms, which would guide the inhibitor to adsorb onto the crystal surface.
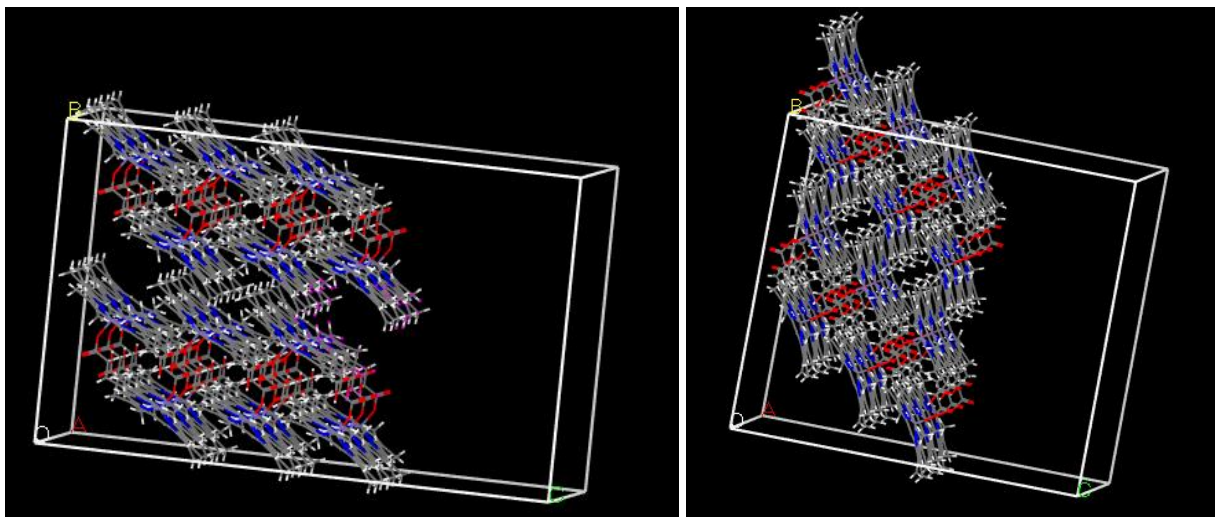
Figure 33: The vacuum slabs.

The vacuum slabs of face {001} (left) and face {011} (right), showing the crystal surface within a vacuum slab.

The adsorption simulation was performed using the Adsorption locater tool in Materials studio, where the adsorption of inhibitors onto the β-haematin crystal surface was investigated.[123] A simulated annealing temperature step was utilised, where the system was heated and allowed to cool again in order to overcome energy barriers and to obtain the lowest energy conformation. Monte Carlo rotations and translations were applied in this simulation in order to find the best fit of the adsorbed inhibitor onto the crystal surface.

An initial simulation was commenced with 5 heating steps, each undergoing 100 000 Monte Carlo cycles, followed by a final geometry optimisation. The best 50 adsorption results were extracted, where the calculated adsorption energies (E_{ads}) were reported. Finally, this simulation was repeated three times for each inhibitor, where after the consistency of the output results was examined. The calculated E_{ads} values, as well as the visual results, were inspected in order to assess whether the output results were of a sufficient standard.

Chapter 2 - The adsorption of inhibitors onto β-haematin

_____

2.3.2 The initial adsorption results

2.3.2.1 Adsorption onto face {011}

The adsorption of the monoprotic and diprotic forms of the quinoline inhibitors onto face {011} was examined first. The quinoline moiety is frequently observed to adsorb flat onto the porphyrin surface, which is most likely promoted by π-π interactions between the quinoline moiety and the porphyrin on the crystal surface. A typical result, exemplified by compound **KN12**, is shown below (Figure 34).
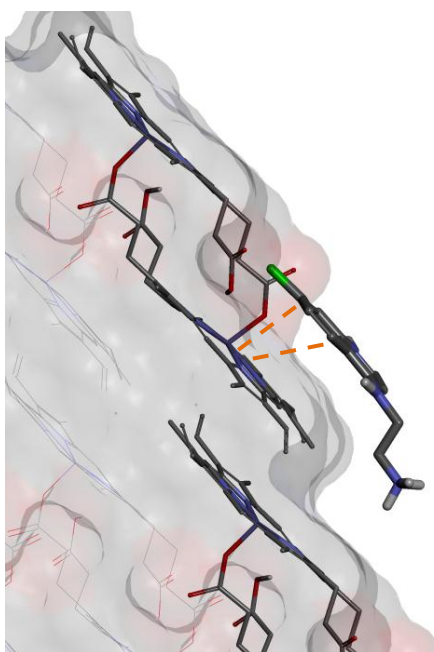
Figure 34: Adsorption of compound KN12 onto face {011}.

*The adsorption of compound **KN12** in the diprotic form onto face {011}, as viewed from the side of the crystal face, is shown as an example. No hydrogen bonding interactions were observed. The inhibitor could form possible π-π interactions to the porphyrin on the β-haematin crystal surface, with measured interaction distances of 3.7 Å. The π-π interactions are indicated by ▪ ▪ .*

_____

This π-π stacking phenomenon is regularly seen with porphyrin structures where the aromatic nitrogen-containing heterocycles have a low π-electron density, thereby favouring π-π interactions above σ-π interactions.[145,146] Strong π-π interactions are favoured with an interplanar separation of 3.3 Å, and weaker interactions occur over distances above 3.6 Å and to a maximum of 3.8 Å.

The results obtained were not consistent, and no preferred target area has been identified. This is not surprising given that there are no distinctive crevices on this surface, as previously shown in Figure 30. Rather, the inhibitors adsorb to multiple areas on the crystal surface and no one adsorption site is preferred over the other. Furthermore, no hydrogen bonding interactions were observed between the **KN** inhibitors and the crystal surface. These inconsistencies were, however, also an indication that the parameters used in this adsorption simulation, may not be adequate and would need to be optimised further.

2.3.2.2 Adsorption onto face {001}

By comparison, for the adsorption onto face {001}, it is found that the inhibitors mostly adsorb into the crevice; as an example, the adsorption of **KN6** is shown below (Figure 35). The area occupied spreads over the width of one β-haematin dimer, with measured dimensions of 7.8 Å by 15.5 Å. For the purposes of this study, this location is referred to as the primary adsorption site. The side-chain moieties of the molecules extend towards the outside of the crevice, where in some cases, a hydrogen boding interaction is formed between an amine functional group on the inhibitor and an exposed carbonyl group on the crystal surface.
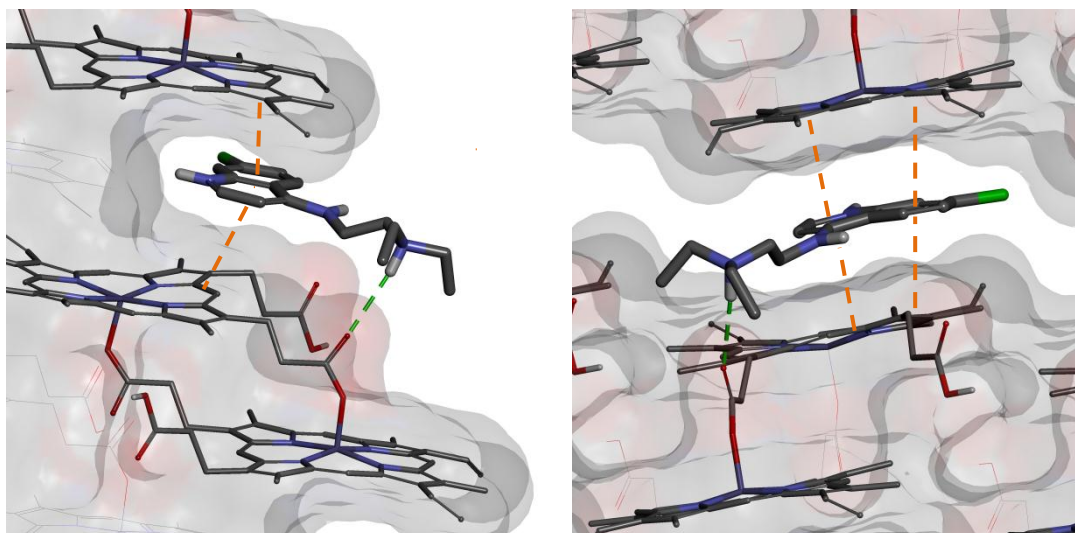
Figure 35: Adsorption of compound KN6 in the primary adsorption site on face {001}.

*The adsorption of compound **KN6** in the diprotic form, as viewed from the side of the crystal face (left) and onto the crystal face (right), is shown as example. The quinoline moiety makes favourable π-π interactions to the porphyrin above and below it, with average interaction distances of 3.6Å and 3.9Å respectively. A further hydrogen bonding interaction, with a measured interaction distance of 2.7Å, is observed between the protonated tertiary amine of compound **KN6** and the carbonyl group on the β-haematin crystal surface. The hydrogen bonding interaction is indicated by ▪ ▪ , and the π-π interactions are indicated by ▪ ▪ .*

Interestingly, compounds **KN7** and **KN11** were observed to adsorb onto the flat porphyrin surface on the outside of the crevice (Figure 36). This is referred to as the secondary adsorption site. Given that both of these compounds contain a -CF$_3$ substituent at the 7-position on the quinoline ring, it is possible that these inhibitors are too bulky to fit into the crevice. Unfortunately, for these compounds, no π-π interactions were observed, and the geometrical results were not consistent. It might be that a more refined geometry optimisation is required to improve these interactions.
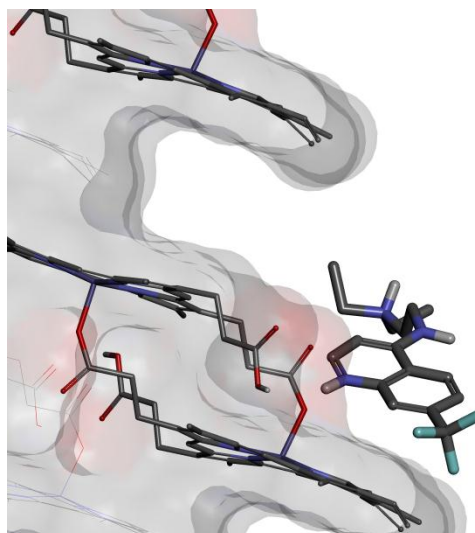
Figure 36: Adsorption of compound KN7 in the secondary adsorption site on face {001}.

*The adsorption of compound **KN7** in the diprotic form is shown, as viewed from the side of the crystal face.*

Upon investigating the results more closely, it was apparent that in some cases the optimal adsorption conformation of the inhibitor was not attained, where by visual inspection, a slight variation in the adsorption geometry would enhance π-π interactions, or the rotation around a bond would allow for a hydrogen bonding interaction to form. Moreover, by analysing the reported E_{ads} values, it was found that the results were not consistent and large standard deviations above 5 kcal.mol^{-1} were calculated. Therefore it was concluded that the adsorption simulation had to be further optimised in order to obtain more refined results.

By evaluating the results obtained from the initial adsorption study, a greater understanding as to how these inhibitors adsorb onto the β-haematin crystal surface, was gained. Moreover, with faces {001} and {011} possessing both π-π and hydrogen bonding interaction sites, and with face {001} having a distinctive crevice on the surface, this might explain why these faces are the preferred growing faces of the β-haematin crystal. Therefore, it was deemed that

73

by focussing the study on the adsorption of inhibitors onto the fastest growing faces, and by rather spending a greater amount of computational time on these, β-haematin inhibition by means of the adsorption of inhibitors could be investigated more thoroughly, where more refined E_{ads} values could be used to evaluate structure-activity relationships.

2.3.3 Optimising the overall adsorption protocol.

2.3.3.1 Improving the adsorption simulation.

Three main areas for improving the adsorption protocol were identified. Firstly, the final geometry optimisation could be optimised or replaced by another minimisation protocol. Also, the number of adsorption heating steps and cycles could be optimised. However, by adding more heating steps or cycles, this would exponentially increase the computational cost. Additionally, the size of the crystal face could also be decreased, thereby defining the adsorption target area more clearly.

In the first attempt to optimise the adsorption simulation, a more refined final geometry optimisation protocol that contains an ultra-fine conjugate gradient algorithm, was investigated. Unfortunately, this had little effect on the final E_{ads} values and the final geometrical adsorption results, as large deviations were still observed. It was therefore concluded that the final geometry optimisation step is not able to overcome high energy barriers to bring about an improved adsorbed geometry. It was therefore preferable to optimise the adsorption simulation itself, since it already includes heating steps with Monte Carlo rotations and translations.

Upon investigating the adsorption target area, it was realised that a larger vacuum slab was necessary in order for the inhibitor to freely move and rotate before adsorbing onto the crystal surface. Therefore a vacuum slab of 50 Å in length was chosen. This provided more than enough space for even larger molecules to move in, where this increase in the size of the vacuum slab had no effect on the computational cost of the simulation.

Furthermore, the number of heating steps or Monte Carlo cycles could be altered. In order to obtain the best adsorption results within adequate computational time, the optimal combination of these had to be determined. For this purpose, the standard deviation of three identical simulations was evaluated for each combination. It is found that by increasing the number of heating steps, the computational time increased exponentially, without necessarily improving the final adsorption results. For instance, a simulation with 3 steps and 1500 000 cycles within 52 h did not present the same consistency as a simulation of 5 steps and 500 000 cycles within 45 h. Furthermore, the same consistency was found for a simulation of 10 steps and 100 000 cycles within 49 h as for the 5 step simulation. Finally, after numerous combinations were investigated, it was determined that the simulation involving 5 steps and 500 000 cycles is an optimum combination for this study, where the final E_{ads} values did not deviate with more than 1.0 kcal.mol^{-1} after 3 repeats of the same simulation. Moreover, a simulation of 5 steps and 700 000 cycles is found to be ideal for the adsorption of larger inhibitors.

In an attempt to reduce the computational time per adsorption simulation, a smaller crystal surface (2 x 1 unit cells) was probed for adsorption. In the end it was concluded that the initial larger crystal surface (3 x 3 unit cells) is still the best to use for more accurate adsorption results.

2.3.3.2 Introducing a dynamics simulation.

After optimising the adsorption simulation, two main concerns were raised with regards to the overall adsorption protocol. Firstly, even though the core adsorption simulation was optimised, the final geometry minimisation was found to be insufficient for all the adsorption simulations, as visual inspection of the results revealed that a slight rotation around a certain bond of the inhibitor could lead to enhanced adsorption of the molecule onto the β-haematin crystal surface. Secondly, for the simulations discussed so far, the absolute minimum energy conformation of each inhibitor was used. Even though the absolute minimum energy conformation is expected to have the lowest internal energy, it was important to consider that another conformation could have a much more favourable interaction energy to such an extent that it would overcome the penalty of a higher internal energy, therefore resulting in a more favoured overall adsorption energy.

To overcome these limitations, a simulated annealing aided dynamics simulation was introduced, where it could serve as a more improved final geometry optimisation protocol, as well as probe the geometric shape for improved conformations. For the quinoline molecules, the quinoline moiety adsorbs into the primary pocket of face {001}, and onto the flat porphyrin surface of face {011}, thereby only allowing the free side-chain to rotate and find the optimal adsorbed geometry.

For this study, the Anneal Dynamics protocol in the Forcite module in Materials studio was used.[123] This protocol is found to be ideal for refining the final adsorption results by overcoming high energy barriers. Unfortunately, a less computationally expensive adsorption protocol could not be considered to obtain the same quality results, as the adsorption protocol allows for the adsorption of the inhibitor at a specific target site. Therefore, it is still ideal to

_____

have a more refined adsorption protocol, followed by the dynamics protocol as a final geometry optimisation.

A video was recorded of this final optimisation, where the ability of this simulation to overcome high energy barriers was investigated. The geometry optimisation of compound **KN12** is shown (Figure 37), where the rotation around one bond allows the side-chain to move closer to a carbonyl moiety on the crystal surface. This favoured the formation of a hydrogen boding interaction between the primary amine and the carbonyl moiety, with a measured interaction distance of 2.2 Å. Possible π-π interactions could form between both the top and bottom porphyrin and the quinoline, with the measured interaction distances being 3.6 Å and 3.8 Å respectively.

Initial   Final
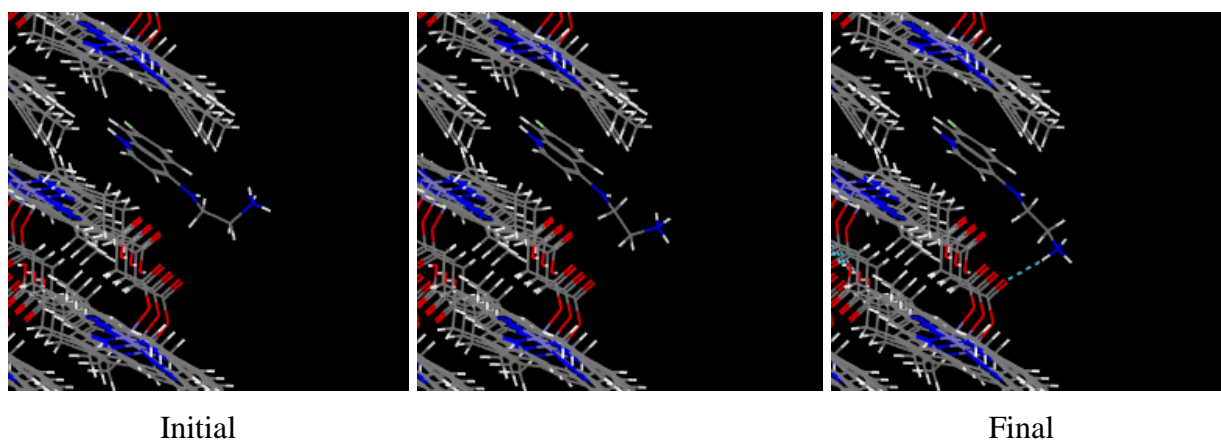
Figure 37: The Forcite Anneal Dynamics simulation.

*Three frames of the Forcite Anneal Dynamics simulation of compound **KN12** in the diprotic form are shown. The final frame shows the hydrogen bonding interaction that was formed.*

Finally, with the adsorption simulation optimised, the initial adsorption results could be reanalysed, where this could allow for more consistent geometry results, as well as more repeatable calculated E_{ads} values for the determination of structure-activity relationships.

2.3.3.3 Improved initial adsorption results

The adsorption of the small set of quinoline compounds onto faces {001} and {011} was analysed for a second time, by exploiting the optimised adsorption protocol. For this, an adsorption simulation with 5 heating steps, 500 000 Monte Carlo cycles, and an ultra-fine geometry optimisation, was applied. This was finally subjected to the Forcite Anneal dynamics simulation, where after the final E_{ads} values were calculated.

When inspecting the visual geometry results, the same trends were observed as before, where the molecules adsorbed in such geometries that π-π interactions are favoured between the inhibitors and the porphyrin surface. For adsorption onto face {001}, the majority of the inhibitors adsorbed into the primary adsorption site, with the exception of compounds **KN3**, **KN7** and **KN11** which adsorbed onto the secondary adsorption site, as previously shown for the adsorption of compound **KN7** in Figure 36.

Furthermore, the calculated E_{ads} values were more consistent, with a standard deviation of less than 1 kcal.mol^{-1}. This allowed for the evaluation of structure-activity relationships, where the calculated E_{ads} values were compared with the β-haematin inhibition activity results reported by Kaschula *et al.* and Nsumiwa *et al.*[120,142] These activity results were determined against acetate-mediated β-haematin formation.

For the purposes of evaluating possible structure-activity relationships, the speciation forms at pH 4.8 for each of the inhibitors were considered. The total adsorption energies (E_{ads}) were calculated from the individual adsorption energies of the individual protic forms, where the observed adsorption energies were weighted according to the fractional abundance of each speciation form (Equation 2.2).

_____

$$E_{ads} = \frac{(\% \, Diprotic)(E_{ads} \, Diprotic)}{100} + \frac{(\% \, Monoprotic)(E_{ads} \, Monoprotic)}{100} \qquad (2.2)$$

These E_{ads} values were then compared to the acetate β-haematin inhibition activity (Acetate $BHIC_{50}$) results. For the adsorption of the short-chain quinoline compounds onto face {001}, a non-significant trend is observed, with an R^2 value of 0.20 and a P value of >0.05 (Table 7, Figure 38).

However, it was observed that while most of the compounds adsorbed into the primary adsorption site, some preferred adsorption onto the secondary adsorption site. Thus, by considering only the adsorption into the primary adsorption site (thereby excluding **KN3** and **KN7**, which have high error values), an R^2 value of 0.59 and a P value of 0.006 are found (Figure 39), which is significant.

_____

Table 7: The determined acetate BHIC$_{50}$ activity of the small quinoline compounds, as well as the calculated E$_{ads}$ values for the adsorption onto face {001}, taking into account the percentage speciation.

Compound	E$_{ads}$ Diprotic face {001} (kcal.mol^{-1})		E$_{ads}$ Monoprotic face {001} (kcal.mol^{-1})		% Diprotic	% Monoprotic	E$_{ads}$ face {001} (kcal.mol^{-1})	Acetate BHIC$_{50}$ (eq)		
KN1	-52.6	± 0.01	−		100	0	-52.6	15.6	±	0.5
KN2	-50.2	± 0.4	−		100	0	-50.2	14.9	±	0.3
KN3	-57.3	± 0.6	−		100	0	-57.3	17.0	±	4.0
KN4	-61.5	± 0.01	−		100	0	-61.5	9.7	±	0.8
KN5	-62.3	± 0.5	−		100	0	-62.3	4.4	±	0.7
KN6	-66.5	± 0.01	−		100	0	-66.5	2.2	±	0.2
KN7	-51.5	± 0.6	−		100	0	-51.5	8.0	±	2.0
KN8	-79.5	± 0.1	-88.1	± 0.0	55	45	-83.4	3.1	±	0.6
KN9	-53.4	± 0.8	−		100	0	-53.4	10.6	±	0.4
KN10	-57.6	± 0.9	−		100	0	-57.6	10.3	±	0.3
KN11	-38.9	± 0.01	−		100	0	-38.9	5.4	±	0.2
KN12	-59.4	± 0.01	−		100	0	-59.4	5.4	±	0.5
KN13	-58.5	± 0.01	-59.8	± 0.6	92	8	-58.6	6.3	±	0.8
KN14	-63.5	± 0.2	-71.7	± 0.0	59	41	-66.9	5.3	±	0.4

[*] *The acetate BHIC$_{50}$ vales were reported by Kaschula et al.[120] and Nsumiwa et al.[142]*

_____
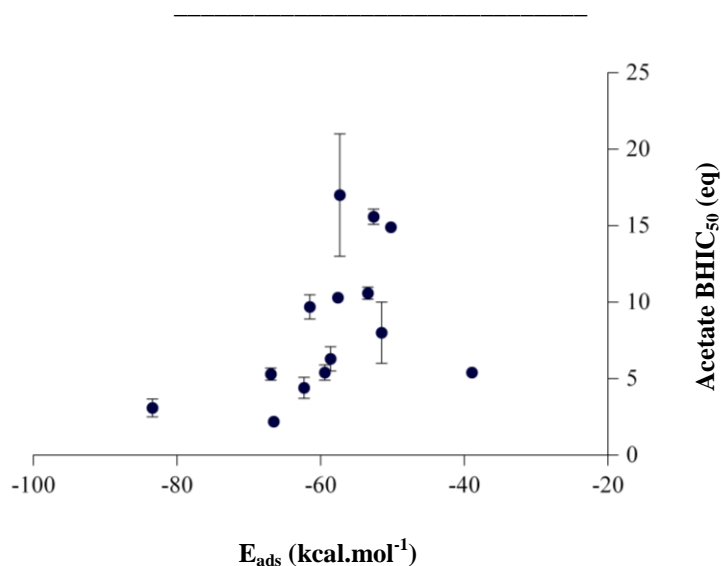
Figure 38: Adsorption of quinoline inhibitors to face {001). A comparison of the calculated E$_{ads}$ and acetate BHIC$_{50}$ values.

An R^2 value of 0.20 and a P value of >0.05 are obtained.
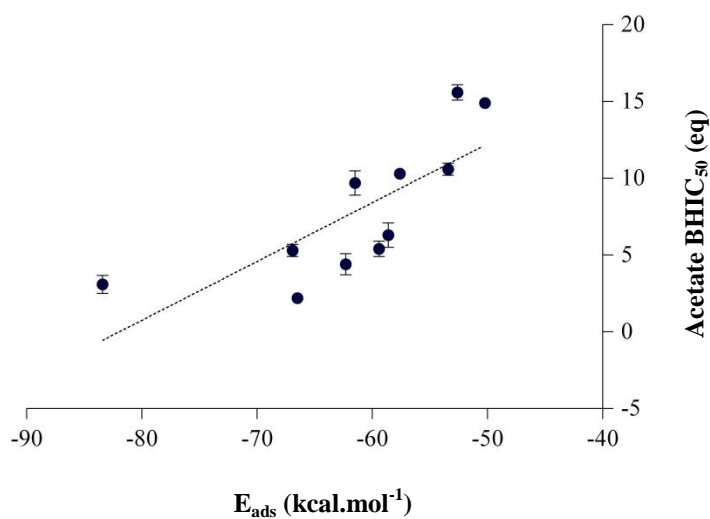
Figure 39: Adsorption of quinoline inhibitors to face {001). A comparison of the calculated E$_{ads}$ and acetate BHIC$_{50}$ values for compounds that adsorb only to the primary adsorption site.

*Compounds **KN3, KN7**, and **KN11** are removed. An R^2 value of 0.59 and an P value of 0.006 are obtained.*

81

Chapter 2 - The adsorption of inhibitors onto β-haematin

_____

On the other hand, by comparing the adsorption of all inhibitors discussed in this chapter onto face {011}, an R^2 value of 0.48 and a P value of 0.006 are found (Table 8, Figure 40). This improved correlation (relative to an R^2 value of 0.20 achieved for face {001}) might be due to the surface having no distinctive crevices, where only one adsorption site is recurring over the surface. Therefore, adsorption could only occur onto one adsorption site, which results in more consistent E_{ads} data.

Table 8: The determined acetate $BHIC_{50}$ activity of the small quinoline compounds, as well as the calculated E_{ads} values for the adsorption onto face {011}, taking into account the percentage speciation.

Compound	E_{ads} Diprotic face {011} (kcal.mol^{-1})		E_{ads} Monoprotic face {011} (kcal.mol^{-1})		% Diprotic	% Monoprotic	E_{ads} face {011} (kcal.mol^{-1})	Acetate $BHIC_{50}$ (eq)		
KN1	-34.2	± 0.2	–		100	0	-34.2	15.6	±	0.5
KN2	-32.6	± 0.01	–		100	0	-32.6	14.9	±	0.3
KN3	-35.7	± 0.3	–		100	0	-35.7	17.0	±	4.0
KN4	-39.4	± 0.0	–		100	0	-39.4	9.7	±	0.8
KN5	-46.5	± 0.0	–		100	0	-46.5	4.4	±	0.7
KN6	-46.4	± 0.2	–		100	0	-46.4	2.2	±	0.2
KN7	-53.1	± 0.01	–		100	0	-53.1	8.0	±	2.0
KN8	-53.9	± 0.5	-52.5	± 0.3	55	45	-53.3	3.1	±	0.6
KN9	-37.1	± 0.01	–		100	0	-37.1	10.6	±	0.4
KN10	-33.7	± 0.1	–		100	0	-33.7	10.3	±	0.3
KN11	-42.7	± 0.01	–		100	0	-42.7	5.4	±	0.2
KN12	-39.9	± 0.01	–		100	0	-39.9	5.4	±	0.5
KN13	-34.0	± 0.01	-39.1	± 0.0	92	8	-34.4	6.3	±	0.8
KN14	-44.0	± 0.01	-47.1	± 0.7	59	41	-45.2	5.3	±	0.4

_____
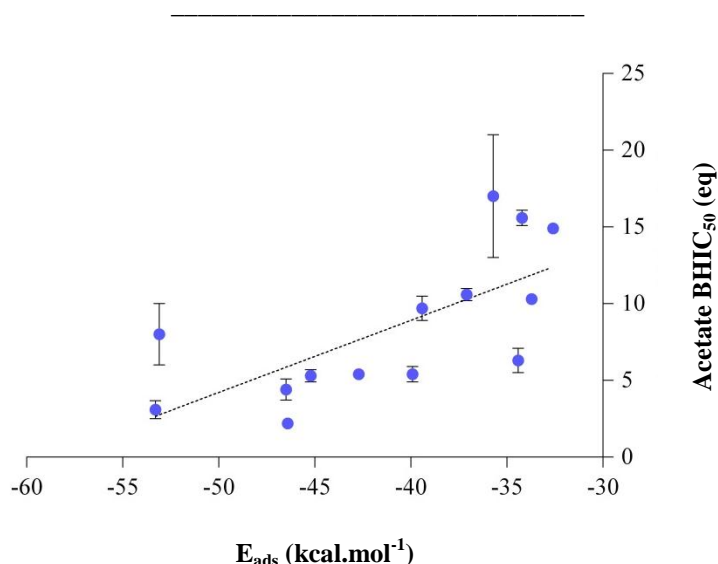
Figure 40: Comparing the calculated E_{ads} vs the acetate $BHIC_{50}$ values for face {011}.

An R^2 value of 0.48 and a P value of 0.006 are obtained.

With the first structure-activity results in hand, possible reasons for the poor correlations observed were considered. Analysis of a larger set of inhibitors might provide greater insight into the adsorption of inhibitors onto β-haematin. More importantly, a comparison of the E_{ads} values obtained in this study to β-haematin inhibition data obtained under more biologically-relevant conditions might give rise to better correlations. Unfortunately, the activities of most of the compounds discussed thus far were only ever investigated in acetate medium.   By comparing the calculated E_{ads} values to β-haematin inhibition activity determined using different assays, these structure-activity correlations could be evaluated more thoroughly.

2.4 ADSORPTION OF THE CLINICALLY-RELEVANT INHIBITORS ONTO THE β-HAEMATIN CRYSTAL SURFACES

With a comprehensive adsorption protocol in hand, which was developed by investigating the adsorption of a small set of quinoline compounds onto β-haematin, the study was extended to evaluate the adsorption of quinoline clinically-relevant antimalarial drugs onto β-haematin.

From the current drugs used for malaria treatment, AQ, CQ, MQ (±), and QN were chosen (Figure 12), as well as quinidine (QD) (Figure 41), an active antimalarial drug which is no longer used for the treatment of malaria due to growing parasite resistance.[62]
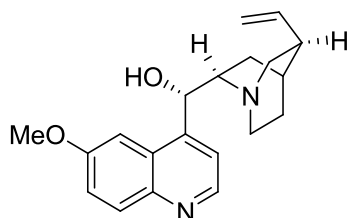
Quinidine (QD)

Figure 41: The chemical structure of quinidine (QD).

Similarly as for the previous set of quinoline compounds, the speciation at pH 4.8 for each of these compounds was calculated (Table 9). AQ and CQ are found to be diprotic at pH 4.8, where MQ(±), QN, and QD are predominantly monoprotic at this pH. Both enantiomers of CQ were initially considered and investigated, however owing to the fact that both showed the same (mirrored) interactions to the crystal surface, and that the same adsorption energies for interaction with face {001} were obtained, we proceeded with only one enantiomer of CQ for the remainder of the study (CQ-*S*).

_____

Table 9: The calculated and experimental pK_a values, as well as the speciation at pH 4.8.

	Quinoline nitrogen, pK_a 1		pK_a 2		% Diprotic	% Monoprotic
	Experimental	Calculated	Experimental	Calculated	Calculated	Calculated
AQ	7.02[a]	6.5	8.14[a]	9.7	100	0
CQ	8.1[b]	7.3	10.2[b]	10.3	100	0
MQ(±)	−	−	8.6[b]	9.5	0	100
QN	−	4.5	8.4[b]	9.1	14	86
QD	−	4.5	−	9.1	14	86

The experimental pK_a values were reported by (a) Hawley et al. and (b) Ginsburg et al.[110,147]

2.4.1 Adsorption onto face {011}

For the adsorption onto face {011}, π-π interactions were not commonly observed. The inhibitors adsorbed in such a way that a hydrogen bonding interaction is observed between a hydrogen donor atom of the inhibitor and a carbonyl group exposed at the crystal surface. This is seen for AQ, MQ(±), QN, and QD. The adsorption geometries were consistent, irrespective of the various protic forms investigated.

MQ(±), QD, and QN adsorbed in a similar way, where only the hydrogen atoms on the protonated quinuclidine and piperidine nitrogens formed hydrogen bonding interactions to a carbonyl group on the crystal surface (Figure 42). The interaction distances were 2.0, 1.8, and 2.2 Å respectively. Strangely, the formation of π-π interactions was not observed.

_____
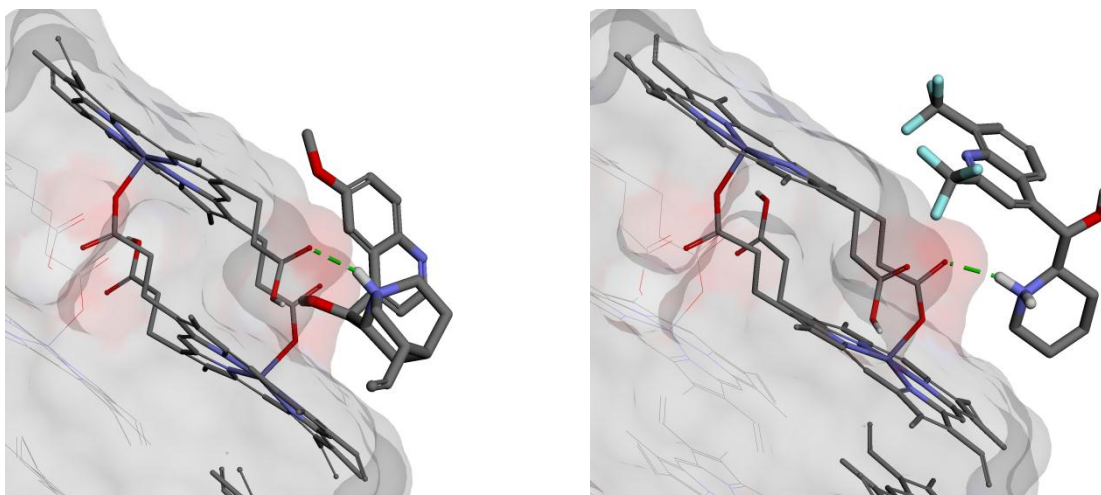
Figure 42: Adsorption of QD and MQ-*S* onto face {011}.

The adsorption of QD (left) and MQ-S (right) in the monoprotic form onto face {011}, as viewed from the side of the crystal face. Hydrogen bonding interactions are indicated by ▪ ▪ .

AQ adsorbed slightly differently, where the molecule stretches over the crystal surface (Figure 43). However, no π-π interaction was observed, although both the protonated tertiary amine and the hydroxyl moiety on the side-chain could form hydrogen bonding interactions to a carbonyl group on the crystal surface, with measured interaction distances of 2.7 and 2.0 Å respectively.

CQ was the only compound in this set that adsorbed in such a way that a π-π interaction could be favoured, in a similar manner to that observed for the adsorption of compound **KN12** in Figure 34. Furthermore, with the π-π interaction being favoured in this case, the side-chain is extended over the crystal surface to an extent that the protonated tertiary amine could not form a hydrogen bonding interaction to one of the carbonyl groups on the surface (Figure 44).

Chapter 2 - The adsorption of inhibitors onto β-haematin

_____
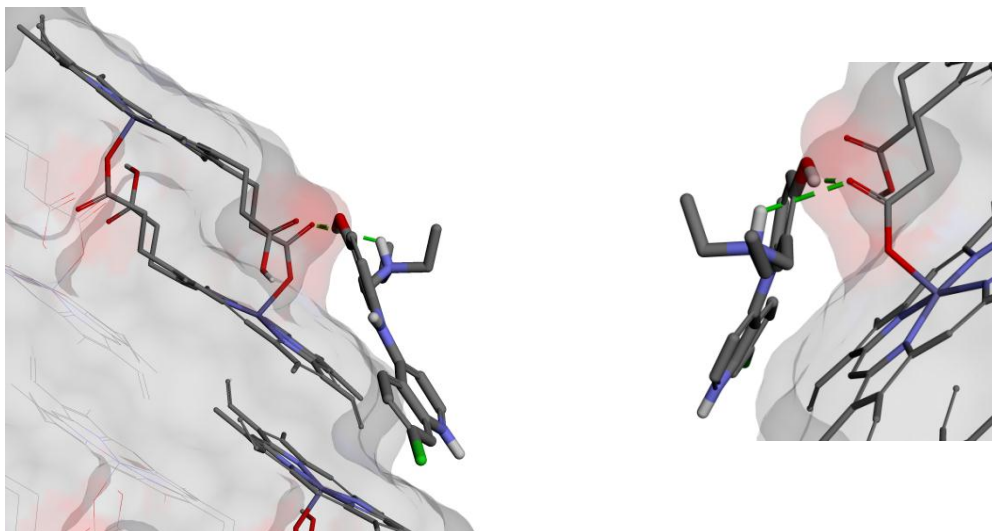
Figure 43: Adsorption of AQ onto face {011}.

The adsorption of AQ in the diprotic form onto face {011}, as viewed from the side of the crystal face (left), as

well as viewed from the back (right). Hydrogen bonding interactions are indicated by ■ ■ .

Figure 44: Adsorption of CQ onto face {011}.

The adsorption of CQ in the diprotic form onto face {011}, as viewed from the side of the crystal face, is shown.

No hydrogen bonding interactions were observed. A possible π-π interaction that forms between CQ and the

porphyrin on the β-haematin crystal surface, with a measured interaction distance of 3.6 Å, is indicated by ■ ■ .

87

For the adsorption onto face {011}, most of the inhibitors adsorb in such a way that hydrogen bonding interactions are formed between the inhibitor and the crystal surface, where CQ is the only inhibitor that adsorbs in such a way that a π-π interaction is formed between the inhibitor and the crystal surface. From this study it is clear that the formation of both hydrogen bonding interactions and π-π interactions is feasible, but it is not clear which of these interactions is necessarily preferred.

2.4.2 Adsorption onto face {001}

In evaluating the adsorption onto face {001}, all the inhibitors adsorbed into the primary adsorption site, with the exception of MQ(±), which, owing to the bulky -CF$_3$ substituent, is too large to fit in the small primary adsorption site. Consequently, both stereoisomers of the latter compound (MQ-*S* and MQ-*R*) show a preference for adsorbing in the secondary adsorption site. As for the adsorption onto face {001}, the adsorption geometries were consistent, irrespective of the various protic forms investigated.

The two stereoisomers of MQ adsorbed onto the crystal surface in an unexpected manner (Figure 45). Even though the -CF$_3$ substituent makes the quinoline too bulky to fit into the primary adsorption site, it was expected that π-π interactions could form between the drug and the porphyrin in the secondary adsorption site, or that a hydrogen bonding interaction could form between the hydroxyl group and the carbonyl on the crystal surface. These interactions were not observed.

However, for the obtained adsorption geometry of MQ, it might be that the -CF$_3$ substituent is too bulky and thus causes repulsion of the quinoline away from the porphyrin surface. It is

possible that the fluorine atoms could form C-H···F interactions to nearby non-polar hydrogen atoms, with measured interaction distances of 2.7, 2.7, and 3.0 Å, respectively. These interactions have been shown to play a role in ligand-protein binding.[148] Furthermore, it is also known for halogens to form an orthogonal C-O···F interaction,[148,149] where this interaction might form between fluorine atoms on both ends of the quinoline to the two carbonyl groups on the crystal surface, with measured interaction distances of 2.9 and 3.0 Å.
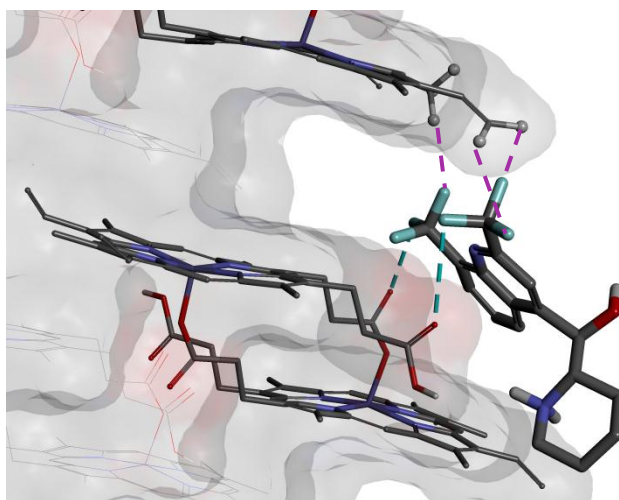
Figure 45: Adsorption of MQ-*R* onto face {001}.

The adsorption of MQ-R in the monoprotic form onto face {001} is shown, as viewed from the side of the crystal face. The C-O···F interactions, with measured interaction distances of 2.7, 2.7 and 3.0 Å, are indicated by ▪ ▪ , and the C-H···F interactions, with measured interaction distances of 2.9 and 3.0 Å, are indicated by ▪ ▪ . The non-polar hydrogen atoms that form C-H···F interactions are indicated as grey balls, as part of the porphyrin structure above the crevice.

In general, the quinoline moieties of each inhibitor occupy the primary adsorption site, where the formation of π-π interactions to the top and the bottom porphyrin on the crystal surface is seen. For AQ and CQ, the side-chains are not observed to participate in hydrogen bonding interactions, as the proton donor atoms extend too far from the carbonyl groups on the crystal surface (Figure 46).
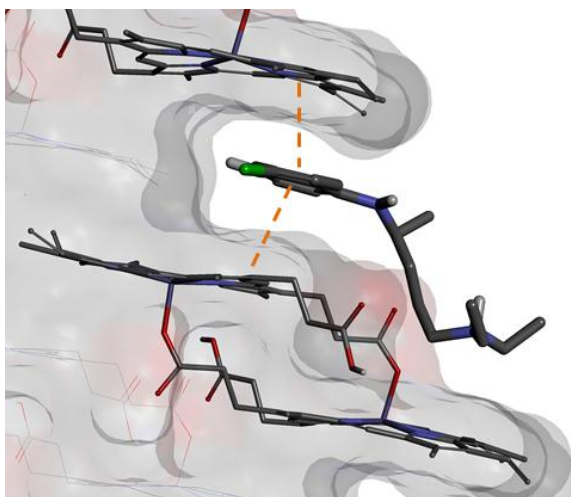
Figure 46: Adsorption of CQ onto face {001}.

The adsorption of CQ onto face {001} in the diprotic form is shown, as viewed from the side of the crystal face. The inhibitor could form possible π-π interactions to the porphyrin on the β-haematin crystal surface, with measured interaction distances of 3.5 and 3.7 Å. These interactions are indicated by ▪ ▪ *.*

QN and QD are able to form both π-π interactions to the porphyrin, as well as hydrogen bonding interactions just outside the primary pocket (Figure 47). In both cases, the side-chain extends to allow the hydrogen atom on the protonated quinuclidine moiety to form a hydrogen bonding interaction to a carbonyl group on the crystal surface, with a measured interaction distance of 2.0 Å.
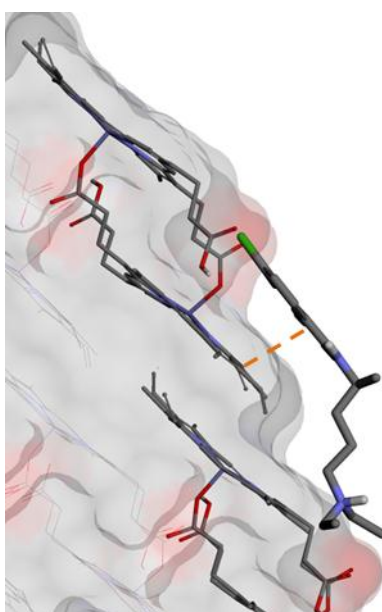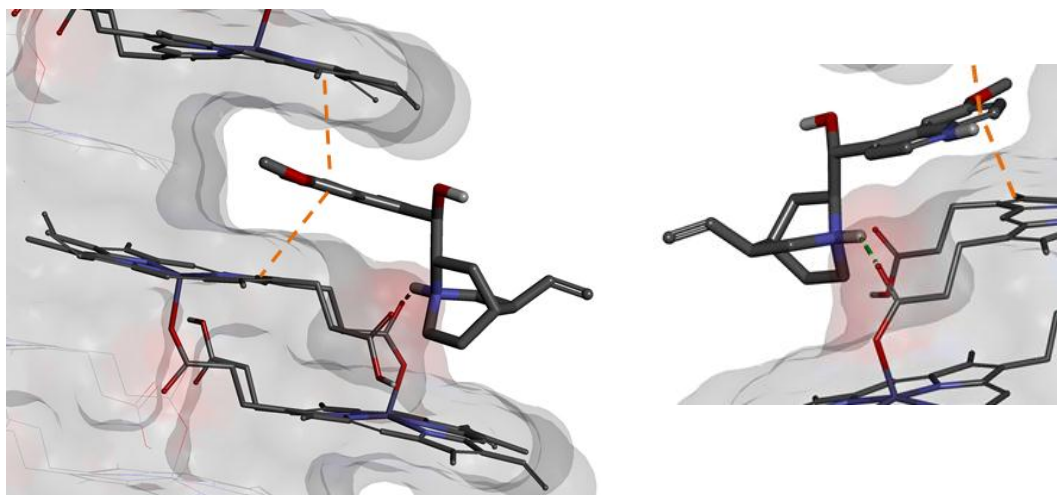
Figure 47: Adsorption of QN onto face {001}.

The adsorption of QN in the diprotic form onto face {001}, as viewed from the side of the crystal face (left), as well as from the back (right), is shown. The hydrogen bonding interaction that forms over a distance of 2.0 Å are indicated by ▪ ▪ , and the π-π interactions, with measured interaction distances of 3.6 and 3.7 Å are indicated by ▪ ▪ .

The adsorption geometry of QN and QD is considered as the ideal adsorption geometry for the adsorption into the primary and secondary adsorption sites, where both π-π intearctions and hydrogen bonding interactions form between the inhibitor and the crystal surface. It is commonly known in drug development that enhaced drug activity is brought about with the formation of an increased number of intermolecular interactions between the drug and the active site.[150] Therefore, for this study, enhanced adsorption could be promoted by increasing the number of intermolecular interactions formed between the inhibitor and the crystal surface. Furthermore, if a correlation is found between an enhanced adsorption energy value (E_{ads}) and a more active β-haematin growth inhibition activity value, a greater number of molecular interactions between the inhibitor and the crystal surface would result in an improved adsorption, an thus an increased β-haematin growth inhibition activity.

Also, considering that face {001} has a distinctive crevice for inhibitors to adsorb into, the formation of π-π interactions in the primary adsorption site, as well as the formation of hydrogen bonding interactions in the secondary adsorption site, could be optimised for enhanced adsorption. Therefore, the computational investigation of the adsorption onto face {001} would be beneficial for future drug design purposes. Also, with the surface of face {001} (secondary adsorption site) being very similar to that of face {011}, by designing a compound for the optimal adsorption onto face {001}, it would be reasonable to expect that it would also favour adsorption onto face {011}.

2.4.3 Investigating structure-activity relationships

2.4.3.1 Comparing the calculated E_{ads} against the lipid $BHIC_{50}$ for the clinically-relevant inhibitors.

One advantage of investigating the adsorption of clinically-relevant antimalarial drugs onto β-haematin, is that these compounds are commercially available and therefore, their β-haematin inhibition activity has been assessed using various assays. Furthermore, by evaluating the adsorption onto the fastest growing faces computationally, the calculated E_{ads} values, as well as the preferred adsorbed geometries of these compounds, could provide a greater understanding in the mechanism of β-haematin inhibition by the adsorption of inhibitors onto the crystal surface.

The three assays that were used are discussed in Section 1.4.4, where Ncokazi *et al*. reported the acetate $BHIC_{50}$ values of these compounds.[107] The set of clinically-relevant compounds was extended by including compounds **KN6** and **KN7** from the previous study, which were

_____

kindly resynthesised by a fellow student within our research group, Jonathan Hay.[151] A larger data set would be more representative and also permit outliers to be excluded if necessary without reducing the data set below the minimum required for a significant correlation. Furthermore, lipid $BHIC_{50}$ values determined by Sharné Fitzroy,[119] and NP40 $BHIC_{50}$ values determined by Dr Kathryn Wicht, using an improved method,[152] were available. Using the same procedure, NP40 $BHIC_{50}$ values for compounds **KN6** and **KN7** were determined in the current study. However, prior to analysis, it was reasoned that with the conditions of the lipid $BHIC_{50}$ assay best representing the physiological environment within the parasite, it would be more suitable to first compare the E_{ads} values against these activity results.

By first evaluating the adsorption onto face {001} against the lipid $BHIC_{50}$ activity, and thereby taking into account the percentages of speciation, an R^2 value of 0.49 and a significant P value of 0.05 is found (Table 10, Figure 48). Furthermore, by evaluating the adsorption onto face {011} against the lipid BHIC50 activity, a non-significant trend is observed, with an R^2 value of 0.1 and a P value of >0.05 (Table 11, Figure 49).

Chapter 2 - The adsorption of inhibitors onto β-haematin

_____

Table 10: The determined lipid BHIC$_{50}$ activity of the clinically relevant-inhibitors, as well as the calculated E$_{ads}$ values for the adsorption onto face {001}, taking into account the percentage speciation.

Compound	E$_{ads}$ Diprotic face {001} (kcal.mol^{-1})			E$_{ads}$ Monoprotic face {001} (kcal.mol^{-1})			% Diprotic	% Monoprotic	E$_{ads}$ face {001} (kcal.mol^{-1})	Lipid BHIC$_{50}$ (µM)		
KN6	-66.5	±	0.3	−			100	0	-66.3	29.8	±	0.7
KN7	-51.5	±	0.01	−			100	0	-51.4	55.5	±	9.9
AQ	-69.8	±	0.2	-70.5	±	0.01	98	2	-69.9	5.9	±	0.3
CQ	-67.0	±	0.01	−			100	0	-66.7	18.8	±	0.6
MQ-*S*	−			-55.7	±	0.01	0	100	-55.7	22.9	±	0.6
MQ-*R*	−			-61.6	±	0.01	0	100	-61.6	22.9	±	0.6
QD	-80.8	±	0.01	-73.6	±	0.01	14	86	-74.6	20.1	±	2.7
QN	-66.2	±	0.01	-65.4	±	0.01	14	86	-65.5	31.0	±	2.5

94

Table 11: The determined lipid BHIC$_{50}$ activity of the clinically-relevant inhibitors, as well as the calculated E$_{ads}$ values for the adsorption onto face {011}, taking into account the percentage speciation.

Compound	E$_{ads}$ Diprotic face {011} (kcal.mol^{-1})			E$_{ads}$ Monoprotic face {011} (kcal.mol^{-1})			% Diprotic	% Monoprotic	E$_{ads}$ face {011} (kcal.mol^{-1})	Lipid BHIC$_{50}$ (μM)		
KN6	-46.4	±	0.1	−			100	0	-46.2	29.8	±	0.7
KN7	-53.1	±	0.01	−			100	0	-53.0	55.5	±	9.9
AQ	-59.1	±	0.01	-58.9	±	0.01	98	2	-59.1	5.9	±	0.3
CQ	-48.3	±	0.01	−			100	0	-48.2	18.8	±	0.6
MQ-*S*	-48.8	±	0.01	-48.8	±	0.01	0	100	-48.8	22.9	±	0.6
MQ-*R*	-55.3	±	0.5	-55.3	±	0.5	0	100	-55.3	22.9	±	0.6
QD	-57.3	±	0.1	-56.3	±	0.01	14	86	-56.4	20.1	±	2.7
QN	-48.5	±	0.01	-49.3	±	0.01	14	86	-49.2	31.0	±	2.5

Chapter 2 - The adsorption of inhibitors onto β-haematin

_____
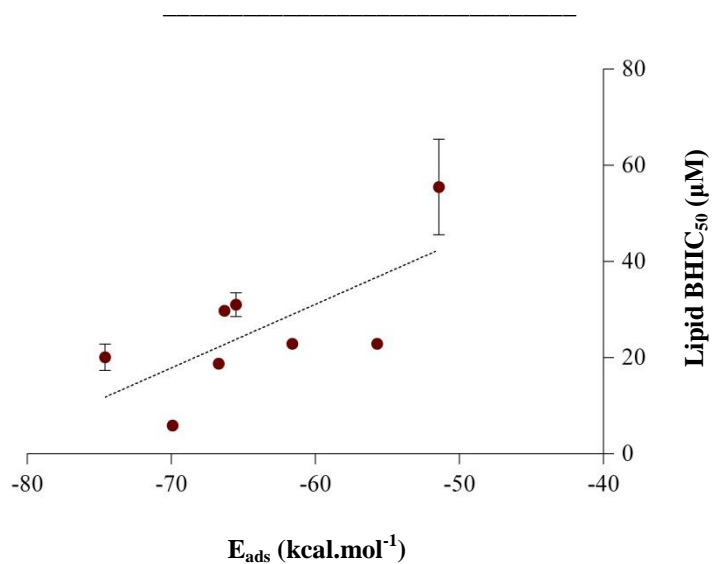
Figure 48: Comparison of the calculated E_{ads} values against the lipid $BHIC_{50}$ activity for adsorption of the clinically-relevant inhibitors and compounds KN6 and KN7 onto face {001}.

An R^2 value of 0.49 and a P value of 0.05 are obtained.
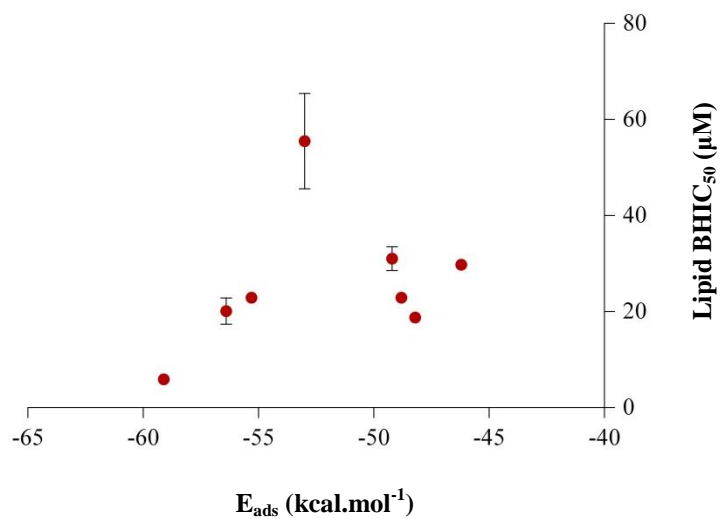
Figure 49: Comparison of the calculated E_{ads} values against the lipid $BHIC_{50}$ activity for adsorption of the clinically-relevant inhibitors and compounds KN6 and KN7 onto face {011}.

An R^2 value of 0.01 and a P value >0.05 are obtained.

96

These trends were somewhat of a surprise, since the trends for the small quinoline compounds were the opposite, where the better correlation was found for the adsorption onto face {011}. This result led to the conclusion that there may be more aspects to consider than only the adsorption of the preferred speciation form onto the two fastest growing faces. Furthermore, it is also found that the E_{ads} values for the adsorption of the clinically-relevant drugs onto face {001}, are generally more favourable than that for the adsorption onto face {011}.

It could be that for a single molecule, the adsorption onto one crystal face could be more favoured than onto the other. Furthermore, it could also be that the adsorption of one speciation form is favoured onto one crystal face, where the adsorption of the other speciation form is favoured onto the other crystal face. Therefore, the various speciation forms, as well as the adsorption onto the two fastest growing crystal faces, had to be evaluated.

2.4.3.2 Introducing multiple correlation studies.

In order to evaluate the contribution of different protic forms, as well as a particular compound's preference for either the {001} or {011} face, a type of multiple correlation calculation was considered. For this evaluation, the Solver module within Microsoft Office Excel was used.

The speciation is accounted for by taking into account a percentage fraction of each speciation form, similar to that discussed in Section 2.3.3. Therefore, y would represent the fraction in the monoprotic form (Equation 2.3), and z would represent the fraction in the diprotic form (Equation 2.4).

_____

$$y = \left(\frac{\% \, Monoprotic}{100}\right) \tag{2.3}$$

$$z = \left(\frac{\% \, Diprotic}{100}\right) \tag{2.4}$$

Furthermore, the preferred crystal face for each of these speciation forms is taken into account by calculating a fraction of the two E_{ads} values obtained for the adsorption of this speciation form onto each of the two crystal faces. For example, for the diprotic form of a compound, a_D is a function of the adsorption onto face {001} (Equation 2.5), and b_D is a function of the adsorption onto face {011} (Equation 2.6).

$$a_D = f_{(001)} = \left\{\frac{[E_{001}]}{[E_{001}]+[E_{011}]}\right\} \tag{2.5}$$

$$b_D = f_{(011)} = \left\{\frac{[E_{011}]}{[E_{001}]+[E_{011}]}\right\} \tag{2.6}$$

Similarly, for the monoprotic form, a_M is a function of the adsorption onto face {001} (Equation 2.7), and b_M is a function of the adsorption onto face {011} (Equation 2.8).

$$a_M = f_{(001)} = \left\{\frac{[E_{001}]}{[E_{001}]+[E_{011}]}\right\} \tag{2.7}$$

$$b_M = f_{(011)} = \left\{\frac{[E_{011}]}{[E_{001}]+[E_{011}]}\right\} \tag{2.8}$$

Finally, by combining all of these parameters, a multiple correlation equation is obtained for the observed adsorption energy (Equation 2.9), where the variables, v_1 - v_4, are allowed to freely refine in order to obtain the best fit of the calculated E_{ads} values to the activity results.

$$E_{ads} = y[v_1 a_M(E_{001}) + v_2 b_M(E_{011})] + z[v_3 a_D(E_{001}) + v_4 b_D(E_{011})] \tag{2.9}$$

_____

Upon applying this multiple correlation equation to the data comparing the calculated E_{ads} values to the lipid $BHIC_{50}$ data for the clinically-relevant antimalarial drugs, the best fit values of the variables v_1 - v_4 were found to be 0.04, 0.53, 0.30, and 0.13 respectively (Table 12), and an R^2 value of 0.78 and corresponding P value of 0.004 are observed (Table 13, Figure 50).

Table 12: Final variables calculated for the clinically-relevant inhibitors

Variable	Value	Crystal face	Speciation form
v_1	0.04	{001}	Monoprotic
v_2	0.53	{011}	Monoprotic
v_3	0.30	{001}	Diprotic
v_4	0.13	{011}	Diprotic

Table 13: The determined lipid $BHIC_{50}$ activity of the clinically relevant inhibitors, as well as the calculated E_{ads} obtained from the multiple correlation.

Compound	E_{ads} (kcal.mol^{-1})	Lipid $BHIC_{50}$ (µM)		
KN6	-73.4	29.8	±	0.7
KN7	-57.0	55.5	±	9.9
AQ	-78.6	5.9	±	0.3
CQ	-73.8	18.8	±	0.6
MQ-*S*	-68.0	22.9	±	0.6
MQ-*R*	-77.8	22.9	±	0.6
QD	-77.0	20.1	±	2.7
QN	-66.4	31.0	±	2.5
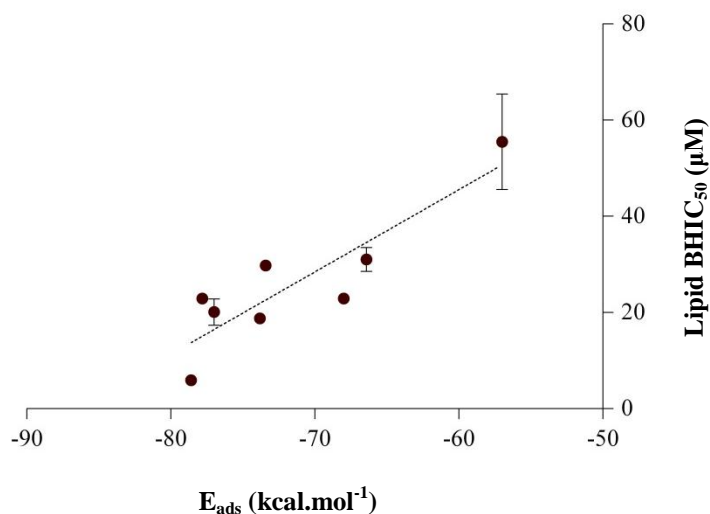
Figure 50: Multiple correlation fit for the clinically-relevant inhibitors.

The multiple correlation fit for comparing the calculated E_{ads} to the lipid $BHIC_{50}$ activity for the clinically-relevant inhibitors. An R^2 value of 0.78 and a P value of 0.004 are found.

With variable v_2 calculated as having the largest contribution to this correlation and variable v_3 calculated as having the second-largest contribution to this correlation, it could be concluded that the clinically-relevant inhibitors have an overall preference to adsorb onto face {011} in the monoprotic form, followed by a preference to adsorb in the diprotic form onto face {001}. This result is reasonable, since half of the inhibitors investigated, are primarily in the monoprotic form at pH 4.8. Furthermore, with compound **KN7**, as well as the two isomers of MQ being unable to adsorb into the primary adsorption site on face {001}, adsorption is primarily preferred onto face {011}.

Similarly, by applying this multiple correlation equation to the data comparing the calculated E_{ads} values to the acetate $BHIC_{50}$ for the small quinoline compounds, the variables v_1 - v_4

_____

were found to be 0.00, 0.57, 0.15, and 0.29 respectively (Table 14), where an R^2 value of 0.56

and a P value of 0.004 are found (Table 15, Figure 51).

Table 14: Final variables calculated for the small quinoline compounds

Variable	Value	Crystal face	Speciation form
v_1	0.00	{001}	Monoprotic
v_2	0.57	{011}	Monoprotic
v_3	0.15	{001}	Diprotic
v_4	0.29	{011}	Diprotic

Table 15: The determined acetate $BHIC_{50}$ activity of the small quinoline compounds, as well as the calculated E_{ads} obtained from the multiple correlation.

Compound	E_{ads} (kcal.mol^{-1})	Acetate $BHIC_{50}$ (eq)
KN1	-45.1	15.6 ± 0.5
KN2	-42.9	14.9 ± 0.3
KN3	-48.0	17.0 ± 4.0
KN4	-52.2	9.7 ± 0.8
KN5	-57.6	4.4 ± 0.7
KN6	-59.2	2.2 ± 0.2
KN7	-60.4	8.0 ± 2.0
KN8	-64.8	3.1 ± 0.6
KN9	-47.4	10.6 ± 0.4
KN10	-46.9	10.3 ± 0.3
KN11	-48.1	5.4 ± 0.2
KN12	-51.7	5.4 ± 0.5
KN13	-47.4	6.3 ± 0.8
KN14	-56.1	5.3 ± 0.4
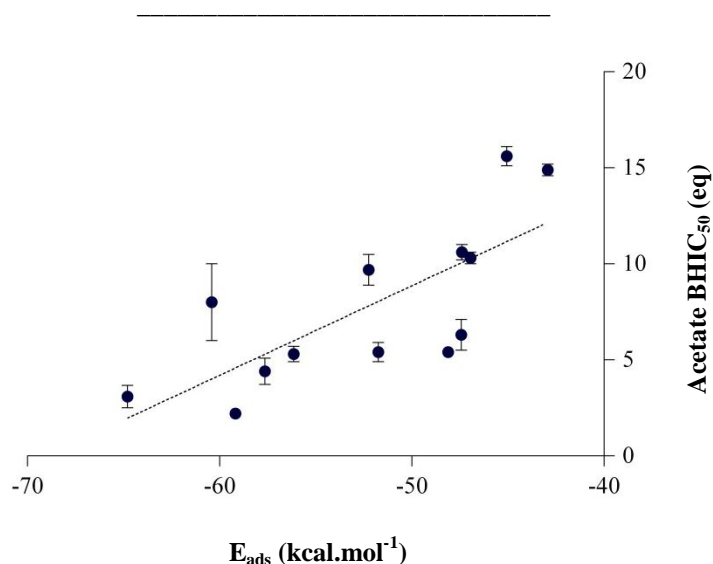
Figure 51: Multiple correlation fit for the small quinoline inhibitors.

The multiple correlation fit for comparing the calculated E_{ads} values to the acetate $BHIC_{50}$ activity for the small quinoline inhibitors. An R^2 value of 0.56 and a P value of 0.004 are found.

Notably, a less significant correlation is found for this larger data set. A slightly greater preference for adsorption onto face {011} in the monoprotic form is found as for the clinically-relevant inhibitors, where variable v_4, for adsorption of the diprotic form onto face {011}, is calculated to have the second-largest contribution to this correlation.

However, only 2 of the 14 compounds were calculated to adsorb partially in the monoprotic form (compounds **KN8** and **KN14**), and only 2 compounds were unable to adsorb into the primary adsorption site on face {001} (compounds **KN7** and **KN11**). Therefore, with most of the compounds showing preference for adsorbing onto face {001} in the diprotic form, a greater contribution of the variable v_3 is expected.

Considering that a linear correlation is found between the lipid $BHIC_{50}$ activity and biological activity, and that a non-significant correlation is found between lipid $BHIC_{50}$ activity and

_____

acetate $BHIC_{50}$ activity, this result does not come as a surprise (Section 1.4.4).[119] In fact, it indicates that the correlations observed here for comparing the E_{ads} values to the two $BHIC_{50}$ activities, agrees with what have been previously reported. Therefore, this highlights the significance of seeing a linear correlation between the calculated E_{ads} values and the lipid $BHIC_{50}$ activities for the clinically-relevant inhibitors.

Finally, from these results, it is concluded that the adsorption of inhibitors onto β-haematin is a more complex process than originally anticipated. However, by taking into account the speciation and the differential adsorption onto both the fastest and the second-fastest growing faces, it is demonstrated that there is a significant correlation between the computed E_{ads} results and the determined lipid $BHIC_{50}$ values.

This finding strongly supports the hypothesis that quinoline antimalarial drugs exert their mechanism of action by adsorbing to the fastest growing faces of β-haematin and thereby inhibit β-haematin growth.

2.5 EXAMINING THE STEP PROPAGATION

Olafson *et al.* reported the formation of new layers onto β-haematin in a step-like manner (Section 1.4.1).[49] Nucleation was mainly observed on the largest crystal face, face {100}, where newly formed islands were observed by AFM to grow in the *b* and *c* directions to form new layers. The results are reportedly consistent with a classical mechanism of crystallisation.

At the start of this study, the insights of Olafson *et al*. regarding the nucleation and growth of β-haematin were not published. However, when their report became available, the current study was extended to investigate the step propagation in Materials Studio as a means of determining the important interaction sites on these crystal faces. Furthermore, with an optimised adsorption protocol in hand, it could be used to compare the adsorption of the clinically-relevant inhibitors onto the newly formed steps to the results presented above.

2.5.1 Investigating the crystal faces formed upon step propagation.

Considering the proposed mechanism of crystal growth on the largest face, face {100}, step formation on the crystal face and subsequent growth in the *b* and *c* directions would result in a newly formed island, having similar sides as to that of the overall β-haematin crystal (Figure 52). These sides are identical to face {010}, face {011}, and face {001}. Therefore, when the crystal grows faster at the fastest growing faces, the island would be extended to grow in length in the *c* direction.

The crystal grows with the addition of one haem molecule, or one β-haematin dimer at a time. The exact mechanism of β-haematin crystal growth is still unknown.[153] Therefore, for the

_____

purposes of this project, crystal growth would be considered as the addition of one β-haematin dimer onto the crystal surface.
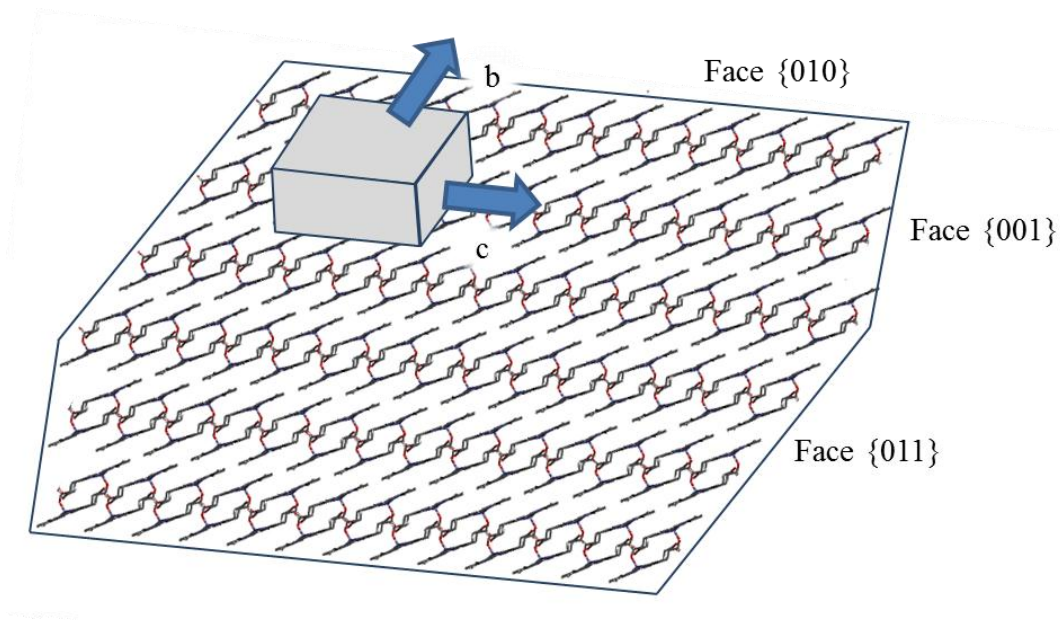
Figure 52: Step propagation onto face {100}.

Face {100} is viewed from the top. Here, step propagation onto face {100} is shown in the grey box, where growth in the b and c directions is indicated by the blue arrows.

_____

Similarly, for step propagation to occur onto face {010} in the *b* direction, both the sides of the newly formed step would predominantly represent the surface of face {011} (Figure 53). However, the corner that forms on the one side of the step between faces {011} and {010}, (indicated in red on the left of the blue box in Figure 53), represents the surface of face {001}. With further growth in the *b* direction, this side would further represent the surface of face {011}.
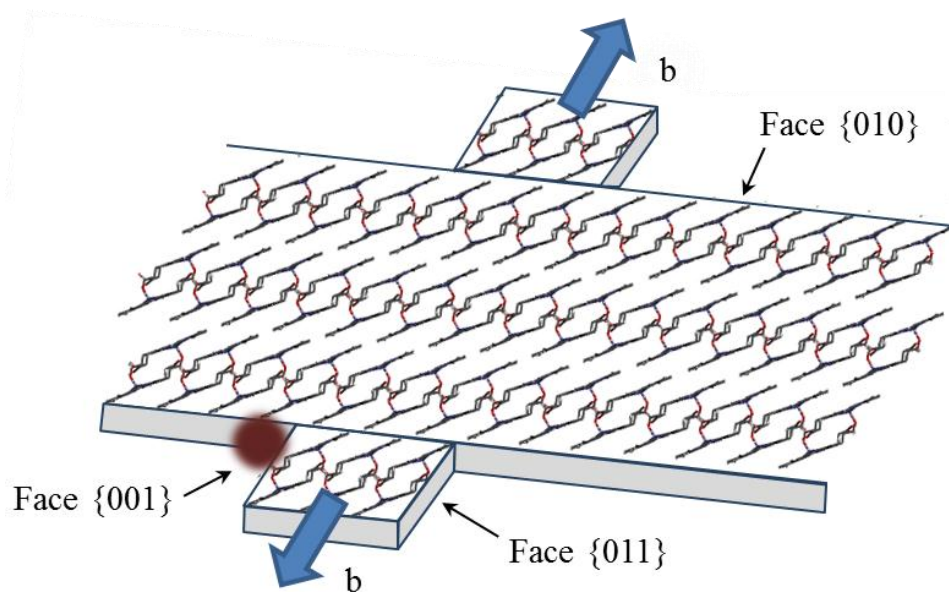
Figure 53: Step propagation onto face {010}.

Step propagation onto face {010} is shown, where growth in the b direction is indicated with a blue arrow. The surface that forms on the sides of the box represents face {011}. However, the intersection that forms on the left of the blue box (indicated in red) represents face {001}. Face {100} is viewed from the top.

When the crystal expands in the *c* direction, steps would form onto face {001} and face {011} (Figure 54). Therefore, step propagation onto both these crystal faces was examined more closely (Figure 55).
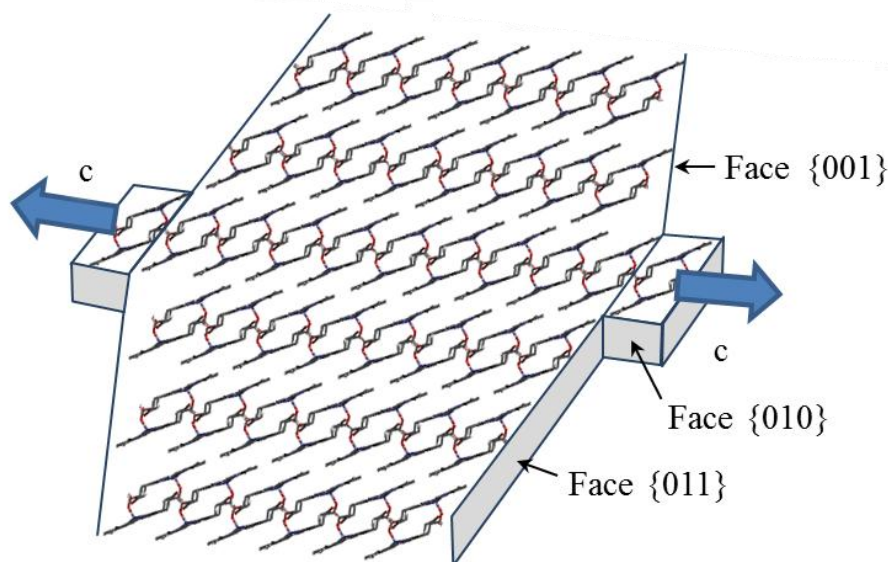
Figure 54: Step propagation onto faces {001} and {011}.

Step propagation onto faces {001} and {011} is shown, where growth in the c direction is indicated by a blue arrow. Face {100} is viewed from the top.

For the step propagation onto face {011} (Figure 55), it is found that the newly formed step has sides that are identical to face {010} and face {001}. However, the same observation is only made for the one side of the step that forms onto face {001}, where the one side represents face {011}. The other side of the step forms a terrace that represents face {010}, where this extends over a primary pocket. Here this terrace forms another hydrophobic porphyrin surface above the primary pocket, to which the clinically-relevant antimalarial drugs could form π-π interactions.

107

_____
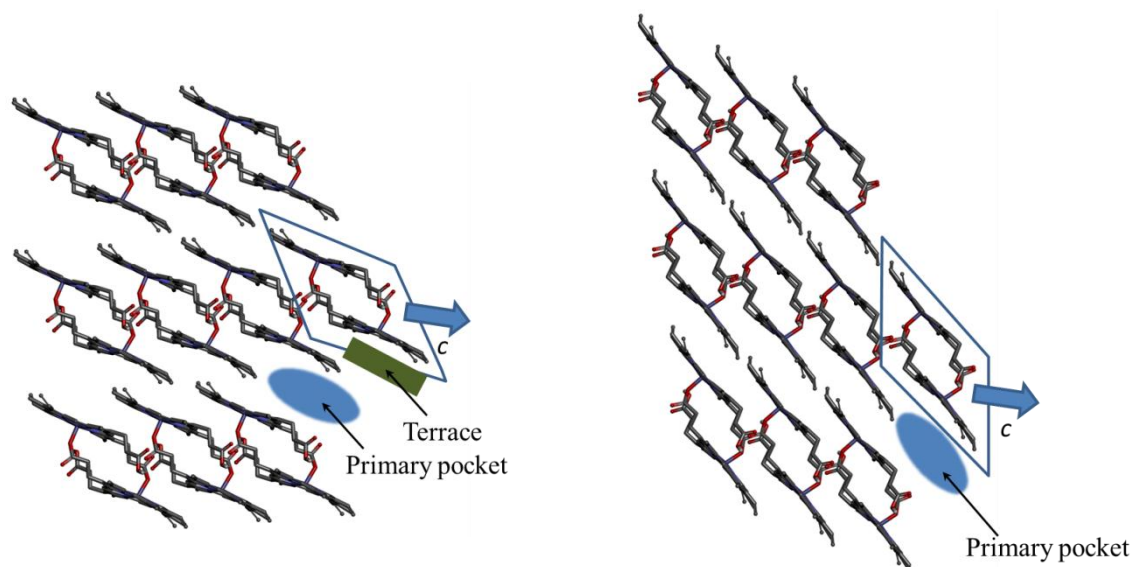
Figure 55: Step propagation onto face {001} (left) and face {011} (right).

Step propagation onto face {001} (left) and face {011} (right), are shown. For the step onto face {011}, the surface above the blue box represents face {010}, where the surface below the blue box represents face {001}. For the step onto face {001}, the surface above the blue box represents face {011}, where the terrace below the blue box represents face {010}. Face {100} is viewed from the top.

With a greater understanding of the crystal morphology attained, this insight was further used to explore step propagation onto the four most dominant crystal faces of β-haematin. Moreover, by having an in-depth understanding of the step propagation onto the two fastest growing faces, faces {001} and {011}, the adsorption of inhibitors onto these more complex surfaces could be investigated.

2.5.2 Adsorption of clinically-relevant inhibitors onto the steps

2.5.2.1 Preparing the vacuum slabs

Once a new step forms on top of face {100}, it will expand in the *b* and c directions, showing faster growth in the *c* direction. By doing so, steps would form onto face {011} and face {001} more rapidly than onto face {010}. Therefore, for the expansion in the *b* direction, face {010} forms a step where the sides represent face {001} and face {011}. Also, the one side of the step onto face {001} represents face {011}, where the one side of the step onto face {011} represents face {001}. The adsorption of the clinically-relevant inhibitors onto the faces {001} and {011} was already investigated and is previously discussed in this chapter (Section 2.4).

However, for step propagation onto face {011}, one of the sides of the step represents face {010}, where the newly formed flat surface adjacent to face {011} might allow for additional π-π interactions to form to it. Furthermore, for step propagation onto face {001}, the one side of the step forms a terrace that represents face {010}. This terrace extends over a primary pocket, where it could allow side-chains of molecules to form π-π interactions or hydrophobic interactions to. Therefore, considering that a new step forms onto the largest crystal face, face {100}, and that fastest growth occurs in the *c* direction, the adsorption of clinically-relevant inhibitors onto these two areas was examined (Figure 56).

For this, vacuum slabs were created that mimicked these corners between the crystal faces. A larger crystal thickness was used compared to the previous studies, where selected unit cells were deleted to create a three dimensional surface that would mimic the corners formed between the crystal faces.

_____

Upon further investigating the new corner that forms between face {001} and face {100}, an additional free carbonyl group is observed on the surface of face {100} in the primary pocket. This could form a hydrogen bonding interaction to either another β-haematin dimer, haem, or an inhibitor. The same is observed for the corner that forms between face {011} and face {100}, but this is not a new interaction on face {011}.

By preparing the vacuum slabs that represent the step propagation at the two corners that form between faces {001} and {100}, and faces {011} and {100}, adsorption of the clinically-relevant inhibitors onto these faces was investigated.

(a)

(b)

(c)

(d)
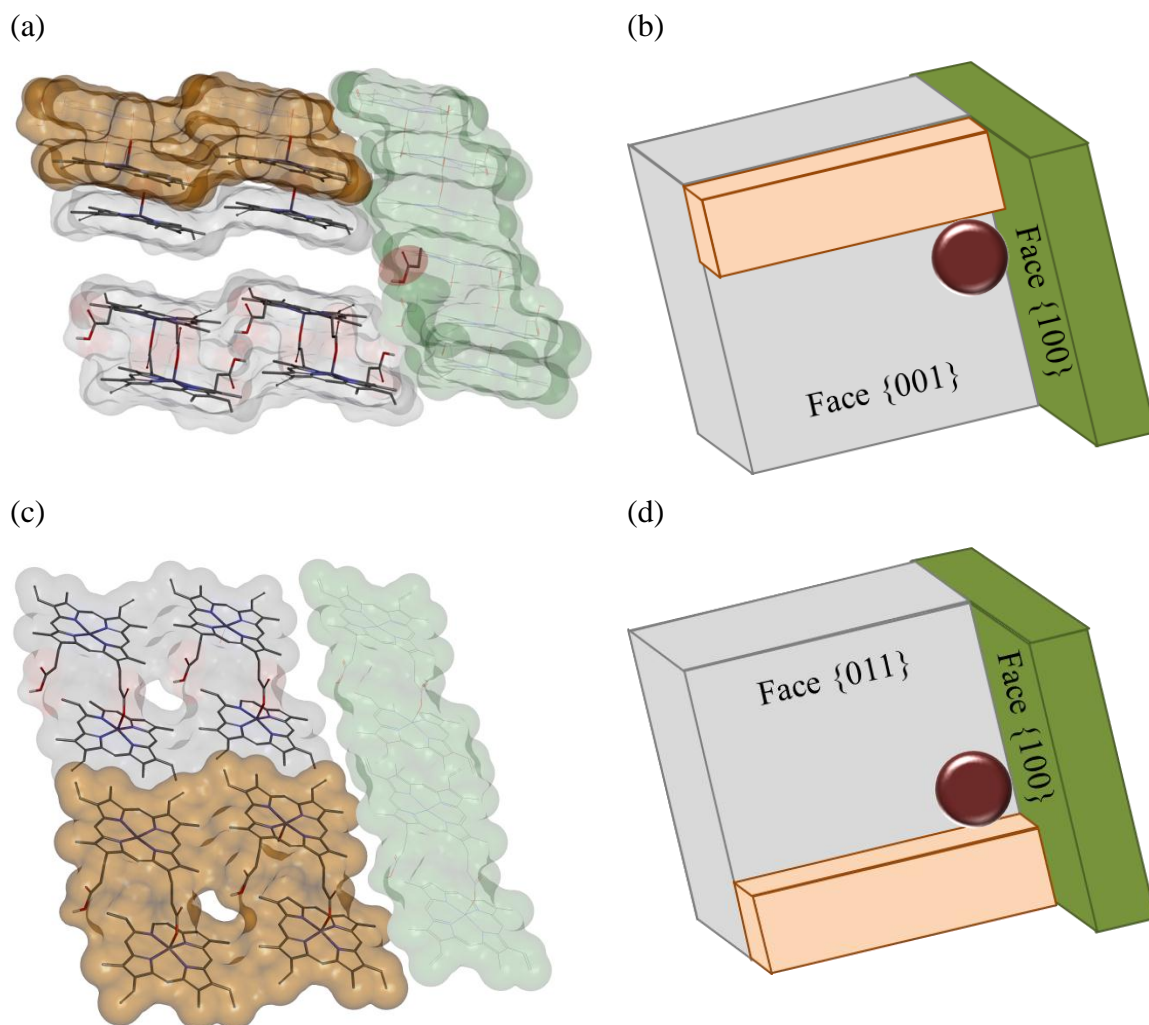
Figure 56: The two crystal surfaces investigated.

The newly formed steps onto face {001} (a and b) and face {011} (c and d) are shown, where the steps are indicated in orange and face {100} is shown in green. The newly formed corner interaction sites are indicated by a red button for face {001} (b) and face {011} (d). The new hydrogen bonding interaction site on face {001} is indicated by ⬤ in (a).

111

2.5.2.2 The results pertaining to the adsorption of clinically-relevant inhibitors onto the steps

2.5.2.2.1 Adsorption with step propagation onto face {001}

For the adsorption of the inhibitors onto face {001}, it is found that these compounds preferentially adsorb into the slightly more embedded primary adsorption site (previously shown in Figure 55), in a manner similar to that observed for the original primary adsorption site investigated, with similar calculated E_{ads} values (Table 16). MQ (both *R* and *S* isomers) and compound **KN7** were excluded from this study, as these compounds showed preference to adsorb onto the secondary adsorption site in the previous study (Section 2.4).

Some of the inhibitors (AQ, CQ, QD) showed a preference for adsorbing into the new corner that formed between face {100} and face {001}, where improved E_{ads} values of up to 5 kcal.mol^{-1} were determined. However, the same geometries as previously observed, is found. It is possible that the increase in the E_{ads} values is simply due to the formation of hydrophobic interactions to the surface on face {100}, therefore allowing for higher interaction energies. For the adsorption of AQ into this corner (as an example), the formation of C-H···Cl halogen bonding interactions between the inhibitor and the porphyrin structure on face {100} are observed, with measured interaction distances of 2.7 and 3.0 Å (Figure 57). This interaction is not possible in the absence of face {100}. Therefore, this interaction was not observed in the previous study (Section 2.4).

Unfortunately, with not all of the inhibitors adsorbing into the corner formed between face {100} and face {001}, structure-activity relationships could not be meaningfully investigated.

_____
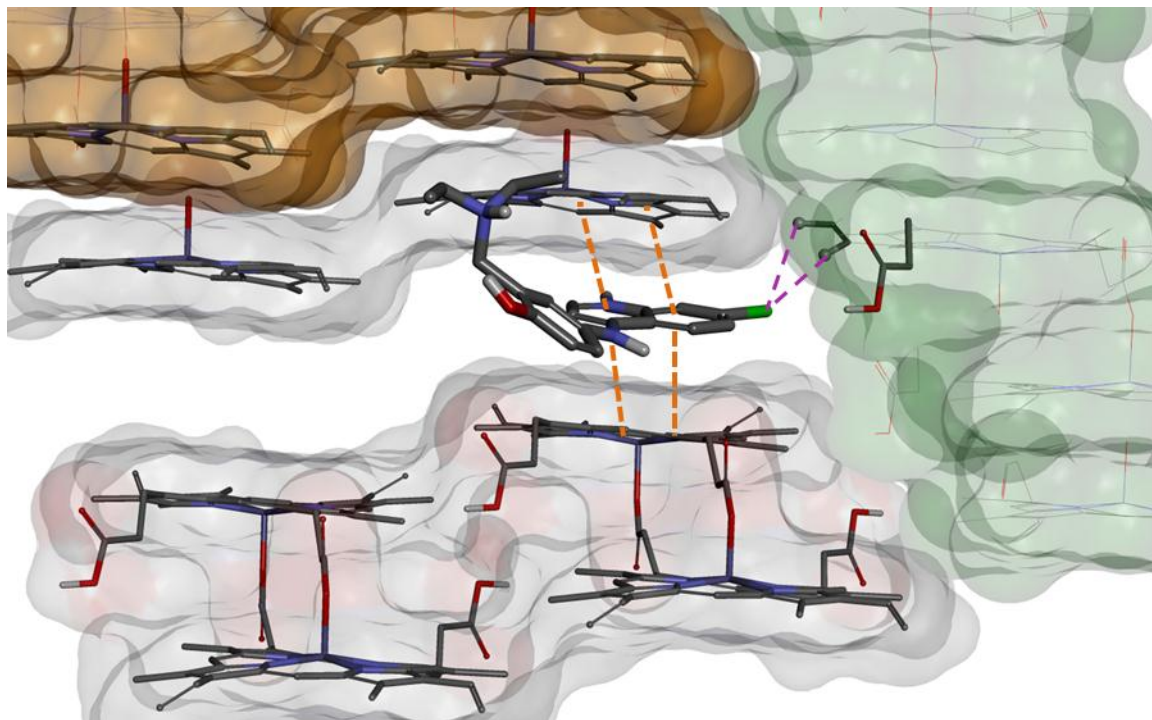
Figure 57: Adsorption of AQ in the corner between faces {001} and {100}.

The adsorption of AQ in the diprotic form, into the corner that forms between faces {001} and {100}, is shown, as viewed from the front of face {001}. The original face {001} is shown in grey, face {100} is shown in green, and the new terrace that forms above the crevice is shown in orange. The formation of π-π interactions, with measured interaction distances between 3.6 and 3.8 Å, are indicated by ▪ ▪ . The C-H⋯Cl interactions that form, are indicated by ▪ ▪, and is measured to 2.7 and 3.0 Å, respectively.

113

Table 16: Calculated E$_{ads}$ values for the step propagation onto face {001}.

Compound	Primary adsorption site (original)[a] E$_{ads}$ (kcal.mol^{-1})			Primary adsorption site (embedded)[b] E$_{ads}$ (kcal.mol^{-1})	Corner primary adsorption site[c] E$_{ads}$ (kcal.mol^{-1})
Diprotic					
KN6	-66.5	±	0.3	-66.5	−
AQ	-69.8	±	0.2	-69.7	-74.5
CQ	-67.0	±	0.01	-67.0	-72.3
QD	-80.8	±	0.01	-80.8	-85.9
QN	-66.2	±	0.01	−	-70.6
Monoprotic					
QD	-73.6	±	0.01	-74.9	-83.7
QN	-65.4	±	0.01	-65.4	−

[a]*The primary site originally investigated in Section 2.4.*

[b]*The new embedded primary site that forms.*

[c]*The primary site that forms between faces {001} and {100}.*

[*]*No standard deviations are reported for the adsorption onto the steps. These results were less consistent, where some of these adsorbed geometries were only observed once. Therefore, the best E$_{ads}$ value for each adsorbed geometry is rather reported for consistency.*

114

2.5.2.2.2 Adsorption with step propagation onto face {011}

Upon evaluating the adsorption of the inhibitors onto face {011}, significantly more favoured E_{ads} values were calculated as compared to the initial adsorption study without the step, where an additional interaction towards the flat surface resembling face {010}, is observed (Table 17).

However, similar E_{ads} values are calculated for inhibitors that adsorbed into the corner formed between face {100} and face {011}, compared to the ones that did not. This might be an indication that the newly formed π-π interactions that form between the inhibitors and the porphyrin structures on face {010}, have a greater contribution to the overall E_{ads} energy, as opposed to the hydrophobic interactions to face {100}. Furthermore, the adsorption onto the flat surface resembling face {010} alone, results in lower E_{ads} values compared to the adsorption onto both faces {011} and {010}. This indicates that adsorption onto both the two crystal faces is required for a significantly improved adsorption.

This result could be explained by evaluating the adsorption of AQ (as an example) onto the crystal surface that forms upon step propagation onto face {011} (Figure 58). The formation of two π-π interactions (measured distances of 3.6 and 3.8 Å, respectively) between the quinoline moiety of the inhibitor and face {011} is observed. A third π-π interaction forms between the benzene ring in the side-chain of the inhibitor and face {010}.

For the adsorption onto face {011} alone (Section 2.4), the formation of this third π-π interaction was not possible. Therefore, with the formation of an increased number of intermolecular interactions, a more favoured E_{ads} value is obtained.
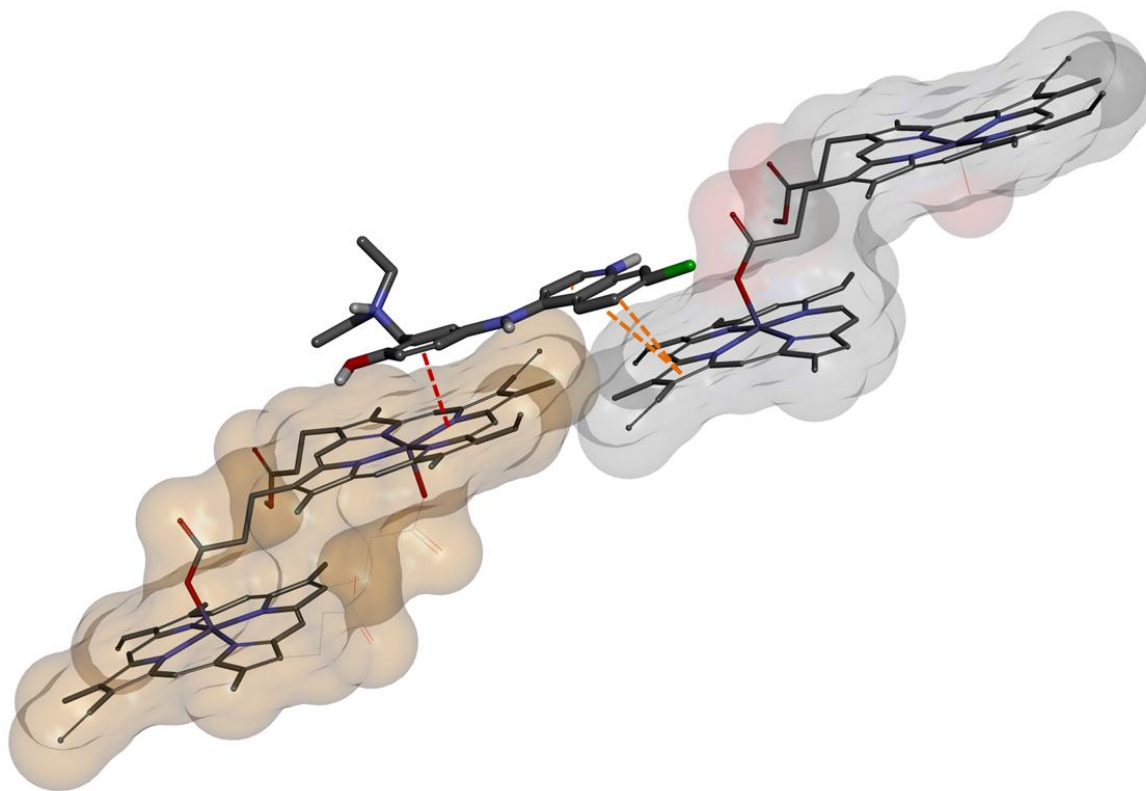
Figure 58: Adsorption of AQ onto the newly formed flat surface

The adsorption of AQ in the diprotic form onto the newly formed flat surface that involves face {011} (grey) and

face {010} (orange), is shown, as viewed from the side of face {011}. Face {100} is omitted from this image.

The newly formed π-π interaction between the inhibitor and the porphyrin structure on face {010}, is indicated

by ▪ ▪ *, and is measured to be 3.7 Å. The two π-π interactions that form between the inhibitor and the*

porphyrin structure on face {011}, is indicated by ▪ ▪ *, and is measured to be 3.6 and 3.8 Å.*

Table 17: Calculated E_{ads} values for the step propagation onto face {011}.

Compound	Face {011} only[a] E_{ads} (kcal.mol^{-1})			Faces {011} and {010}[b] E_{ads} (kcal.mol^{-1})	New flat surface[c] E_{ads} (kcal.mol^{-1})	Corner between faces {011} and {010}, and {100}.[d] E_{ads} (kcal.mol^{-1})
Diprotic						
KN6	-64.4	±	0.1	−	-60.5	−
AQ	-59.1	±	0.01	−	-77.3	-77.3
CQ	-48.3	±	0.01	-73.4	-62.3	-69.7
QD	-57.3	±	0.1	-85.5	−	-81.7
QN	-48.5	±	0.01	-68.8	-60.4	-69.2
Monoprotic						
QD	-56.3	±	0.01	-74.7	-59.5	−
QN	-49.3	±	0.01	-65.8	-61.6	−

[a] *The original surface investigated in Section 2.4.*

[b] *The new surface that forms with face {011} and {010}.*

[c] *The new flat surface (face {010}).*

[d] *The new corner that forms between the surface of face {011} and {010}, and that of face {100}.*

[*] *No standard deviations are reported for the adsorption onto the steps. These results were less consistent, where some of these adsorbed geometries were only found once. Therefore, the best E_{ads} value for each adsorbed geometry found, is rather reported.*

117

As not all of the inhibitors adsorb onto the same adsorption site, structure-activity relationships could not be determined for this part of the study. However, a more in-depth understanding as to how the clinically-relevant inhibitors might adsorb onto these steps, has been obtained, and the interaction sites that might be involved in this process, were identified.

The formation of additional intermolecular interactions between the inhibitors and the new crystal face that is introduced, has been observed, which also resulted in more favoured E_{ads} values. This has demonstrated that an increased number of intermolecular interactions results in more favoured E_{ads} values.

Olafsen *et al.* demonstrated that the β-haematin crystal grows in a step-like manner, where the inhibitors could also adsorb onto these steps to inhibit further crystal growth. What is not yet clear, is to what extent the inhibitors would prefer to adsorb onto the corners of these steps, as opposed to the larger crystal faces (faces {001} and {011}). It might be that a larger percentage of adsorption could occur onto the larger crystal faces, as opposed to the steps, since the available adsorption sites might be more abundant.

To one end, it is pleasing to find that the clinically-relevant inhibitors adsorb onto these step-like surfaces (especially onto face {001}) in a similar manner as for the adsorption study performed without considering the step. This suggests that the less complex simulation is sufficiently valid as a model system for investigating the adsorption of small inhibitors onto β-haematin. This protocol could be used to design more potent β-haematin inhibitors.

_____

2.6 CONCLUDING REMARKS PERTAINING TO CHAPTER 2

2.6.1 The significance of this chapter

Solomonov *et al.* reported physical evidence that β-haematin growth is inhibited in the presence of quinoline antimalarial drugs,[73] where Buller *et al.* proposed possible geometries for the adsorption of clinically-relevant inhibitors onto the fastest growth face of β-haematin.[54] However, in order to gain a more comprehensive understanding of the adsorption of inhibitors onto the β-haematin crystal, a more in-depth study was needed.

The main aim of this chapter was to investigate the adsorption of clinically-relevant inhibitors onto the fastest growing crystal faces. In order to achieve this goal, a force field was parameterised that is able to accommodate the high-spin Fe (III) atom. An additional investigation was performed where the crystal morphology of the β-haematin crystal was computed, and possible interaction sites on the four largest expressed crystal faces were identified. To this end, the adsorption of a set of quinoline compounds onto the fastest and the second fastest growth faces were evaluated by means of a simulated annealing adsorption protocol, where this data set was used to determine the optimum parameters needed for this protocol.

Finally, with this adsorption protocol optimised, it was applied to evaluate the adsorption of clinically-relevant inhibitors onto face {001}, as well as onto face {011}. The adsorbed geometries that were obtained for the adsorption of the inhibitors onto face {001}, were similar to that reported by Buller *et al*., where the inhibitors were fitted manually onto the crystal surface.[54] The ideal adsorbed geometry is obtained for the adsorption of QN and QD into the primary adsorption site, where both the formation of hydrogen and π-π interactions

between the inhibitor and the crystal surface is observed. It is found that larger molecules, such as MQ, preferred adsorption onto the secondary adsorption site. For the adsorption onto face {011}, the adsorption geometries obtained were less favoured, where this crystal surface resembles the secondary adsorption site on face {001}.

To this end, structure-activity relationships were evaluated, where the calculated E_{ads} values were compared to the determined lipid $BHIC_{50}$ activities. A linear correlation is obtained for the adsorption onto face {001}, when taking into account the percentage speciation at pH 4.8. This correlation is considered to be significant, with an R^2 value of 0.49 and a P value of 0.05. By considering that adsorption occurs onto both of the fastest growing crystal faces, a multiple correlation equation was applied to the data, where an improved correlation is found, with an R^2 value of 0.78 and a P value of 0.004. It is thus demonstrated that a linear correlation exists between the calculated E_{ads} values, and the determined lipid $BHIC_{50}$ activities, for clinically-relevant quinoline β-haematin inhibitors, when taking into account adsorption onto both faces {001} and {011}, and the percentage speciation at pH 4.8. This is a significant contribution, and adds weight to the argument that quinoline antimalarial drugs execute their mechanism of action by adsorbing onto the β-haematin crystal surface, and thereby hinder further crystal growth.

2.6.2 Conclusion

By parameterising a force field that is able to accommodate the high-spin Fe(III)-complex, and by optimising the adsorption protocol, a comprehensive study on the adsorption of clinically-relevant inhibitors onto both the fastest and the second fastest β-haematin crystal faces, was performed.

To this end, it is established that the adsorption of inhibitors onto β-haematin is a more complex process than originally anticipated, since multiple factors need to be considered. As a result, it has been demonstrated that a linear correlation exists between the calculated E_{ads} values and the determined lipid $BHIC_{50}$ activities, when the adsorption onto both the fastest and the second fastest growth faces is considered, as well as the percentage speciation at pH 4.8.

This finding contributes significantly to the understanding that clinically-relevant inhibitors brings about β-haematin growth inhibition by adsorbing onto the fastest growing crystal surfaces.

CHAPTER 3

NON-QUINOLINE INHIBITORS

The current antimalarial drugs used in ART treatment are quinoline-based or artemisinin-based, where the artemisinin compounds are believed to have a different mode of action. However, due to growing resistance to quinoline compounds, a greater emphasis is set on finding more potent antimalarial drugs, especially with non-quinoline scaffolds.

With this research project forming part of a larger collaborative project, three small libraries of larger non-quinoline compounds were accessible, where the adsorption of these compounds onto the two fastest growing faces of β-haematin could be investigated. Rather than opting for a larger library, a more thorough investigation could be performed by studying a smaller library more closely. It is anticipated that these compounds would follow the same structure-activity trend as seen for the clinically-relevant antimalarial drugs, where these findings could be combined with the results obtained in the initial adsorption study, in order to strengthen the argument on β-haematin inhibition by adsorption of antimalarial drugs onto the crystal surface.

3.1 INVESTIGATING THE ADSORPTION GEOMETRY OF NON-QUINOLINE INHIBITORS ONTO β-HAEMATIN

3.1.1 Introducing the three libraries of inhibitors

The three libraries of compounds used in this study were chosen based on their ability to inhibit β-haematin formation, as well as for the variance in molecular structure that they offer. These molecules were shown to be active β-haematin inhibitors in previous studies within our research group; therefore it was reasoned that by analysing the adsorption of these inhibitors onto β-haematin, a greater understanding of how these non-quinoline inhibitors might affect β-haematin growth by adsorption could be gained.
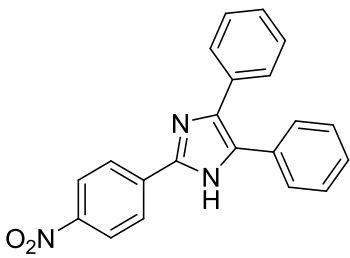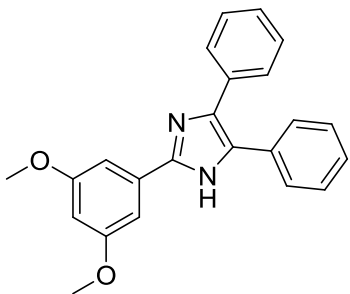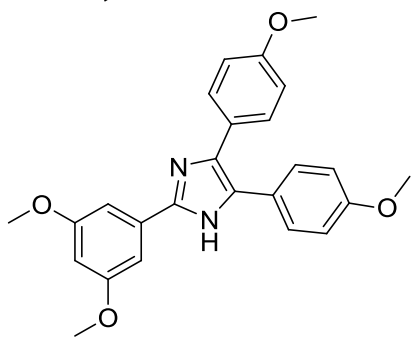
Given the findings in the preceding chapter, it seemed reasonable that the smaller compounds would be able to fit into the primary adsorption site on face {001}, where the larger compounds would be left to adsorb onto the secondary adsorption site. Furthermore, given the more even topology of face {011}, the possibility that the larger compounds may prefer adsorption on this face is not excluded.

3.1.1.1 2,4,5-Triaryl substituted imidazole inhibitors

The first set of inhibitors to be investigated was a library of three 2,4,5-triaryl substituted imidazole compounds (Table 18). These were synthesised, and the NP40 BHIC$_{50}$ activities were determined by Kathryn Wicht.[121,122] The speciation of these inhibitors was determined to be neutral and monoprotic of nature at pH 4.8, where the second nitrogen in the imidazole ring could be protonated.

Table 18: The speciation of the 2,4,5-triaryl substituted imidazole inhibitors at pH 4.8.

Compound		% Monoprotic	% Neutral
KW1		59	41
KW2		54	46
KW3		52	48

[*] *These inhibitors were synthesised and the NP40 BHIC$_{50}$ activities were determined by*

Kathryn Wicht.[122]

124

_____
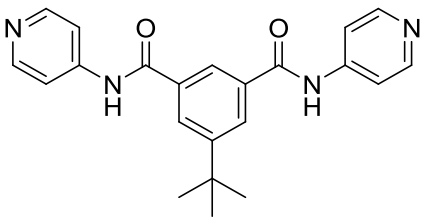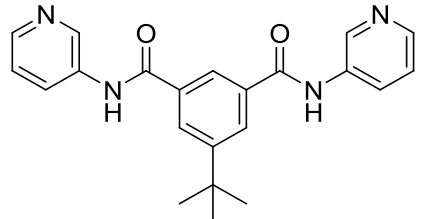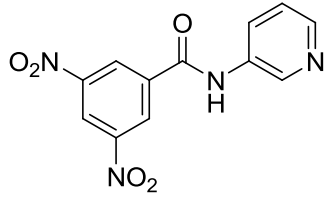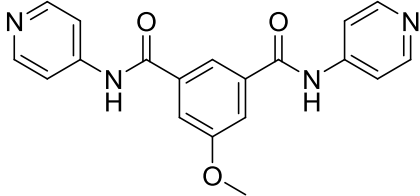
3.1.1.2 Benzamide inhibitors

The benzamide inhibitors used in this study were also synthesised by Kathryn Wicht, and the NP40 BHIC$_{50}$ activities were subsequently determined, using the standard protocol (Table 19).[121,122] The speciation of these inhibitors was predicted to be diprotic, monoprotic, as well as neutral of nature at pH 4.8, where either one or both of the pyridine nitrogen atoms could be protonated [143]

Table 19: The speciation of the benzamide inhibitors at pH 4.8.

Compound		% Diprotic	% Monoprotic	% Neutral
KW4		75	25	0
KW5		7	39	54
KW6		0	27	73
KW7		75	25	0

*These inhibitors were synthesised and the NP40 BHIC$_{50}$ activities were determined by Kathryn Wicht.[122]

125

_____
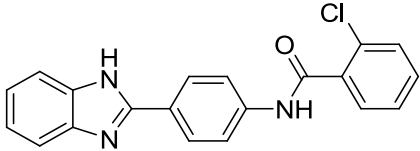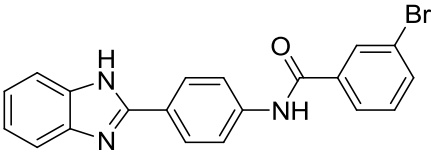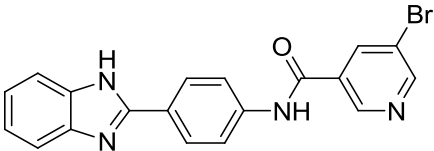
3.1.1.3 Benzimidazole inhibitors

The benzimidazole inhibitors investigated in this study were synthesised, and the NP40 $BHIC_{50}$ activities were determined by Fabrizio L'abbate, where this research forms part of his current PhD project (Table 20).

The speciation of these inhibitors at pH 4.8 was determined.[143] For all three inhibitors it is found to be 70% monoprotic and 30% neutral, where the second nitrogen in the benzimidazole ring could also be protonated.

Table 20: The speciation of the benzimidazole inhibitors at pH 4.8.

Compound		% Monoprotic	% Neutral
FL1		70	30
FL2		70	30
FL3		70	30

[*]*These inhibitors were synthesised and the NP40 $BHIC_{50}$ activities were determined by Fabrizio L'abbate.*

_____

3.1.2 Adsorption of non-quinoline inhibitors onto the β-haematin crystal surfaces

3.1.2.1 Adsorption onto face {011}

3.1.2.1.1 Adsorption of 2,4,5-triaryl substituted imidazole inhibitors

For the adsorption onto face {011}, compounds **KW1** and **KW3** adsorbed in such a manner that maximised the formation of π-π interactions. However, these interactions were long-range in nature and measured to be greater than 4 Å (Figure 59). Therefore, it is more likely that the adsorption of these inhibitors onto the crystal surface is rather promoted by hydrophobic attractions.

The adsorption geometry of compound **KW2** is considered slightly more favourable than that of compounds **KW1** and **KW3**. For this compound, the formation of π-π interactions is observed between the aromatic rings of the inhibitor and a porphyrin on the crystal surface, with measured distances of 3.5 and 3.9 Å (Figure 60). Furthermore, a hydrogen bonding interaction is observed between the protonated nitrogen atom in the imidazole ring and a carbonyl group on the crystal surface, with a measured distance of 2.6 Å.
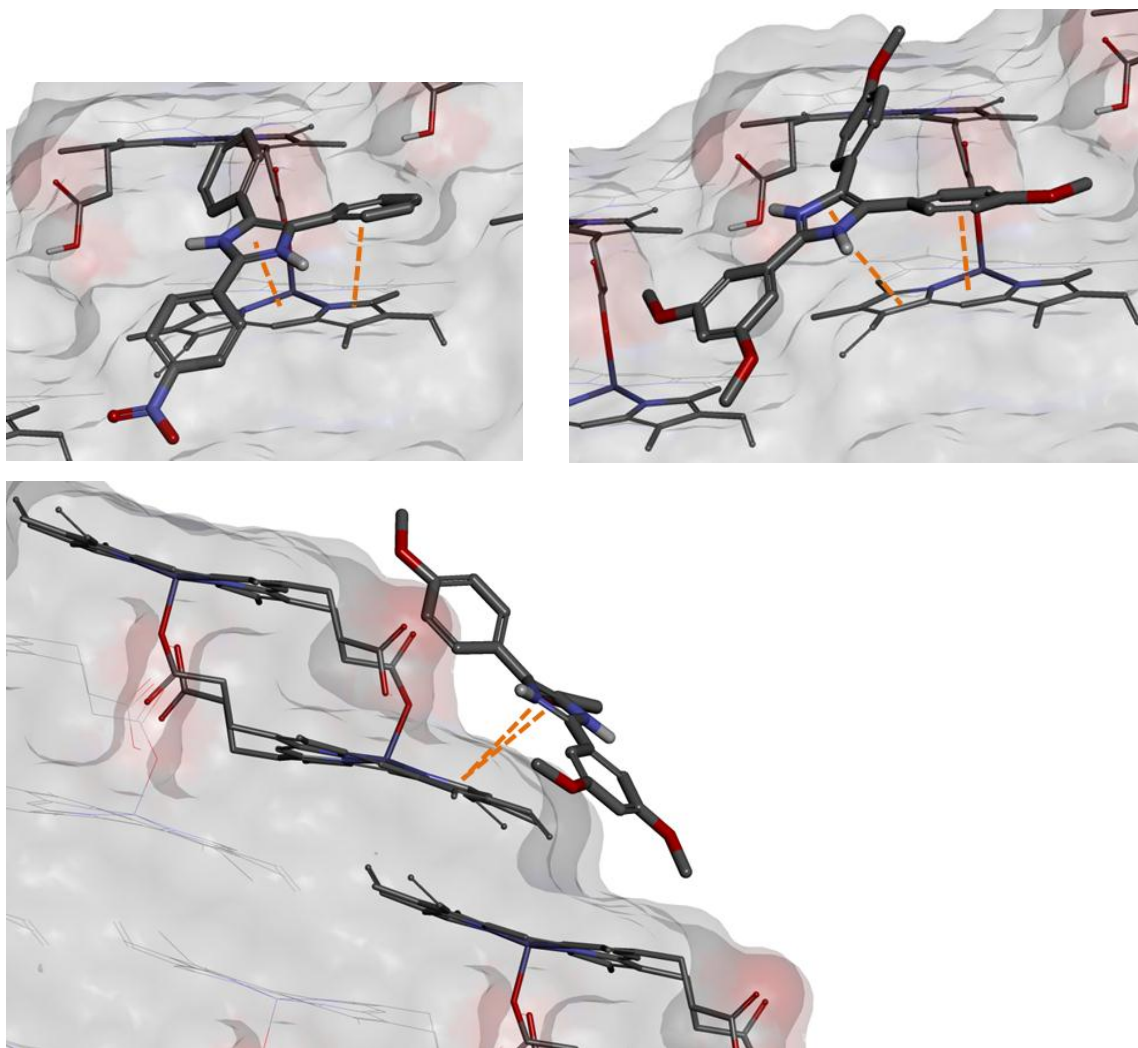
Figure 59: Adsorption of compounds KW1 and KW3 onto face {011}

*The adsorption of compounds **KW1**(top left) and **KW3**(top right) in the monoprotic forms onto face {011}, as viewed from above, is shown. The adsorption of compound **KW3**(bottom left) in the monoprotic form onto face {011}, as viewed from the side of the crystal face, is also shown. Weak π-π interactions, with measured interaction distances >4.0 Å, are indicated by ▪ ▪ .*

_____
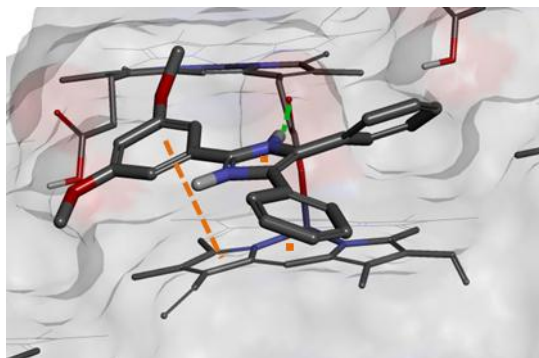
Figure 60: Adsorption of compound KW2 onto face {011}.

*The adsorption of compound **KW2** in the monoprotic form onto face {011} as viewed from above, is shown. The*

hydrogen bonding interaction, with a measured interaction distance of 2.6 Å, is indicated by ■ ■ .

The π-π interaction to the imidazole ring is indicated by two dots (■ *), and the other π-π interaction is indicated*

by ■ ■ . *The measured interaction distances are 3.5 and 3.9 Å, respectively.*

3.1.2.1.2 Adsorption of benzamide inhibitors onto face {011}

Compounds **KW4** and **KW5** adsorbed onto face {011} in the same manner, where for compound **KW4**, two π-π interactions, with measured distances of 3.5 and 3.6 Å, respectively, were observed between the inhibitor and the porphyrin moiety, as well as a hydrogen bonding interaction between the amide N-H and a carbonyl group on the crystal surface, with a measured interaction distance of 2.7 Å (Figure 61). Only two of the aromatic rings are able to form π-π interactions to a porphyrin on the crystal surface, as the molecule extends too widely relative to the porphyrin moiety to allow for all three aromatic rings to form π-π interactions.

Figure 61: Adsorption of compounds KW4 and KW5 onto face {011}

*The adsorption of compounds **KW4**(left) and **KW5**(right) in the diprotic form onto face {011}, as viewed from above, is shown. Hydrogen bonding interactions, with measured interaction distances of 2.7 and 2.6 Å, respectively, are indicated by* ▪ ▪ *, and π-π interactions, with measured interaction distances between 3.5 and 3.8 Å, are indicated by* ▪ ▪ *.*

Compounds **KW6** and **KW7** adsorbed in a slightly different geometry as seen above for compounds **KW4** and **KW5** (Figure 62), where for compound **KW6** two π-π interactions to the porphyrin structure are formed, with measured distances of 3.5 Å, and a hydrogen bonding interaction with a measured distance of 2.7 Å. Again, for compound **KW7**, two π-π interactions were observed at measured distances of 3.4 and 3.5 Å, as well as a hydrogen bonding interaction at a distance of 2.5 Å.

Interestingly, it is noticed that compound **KW7** extends towards an adjacent porphyrin in another unit cell. No significant interactions are observed in this second unit cell. Furthermore, if compound **KW7** had adsorbed slightly to the left on the crystal surface, a similar adsorption geometry as for compounds **KW4** and **KW5** would be obtained, and the hydrogen bonding interaction would rather form between the amide N-H on the left hand side of the molecule. With the current adsorbed geometry, this interaction distance is measured to be 3.4 Å, which is too long to form a strong hydrogen bonding interaction.

130

Figure 62: Adsorption of compounds KW6 and KW7 onto face {011}

*The adsorption of compounds **KW6**(top) in the monoprotic form and **KW7**(bottom) in the diprotic form onto*

face {011}, as viewed from above, is shown. Hydrogen bonding interactions, with measured interaction

distances of 2.7 and 2.5 Å, respectively, are indicated by ▪ ▪ , and π-π interactions, with measured interaction

distances between 3.5 and 3.8 Å, are indicated by ▪ ▪ .

3.1.2.1.3 Adsorption of benzimidazole inhibitors

Compounds **FL1**-**3** adsorbed onto the β-haematin crystal surface in the same manner, where

the formation of two π-π interactions between the aromatic rings and the porphyrin moiety on

the crystal surface are observed, with measured interaction distances of 3.6 Å each.

Moreover, a hydrogen bonding interaction between the amide N-H and a carbonyl group on

the crystal surface is observed, with a measured distance of 2.6 Å (Figure 63). As seen for

compound **KW7**, these inhibitors adsorbed such that the molecule in each case extends over

two unit cells.

Figure 63: Adsorption of compound FL3 onto face {011}

*The adsorption of compound **FL3** in the monoprotic form onto face {011}, as viewed perpendicular to the crystal face, is shown. The hydrogen bonding interaction of 2.6 Å is indicated by* ▪▪ *, and π-π interactions, with measured interaction distances 3.6 Å, are indicated by* ▪▪ *.*

When adsorbing onto face {011}, the molecules mostly form two π-π interactions, as well as a hydrogen bonding interaction to the crystal surface. With the molecules observed to extend over an adjacent unit cell, it gives rise to the possibility that longer and more planar molecules could be able to form additional interactions on the crystal surface in the neighbouring unit cell. Therefore, by optimising the intermolecular interactions that could form, the adsorption onto face {011} could be enhanced for greater β-haematin inhibition.

3.1.2.2 Adsorption onto face {001}

3.1.2.2.1 Adsorption of 2,4,5-triaryl substituted imidazole inhibitors onto face {001}

Compounds **KW1**-**3** were found to adsorb into the primary adsorption site on face {001} (Figure 64). For these, π-π interactions are formed between the aromatic rings and the porphyrins on the crystal surface, with measured interaction distances of 3.5-3.7 Å. For all

three of these compounds, one of the aromatic rings is angled towards the outside of the

crevice. This is seen to the left of the images in the case of compounds **KW1** and **KW2**, and

to the right of the image for compound **KW3**.
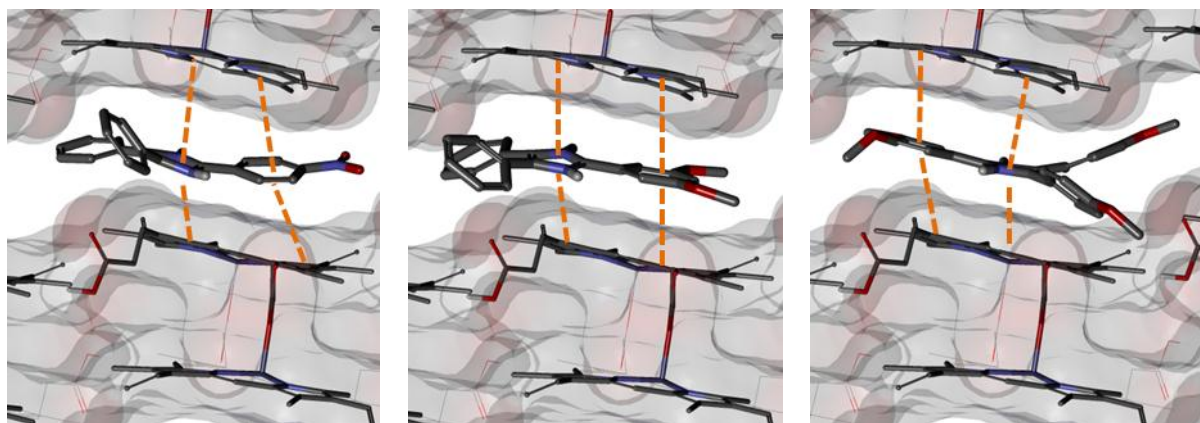
Figure 64: Adsorption of compounds KW1-3 onto face {001}.

*The adsorption of compounds **KW1**(left), **KW2**(middle), and **KW3**(right) in the monoprotic form onto*

face {001}, as viewed onto the crystal face, is shown. The π-π interactions, with measured interaction distances

between 3.5 and 3.8 Å, are indicated by ▪ ▪ .

3.1.2.2.2 Adsorption of benzamide inhibitors onto face {001}

For the adsorption onto face {001}, compounds **KW4**-**7** adsorbed into the primary adsorption

site (**KW5** and **KW6** are shown as examples in Figure 65). Interestingly, compounds

KW4 (monoprotic only), **KW5**, and **KW7** (monoprotic only) adsorbed in such a manner that

two adjacent primary adsorption sites are occupied, where π-π interactions are formed

between the aromatic rings and the porphyrins on the crystal surface. These interaction

distances were measured to be in the range of 3.4-3.8 Å. The more bulky functional groups

are orientated towards the outside of the primary adsorption site, as illustrated by the

tert-butyl moiety of compound **KW5**.

133
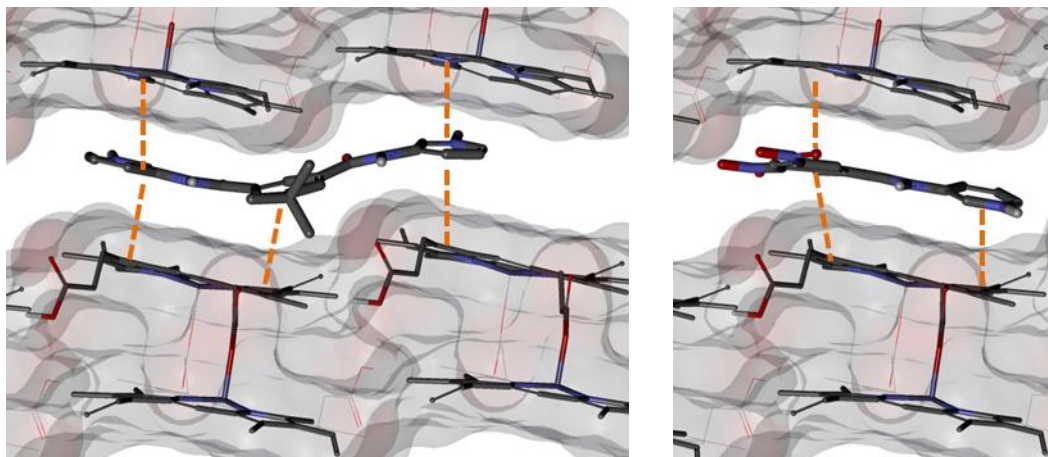
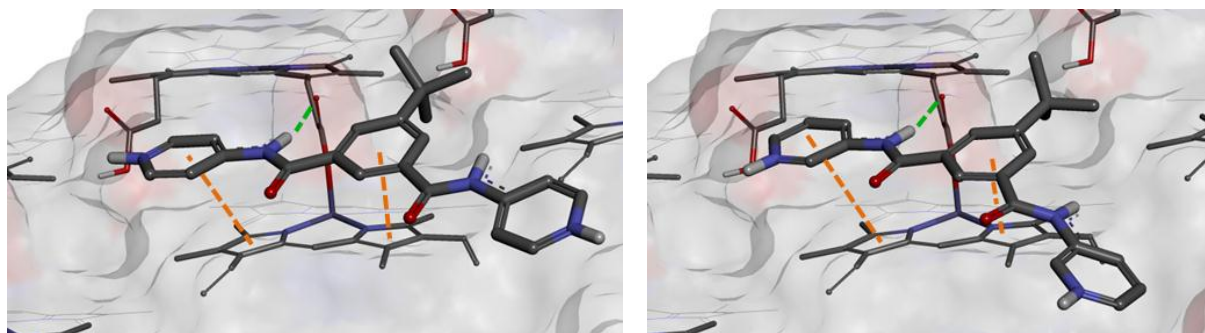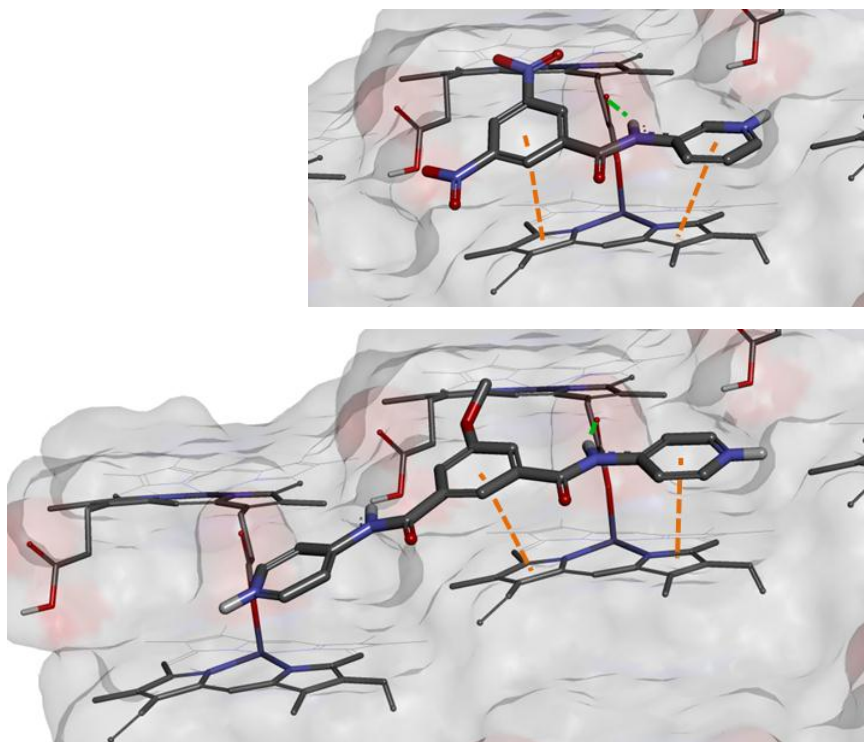**Figure 65: Adsorption of compound KW5 and KW6 onto face {001}.**

*The adsorption of compounds **KW5** (left) in the diprotic form and **KW6** (right) in the monoprotic form onto*

face {001}, as viewed onto the crystal face, is shown. The π-π interactions, with measured interaction distances

between 3.5 and 3.8 Å, are indicated by ▪ ▪ .

Compounds **KW4** and **KW7** displayed different adsorption geometries depending on whether the diprotic or monoprotic species were investigated. This was indeed a surprise, since for all of the other compounds investigated thus far, the same adsorption geometry, irrespective of the protic form, was observed. As shown below, compounds **KW4** and **KW7** in the diprotic form are able to occupy both the primary and the secondary adsorption sites (Figure 66). It could be that the protonation on the pyridine nitrogen atom prevents the molecule from fitting soundly into the two adjacent primary adsorption sites, therefore promoting this alternative adsorption geometry.
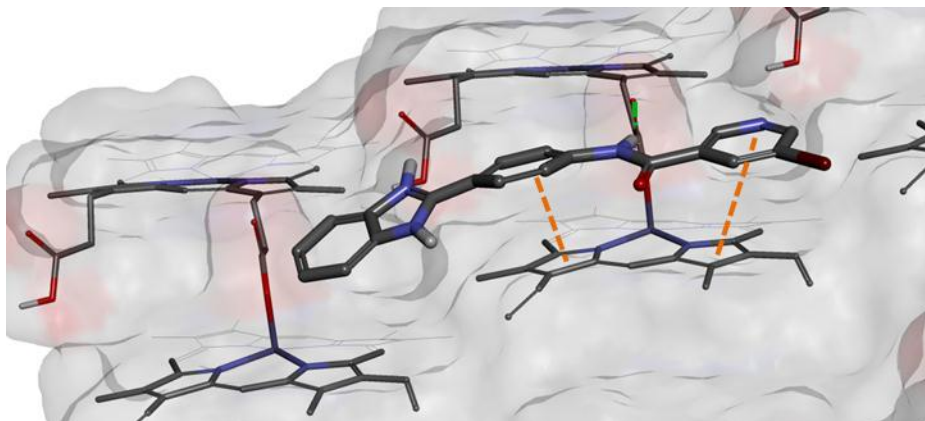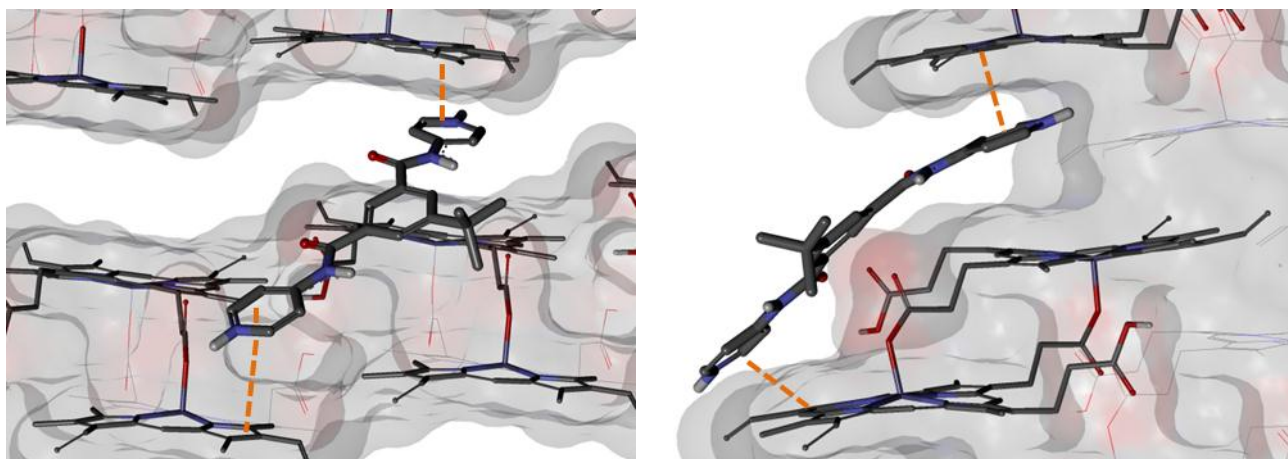
Figure 66: Adsorption of compound KW4 onto face {001}.

*The adsorption of compound **KW4** in the diprotic form onto face {001}, as viewed onto the crystal face (left), and as viewed from the side (right), is shown. The π-π interactions, with measured interaction distances between 3.5 and 3.8 Å, are indicated by ▪ ▪ .*

3.1.2.2.3 Adsorption of benzimidazole inhibitors onto face {001}

The benzimidazole inhibitors adsorbed onto face {001} in a similar way as seen for the benzamide inhibitors. Compound **FL1** adsorbed in a similar geometry as compound **KW4** in its diprotic speciation form, where both the primary and the secondary adsorption sites are occupied (Figure 67). Here, it is more obvious that the chlorine atom in the 2-position of the aromatic ring may be responsible for preventing the molecule from adsorbing into the crevice, where in the absence of this chlorine atom, it would most likely occupy the two neighbouring primary adsorption sites simultaneously. The formation of π-π interactions between the aromatic rings and the porphyrins on the crystal surface is observed, with measured distances of 3.6 and 3.7Å, as well as a hydrogen bonding interaction between the benzimidazole N-H and a carbonyl oxygen on the crystal surface. This interaction distance was measured to be 2.4 Å.

_____

Compound **FL2** and **FL3** adsorbed in similar geometries as compound **KW5** (Figure 67), where two adjacent primary adsorption sites are occupied. The formation of π-π interactions between the aromatic rings and the porphyrins on the crystal surface is seen, with measured interaction distances of 3.4-3.7 Å. Moreover, a hydrogen bonding interaction is formed between the amide N-H and a carbonyl group on the crystal surface, with a measured interaction distance of 2.4 Å.
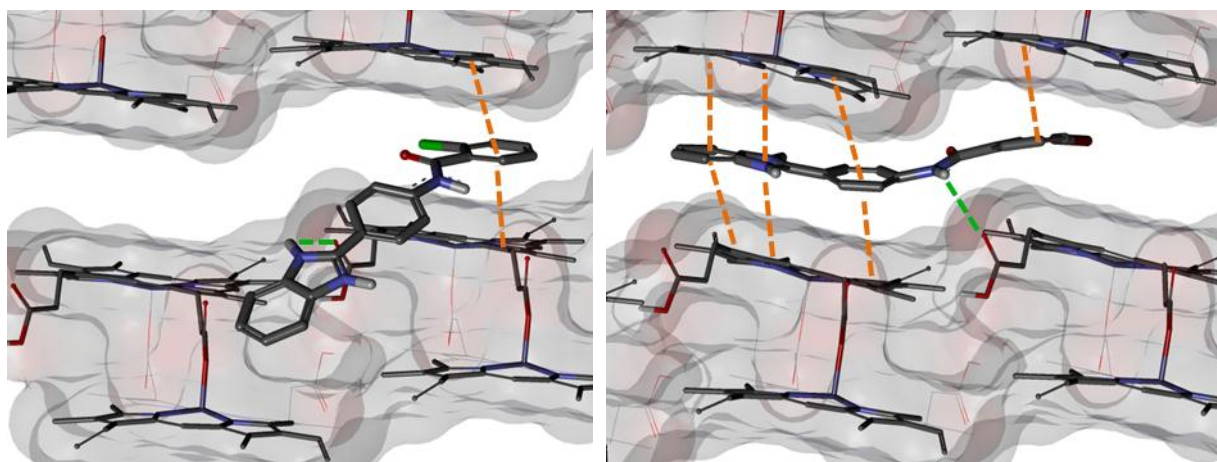
Figure 67: Adsorption of compounds FL1 and FL2 onto face {001}.

*The adsorption of compounds **FL1**(left) and **FL2**(right) in the monoprotic form onto face {001}, as viewed onto the crystal face, is shown. Hydrogen bonding interactions of 2.4 Å are indicated by* ▪ ▪ *, and π-π interactions, with measured interaction distances between 3.5 and 3.7 Å, are indicated by* ▪ ▪ *.*

Upon evaluating the adsorption of the non-quinoline inhibitors onto the crystal surfaces, it appears that compounds **KW1**-**3**, **KW5**, **KW6**, **FL2**, and **FL3**, had the optimum adsorbed geometries, where the interaction surfaces were probed to such an extent that the maximum number of intermolecular interactions were formed. These molecular scaffolds, especially those of compounds **KW5** and **FL2**, which occupy two primary adsorption sites, could be used as a starting point for designing new non-quinoline β-haematin inhibitors.

The results suggest that improved adsorption is obtained when the inhibitor adsorbs over two unit cells, thereby occupying two primary adsorption sites simultaneously. For all compounds that were able to occupy two neighbouring primary adsorption sites, adsorption onto face {001} was more ideal than for the adsorption onto face {011}, as the formation of a greater number of intermolecular interactions is observed. However, for compounds **KW4**, **KW7**, and **FL1**, that were unable to occupy the two neighbouring primary adsorption sites, adsorption onto face {011} was more favoured.

For the adsorption onto face {011}, and the primary adsorption site on face {001}, the same linear and relatively planar configurations are favoured. Therefore, it is suggested that if an inhibitor is structurally optimised for the adsorption into the primary adsorption site on face {001}, it would also show favoured adsorption onto face {011}.

Furthermore, as seen for the adsorption of QN in Section 2.4.1.2, adsorption geometries are observed in which both the primary and secondary adsorption sites on face {001} are occupied. These geometries could be optimised for enhanced adsorption onto face {001}. The synthesis of molecules that exploit the maximal interaction opportunities by adsorbing into both the primary and secondary adsorption sites on face {001}, is currently being investigated by a student in our collaborator's research group, Fabrizio L'abbate, where this work forms part of his PhD thesis. Therefore, this rationale was not investigated further in this dissertation.

3.1.3 Conformational analysis of the non-quinoline inhibitors

Unlike the clinically-relevant quinoline inhibitors, it was found that the dynamics simulation was not sufficient to overcome high energy barriers in order to probe various conformations of the non-quinoline inhibitors. In fact, for the inhibitors that completely adsorbed into the primary adsorption sites, such as compounds **KW5** and **FL2**, no significant change in the adsorption geometry was observed.

Once an inhibitor adsorbs into the primary adsorption site, rotations about certain single bonds would bring about up to 90°, and finally 180° rotations of aromatic rings. This is not possible due to the height restriction inside the crevice once the inhibitor is adsorbed into the crevice, and therefore these conformations were not investigated during the dynamics simulation. In order to overcome this limitation, it was imperative to consider the adsorption of more than one starting conformation in order to ensure that the absolute minimum adsorbed conformation is found.

Excluding peripheral methoxy substituents, compounds **KW1**-**3** are somewhat symmetrical. Rotation around single bonds did not yield any new conformations (Figure 68). Therefore, a conformational search was not performed on these compounds and the final dynamics optimisation was considered to be sufficient.

_____
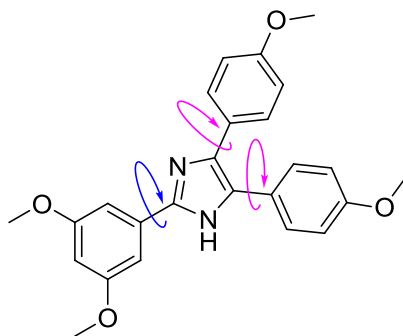
Figure 68: The three rotatable bonds of compound KW3 of interest in generating different conformations.

The rotatable bonds for compounds **KW5** (a representative benzamide) and **FL2** (a representative benzimidazole) were identified, where the conformations of interest were generated by rotating these bonds by 180° (Figure 69). Considering that these inhibitors were previously observed to adsorb into the primary adsorption site, and form π-π interactions in the secondary adsorption site, only conformations where the aromatic rings are planar to one another were investigated. Otherwise, the molecules would not be able to form the optimum molecular interactions to the crystal surface.
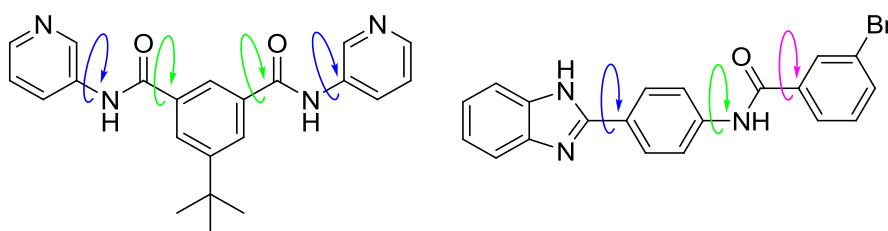
Figure 69: Rotatable bonds of interest for compounds KW5 (left) and FL2 (right).

3.1.3.1 Results pertaining to the conformational analysis

In order to justify our decision to only rotate the bonds by 180° and not by just 90°, an adsorption simulation, followed by a dynamics optimisation was performed on a non-planar conformation where a single bond was rotated by only 90° degrees (Figure 70). It is found that during the dynamics simulation, the bond rotated to ensure a planar configuration in the end, where the molecule was able to fit into the primary adsorption site. However, it did not always rotate back in the same direction to form the original conformation. In some cases a full 180° rotation was obtained. Therefore, we deemed it suitable to investigate the conformations that could form by performing 180° rotations around the identified single bonds.
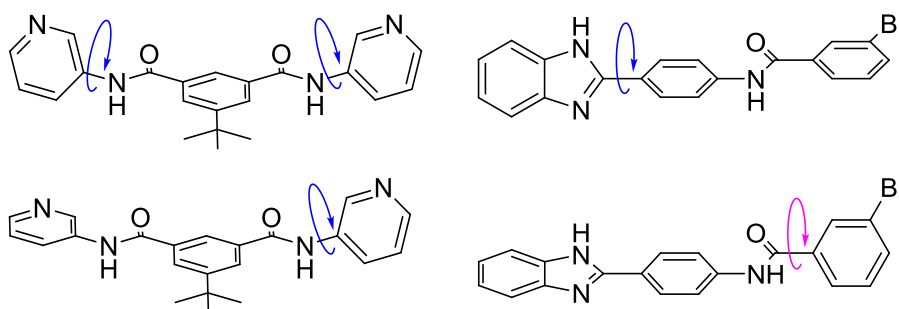
Figure 70: The conformations investigated with 90° rotations around single bonds.

*The conformations investigated for compound **KW5***(top left and bottom left), and compound ***FL2****(top right and bottom right), when only a 90° rotation is permitted around a single bond, as indicated.*

The newly-generated starting conformations were subjected to a full adsorption simulation, followed by the dynamics optimisation, where after the adsorption energies (E_{ads}) were calculated by using the initial energies of the new conformations.

For the adsorption onto face {001}, it is found that the lowest energy conformations, which were generated by using the standard protocol, still had the most favoured E_{ads} values. Furthermore, it is found that the E_{ads} values obtained for the adsorption onto face {011} were similar to those of the original lowest energy conformation. This is not surprising, as no distinctive crevices are present on this face for the inhibitors to adsorb into, and the formation of π-π interactions is mostly observed. Therefore, it is not surprising that the 180° rotation of an aromatic ring would not cause a large variance in the calculated E_{ads} value.

With the E_{ads} value being calculated as the difference in energy of the system before and after adsorption, the initial internal energy of the new conformation is used in this calculation. Considering that for the less favoured conformations, an internal energy penalty is added in the form of a higher energy, the calculated E_{ads} values were less favoured. The E_{ads} values of the original lowest energy conformation are found to be lower and thus more favoured. Therefore, it was possible to confirm that the adsorption results obtained by using the lowest energy conformation are reasonable, and are deemed suitable for our purposes.

3.2 DETERMINING STRUCTURE-ACTIVITY RELATIONSHIPS

3.2.1 Investigating structure activity relationships of the non-quinoline inhibitors

The structure-activity study discussed in Chapter 2 has shown that more than one parameter needs to be taken into account in order to appreciate the linear correlation between the calculated E_{ads} values and the experimentally determined β-haematin inhibition activity. For the clinically-relevant inhibitors, a linear correlation was found between the calculated E_{ads} results and the lipid $BHIC_{50}$ ($LBHIC_{50}$). Similarly, for the small quinoline inhibitors, a correlation was found between the calculated E_{ads} results and the acetate $BHIC_{50}$ ($ABHIC_{50}$).

Unfortunately, in an attempt to determine the $LBHIC_{50}$ of the non-quinoline inhibitors, it was found that the inhibitors were not soluble in the buffer solution at pH 4.8. Therefore, the $LBHIC_{50}$ were not determined, and the NP40 $BHIC_{50}$ values that had been determined by the students who have synthesised the compounds were used to evaluate structure-activity relationships.

A linear correlation is found between the $LBHIC_{50}$ activities and the NP40 $BHIC_{50}$ activities.[119] Therefore, the NP40 $BHIC_{50}$ activity results were deemed suitable for evaluating structure-activity relationships for the non-quinoline inhibitors.

With the non-quinoline inhibitors also being present in the neutral form, this speciation form was also considered at pH 4.8 (Equation 3.1).

$$x = \left(\frac{\% \, Neutral}{100} \right) \tag{3.1}$$

Furthermore, the parameters for this speciation form were included into the multiple correlation calculation, where for the neutral form, a_N is a function of the adsorption onto

face $\{001\}$ (Equation 3.2), and b_N is a function of the adsorption onto face $\{011\}$ (Equation 3.3).

$$a_N = f_{(001)} = \left\{\frac{[E_{001}]}{[E_{001}]+[E_{011}]}\right\} \tag{3.2}$$

$$b_N = f_{(011)} = \left\{\frac{[E_{011}]}{[E_{001}]+[E_{011}]}\right\} \tag{3.3}$$

Finally, by combining all of these parameters, a multiple correlation equation is obtained (Equation 3.4), where the variables, v_1 - v_6, were allowed to freely refine in order to obtain the best fit between the calculated E_{ads} values and the activity results across the whole data set.

$$E_{ads} = y[v_1 a_M(E_{001}) + v_2 b_M(E_{011})] + z[v_3 a_D(E_{001}) + v_4 b_D(E_{011})]$$
$$+ x[v_5 a_N(E_{001}) + v_6 b_N(E_{011})] \tag{3.4}$$

3.2.1.1 Results pertaining to the structure activity relationships of the

non-quinoline inhibitors

For the adsorption of the non-quinoline inhibitors onto face $\{001\}$ (Table 21, Figure 71) and face $\{011\}$ (Table 22, Figure 72), no structure-activity correlation was found. The R^2 values of 0.13 and 0.00045 that were found are not significant.

Table 21: The determined NP40 BHIC$_{50}$ activity of the non-quinoline inhibitors, as well as the calculated E$_{ads}$ for the adsorption onto face {001}, taking into account the percentage speciation.

Compounds	E$_{ads}$ Diprotic face {001} (kcal.mol^{-1})			E$_{ads}$ Monoprotic face {001} (kcal.mol^{-1})			Eads Neutral face {001} (kcal.mol^{-1})			% Diprotic	% Monoprotic	% Neutral	E$_{ads}$ face {001} (kcal.mol-1)	NP40 BHIC$_{50}$ (µM)		
KW1	–			-80.1	±	0.01	-82.9	±	0.2	0	59	41	-81.2	18.7	±	0.1
KW2	–			-70.0	±	0.7	-74.5	±	0.5	0	54	48	-73.7	14.6	±	0.2
KW3	–			-77.4	±	0.9	-82.9	±	0.1	0	52	46	-78.3	13.8	±	0.4
KW4	-71.7	±	0.2	-86.6	±	0.8	–			75	23	0	-73.9	13.3	±	0.7
KW5	-93.6	±	0.1	-96.1	±	0.01	-96.4	±	0.01	7	39	53	-96.1	9.1	±	0.7
KW6	–			-72.5	±	0.01	-73.2	±	1.0	0	27	73	-73.0	12.7	±	1.4
KW7	-78.7	±	0.1	-84.5	±	0.01	–			75	23	0	-78.7	22.2	±	1.4
FL1	–			-67.3	±	0.01	-90.6	±	0.01	0	70	30	-74.3	38.2	±	1.4
FL2	–			-72.0	±	0.01	-99.1	±	0.01	0	70	30	-80.2	24.5	±	4.2
FL3	–			-68.9	±	0.3	-89.8	±	0.4	0	70	30	-75.2	32.0	±	1.4

144

Table 22: The determined NP40 BHIC$_{50}$ activity of the non-quinoline inhibitors, the calculated E$_{ads}$ for the adsorption onto face {011}, taking into account the percentage speciation.

Compounds	E$_{ads}$ Diprotic face {011} (kcal.mol^{-1})			E$_{ads}$ Monoprotic face {011} (kcal.mol^{-1})			E$_{ads}$ Neutral face {011} (kcal.mol^{-1})			% Diprotic	% Monoprotic	% Neutral	E$_{ads}$ face{011} (kcal.mol^{-1})	NP40 BHIC$_{50}$ (µM)		
KW1		−		-56.0	±	0.8	-55.7	±	0.01	0	59	41	-55.9	18.7	±	0.1
KW2		−		-57.4	±	0.1	-53.3	±	0.2	0	54	48	-56.7	14.6	±	0.2
KW3		−		-65.5	±	0.7	-66.8	±	0.7	0	52	46	-64.7	13.8	±	0.4
KW4	-63.6	±	0.1	-63.9	±	0.4		−		75	23	0	-62.5	13.3	±	0.7
KW5	-61.1	±	0.2	-63.3	±	0.3	-63.1	±	0.4	7	39	53	-63.0	9.1	±	0.7
KW6		−		-59.8	±	0.01	-62.0	±	0.01	0	27	73	-61.4	12.7	±	1.4
KW7	-64.6	±	0.1	-65.5	±	0.1		−		75	23	0	-63.7	22.2	±	1.4
FL1		−		-61.8	±	0.8	-58.4	±	0.8	0	70	30	-60.8	38.2	±	1.4
FL2		−		-62.7	±	0.9	-63.6	±	0.01	0	70	30	-63.0	24.5	±	4.2
FL3		−		-61.9	±	0.01	-65.1	±	0.01	0	70	30	-62.9	32.0	±	1.4

145

_____
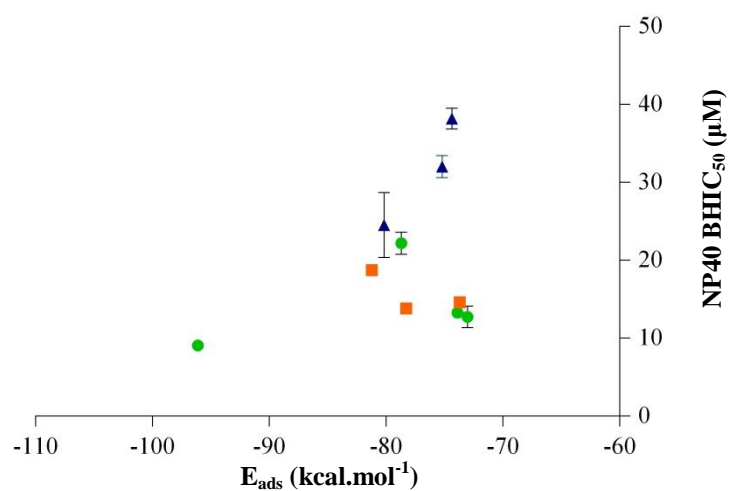
Figure 71: Comparing the calculated E_{ads} vs the NP40 BHIC$_{50}$ for adsorption of

non-quinoline inhibitors onto face {001}.

The 2,4,5-triaryl substituted imidazole inhibitors are indicated in orange, the benzamide inhibitors are indicated

in green, and the bezimidazole inhibitors are indicated in blue.

An R^2 value of 0.13 and a P value of >0.05 are found.

Chapter 3 - Non-quinoline inhibitors

_____
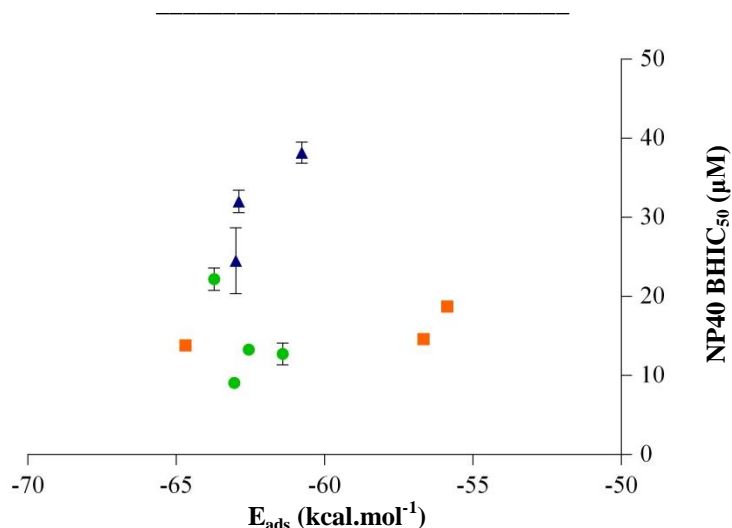
Figure 72: Comparing the calculated E_{ads} vs the NP40 $BHIC_{50}$ for adsorption of

non-quinoline inhibitors onto face {011}.

The 2,4,5-triaryl substituted imidazole inhibitors are indicated in orange, the benzamide inhibitors are indicated

in green, and the bezimidazole inhibitors are indicated in blue.

An R^2 value of 0.00045 and a P value of >0.05 are found.

However, by evaluating only the three benzimidazole inhibitors (shown in blue), a favourable trend is observed for both the adsorption onto face {001} and face {011}. For the adsorption onto face {001}, more favoured E_{ads} values were obtained for the adsorption in the neutral form compared to those in the monoprotic form. The same is not found for the adsorption onto face {011}. Since the monoprotic forms of **FL1** and **FL3** were not able to adsorb into the crevice on face {001}, it might be that improved adsorption is obtained when the two neighbouring primary adsorption sites (only the neutral forms) are occupied.

Upon applying the multiple correlation equation (eqn 3.4) to the data comparing the calculated E_{ads} values to the NP40 $BHIC_{50}$ for the non-quinoline compounds, a linear correlation, with and R^2 value of 0.72 and a P value of 0.002, is found (Table 23, Table 24, and Figure 73). Therefore, a linear correlation exists between the calculated E_{ads} values and

_____

the determined NP40 BHIC$_{50}$ activity of the non-quinoline inhibitors, when the speciation

and the adsorption onto the two fastest growing faces are taken into account.

Table 23: Final variables calculated for the multiple correlation calculation

Variable	Value	Crystal face	Speciation form
v_1	0.20	{001}	Monoprotic
v_2	0.00	{011}	Monoprotic
v_3	0.00	{001}	Diprotic
v_4	0.37	{011}	Diprotic
v_5	0.06	{001}	Neutral
v_6	0.37	{011}	Neutral

Table 24: The determined NP40 BHIC$_{50}$ activity and the calculated E$_{ads}$ values obtained from the multiple correlation, of the non-quinoline inhibitors.

Compounds	E$_{ads}$ (kcal.mol^{-1})	NP40 BHIC$_{50}$ (µM)		
KW1	-59.8	18.7	±	0.1
KW2	-55.1	14.6	±	0.2
KW3	-62.9	13.8	±	0.4
KW4	-62.4	13.3	±	0.7
KW5	-70.6	9.1	±	0.7
KW6	-68.1	12.7	±	1.4
KW7	-60.6	22.2	±	1.4
FL1	-59.8	38.2	±	1.4
FL2	-55.1	24.5	±	4.2
FL3	-59.8	32.0	±	1.4

148
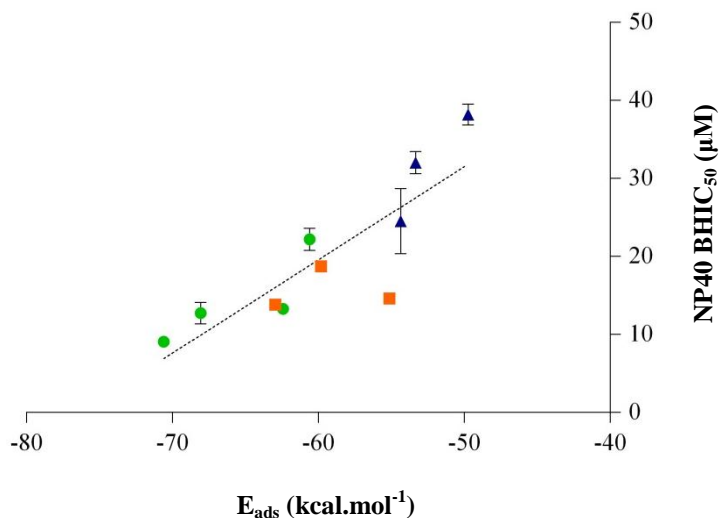
Figure 73: Multiple correlation fit for the non-quinoline inhibitors.

The multiple correlation fit for comparing the calculated E_{ads} to the NP40 BHIC$_{50}$ activity for the non-quinoline inhibitors. The 2,4,5-triaryl substituted imidazole inhibitors are indicated in orange, the benzamide inhibitors are indicated in green, and the bezimidazole inhibitors are indicated in blue. An R^2 value of 0.72 and a P value of 0.002 are found.

A greater contribution of v_1 is calculated for the adsorption in the monoprotic form onto face {001}, where the greater contribution of v_4 and v_6 is calculated for the adsorption in the diprotic and neutral forms onto face {011}. This result is consistent with the adsorbed geometries, where three of the compounds are unable to adsorb into the crevice on face {001}, which would allow for a greater contribution of the adsorption onto face {011}.

With a significant linear correlation obtained, this is a very pleasing result, as the same trend is observed as seen for the clinically-relevant inhibitors in the previous chapter, where compounds with lower E_{ads} values showed greater β-haematin growth inhibition. If these two

results agree, then it should give the same multiple correlation when these data sets are combined. This would strengthen the argument that a linear correlation exists between the adsorption of these inhibitors onto β-haematin, and the determined β-haematin inhibition activity.

3.2.2 Combining the non-quinoline inhibitors with the clinically-relevant inhibitors

In this project, structure activity relationships were determined for both clinically-relevant inhibitors (Chapter 2), as well as for a set of non-quinoline inhibitors (current chapter). In both cases a linear correlation is found when the calculated E_{ads} values are compared to the determined β-haematin inhibition activity, when the speciation as well as the adsorption onto the two fastest growing faces is considered. For the clinically-relevant inhibitors, this correlation was initially determined with the $LBHIC_{50}$ activity data, however the relevant NP40 $BHIC_{50}$ activity data is also available.

Therefore, by combining the two data sets for the multiple correlation, and by including all the molecules that adsorb into the primary, as well as onto the secondary adsorption sites (including MQ and compound **KN7**), a correlation with an R^2 value of 0.67 and a P value of <0.0001, is obtained (Table 25, Table 26, and Figure 74). The two data points to the far right of the trend are that of MQ(*R* and *S*), and the one on the far right on the trend line, is that of compound **KN7**.

The greatest contribution is calculated for v_1, v_3 and v_6, where adsorption is favoured onto face {001} in the monoprotic and diprotic forms, and adsorption is favoured onto face {011}

_____

in the neutral form. This result is indeed satisfying, and is consistent with the previous structure-activity relationships evaluated for the adsorption onto β-haematin.

Even though a linear correlation between the calculated E_{ads} values and NP40 $BHIC_{50}$ activity is seen for the clinically-relevant inhibitors when adsorption onto the secondary adsorption site is also considered, the graph tends towards an exponential curve. However, with only three less active inhibitors in this data set (NP40 $BHIC_{50}$ activity above 100 μM), this observation is not conclusive, and a more definitive conclusion could only be made by also evaluating structure-activity relationships of additional less active inhibitors for the adsorption onto β-haematin.

Table 25: Final variables calculated for the combined correlation of the non-quinoline and clinically-relevant inhibitors.

Variable	Value	Crystal face	Speciation form
v_1	0.24	{001}	Monoprotic
v_2	0.00	{011}	Monoprotic
v_3	0.22	{001}	Diprotic
v_4	0.13	{011}	Diprotic
v_5	0.11	{001}	Neutral
v_6	0.31	{011}	Neutral

_____

Table 26: The determined NP40 BHIC$_{50}$ activity and the calculated E$_{ads}$ values obtained from the multiple correlation, of the non-quinoline and the clinically relevant inhibitors.

Compounds	E$_{ads}$ (kcal.mol^{-1})	NP40 BHIC$_{50}$ (μM)		
KN6	-91.5	58.8	$\pm$	3.8
KN7	-75.0	134.6	$\pm$	10.4
KW1	-98.0	18.7	$\pm$	0.1
KW2	-88.6	14.6	$\pm$	0.2
KW3	-98.6	13.8	$\pm$	0.4
KW4	-99.0	13.3	$\pm$	0.7
KW5	-118.4	9.1	$\pm$	0.7
KW6	-102.3	12.7	$\pm$	1.4
KW7	-104.6	22.2	$\pm$	1.4
FL1	-82.2	38.2	$\pm$	1.4
FL2	-89.8	24.5	$\pm$	4.2
FL3	-86.4	32.0	$\pm$	1.4
AQ	-97.6	7.2	$\pm$	0.5
CQ	-92.3	31.5	$\pm$	2.0
MQ-*S*	-58.9	304.8	$\pm$	9.2
MQ-*R*	-64.4	304.8	$\pm$	9.2
QD	-86.8	25.6	$\pm$	2.0
QN	-76.5	61.8	$\pm$	1.8
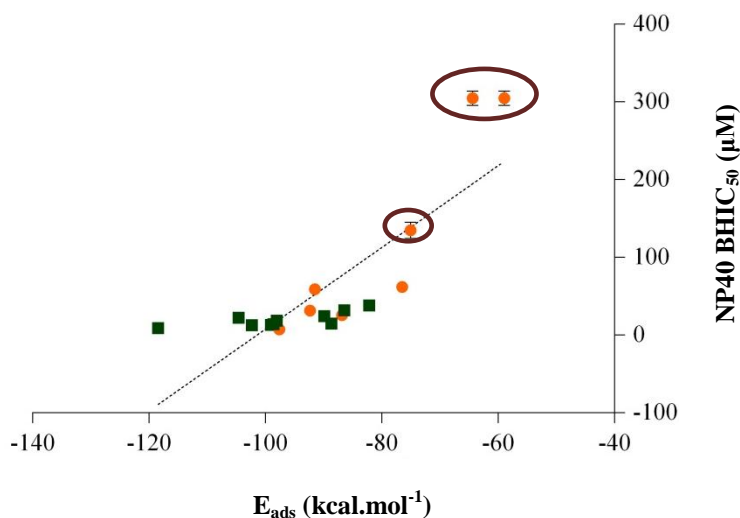
Figure 74: Multiple correlation fit for all the clinically-relevant and the non-quinoline inhibitors.

The non-quinoline inhibitors are indicated in green, and the clinically-relevant inhibitors are indicated in orange. An R^2 value of 0.67 and a P value of <0.0001 are obtained.

The multiple correlation calculation was carried out a second time on the two data sets, this time excluding the inhibitors that adsorbed onto the secondary adsorption site (MQ(±) and compound **KN7**). Interestingly, an improved linear correlation, with an R^2 value of 0.73 and a P value of <0.0001, is found (Table 27, Table 28, Figure 75).

However, for this correlation, the greatest contribution is calculated for v_4 and v_6, where adsorption is favoured onto face {011} in the diprotic and neutral forms respectively. It is rather expected that when only inhibitors which are able to adsorb into the primary adsorption site on face {001} are included in the correlation, that the variables for adsorption onto face {001} would have the greatest contribution. Therefore, the improved linear correlation that exists between the calculated adsorption results and the determined NP40 BHIC$_{50}$ activity results, for both sets of clinically-relevant inhibitors and non-quinoline inhibitors when these compounds are able to adsorb into the primary adsorption site, is not convincing.

153

_____

This raises the question as to whether different types of compounds could be combined into one correlation.

Furthermore, this highlights the importance of evaluating a larger and a more representative data set, where both active and less active inhibitors are included in the study. Therefore, structure-activity relationships for the adsorption of additional less active inhibitors (with NP40 $BHIC_{50}$ activities of >100 μM) onto β-haematin, also need to be evaluated.

Table 27: Final variables calculated for the combined correlation of the non-quinoline and clinically-relevant inhibitors that adsorb into the primary adsorption site.

Variable	Value	Crystal face	Speciation form
v_1	0.15	{001}	Monoprotic
v_2	0.07	{011}	Monoprotic
v_3	0.00	{001}	Diprotic
v_4	0.39	{011}	Diprotic
v_5	0.09	{001}	Neutral
v_6	0.31	{011}	Neutral

_____

Table 28: The determined NP40 BHIC$_{50}$ activity and the calculated E$_{ads}$ values obtained from the multiple correlation, of the non-quinoline and the clinically relevant inhibitors which were able to adsorb into the primary adsorption site.

Compound	E$_{ads}$ Primary* (kcal.mol^{-1})	NP40 BHIC$_{50}$ (μM)		
KN6	-57.0	58.8	±	3.8
KN7	–	134.6	±	10.4
KW1	-75.8	18.7	±	0.1
KW2	-71.7	14.6	±	0.2
KW3	-81.0	13.8	±	0.4
KW4	-84.4	13.3	±	0.7
KW5	-90.3	9.1	±	0.7
KW6	-85.6	12.7	±	1.4
KW7	-82.3	22.2	±	1.4
FL1	-67.8	38.2	±	1.4
FL2	-72.9	24.5	±	4.2
FL3	-71.2	32.0	±	1.4
AQ	-80.8	7.2	±	0.5
CQ	-60.6	31.5	±	2.0
MQ-*S*	–	304.8	±	9.2
MQ-*R*	–	304.8	±	9.2
QD	-63.7	25.6	±	2.0
QN	-56.4	61.8	±	1.8

* *Calculated E$_{ads}$ values obtained from the multiple correlation of inhibitors which were able to adsorb into the primary adsorption site.*
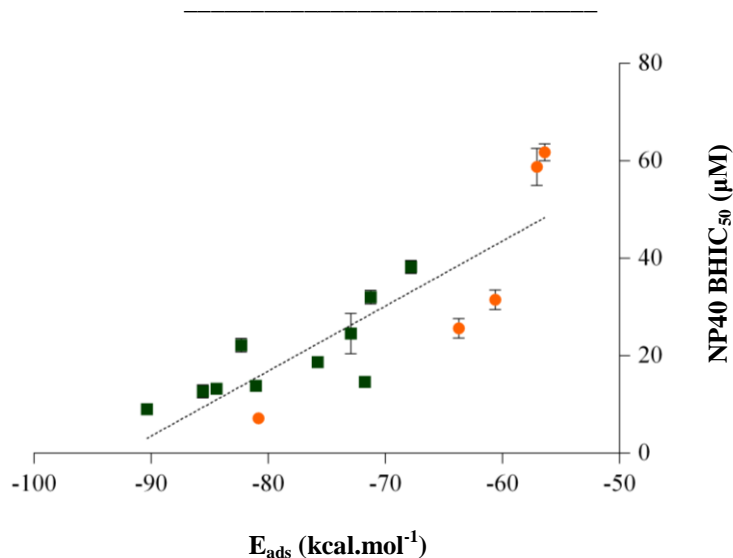
_____

Figure 75: Multiple correlation fit for the clinically-relevant and the non-quinoline inhibitors that adsorb into the primary adsorption site.

The non-quinoline inhibitors are indicated in green, and the clinically-relevant inhibitors are indicated in orange. An R^2 value of 0.74 and a P value of <0.0001 are observed. Note that when different variables are included in the multiple correlation equation, the final E_{ads} values differ (compare to figure 74).

From this study, it is obvious that more active β-haematin inhibitors have more favoured adsorbed geometries, as well as more favoured E_{ads} values for the adsorption onto the two fastest growing faces, faces {001} and {011}. Furthermore, a significant linear correlation is found when the E_{ads} values are compared to the determined NP40 BHIC$_{50}$ activities, for the adsorption of all the clinically-relevant and non-quinoline compounds, without excluding any outliers.

Therefore, it could be concluded that this computational adsorption study is suitable to evaluate the adsorption of inhibitors onto the fastest growing faces of β-haematin, for quinoline as well as for non-quinoline compounds.

_____

3.3 CONCLUDING REMARKS PERTAINING TO CHAPTER 3

3.3.1 The significance of this chapter

In Chapter 2, a thorough investigation was performed on evaluating the adsorption of clinically-relevant quinoline inhibitors, where a linear correlation was found when comparing the determined NP40 BHIC$_{50}$ activities to the calculated E$_{ads}$ values for the adsorption onto faces {001} and {011} when different speciation forms are taken into account. This was indeed a remarkable breakthrough. Therefore, this study was also extended to evaluate the adsorption of non-quinoline inhibitors onto β-haematin; such work has not yet been reported in literature.

With this study forming part of a larger research project, a small library of active 2,4,5-triaryl substituted imidazole, benzamide, and benzamidazole β-haematin inhibitors was available. It is found that these compounds adsorbed onto face {011} in such a manner that the molecules extended over two unit cells. Similar adsorption geometries were obtained for the adsorption onto face {001}, where most of these molecules were able to adsorb into two neighbouring primary adsorption sites. This is the first time that these geometries were observed. Furthermore, it is found that the molecules that were not able to adsorb into the two primary adsorption sites, preferred an adsorbed geometry where both the primary and the secondary adsorption sites were occupied. In this case, the formation of a hydrogen bonding interaction was seen between the inhibitor and a free carbonyl group outside of the crevice.

In evaluating structure-activity relationships for the adsorption of these inhibitors onto β-haematin, no correlations were found when the adsorption onto face {001} or face {011} were evaluated separately. Finally, by applying the multiple correlation calculation, and

thereby combining both the speciation and the adsorption onto both faces, a significant linear correlation, with an R^2 value of 0.72 and a P value of 0.002, was found, where the determined variables were representative of the data set. In this study, unlike for the clinically-relevant inhibitors, a greater percentage of the molecules preferred adsorption onto the second fastest growth face, and therefore a larger contribution of the E_{ads} values for the adsorption onto this face was accounted for.

This result again highlights the importance of considering both the adsorption onto face {001} and face {011}. Furthermore, with these crystal faces being similar in geometry, where the secondary adsorption site on face {001} closely resembles the surface of face {011}, this observation for the adsorption of these larger molecules, could possibly be rationalised.

In the end, these results were combined with those obtained for the adsorption of the clinically-relevant inhibitors. By applying the multiple correlation calculation, a significant linear correlation, with an R^2 value of 0.67 and a P value of <0.0001, was obtained. However, when visually inspecting this graph, it is seen that the larger, less active inhibitors (MQ(±) and **KN7**) did not fit this trend well. Rather, the data tend toward an exponential function. However, with only two of these less active inhibitors forming part of the correlation, this is not conclusive. Therefore, in order to determine whether an exponential curve might be valid, additional less active inhibitors need to be included in this correlation.

What is however, still significant to see, is that the non-quinoline and quinoline inhibitors could be combined to obtain a linear correlation, when comparing the molecular modelling

results for the adsorption onto the two fastest growing faces of β-haematin and the determined β-haematin growth inhibition activities.

This adds merit to the hypothesis that antimalarial drugs that target the β-haematin pathway, may indeed exert their mechanism of action by adsorbing onto the two fastest growing faces of the β-haematin crystal, and thereby impeding further crystal growth.

3.3.2 Final conclusion

In extending the work discussed in the previous chapter to evaluating the adsorption of active non-quinoline β-haematin inhibitors, a new geometry for the adsorption onto face {001}, as well as for the adsorption onto face {011} is observed, where the inhibitors were able to adsorb onto two neighbouring porphyrin structures.

Furthermore, by evaluating structure-activity relationships, the significance of evaluating the adsorption onto both the fastest and the second fastest growth faces, was emphasised.

Therefore, in the end of this chapter, it can be concluded that a linear correlation exists, for both quinoline and non-quinoline compounds, between the β-haematin inhibition activity and the ability of a compound to adsorb onto both the fastest and the second fastest growth faces, when the speciation at pH 4.8 is also taken into account.

CHAPTER 4

ADSORPTION INTO THE PRIMARY ADSORPTION SITE

In the previous two chapters, a thorough investigation was performed on the adsorption of clinically-relevant inhibitors and non-quinoline inhibitors onto the two fastest growing crystal faces of β-haematin.

The clinically-relevant inhibitors and the small quinoline inhibitors mainly showed preference for adsorbing into the primary adsorption site on face {001}, where more bulky inhibitors, such as MQ, showed preference for adsorbing onto the secondary adsorption site on face {001}. It is concluded that the optimum adsorbed geometry is obtained for the adsorption of QN and QD in the primary adsorption site. The quinoline moiety of the inhibitors were able to form π-π interactions to the porphyrin structures in the crevice, and hydrogen bonding interactions were formed between amine hydrogen atoms on the inhibitor and free carbonyl groups on the crystal surface outside of the crevice.

This observation has previously been discussed by Buller *et al.*[54] With a greater understanding of the preferred adsorbed geometries onto face {001}, as well as with a linear correlation found between the calculated E_{ads} values and the determined NP40 $BHIC_{50}$ activities for the adsorption of the clinically-relevant inhibitors onto β-haematin (Section 2.4), a comprehensive study is currently being performed on further evaluating this adsorption geometry, as part of another PhD project.

However, upon evaluating the adsorption of the non-quinoline inhibitors onto β-haematin (Chapter 3), a new adsorption geometry is found, that has not yet been reported in literature.

160

Here, the long linear non-quinoline inhibitors adsorbed in such a manner that two neighbouring primary pockets on face {001} were occupied, consequently forming molecular interactions to two neighbouring porphyrin structures in two adjacent unit cells. Moreover, these molecules have shown favourable adsorption onto face {011}, where multiple π-π interactions were formed to the porphyrin structures on the crystal surface.

These molecular scaffolds that are able to adsorb into two neighbouring primary adsorption sites, could be used as a guide for developing more active β-haematin inhibitors. The formation of a greater number of molecular interactions between the molecule and the crystal surface would result in a more favourable adsorption onto the crystal surface. With a linear correlation found between the calculated E_{ads} values and the determined NP40 $BHIC_{50}$ activity, enhanced adsorption onto the β-haematin crystal surface may also translate into improved β-haematin inhibition.

Therefore, by evaluating the adsorption of both molecules that adsorb favourably, as well as less favourably into two neighbouring primary adsorption sites on face {001}, and by comparing the determined NP40 $BHIC_{50}$ activities, this hypothesis would either be supported, or disproved.

4.1 INVESTIGATING SMALL MOLECULAR STRUCTURES TO ADSORB INTO THE PRIMARY ADSORPTION SITE

4.1.1 The small molecular structures investigated

In order to fully understand the adsorption of the quinoline inhibitors into the primary adsorption site, the optimum size molecular scaffold that would best fit into the primary adsorption site, had to be determined. Thereafter, the overall molecule could be optimised for enhanced adsorption into two neighbouring primary adsorption sites.

For the clinically-relevant inhibitors, the quinoline moiety was observed to fit into the primary adsorption site, with the side-chain protruding towards the outside of the crevice. Therefore, without the side-chain, the adsorption into only one primary adsorption site could be evaluated.

Larger aromatic systems are also used as scaffolds in antimalarial drugs. For example, the active antimalarial drugs quinacrine (QC) and pyronaridine contains benzo(b)-(1-5)napthyridine scaffolds (Figure 76), where QC has the same side-chain as CQ.
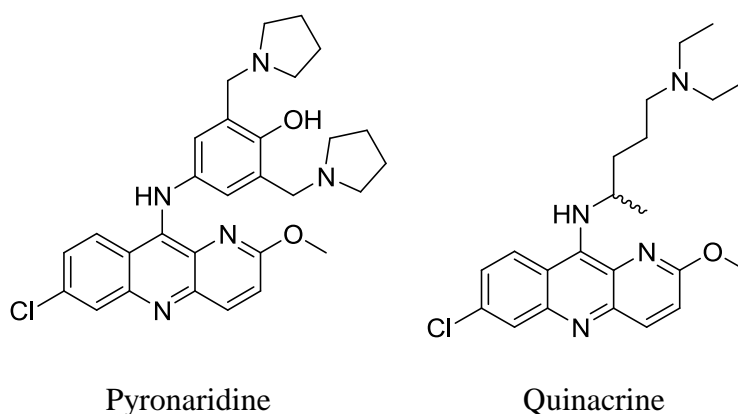

Pyronaridine   Quinacrine

Figure 76: The chemical structures of pyronaridine and quinacrine
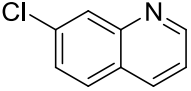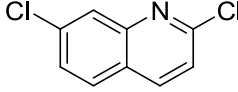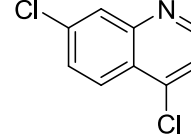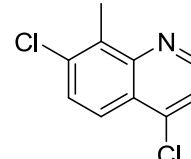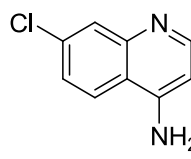
Therefore, by starting from a small quinoline scaffold, such as 7-chloroquinoline (compound **S1**), and by gradually changing the size of the molecule by adding aromatic rings, or by varying the size of the aromatic rings (Compounds **S1**, **S5**-**10**, Table 29 and Table 30), adsorption studies would provide valuable information as to how these molecules would adsorb into the primary adsorption site. In order to achieve this, three different scaffolds were chosen, namely quinolines, carbazoles, and benzonapthypyridines. In particular, the carbazole scaffold had been identified in a screen of compounds that are available through the collaborative NIH project, while the benzonaphypyridine scaffold is present in clinically-relevant antimalarial drugs, such as pyronaridine and quinacrine.
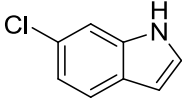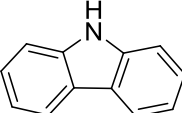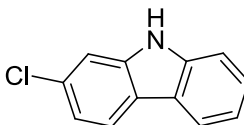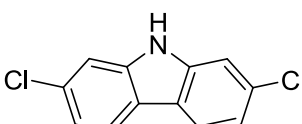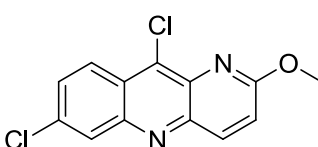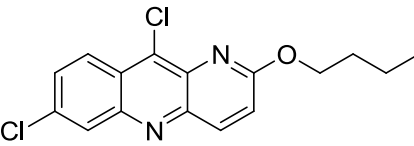
The intermolecular contribution of halogen bonding interactions could be evaluated by varying the number of halogen atoms on the aromatic rings, as well as the positions thereof (as seen for compounds **S2** and **S3**, Table 29). Moreover, the effect of steric bulk on the adsorption geometry of the molecules could be investigated by adding a methyl group (compound **S4**), or by extending the side-chain (compound **S10**).

It is considered that when determining the NP40 $BHIC_{50}$ activity of these small molecular scaffolds, solubility in the assay medium might be a problem. However, with most of these molecules being commercially available, it is still worth evaluating the adsorption of these into the primary adsorption site computationally, as well as attempt to determine the NP40 $BHIC_{50}$ activities, in order to gain a greater understanding on how these small scaffolds would occupy a single primary adsorption site.

_____

Table 29: Quinoline compounds investigated in this study

Compound	Chemical structure
S1	
S2	
S3	
S4	
S11	

164

_____

Table 30: Non-quinoline scaffolds investigated in this study

Compound	Chemical structure
S5	
S6	
S7	
S8	
S9	
S10	

_____

4.1.2 Adsorption of the small molecular scaffolds into the primary adsorption site

For these small molecules, the same adsorption protocol was used as applied in the previous adsorption studies. Similarly as for compounds **KW5** and **FL2**, it is found that the dynamics optimisation had no effect on the final adsorption geometries. Furthermore, all of the small scaffolds are calculated to be in the neutral speciation form at pH 4.8.

Compounds **S1** and **S2** adsorbed in a similar manner into the primary adsorption site, where the chlorine atoms faced into the crevice (Figure 77). Interestingly, compound **S5** adsorbed with the indole N-H facing towards the outside of the crevice. It might be that this adsorption geometry is simply preferred due to the steric bulk of the hydrogen atom on the indole nitrogen.

Figure 77: Adsorption of compounds S1, S2 and S5 in the primary adsorption site

*The adsorption of compounds **S1**(left), **S2**(middle) and **S5**(right) in the neutral form onto face {001}, is shown, as viewed from above. The π-π interactions are indicated by ▪ ▪ , and are measured to be between 3.5 and 3.8 Å.*

Compounds **S6-8** adsorbed with the carbazole N-H towards the outside of the crevice (Figure 78). Comparing the adsorbed geometries of these molecules, it is found that compound **S8** had the optimal adsorption geometry for the adsorption into a single primary adsorption site, since the internal space of the adsorption site is fully occupied.

Figure 78: Adsorption of compounds S6-8 in the primary adsorption site

The adsorption of compounds S6 (left), S7 (middle) and S8 (right) in the neutral form onto face {001}, is shown, as viewed from above. The π-π interactions are indicated by ▪ ▪ *, and are measured to be between 3.5 and 3.8 Å.*

The adsorption of compound **S6** into the primary pocket is found to be slightly more random, where after successive adsorption simulations, the output geometry results varied. The compound did not show preference for adsorbing to the left, to the right, or into the centre of the adsorption site. All of the other compounds adsorbed to one side of the adsorption site. Furthermore, the calculated E_{ads} values of compounds **S7** and **S8** of −58.0 and −58.2 kcal.mol^{-1} respectively, are considered more favourable than the calculated E_{ads} value of compound **S6** of −52.0 kcal.mol^{-1} (Table 31). With the E_{ads} values for compound **S7** and **S8** being almost similar, this suggests that the chlorine atoms might play a directing role for the adsorption location in the primary adsorption site.

_____

Table 31: The calculated E_{ads} values of compounds S6-8.

Compound	E_{ads} (kcal.mol^{-1})		
S6	-52.2	±	0.01
S7	-58.0	±	0.01
S8	-58.2	±	0.01

Compound **S3** showed preference for adsorbing with this chlorine atom (in the 4-position) facing into the crevice. The aromatic scaffold was still located in the crevice and weak π-π interactions were formed between the quinoline moiety and the porphyrin structure on the crystal surface, with measured interaction distances of 3.9 and 4.0 Å. It is possible that this chlorine atom in the 4-position of the quinoline forms hydrophobic C-H⋯Cl halogen bonding interactions to non-polar hydrogen atoms in the back of the crevice (Figure 80).[154] Furthermore, compound **S4** adsorbed into the primary adsorption with the large methyl group protruding towards the outside of the crevice (Figure 79). As a result, the 4-chloro group is directed into the crevice.
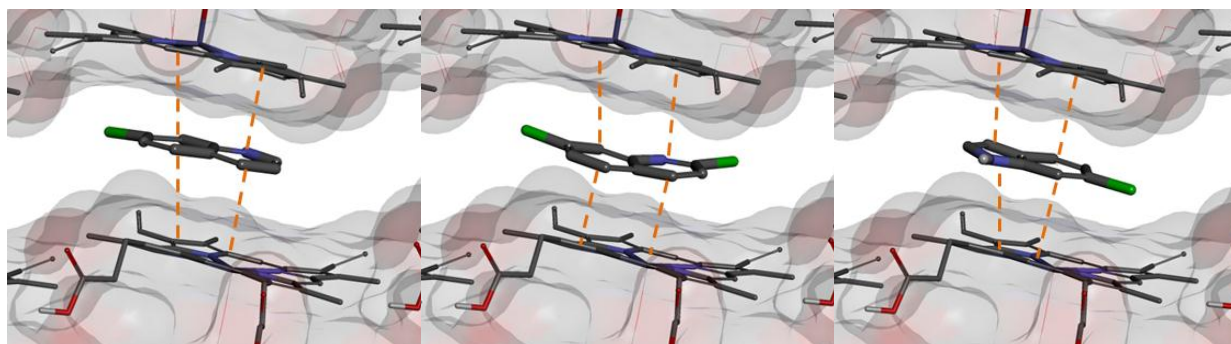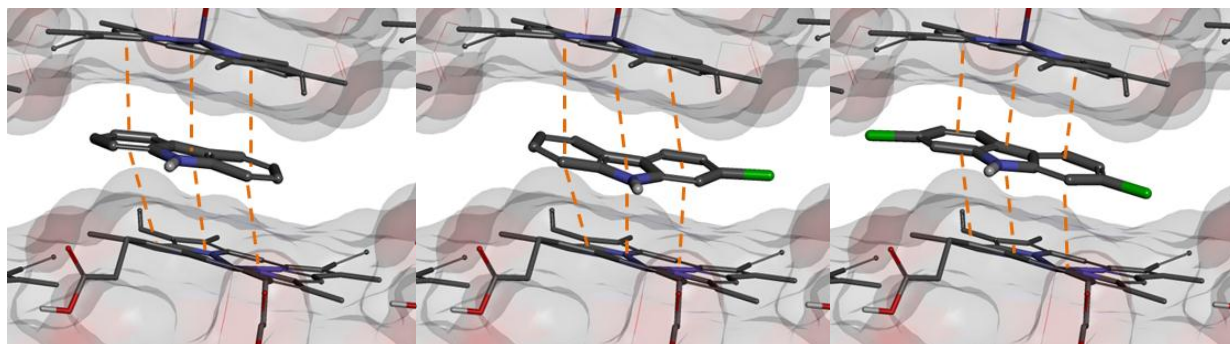
Figure 79: Adsorption of compounds S3 and S4 in the primary adsorption site

*The adsorption of compounds **S3** (left), and **S4** (right) in the neutral form onto face {001}, is shown, as viewed*

from above. The π-π interactions are indicated by ▪ ▪ *, and are measured to be between*

3.5 and 3.8 Å.
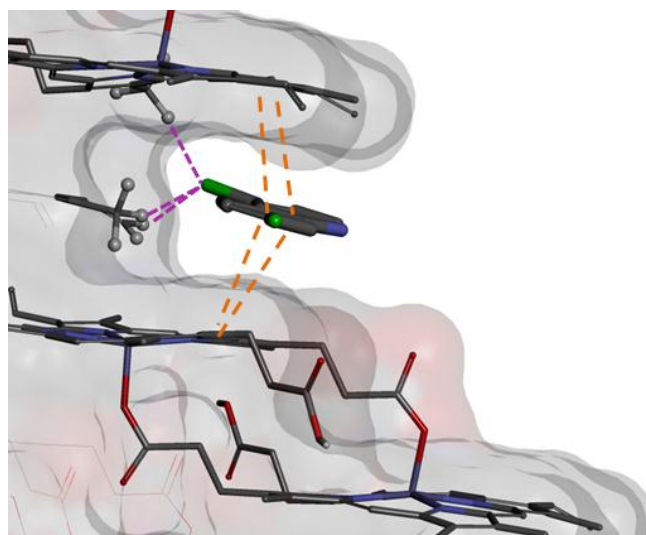
Figure 80: Adsorption of compound S3 in the primary adsorption site

*The adsorption of compound **S3** in the neutral form onto face {001}, is shown, as viewed from the side of the*

crystal face. The π-π interactions are indicated by ▪ ▪ *, and are measured to be between 3.5 and 3.8 Å, where*

the C-H···Cl interactions are indicated by ▪ ▪ *, and are measured to be 2.2, 2.5, and 2.7Å . The non-polar*

hydrogen atoms in the back of the crevice are indicated as grey balls.

By replacing this chlorine atom in the 4-position of compound **S3** with an amine group (compound **S11**), this halogen bonding interaction is not possible. Therefore, it is found that the 4-amino-7-chloroquinoline molecule adsorbs in the same geometry as CQ (Figure 81).
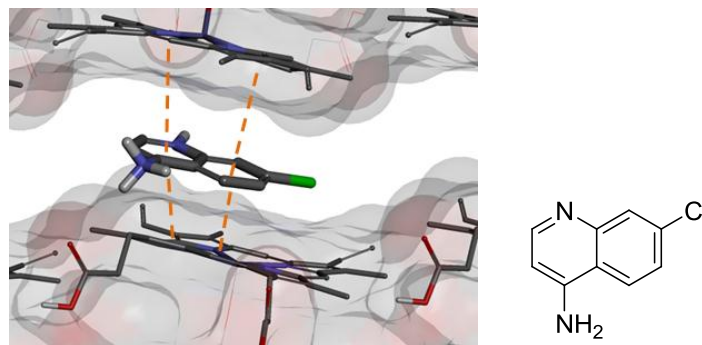
Figure 81: Adsorption of compound S11 in the primary adsorption site

*The adsorption of compound **S11** in the diprotic form onto face {001}, is shown (left), as viewed from above.*

The π-π interactions are indicated by ▪ ▪ , and are measured to be between 3.5 and 3.8 Å.

*The chemical structure of compound **S11** is shown (right), where this compound is 100% diprotic at pH 4.8.*

When investigating the adsorption of the larger benzo(b)(1-5)napthyridine compounds, it is found that compound **S9** was not able to adsorb completely into the primary adsorption site (Figure 82). All three aromatic rings of compound **S9** were able to form π-π interactions to the porphyrin structure on the crystal surface, where only two of the aromatic rings of compound **S10** were able to form these π-π interactions. The other aromatic ring was too far out of the crevice to form a favourable π-π interaction, with a measured interaction distance above 4.0 Å.
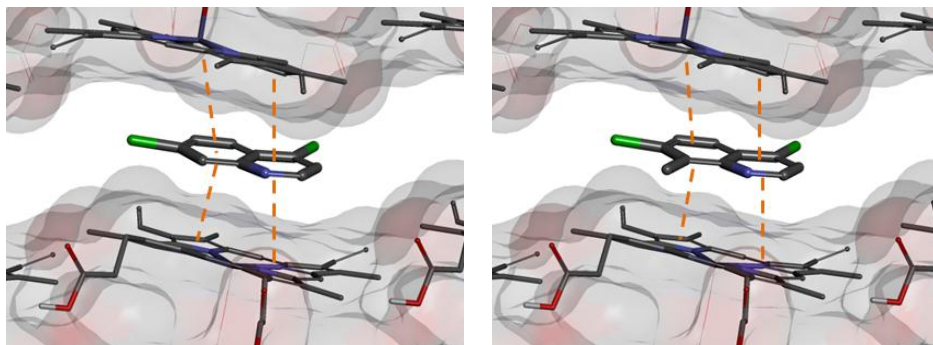
170
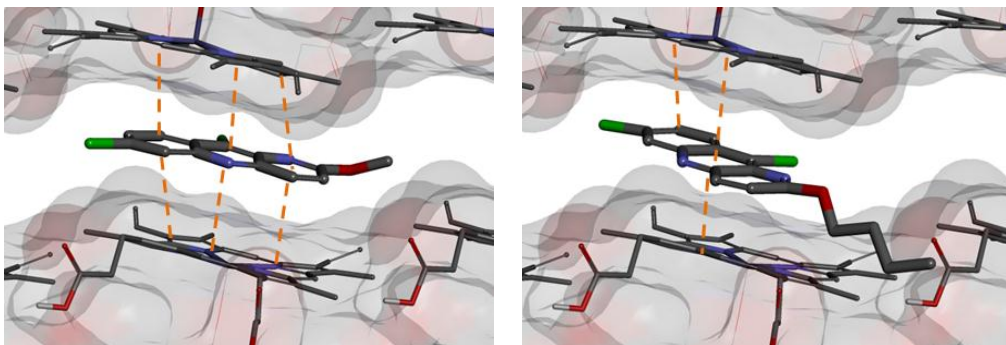
Figure 82: Adsorption of compounds S9 and S10 in the primary adsorption site

*The adsorption of compounds **S9** (left) and **S10** (right) in the neutral form onto face {001}, is shown, as viewed*

from above. The π-π interactions are indicated by ▪ ▪ , and are measured to be between

3.5 and 3.8 Å.

This observed adsorption geometry of compound **S9** was not as expected, when comparing it to the adsorption of QC into the primary adsorption site (Figure 83). QC showed preference for adsorbing into the primary adsorption site, where the chlorine atom, as well as the methoxy side-chain were able to adsorb into the crevice. The methoxy side-chain probed into a second primary adsorption site. For the adsorption of compound **S9**, it is considered that the chlorine atom in the 10-position of the benzo(b)(1-5)napthyridine shows preference for adsorbing into the primary adsorption site, as seen for compound **S3** (Figure 80). It is possible that this chlorine atom forms C-H···Cl halogen bonding interactions (2.2-2.7 Å) to non-polar hydrogen atoms in the back of the crevice.[154]

171

_____
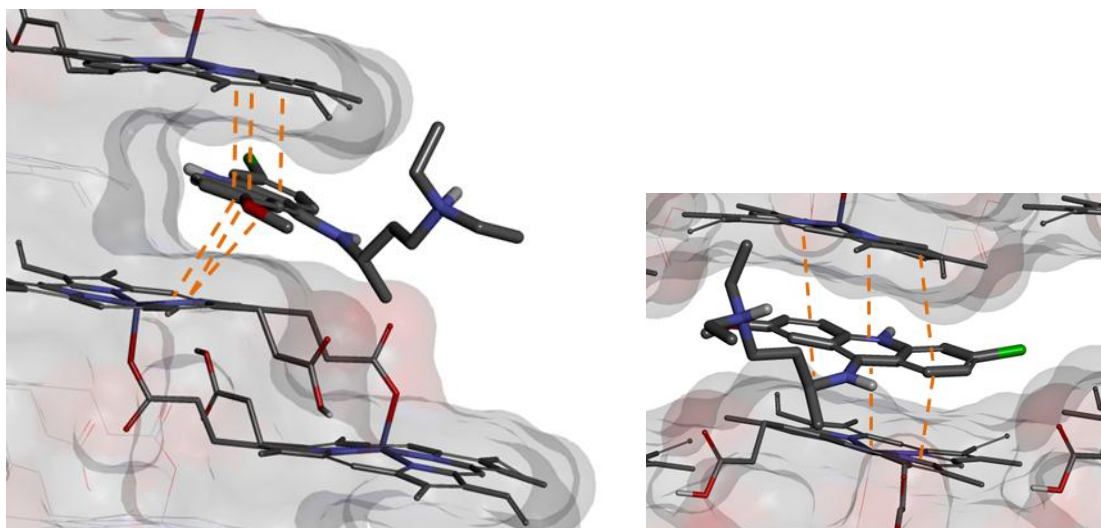
Figure 83: The adsorption of quinacine in the primary adsorption site

The adsorption of quinacrine in the diprotic form onto face {001}, is shown, as viewed from the side of the crystal face (left), and as viewed from above (right). The π-π interactions are indicated by ▪ ▪ , and are measured to be between 3.5 and 3.8 Å.

As noticed for the adsorbed geometries of QC and CQ, by adding a larger side-chain at this position (4-position of the quinoline and the 10-position of the benzo(b)(1-5)napthyridine), the larger side-chain would be too big to fit into the crevice, and the molecule would show preference for adsorbing with the aromatic rings into the primary adsorption site, in order to form π-π interactions to the porphyrin on the crystal surface. As a result, the larger side-chain is permitted to probe towards the outside of the crevice. The contribution of this side-chain for the adsorption into the primary adsorption site is not clear. It might be that this side-chain rather plays a larger role in the crossing of cell membranes, or promotes adsorption onto the second fastest growth face, face {011}. Indeed, QC is known to be a more potent antimalarial drug than CQ,[155] and related to this, the NP40 BHIC50 activity will be discussed later in Section 4.1.5.

Overall, by evaluating the adsorption of these small molecular fragments onto face {001}, a greater understanding is obtained on how these would adsorb, as well as how a small change in the molecular structure would affect the adsorption geometry.

4.1.3 Synthetic strategies for obtaining the small molecular scaffolds

Most of the compounds used in this study were commercially available at the time, although compound **S8** was considered too expensive to purchase. Compound **S11** was effortlessly synthesised, and the starting reagents were readily available. At the same time the synthesis of the compounds **S2** and **S7** was considered, as they had been previously reported in literature in good yields.

4.1.3.4 Towards the synthesis of the desired 2,7-dichloroquinoline

For the synthesis of compound **S2**, Zaragoza *et al.* reported a general procedure for the preparation of substituted 1*H*-2-quinolines (Scheme 1), where they have used a known method for chlorinating these to substituted 2-chloroquinolines upon treatment with phosphorus oxychloride (Scheme 2).[156]

Starting from compound **1**, the ester was saponified, where after the carboxylic acid **2** was converted to the corresponding acid chloride **3**. This was again treated with 3-chloroaniline, which acted as a nucleophile in order to obtain the anilide **5**. This was subsequently cyclised in the presence of glacial sulphuric acid to obtain 7-chloroquinolone **6** as the major product, and 5-chloroquinolone **7** as the minor product. Upon treating 7-chloroquinolone with phosphorus oxychloride, the desired 2,7-dichloroquinoline **S2** was obtained.
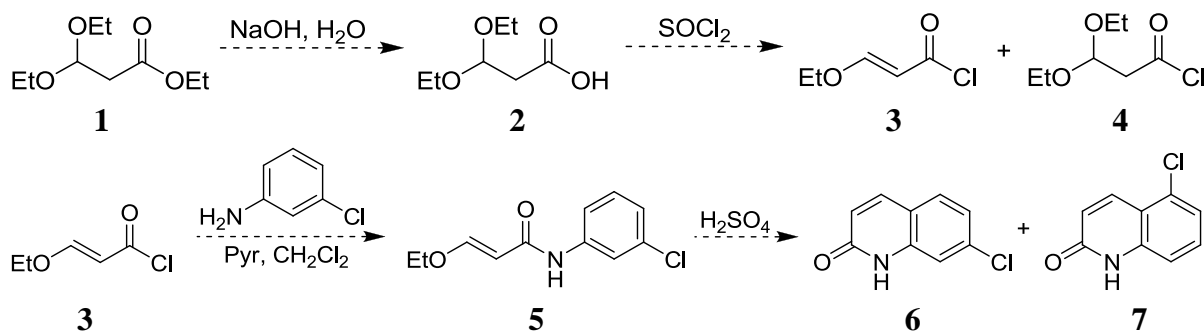
Scheme 1

Scheme 2
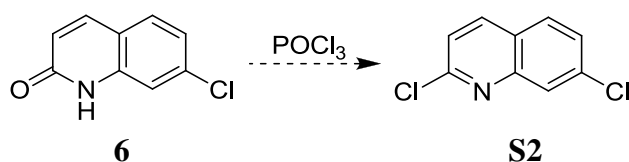
4.1.3.5 Towards the synthesis of the carbazoles

As compound **S7** is not commercially available and compound **S8** is deemed too expensive to purchase, it is reasonable to also synthesise compound **S6**. Gao *et al*. reported a procedure for developing structurally diverse carbazoles by an intermolecular amination of an aromatic bond, under mild reaction conditions.[157] Based on DFT studies, it is proposed that, starting from a nitroso intermediate, an O-addition of phenyl magnesium bromide, followed by an N-O bond cleavage, an aromatic addition, and finally a hydrogen migration, results in the formation of a carbazole (Scheme 3).
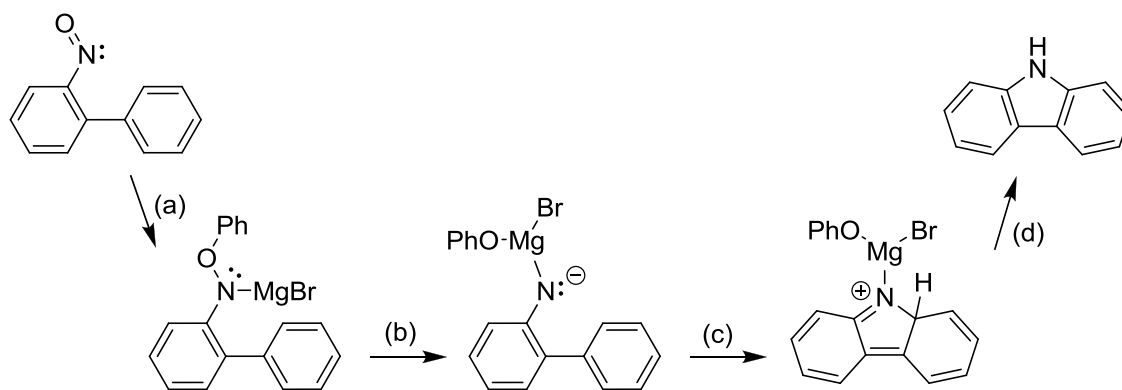
Scheme 3

The reaction mechanism proposed by Gao et al. for the formation of a carbazole from a nitroso intermediate is shown.[157] *The O-addition of phenyl magnesium bromide (a), the N-O bond cleavage (b),*

the aromatic addition (c), as well as the hydrogen migration (d), are indicated.

The same synthetic route would be used for the synthesis of compounds **S6**-**8**. Therefore, by starting from a 2-bromo-nitrobenzene derivative, a Suzuki coupling reaction would provide a 2-nitrobiphenyl derivative, upon which the intermolecular amination reaction would be performed (Scheme 4).

Scheme 4
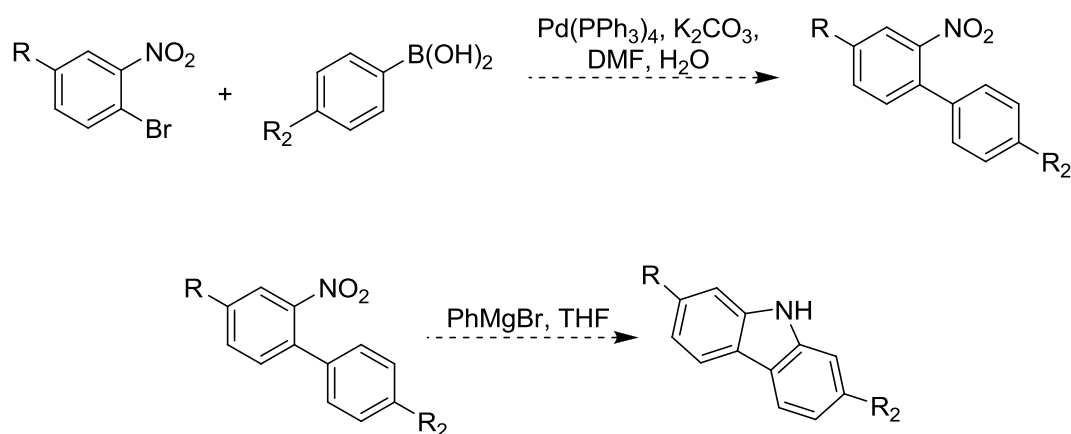
Compound **S6:** R = H, R$_2$ = H;   Compound **S7:** R = Cl, R$_2$ = H;   Compound **S8:** R = Cl, R$_2$ = Cl.

175

_____

The Suzuki reaction was first published by Akira Suzuki and his co-workers in 1979,[158] upon which he was awarded a joint Nobel Prize for his contribution to palladium-catalysed cross couplings in organic synthesis.[159] Traditionally, this reaction is performed using palladium-tetrakis(triphenylphosphine) as catalyst. However, to date, several new variations of this coupling reaction have been reported, where numerous catalysts have been developed to achieve more selective couplings.[160–164]

For the purposes of this project, the Suzuki-Mayaura transmetalation coupling reaction was used (Scheme 5).[164] Starting form palladium(0)-tetrakis(triphenylphosphine), the halide is introduced by means of an oxidative addition, where a palladium(II) species is formed. The boronic acid is activated in the presence of base (potassium carbonate), where after the transmetalation reaction proceeds. Finally, the complex undergoes reductive elimination, which yields the final coupled product and the regenerated palladium(0) catalyst.

Chapter 4 – Adsorption into the primary adsorption site

_____
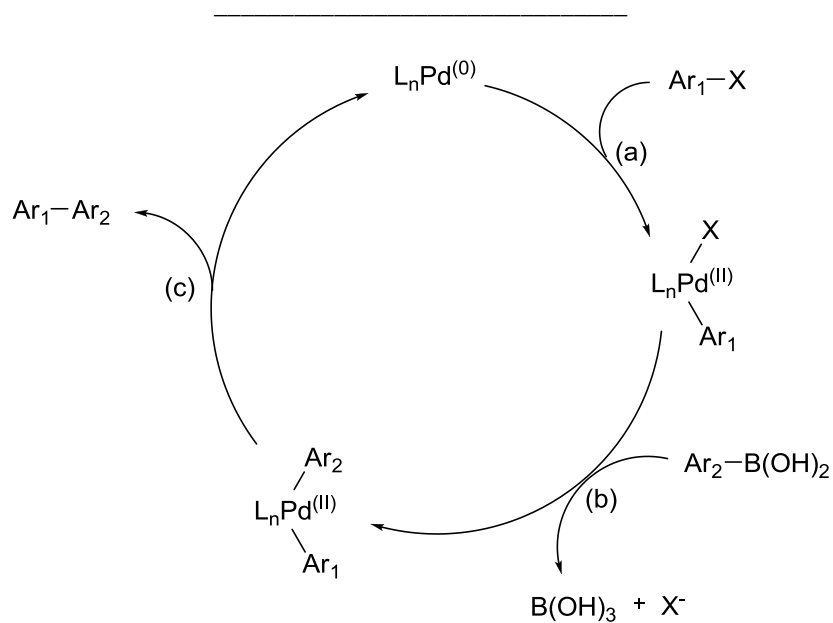
As an example, for the synthesis of compound **S6:**

$Ar_1 =$

$Ar_2 =$
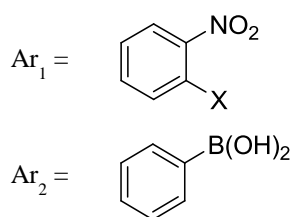
Scheme 5

The reaction mechanism proposed by Lennox et al. for the Suzuki-Mayaura cross-coupling reaction is shown.[164]

The reaction proceeds via the oxidative addition of the halide (a), followed by the transmetalation step by

introducing the boronic acid (b), and then the final reductive elimination (c), which results in the regeneration

of the catalyst.

The synthesis of compound **S11** would be commenced by treating 4,7-dichloroquinoline with sodium azide to obtain the 4-azido-7-chloro intermediate, where after the azide functional group could be reduced in the presence of Raney[®]-Nickel in order to obtain the desired amine product **S11** (Scheme 6).

Scheme 6
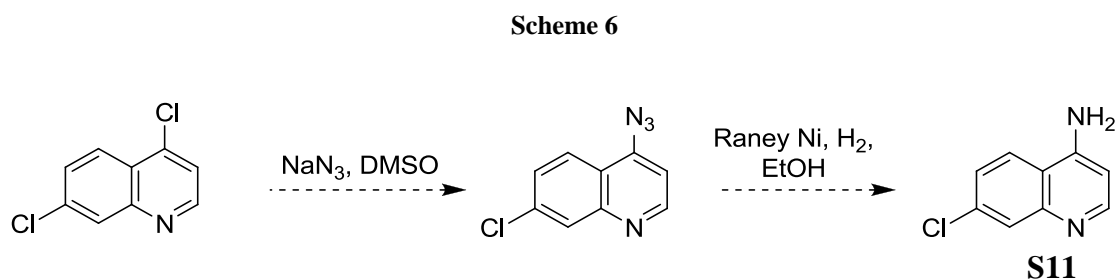
The reasons for this choice of synthetic route will be discussed later in this chapter for the synthesis of 2-aminoquinoline **L16** (Section 4.2.4.1), as this compound was synthesised prior to compound **S11**. However, unlike the synthesis of 2-aminoquinoline, the synthesis of the azide intermediate via this synthetic route has to be undertaken carefully, as the azide functional group might be introduced on both the 4- and the 7-position of the quinoline. As a result, milder reaction conditions might be required.

With the synthetic strategy outlined, the small molecular scaffolds that were not purchased could be synthesised, and structure-activity relationships could be evaluated.

4.1.4 Synthesis of the small molecular scaffolds

4.1.4.1 Synthesis pertaining to the 7-chlorquinoline

4.1.4.1.1 Synthesis of 3,3-diethoxypropanoic acid - 2

As an introduction to our synthetic venture, a simple saponification of commercially available ethyl 3,3-diethoxypropanoate **1**, was commenced in order to obtain compound **2** (Scheme 7).[156]

Scheme 7

1   NaOH, H$_2$O, 110°C, 1h   **2**
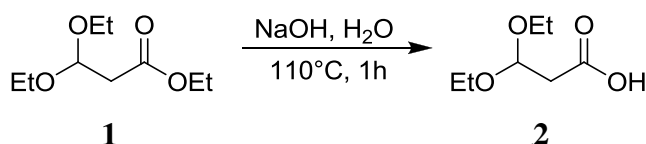
The starting material was exposed to a strong sodium hydroxide solution, whereupon the reaction mixture was refluxed at 110 °C for 4 hours. Upon completion, the starting material was extracted from the basic reaction mixture with ethyl acetate. The water layer was acidified with 2M hydrochloric acid, whereupon the desired product **2** was extracted with ethyl acetate. The solvent was dried on magnesium sulphate, where after it was filtered and removed *in vacuo* to obtain the desired product as an yellow oil that needed no further purification, in a high 85% yield.

2
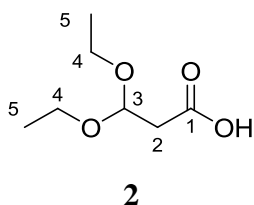
A broad O-H stretch observed in the infrared spectra at 3427 cm^{-1}, as well as a strong C=O stretch at 1667 cm^{-1}, are indicative of the present carboxylic acid. Furthermore, in the ^{1}H NMR, only two chemically equivalent ethyl chains are integrated for, where a carbonyl peak is observed in the ^{13}C NMR spectrum at 173.52 ppm.

4.1.4.1.2 Synthesis of (E)-N-(3-chlorophenyl)-3-ethoxyacrylamide - 5

For the synthesis of compound **5** from **2**, the carboxylic acid was first converted to the acid chloride **3** (not isolated), which was subsequently treated with 3-chloroanaline to obtain the desired anilide **5** (Scheme 8).[156]

Scheme 8
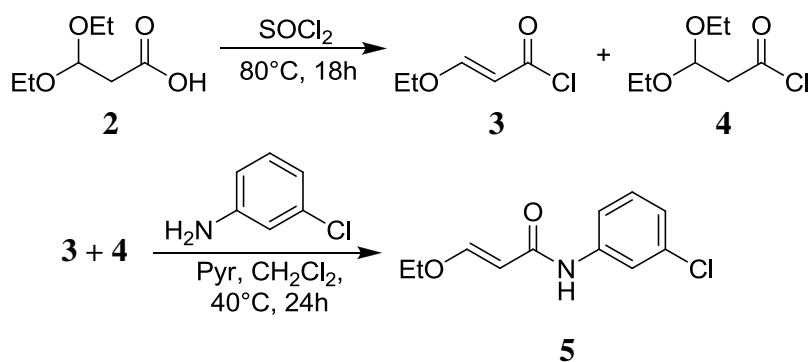
The carboxylic acid was dissolved in a small amount of dichloromethane, whereupon it was refluxed in the presence of an excess amount of thionyl chloride overnight. Upon completion, the thionyl chloride was evaporated off, and the resulting acid chlorides were diluted in a small amount of dichloromethane.

This was slowly added to a solution of pyridine, dichloromethane, and 3-chloroaniline, by means of a dropping funnel. The resulting reaction mixture was gently heated at 40 °C overnight, where after it was acidified with 2M hydrochloric acid, and the product was extracted with copious amounts of dichloromethane.

The purification of product **5** was challenging, since the residue that was obtained did not easily dissolve in organic solvents. Therefore, the excess impurities were removed by means of column chromatography by using a large silica column. Compound **5** was finally purified

by recrystallisation from hot ethyl acetate, in a moderate yield of 41%, although this was of a crude product.

Unfortunately, upon evaluating the ^{1}H NMR and ^{13}C NMR spectra, it was found that the product was still not pure. After many attempts of further purification, the desired product was not purified. With this product not being a final product, we considered it of sufficient purity to proceed with the subsequent step in the total synthesis of 2,7-dichloroquinoline, compound **S2**.
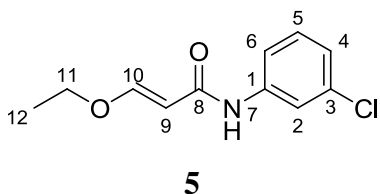
Even though the ^{1}H NMR and ^{13}C NMR spectra indicated that an impure product was obtained, the result of the mass spectral analysis of 226.0606 amu correlated well with the expected mass of 226.0635 amu.

4.1.4.1.2 Synthesis of 2,7-dichloroquinoline - S2

Compound **S2** was finally synthesised from **5**, where **5** was first cyclised to form a mixture of the quinolone intermediates **6** and **7**. This was subsequently treated with phosphorus oxychloride to obtain the desired product (Scheme 9).[156]

Scheme 9
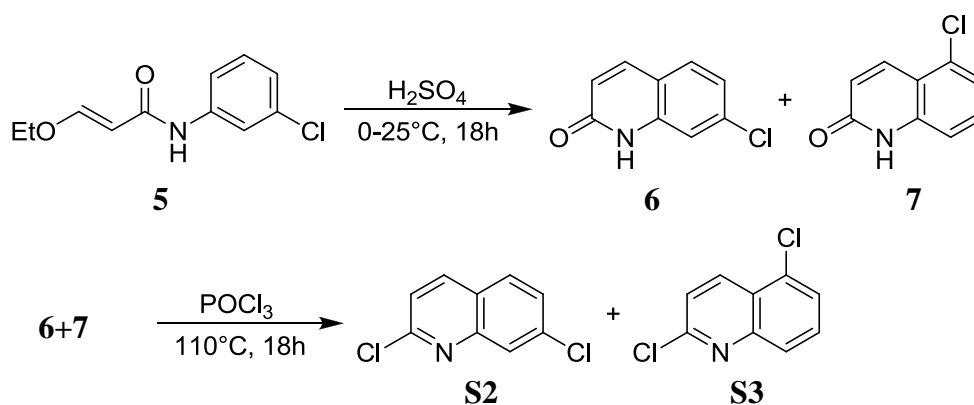
Compound **5** was dissolved in a small amount of dichloromethane and was cooled by means of an ice-bath for the slow addition of glacial sulphuric acid, over a 15 minute period. The reaction was thereafter allowed to slowly warm to room temperature overnight.

Upon completion, the reaction mixture was quenched with an aqueous ammonium chloride solution, whereupon the resulting waxy residue was filtered off and washed with hexane. The filtrate was extracted with ethyl acetate in order to ensure that all the product was isolated.

Finally, this waxy solid was refluxed in phosphorus oxychloride overnight, whereupon the reaction was quenched on ice. The quinoline products were extracted with ethyl acetate and purified by means of column chromatography. Product **S2** was obtained in a low 31% yield as the major product, while product **S3** was obtained in a low 3% yield.

_____
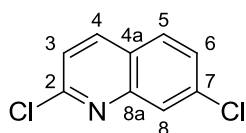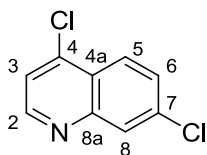
In the ^{1}H NMR spectra, the absence of the signals corresponding to the ethyl chains was noticed, where the only peaks that were seen, were in the aromatic region. COSY and gHSQC NMR studies were performed in order to distinguish between compounds **S2** and **S3**. Furthermore, thin layer chromatography analysis confirmed that the R_f value of compound **S3** correlated with that of commercially obtained 4,7-dichloroquinoline (R_f = 0.75, 20% EtOAc/Hexane).

4.1.4.2 Synthesis pertaining to the carbazole compounds

4.1.4.2.1 Synthesis of 2-nitrobiphenyl - 10

Compound **10** was easily synthesised from **8**, by performing a Suzuki coupling reaction (Scheme 10).[157] The boronic acid **9** and compound **8** were dissolved in *N*,*N*-dimethylformamide, whereupon potassium carbonate was added, together with a small amount of water to dissolve the base. The reaction mixture was heated to 80 °C for five minutes, whereafter the palladium catalyst was added.

Scheme 10
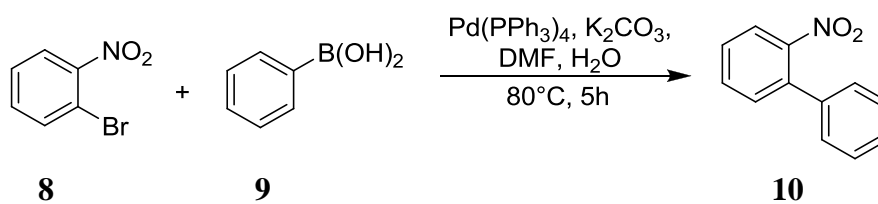
Upon completion, the reaction was quenched with water and the product was extracted with ethyl acetate. The final product is purified by means of column chromatography, where it is obtained in a high yield of 91 %.
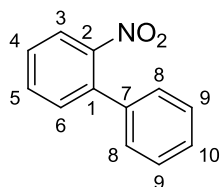
This compound is found to be very unstable, with a melting point of 40-45 °C. The ^{1}H NMR spectrum integrated for two aromatic rings. A peak is observed at 149.4 ppm for C_2 in the ^{13}C NMR spectrum, indicating the presence of the nitro group. Also, an N=O stretch is observed in the IR spectrum at 1354 cm^{-1}.

4.1.4.2.2 Synthesis of 9-H carbazole - S6

For the synthesis of compound **S6** from **10**, care was taken not to allow the reaction temperature to rise above 3 °C, and the reaction was performed under inert conditions (Scheme 11).[157] The reaction was cooled in an ice-bath, and the reagents were added slowly.

Scheme 11
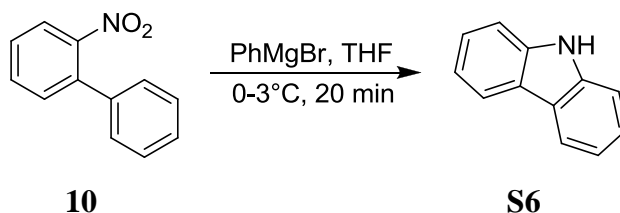
Compound **10** was dissolved in dry tetrahydrofuran. Phenylmagnesium bromide was slowly added over a period of 20 minutes, whereupon the reaction mixture was allowed to stir for another 10 minutes before it was quenched with an aqueous ammonium chloride solution.

184

The product was finally extracted with ethyl acetate and purified by means of column chromatography, to obtain **S6** in a high yield of 86%.
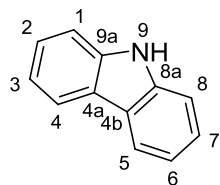
S6

A new N-H peak at 11.22 ppm in the ^{1}H NMR spectrum is indicative of the carbazole formation. Also, an N-H stretch is observed at 3416 cm^{-1} in the IR spectrum. The result of the mass spectral analysis of 168.0813 amu correlated well with the expected mass of 168.0816 amu.

4.1.4.2.3 Attempted synthesis of 4-chloro-2-nitrobiphenyl - 12

For the synthesis of compound **12** from **11**, the same procedure for the Suzuki coupling was performed as mentioned above (Scheme 12). Unfortunately, an inseparable mixture of compounds was obtained, where these had the same R_f value (R_f = 0.44, 2% EtOAc/Hexane), as determined by means of thin layer chromatography. It might be that the phenyl ring also coupled onto the 4-position of the nitro-containing ring, resulting in an inseparable mixture of 4-chloro-2-nitrobiphenyl and 4-bromo-2-nitrobiphenyl. It was considered that by proceeding in performing the ring-closing procedure, the two carbazole products could be separated.

Scheme 12
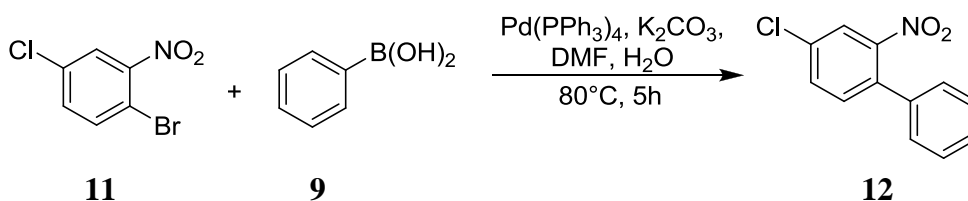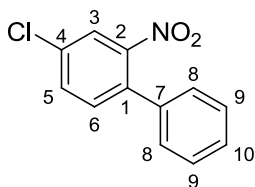
12

Similarly as for compound **12**, a peak is observed at 149.79 ppm for C_2 in the ^{13}C spectrum, where an N=O stretch is seen at 1358 cm^{-1} in the IR spectrum. This indicates the presence of a nitro group at C_2. Furthermore, the ^1H NMR spectrum only showed the presence of aromatic rings. Unfortunately, these integrated for more than two aromatic rings, which revealed that a mixture of two aromatic products was obtained.

4.1.4.2.4 Attempted synthesis of 2-chloro-9H-carbazole - S7

For the synthesis of compound **S7** from the impure mixture of **12**, the same ring-closing procedure for the synthesis of compound **S6** was performed (Scheme 13). Upon purification of the reaction mixture by means of column chromatography, a white crystalline powder was obtained. Unfortunately this product was light sensitive and turned into a blue powder within a period of 30 minutes. It decomposed into multiple compounds, as determined by means of thin layer chromatography. Consequently, the desired product **S7** was not obtained.

Scheme 13

12   **S7**
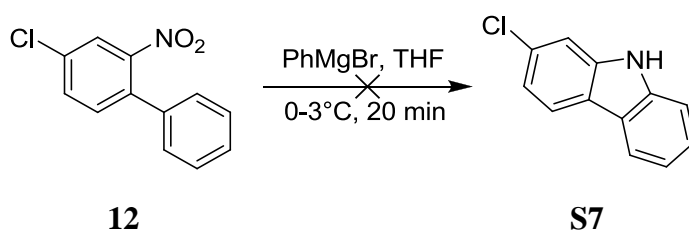
With the complications encountered in purifying compound **12**, by performing the Suzuki coupling under milder reaction conditions, this difficulty could be overcome, as a larger percentage of the major product would be obtained. However, the same problem might be encountered for the synthesis of compound **S8**, where coupling could once again occur on both the 2- and 4-position of compound **11**.

Therefore, also taking into account the complications encountered with the synthesis and purification of compound **12**, the synthesis of compounds **S7** and **S8** were not pursued further.

The bromine derivatives of both of these compounds were commercially available (Figure 84). Therefore, even though it would have been preferable to have chlorine atoms on the carbazole rings to match the other small molecular scaffolds that are investigated, the bromine derivatives could also provide us with the information that we require by determining the NP40 BHIC$_{50}$ activities thereof.
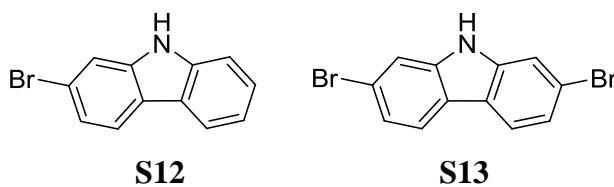
Figure 84: The chemical structures of compounds S12 and S13.

4.1.4.3 The synthesis pertaining to compound S11

For the synthesis of compound **S11**, the same synthetic procedure is used as for the synthesis of compound **L16** that would be discussed in detail in Section 4.2.4.1.

4.1.4.3.1 Synthesis of 4-azido-7-chloroquinoline - 14

Compound **14** was synthesised from **13** in the presence of sodium azide (Scheme 14).[165] The starting reagent **13** was dissolved in dimethyl sulfoxide. The reaction mixture was heated to 60 °C for 18 hours.

Scheme 14
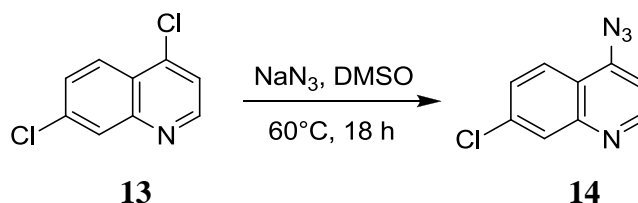
**13**   NaN$_3$, DMSO   60°C, 18 h   **14**

Upon completion, the reaction mixture was quenched with water and the product was extracted with ethyl acetate. Finally, upon purification by means of column chromatography, the desired product **14** is obtained in a high yield of 93%.
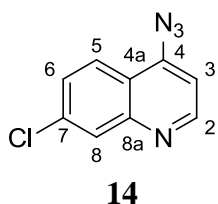
14

The presence of the azide moiety was established by a N$_3$ stretch at 2250 cm^{-1} in the infrared spectrum. The ^{1}H NMR and the IR characterisation are in agreement with that reported by Pereira *et al.* and Hollywood *et al.*[166,167]

4.1.4.3.2 Synthesis of 4-amino-7-chloroquinoline - S11

Compound **S11** was synthesised by the reduction of **14** with freshly prepared Raney®-Nickel under a positive pressure of hydrogen gas (Scheme 15).

Scheme 15
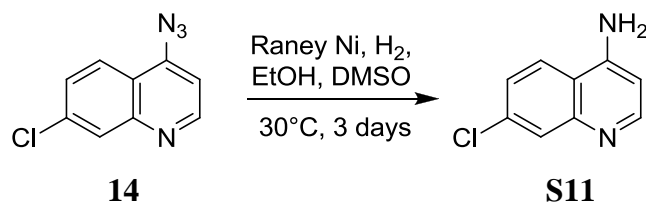
This reaction was commenced by dissolving compound **14** in a small amount of dimethyl sulfoxide and dry ethanol, where a spatula scoop (approximately 5 mL) of freshly prepared Raney®-Nickel was added. This was repeated twice at 4 hour intervals, where after the reaction mixture was left to stir overnight. The reaction was kept at 30 °C and under a positive pressure of nitrogen in order to ensure the reduction of the azide in the 4-position of the quinoline.

Upon completion, the reaction mixture was filtered through celite, whereupon the filtrate was washed with ethyl acetate. The solvent was removed *in vacuo*, whereupon the product was isolated by means of column chromatography, in a high yield of 77%.

S11
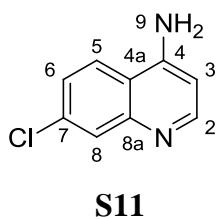
The presence of a broad singlet, integrating for 2 protons at 6.93 ppm in the ^{1}H NMR spectra for H_9, was indicative of the formation of the amine in the 4-position of the quinoline. Furthermore, the result of the mass spectral analysis of 179.0381 amu and 181.0342 amu correlated well with the expected mass of 179.0376 amu and 181.0348 amu.

189

Chapter 4 – Adsorption into the primary adsorption site

_____

Finally, with the desired small molecular fractions obtained, the NP40 BHIC$_{50}$ activities could be determined. Thereby, structure-activity relationships for the adsorption of these small molecules into the primary adsorption site, could be evaluated.

4.1.5 Investigating structure-activity relationships for the small molecular scaffolds

Upon determining the NP40 BHIC$_{50}$ activities of the small molecular scaffolds, it is found that these compounds were not all soluble in the buffer solution above a concentration of 180 mM. Furthermore, some of these compounds precipitated out during the 4 hour incubation period, at a temperature of 37 °C. Therefore, NP40 BHIC$_{50}$ activities were only determined for compounds that were soluble in the acetate buffer (Table 32).

Table 32: The calculated E$_{ads}$ for the adsorption onto face {001}, and determined NP40 BHIC$_{50}$ activity of the small molecular scaffolds, QC, and CQ.

Compound	scaffold	E$_{ads}$ (kcal.mol^{-1})		NP40 BHIC$_{50}$ (µM)	
S1	quinoline	-52.8	± 0.01	−	
S2	quinoline	-50.0	± 0.01	−	
S3	quinoline	-49.0	± 0.9	−	
S4	quinoline	-50.0	± 1.3	−	
S5	indole	-48.8	± 0.01	2351	± 138
S6	carbazole	-52.2	± 0.01	7216	± 3157
S9	benzo(b)-(1-5)napthyridine	-65.2	± 2.4	59.7	± 2.6
S11	quinoline	-49.4	± 0.5	100.3	± 2.0
S12	carbazole	-58.7	± 0.01	6806	± 631
S13	carbazole	-58.0	± 0.01	6125	± 877
QC	benzo(b)-(1-5)napthyridine	-75.1	± 0.01	6.28	± 0.5
CQ	quinoline	-67.0	± 0.01	31.5	± 2.0

[*]*The small molecular fractions are present in the neutral speciation form, and compound **S11**, **QC** and CQ, are present in the diprotic form, at pH 4.8.*

For the determination of the NP40 $BHIC_{50}$ activities, compounds **S3**, **S6**, **S12** and **S13** were found to be inactive, with large standard deviations. Based on the molecular modelling results, it is expected that the larger carbazole structures would be more active. It is found not to be the case when comparing the activity of compound **S5** (indole) to that of compounds **S3**, **S12** and **S13** (carbazole). It might be that this inconsistent result is obtained due to the low solubility of these compounds in the buffer solution. Therefore, structure-activity relationships could not meaningfully be investigated for these compounds.

Both the two benzo-(b)(1-5)napthyridine compounds **S9** and QC are found to be active β-haematin inhibitors. However, even though these two compounds include the same benzo-(b)(1-5)napthyridine scaffold, these were found to adsorb differently into the primary adsorption site. Therefore, a direct structure-activity relationship could not be made.

The NP40 $BHIC_{50}$ activity of compound **S11** could be compared directly to that of CQ, as these two compounds include the same 7-chloroquinoline scaffold, and these two compounds preferred the same adsorbed geometry inside the primary adsorption site. Both these compounds are 100% diprotic at pH 4.8. Even though compound **S11** is considered as an active β-haematin inhibitor (NP40 $BHIC_{50}$ activity of 100.3 ± 2.0 μM), CQ exerts three times the inhibition capacity (NP40 $BHIC_{50}$ activity of 31.5 ± 2.0 μM). This again highlights that more than just the adsorption into the primary adsorption site should be considered for β-haematin inhibition, as adsorption does not only occur on the fastest growing crystal face.

With water molecules being present in solution, it is known to manually include these in the molecular modelling studies. Therefore, as suggested by Buller *et al.*(Section 1.4.2),[54] these could contribute in promoting hydrogen bonding interactions. It has been suggested that a

hydrogen bonding interaction forms between the amine in the side-chain and a water molecule, and then again between the same water molecule and a carbonyl group on the crystal surface (secondary adsorption site). However, for the purposes of this project, the manual alteration of the final molecular modelling results is not encouraged, as this would affect the final calculated E_{ads} values that are used in evaluating structure-activity relationships.

By performing this adsorption study, a noteworthy structure-activity relationship is found. With a determined NP40 BHIC$_{50}$ activity of 6.28 ± 0.5 µM, QC is a significantly more potent β-haematin inhibitor than CQ, $(31.5 \pm 2.0$ µM). Moreover, considering that QC and CQ have the same side-chain, the contribution of a larger molecular scaffold for the adsorption into the primary adsorption site, is demonstrated. The benzo-(b)(1-5)napthyridine scaffold of QC is able to form more π-π interactions to the porphyrin structure inside the primary adsorption site than observed for the quinoline scaffold of CQ. It therefore seems reasonable that this additional intermolecular π-π interactions result in an improved β-haematin growth inhibition.

Therefore, it is concluded that larger molecular structures, that are able to form an increased number of π-π interactions in the primary adsorption site, would be ideal for developing novel and more potent β-haematin inhibitors.

4.2 INVESTIGATING LINEAR MOLECULES THAT ADSORB INTO TWO NEIGHBOURING PRIMARY ADSORPTION SITES

4.2.1 The larger bis-quinoline compounds investigated

In Chapter 3 it is found that many of the larger non-quinoline inhibitors preferred adsorption geometries where two neighbouring primary adsorption sites were occupied. By combining the information obtained from the previous adsorption studies, new molecules could be designed with the purpose of improved adsorption into the two primary adsorption sites.

However, with the focus of this project being on investigating the adsorption of β-haematin inhibitors onto β-haematin and evaluating structure-activity relationships, it was considered preferable to evaluate the adsorption of compounds of which the structure-activity relationships would contribute towards a greater understanding of the manner in which inhibitors adsorb into the primary adsorption site. The information obtained could then later be used to design active β-haematin inhibitors with the desired pharmacokinetics ADME properties (adsorption, digestion, metabolism, and excretion), as potential antimalarial drug candidates.

As mentioned before, a favoured adsorption is obtained when an inhibitor is able to adsorb into both the primary and secondary adsorption sites on face {001}, as seen for QN and QD. However, this forms part of another PhD project, and therefore this adsorption geometry would not be discussed in this project.

With compounds **KW5** and **FL2** showing the most favoured adsorption geometries for the adsorption into two neighbouring primary adsorption sites (Figure 85), similar compounds could be considered where these could be varied in length to optimise the adsorption

geometry. These results would strengthen the argument that a more favoured adsorption and thus an increased β-haematin inhibition activity is obtained when a compound is able to adsorb into two neighbouring primary adsorption sites.
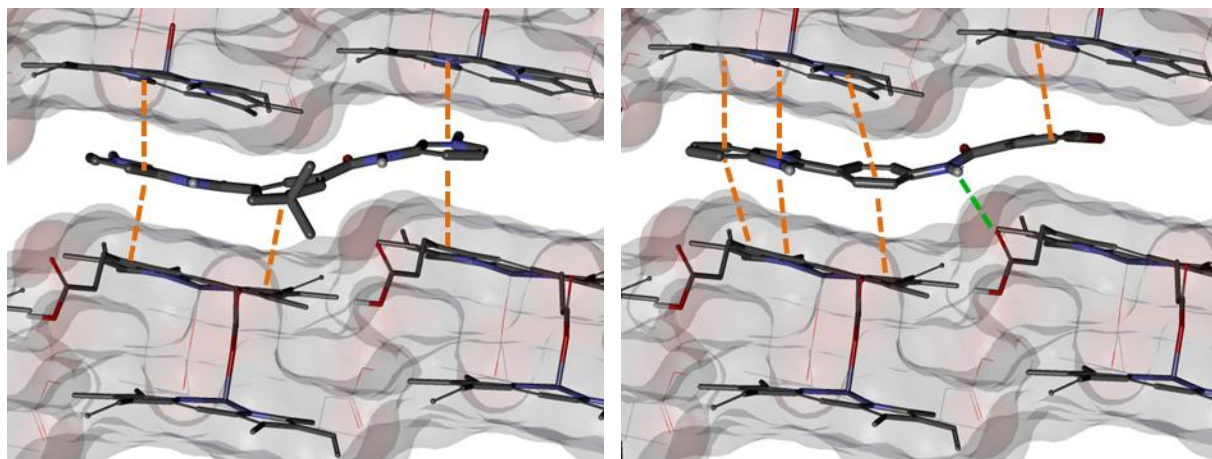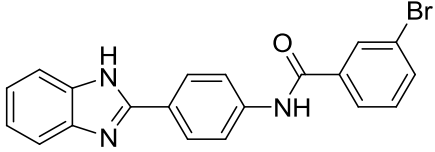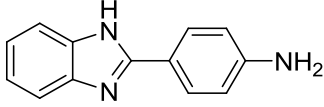
Figure 85: The adsorption of compound KW5 (left) and FL2 (right) in the crevice on face {001}.

*The adsorption of compound **KW5** (left) in the diprotic form, and compound **FL2** (right) in the monoprotic form onto face {001}, as viewed perpendicular to the crystal face, is shown. Hydrogen bonding interactions are indicated by ▪ ▪ , and π-π interactions are indicated by ▪ ▪ .*

For instance, by cleaving compound **FL2** at the amide nitrogen to obtain compound **RM1**, a smaller molecule would be obtained, which might result in a less favoured adsorption geometry, as only one primary adsorption site would be occupied (Table 33). Similarly, by replacing the phenyl ring with a quinoline moiety to obtain compound **RM2**, a more favoured adsorption geometry is expected, since an increased number of π-π interactions would form between the aromatic rings and the porphyrin structure on the crystal surface.
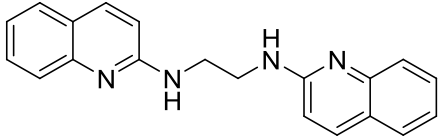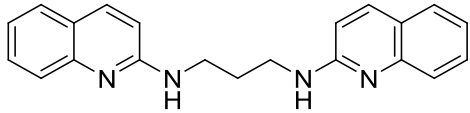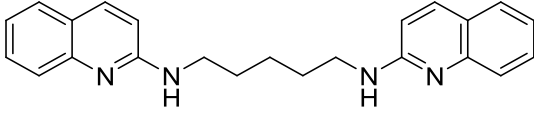
Table 33: Comparing the chemical structures of compounds RM1 and RM2 to that of FL2.

Compound	Chemical structure
FL2	
RM1	
RM2	

Alternatively, the length of the molecule could be altered systematically by forming a bis-quinoline compound with a linear chain in between, as seen for compounds **RM3 - RM5** (Table 34). The molecules would be able to extend into only one, and finally into two primary adsorption sites, where it could be lengthened even more until the molecule is too large to fit into two neighbouring primary adsorption sites.

Table 34: The chemical structures of compounds RM3 - RM5

Compound	Chemical structure
RM3	
RM4	
RM5	

Unfortunately, the linear alkyl chains could also rotate into non-linear conformations, which would affect the final adsorption geometries. Therefore, the adsorption of more rigid structures was rather evaluated in this study.

Moreover, with the growing malaria resistance against quinoline drugs (Section 1.3.2.1), indole scaffolds were also considered. It was suggested that an ester functional group could be utilised to connect the bis-indoles together (Table 35). However, when the adsorption of compounds **RM6** and **RM7** into the crevice was evaluated, the amide functional group is preferred, since the amide N-H forms a hydrogen bonding interaction to a carbonyl group on the crystal surface, as seen for **FL2** in Figure 85. Also, the amide functional group would improve the water-solubility of the compound, which is an essential property needed to determine the NP40 BHIC$_{50}$ activity.

The location of the amide functional groups in the molecules could also be varied (Table 35). However, when comparing the adsorption of compounds **RM7** and **RM8**, a more favoured adsorbed geometry is obtained for compound **RM7**, where the formation of the preferred hydrogen bonding interaction was consistently seen in the results of three consecutive simulations that were performed. The modelling results were found to be less consistent for the adsorption of compound **RM8** onto face {001}.

Table 35: The chemical structures of compounds RM6 - RM22

Compound	Chemical structure
RM6	
RM7	
RM8	

In an attempt to synthesise compound **RM7**, it was realised that the 2,6-dichloroindole intermediate needed for the synthesis of the indole compounds, is unstable (Scheme 16). The preparation of this intermediate was attained by treating 6-chloroindolin-2-one with phosphorus oxychloride. However, upon purification, as well as in an attempt to stabilise the compound by introducing a *tert*-butyloxycarbonyl (Boc) protecting group on the indole nitrogen atom under mild reaction conditions, the compound decomposed and was therefore not isolated.

Scheme 16
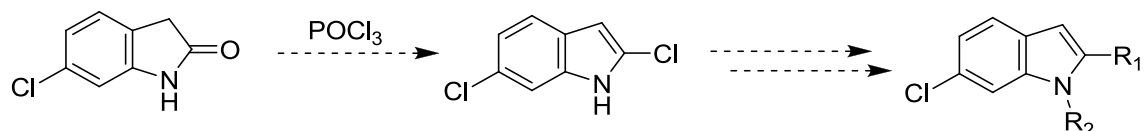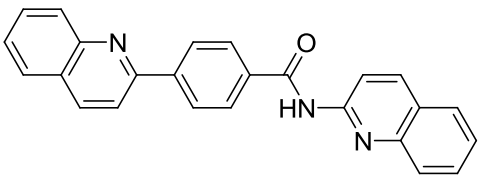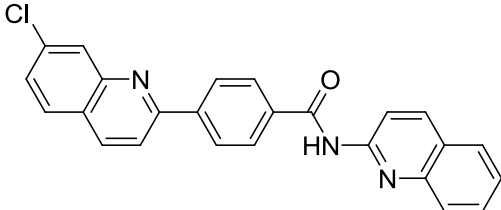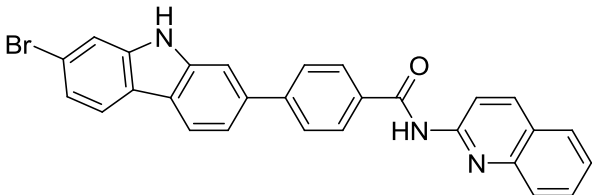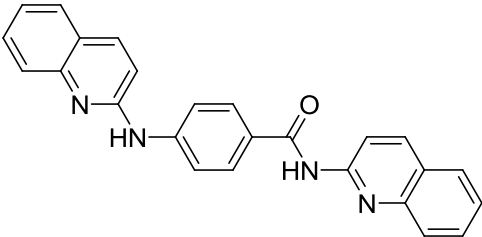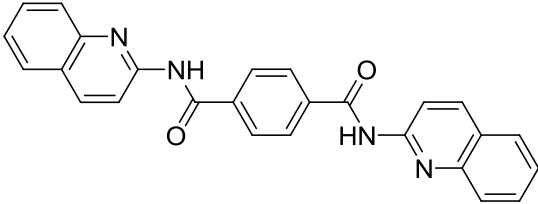
R_1 = -Cl, -NH$_2$, or Phenyl
R_2 = Boc, or -H

_____

Therefore, owing to the fact that quinoline drugs are known for their ability to act as β-haematin inhibitors and are still widely used in ACT treatments to combat malaria, as well as with the persisted activity of bis-quinoline compounds against CQ-resistant strains (Section 1.3.3), the synthesis of quinoline compounds was rather pursued in the remainder of this study (Table 36).

Table 36: The chemical structures, and the speciation of compounds RM9 - RM13 at pH 4.8.

Compound	Chemical structure	% Monoprotic	% Neutral
RM9		–	100
RM10		–	100
RM11		–	100
RM12		45	55
RM13		–	100

198

_____

It is considered that compound **RM9** would occupy the two neighbouring primary adsorption sites in a similar geometry as compound **FL2**. Therefore, a chlorine atom could be introduced in the 7-position of the quinoline to obtain compound **RM10**, where a carbazole, being commercially available, could be introduced (**RM11**) in order to evaluate the adsorption of a larger aromatic ring system.

Furthermore, by introducing different functional groups between the two quinoline scaffolds (compounds **RM12** and **RM13**), the quinoline rings would be extended further apart. For these, more flexible molecules would be obtained, which might contribute to a more favourable adsorption geometry. When evaluating the two lowest energy conformations of compound **RM12** and **RM13**, the conformations on the right in Figure 86 were found to be the absolute minimum energy conformations. Therefore, the adsorption of these conformations onto face {001} was evaluated.

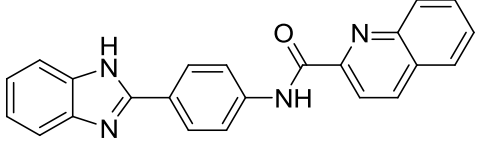Also, in order to evaluate whether it is truly beneficial for a molecule to adsorb into both neighbouring primary adsorption sites, the adsorption of smaller molecules onto face {001} could also be considered (Table 37).
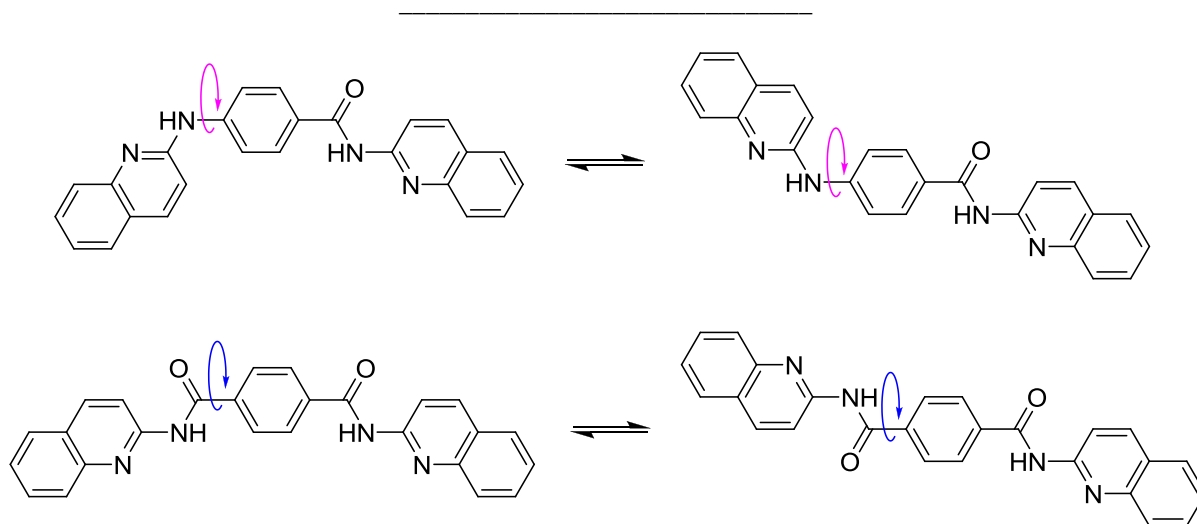
Figure 86: Lowest energy conformations of compounds RM12 and RM13

*The two lowest energy conformations of compounds **RM12** (top) and **RM13** (bottom) are shown, where those on the right are found to be the absolute minimum energy conformations.*

Table 37: The chemical structures and the protic forms at pH 4.8, of compounds RM14-16

Compound	Chemical structure	% Diprotic	% Neutral
RM14		0	100
RM15		0	100
RM16		100	0

200

When evaluating the chemical structure of the bis-quinoline **RM9**, it is possible that by only having a phenyl ring on the one end (compound **RM14**), a less favoured adsorption into the crevice would be obtained, since the formation of fewer π-π interactions between the inhibitor and the porphyrin structure in the second primary adsorption site is expected. Similarly, this phenyl ring could be removed to evaluate the adsorption of the smaller compound **RM15**. Compound **RM16** would only be able to occupy one primary adsorption site.

Therefore, by evaluating the adsorption and structure-activity relationships of these compounds, it was reasoned that a greater understanding would be obtained as to whether a more favoured adsorption is gained when an inhibitor is able to adsorb into two primary adsorption sites.

4.2.2 Adsorption of the bis-quinoline compounds onto face {001}

Interestingly, the quinoline compounds preferred adsorption geometries where either the compounds adsorbed entirely into the two neighbouring primary adsorption sites where no hydrogen bonding interaction is formed, or the lengthier compounds were not able to adsorb entirely into the two neighbouring primary adsorption sites, where the formation of hydrogen bonding interaction between the amide N-H and a carbonyl group on the crystal surface is found.

Compounds **RM10** and **RM12** had the most favoured adsorption geometries, where these molecules were able to fully occupy two neighbouring primary adsorption sites (Figure 87). The quinoline moieties on both ends of the molecules formed π-π interactions to the

porphyrin structures in both primary adsorption sites. However, for both of these compounds, the formation of hydrogen bonding interactions is not observed.
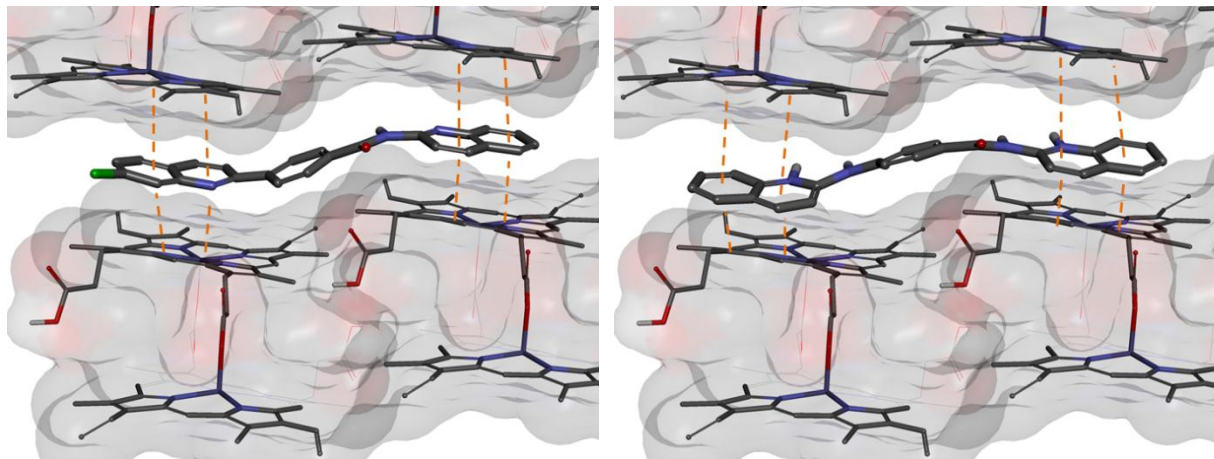
Figure 87: Adsorption of compounds RM10 and RM12 onto face {001}

*The adsorption of compounds **RM10** (left)in the neutral form and **RM12** (right) in the monoprotic form onto face {001}, as viewed from above, is shown. The π-π interactions are indicated by ▪ ▪ .*

When evaluating the adsorbed geometries of the smaller compounds **RM14**-**16**, it is found that these were able to form fewer π-π interactions in the crevice (Figure 88). Compound **RM16** only occupied one primary adsorption site, where both compounds **RM14** and **RM15** were able to extend into the second primary adsorption site. Even though the quinoline moiety of compound **RM15** adsorbed in the left corner of the primary adsorption site, and the quinoline moiety of compound **RM14** adsorbed in the right corner of the primary adsorption site, these two adsorption geometries are considered comparable. For example, by rotating the quinoline moiety of compound **RM15**, it could also have adsorbed in the right corner, where the same intermolecular interactions would form between the inhibitor and the crystal surface. What is however significant, is the increased number of intermolecular interactions

formed between the additional phenyl ring of compound **RM14**. Moreover, when evaluating the adsorbed geometry of both compounds **RM14** and **RM15** more closely, additional alkyl-π (T-shape) interactions could form between the phenyl ring and alkyl groups in close proximity.

It has been reported that dispersion effects have the greatest contribution in promoting these alkyl-π interactions, where the alkyl hydrogen atom acts as a weak hydrogen bond donor.[168] By performing DFT calculations, it has been demonstrated that the optimum calculated interaction distance is between 4.8 and 5.0 Å, when the alkyl C-H bond is perpendicular to the aromatic ring.[168]

The measured alkyl-π interaction distances between compound **RM15** and the porphyrin structure are between 3.5 and 4.2 Å. These are less favoured interaction distances, and the interactions between the alkyl C-H bond and the benzene ring do not occur at right angles (75-80°). Therefore, from a computational perspective, it is considered that these interactions do not contribute significantly to a more favoured adsorption geometry.

Based on the number of intermolecular interactions formed, the adsorbed geometry of compound **RM14** is considered more ideal, followed by that of compound **RM15**. Compound **RM16** is considered to have the least favoured adsorbed geometry, since it is only able to occupy one primary adsorption site.

(a)

(b)

(c)
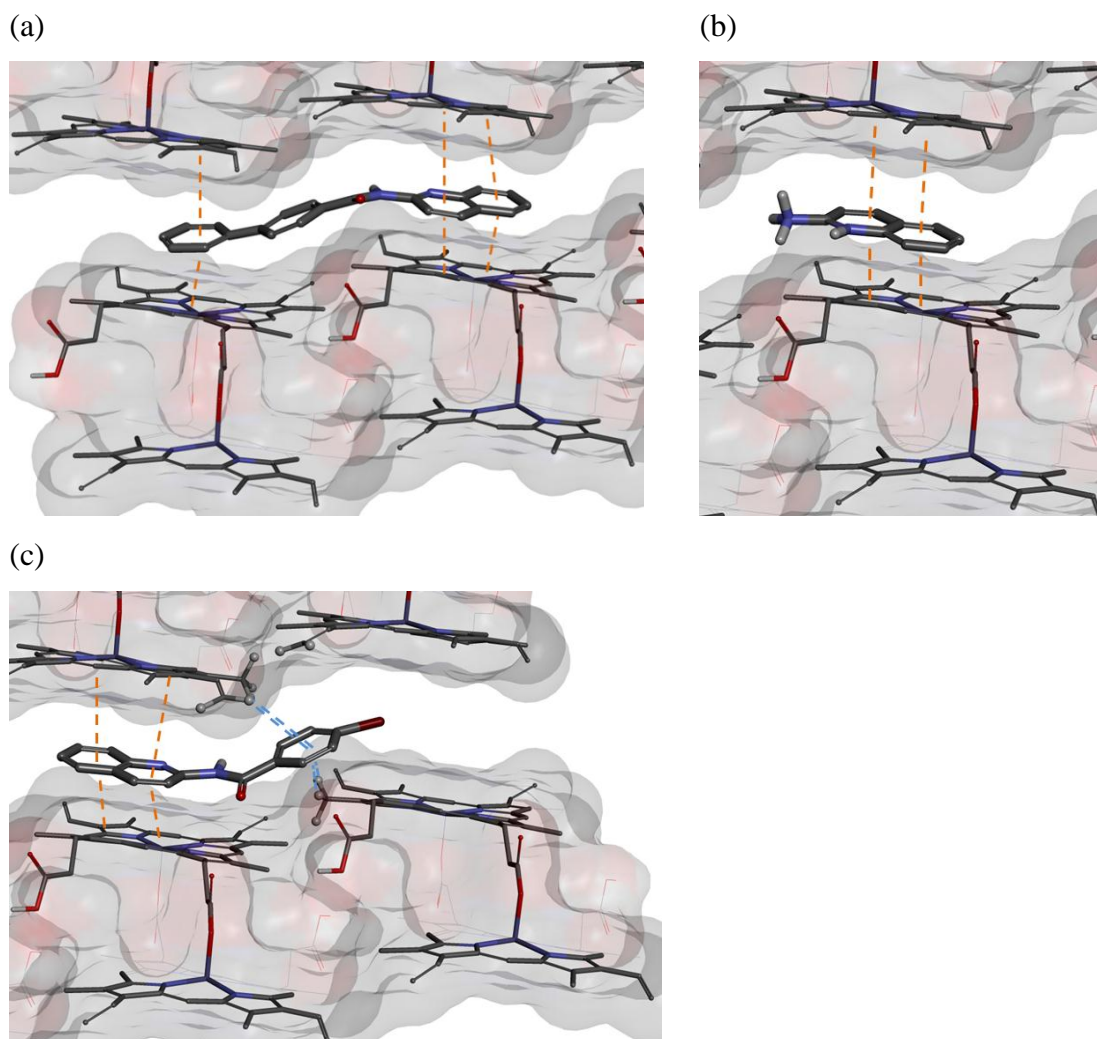
Figure 88: Adsorption of compounds RM14-16 onto face {001}

*The adsorption of compounds **RM14** (a) and **RM15** (c) in the neutral form, and **RM16** (b) in the diprotic form onto face {001}, as viewed from above, is shown. The π-π interactions are indicated by* ▪ ▪*, and are measured to be between 3.5 and 3.8 Å. The alkyl-π interactions are indicated by* ▪ ▪ *, and are measured to be between 3.5 and 4.2 Å. The hydrogen atoms involved in these interactions are indicated as grey balls.*

It is found that the larger compounds **RM11** and **RM13** are too long to adsorb into both primary adsorption sites, and a hydrogen bonding interaction between the amide N-H and the carbonyl group on the crystal surface is rather preferred. Consequently, adsorbed geometries are obtained where the molecules adsorb into both the primary and the secondary adsorption sites (Figure 89).

Compound **RM9** adsorbed in a similar manner as compounds **RM11** and **RM13** (Figure 90). It is possible that the chlorine atom in the 7-position of the second quinoline group of compound **RM10** promoted the adsorption into the second primary adsorption site.
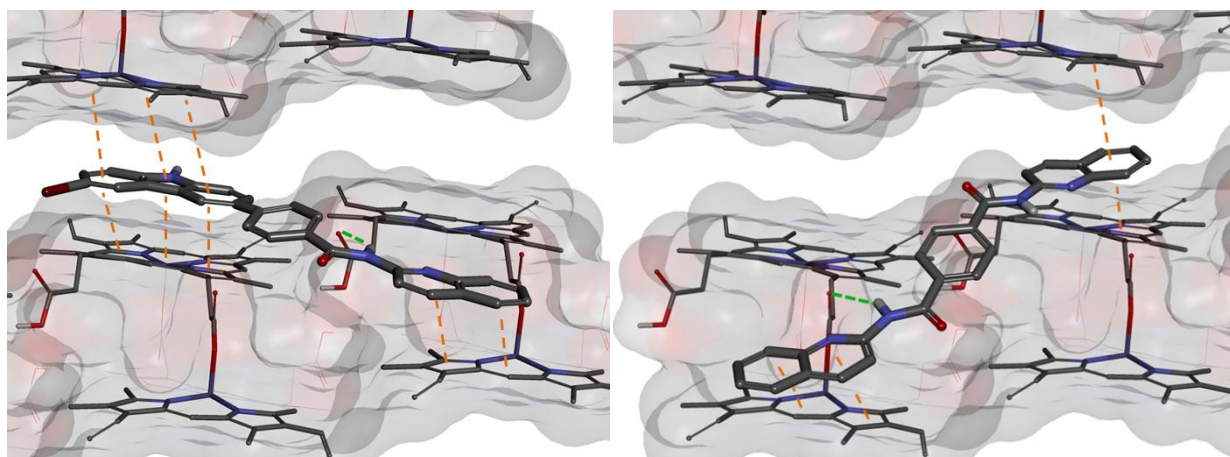
Figure 89: Adsorption of compounds RM11 and RM13 onto face {001}

*The adsorption of compounds **RM11** (left) and **RM13** (right) in the neutral form onto face {001}, is shown, as viewed from above. The hydrogen bonding interaction is indicated by ▪ ▪, and π-π interactions are indicated by ▪ ▪ , and are measured to be between 3.5 and 3.8 Å.*
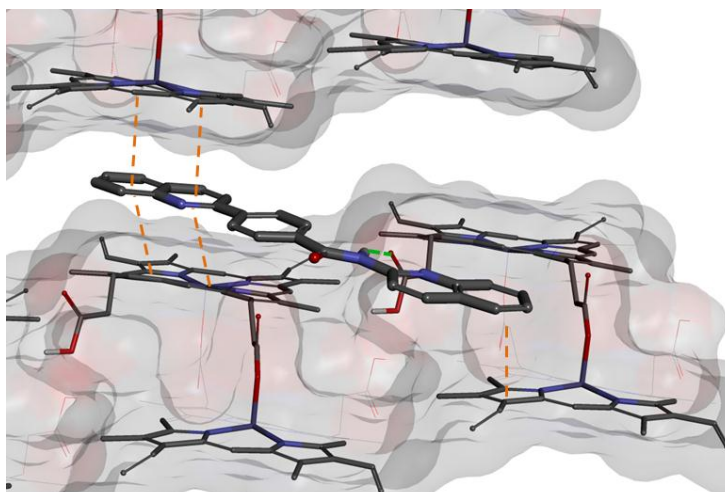
Figure 90: Adsorption of compound RM9 onto face {001}

*The adsorption of compound **RM9** in the neutral form onto face {001}, is shown, as viewed from above. The hydrogen bonding interaction is indicated by ■ ■, and π-π interactions are indicated by ■ ■ , and are measured to be between 3.5 and 3.8 Å.*

With these larger molecules (**RM9**, **RM11** and **RM13**) not being able to adsorb into the crevice, adsorption of these onto the second fastest growth face, face {011}, was also evaluated. Interestingly, for the adsorption of compound **RM11**, a more favoured E_{ads} value was calculated for the adsorption onto face {011} than for the adsorption onto face {001} (Figure 91, Table 38).

Table 38: E_{ads} values for the adsorption of compound RM11 onto face {001} and face {011}

	E_{ads} face {001} (kcal.mol^{-1})	E_{ads} face {011} (kcal.mol^{-1})
RM11	-76.5 ± 0.02	-80.0 ± 0.001

_____
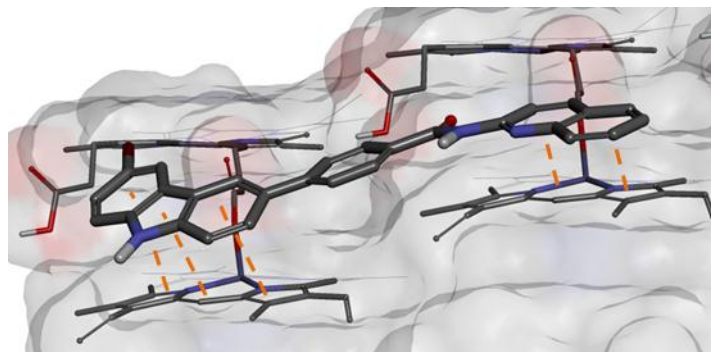
Figure 91: Adsorption of compound RM11 onto face {011}

*The adsorption of compound **RM11** in the neutral form onto face {011}, is shown, as viewed from above.*

The π-π interactions are indicated by ▪ ▪ *, and are measured to be between 3.5 and 3.8 Å.*

For the adsorption of the larger molecules onto face {011}, adsorption geometries were preferred where additional interactions formed between the inhibitor and the secondary adsorption site on the crystal surface. These additional interactions would contribute to an enhanced adsorption, and may therefore contribute to an improved NP40 $BHIC_{50}$ activity. Since a more favoured adsorption is found for compound **RM11** onto face {011} for example, it provides an opportunity to determine the relationship, if any, between adsorption and an overall improved NP40 $BHIC_{50}$ activity.

Therefore, with these larger compounds showing more favoured intermolecular interactions outside of the crevice, and also for the adsorption onto face {011}, these could not be used to evaluate adsorption into the two neighbouring primary adsorption sites on face {001}.

It is therefore concluded that the smaller compounds **RM10, RM12**, and **RM14-16** could be used to determine structure-activity relationships for the adsorption into two neighbouring primary adsorption sites. By this means, the ability of this adsorption protocol to predict the

_____

activity of β-haematin inhibitors for the adsorption into two neighbouring primary adsorption sites, could be assessed.

4.2.3 Towards the synthesis of the bis-quinoline compounds

Yang *et al.* reported an Ullmann-type synthetic procedure for a one-pot copper-catalysed oxidative amination of aldehydes from 2-aminopyridines.[169] Various reaction conditions were considered, where the optimum yield is obtained by using air or oxygen gas as an oxidant in the presence of 10 mol % copper iodide. This was heated to 80 °C in *N,N*-dimethylformamide for 24 hours. A reaction mechanism is proposed (Scheme 17), where the copper coordinates with the pyridine nitrogen and the aldehyde oxygen, thereby bringing the carbonyl bond in close proximity to the amine. The amine is able to act as a nucleophile and attack the carbonyl group to form the hemiaminal, which is subsequently oxidised to form the amide product.

Chapter 4 – Adsorption into the primary adsorption site

_____
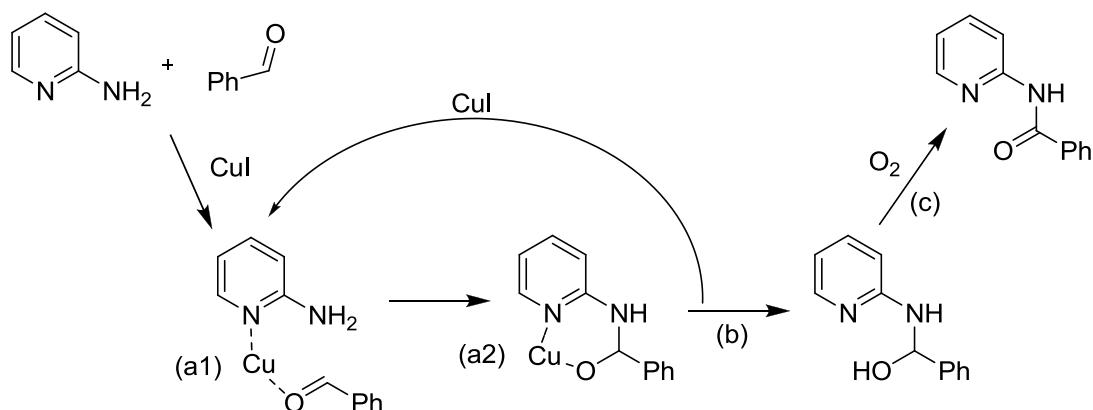
Scheme 17

The reaction mechanism proposed by Yang et al. for the copper-catalysed oxidative amination, is shown.[169] *The*

copper-coordinates to the pyridine nitrogen and the carbonyl oxygen (a1-2), which results in the formation of

the hemiaminal (b). Finally, this is then oxidised (c) to form the desired product.

By using this Ullmann-type coupling procedure, an inconvenient acylation reaction could be avoided, and a coupling reaction could be performed directly between the aldehyde and the amine to achieve the formation of an amide.

For this synthetic endeavour, the amine could be introduced in the 2-position of the quinoline by performing an Ullmann coupling reaction. This could be achieved by treating the 2-bromoquinoline **15** with ammonium hydroxide at high temperatures to afford the 2-aminoquinoline **RM16** in one reaction (Scheme 18).

Scheme 18
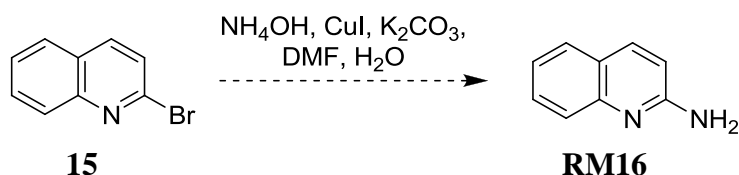
Compounds **RM10** and **RM14** could be synthesised by performing a Suzuki coupling to obtain the intermediate aldehyde compounds, where after the Ullmann-type coupling could be performed to obtain the desired amides (Scheme 19).

Scheme 19
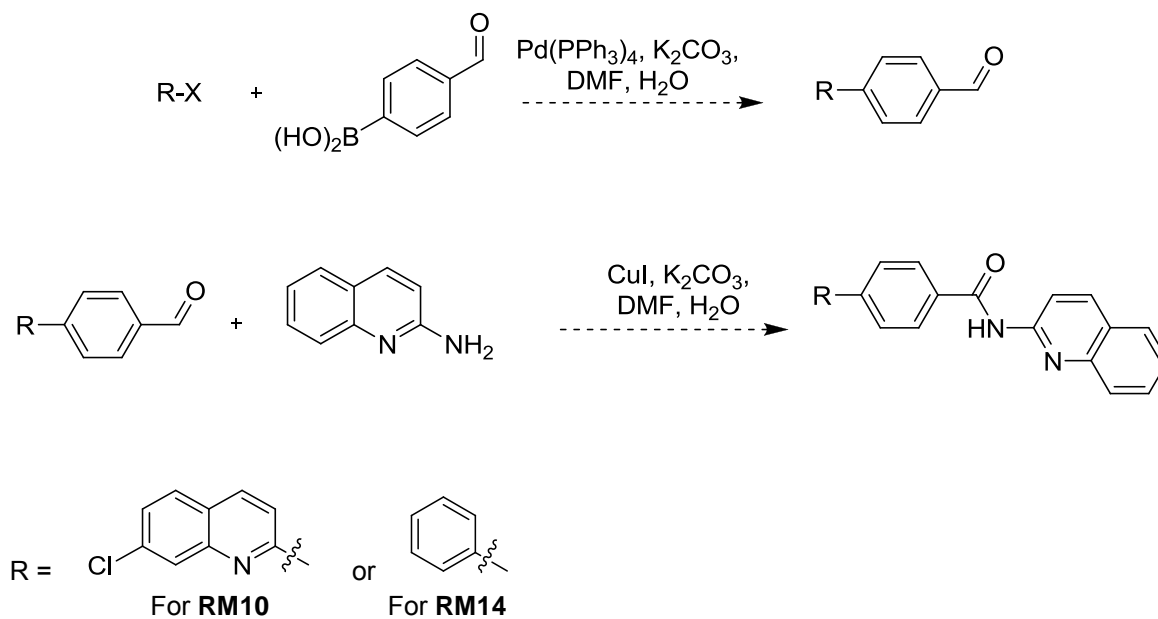
By performing the Ullmann-type coupling between compound **16** and **RM16**, in the presence of atmospheric oxygen, only compound **RM15** would be obtained (Scheme 20).

Therefore, for the synthesis of compound **RM12**, a one-pot reaction could be considered, where an amination reaction and an Ullmann-type coupling could be performed (Scheme 20). By maintaining the reaction mixture under a positive pressure of nitrogen gas, only the amination reaction would proceed. Once the reaction mixture is exposed to atmospheric oxygen, the Ullmann-type coupling would commence to form the amide.

Scheme 20
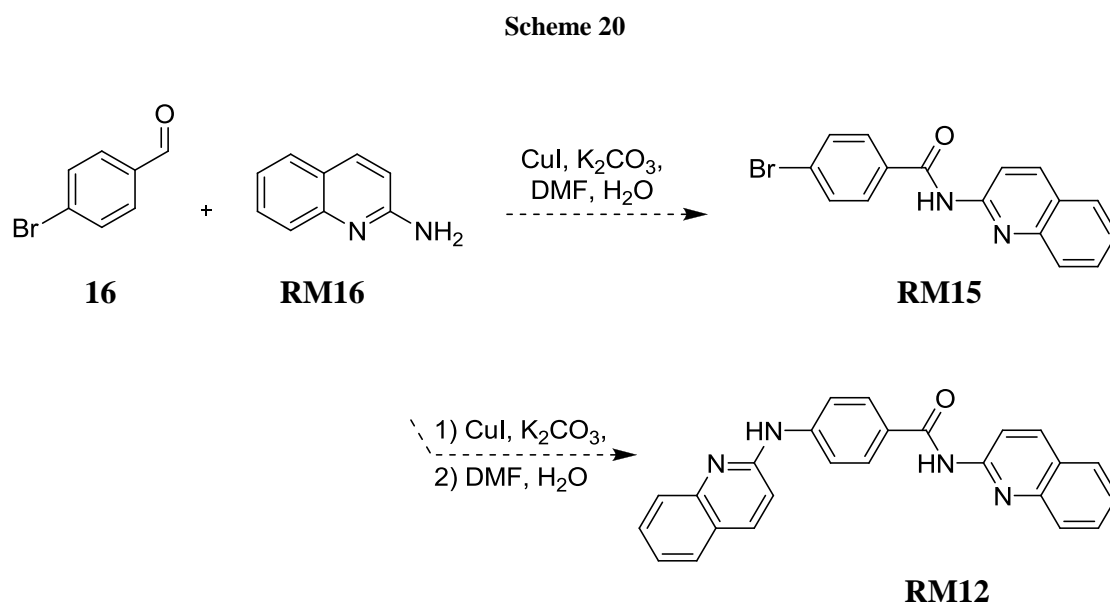
With the synthetic strategy outlined, the target molecules could be synthesised in order to determine the NP40 $BHIC_{50}$ activities thereof, and to evaluate structure-activity relationships.

4.2.4 Synthesis of the bis-quinoline compounds

4.2.4.1 Synthesis pertaining to 2-aminoquinoline - RM16

4.2.4.1.1 Attempted synthesis of 2-aminoquinoline - RM16

Compound **RM16** could be synthesised by means of a Ullmann coupling upon exposing compound **15** to ammonium hydroxide at high temperatures, with copper iodide acting as a catalyst (Scheme 21).

Scheme 21
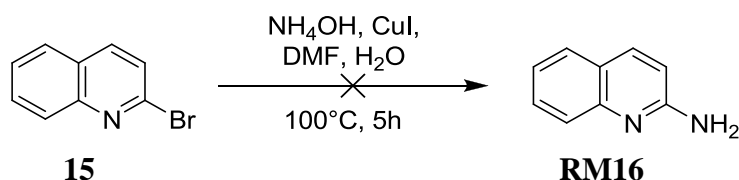
In proceeding with the synthesis of compound **RM16**, compound **15** was dissolved in *N*,*N*-dimethylformamide, and an excess amount of ammonium hydroxide, 0.5 mL water, and copper iodide was added. This reaction mixture was refluxed for 5 hours, until the full consumption of the starting material was attained.

Unfortunately, after quenching the reaction mixture on ice and by neutralising it with 2M hydrochloric acid, the desired product was not extracted with ethyl acetate. It is probable that the product **RM16** is water-soluble.

Another synthetic route was rather considered where the product could be formed in the absence of water. With the formation of an azide intermediate **17** from **16**, it could be reduced in the presence of hydrogen gas in order to obtain the desired product **RM16** (Scheme 22).

_____

Scheme 22

16   **17**   **RM16**
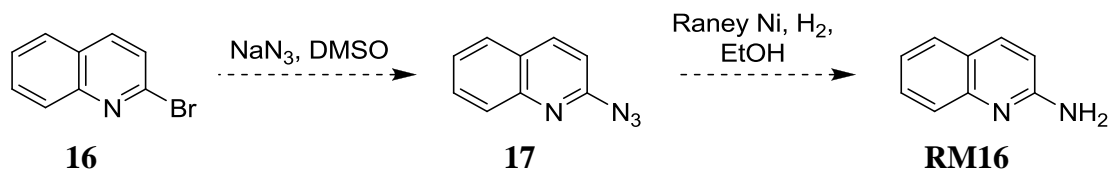
4.2.4.1.2 Synthesis of 2-azidoquinoline - 17

Compound **17** was synthesised from **16** in the presence of sodium azide (Scheme 23).[165] The starting reagent **16** was dissolved in dimethyl sulfoxide. Sodium azide was added, which only dissolved in the solvent upon heating the reaction mixture above 80 °C. However, at this temperature, the reaction did not proceed, and the reaction mixture was heated to 100 °C for two days.

Scheme 23
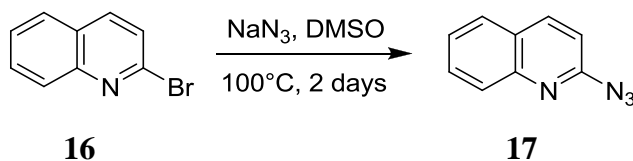
16   **17**

Upon completion, the reaction mixture was quenched with water and the product was extracted with ethyl acetate. Finally, upon purification by means of column chromatography, the desired product **17** was obtained in a decent 75% yield.
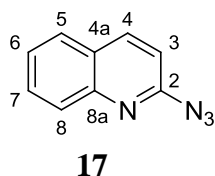
17

The presence of the azide moiety was established by a N_3 stretch at 2250 cm^{-1} in the infrared spectrum. Moreover, the result of the mass spectral analysis of 171.0652 amu correlated well with the expected mass of 171.0671 amu.

213

4.2.4.1.2 Synthesis of 2-aminoquinoline - RM16

Compound **RM16** was finally synthesised by the reduction of **17** with freshly prepared Raney[®]-Nickel under a positive pressure of hydrogen gas (Scheme 24). The Staudinger reaction was also attempted for the reduction of the azide in the presence of triphenylphosphine, however the reaction did not proceed to completion. Therefore, the above mentioned method was rather preferred.

Scheme 24

17   **RM16**
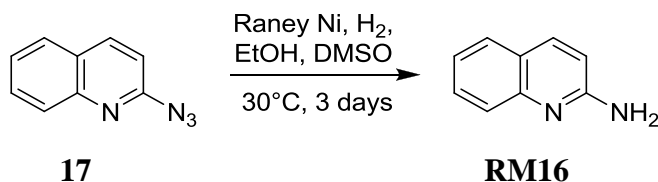
Compound **17** was dissolved in a small amount of dimethyl sulphoxide and dry ethanol, whereupon a spatula scoop (approximately 5 mL) of freshly prepared Raney[®]-Nickel was added twice a day over a period of three days. The reaction was kept at 30 °C and under a positive pressure of nitrogen in order to ensure the protonation of the nitrogen in the 2-position of the quinoline.

After full consumption of the starting reagent, the reaction mixture was filtered through celite, whereupon the filtrate was washed with ethyl acetate. The solvent was removed *in vacuo*, whereupon the product was isolated by means of column chromatography, in a high yield of 94%.
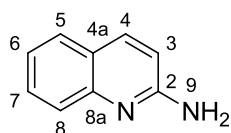
RM16

In the obtained ^{1}H NMR spectrum, a singlet, integrating for 2 protons at 6.41 ppm, was indicative of the secondary amine H_9. Furthermore, a peak at 158.22 ppm for C_2 is found in the ^{13}C NMR spectra.

With the successful synthesis of compound **RM16**, it was used to synthesise the other target compounds.

4.2.4.2 Synthesis pertaining to compound RM14

For the synthesis of the target molecules, it was deemed best to first synthesise the aldehyde intermediate **19**, as this compound could be synthesised from commercially available reagents in one reaction step. This could then be used to evaluate and optimise the reaction conditions required for the Ullman-type coupling reaction, in order obtain the desired amide product **RM14**. These optimised reaction conditions could then be applied to synthesise the other remaining target compounds.

4.2.4.2.1 Synthesis of biphenyl-4-carbaldehyde - 19

Compound **19** was synthesised from commercially available **15** and **18** by means of a Suzuki coupling reaction (Scheme 25).

Scheme 25

215
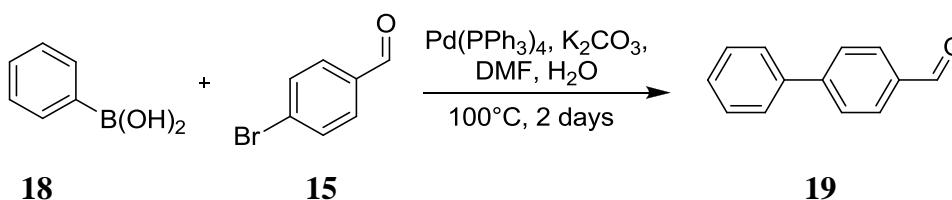
The starting reagent **15** and the boronic acid **18** were dissolved in *N,N*-dimethylformamide, whereupon a small amount of water and potassium carbonate were added. The reaction mixture was refluxed for 10 minutes at 100 °C under a positive pressure of nitrogen, where after the air and light sensitive palladium catalyst was added.

The reaction did not proceed to completion, and was quenched after 2 days with water. The product was extracted with ethyl acetate and finally purified by means of column chromatography to obtain the desired product in a reasonable 59% yield.
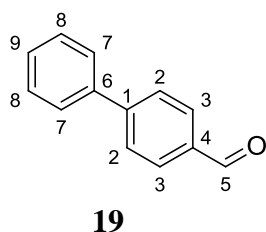
The presence of the aldehyde was confirmed by a doublet integrating for 1 at 10.06 ppm in the ^{1}H NMR spectrum for H_5 and peak at 192.06 ppm for C_5 in the ^{13}C NMR spectrum was observed. The aromatic signals integrated for 9 protons, which was indicative of the presence of both aromatic rings.

4.2.4.2.2 Synthesis of N-(quinolin-2-yl) biphenyl-4-carboxamide - RM14

Upon performing the Ullmann-type coupling reaction, compound **RM14** was synthesised from **RM16** and **19** under mild reaction conditions (Scheme 26).[169]

Scheme 26

216
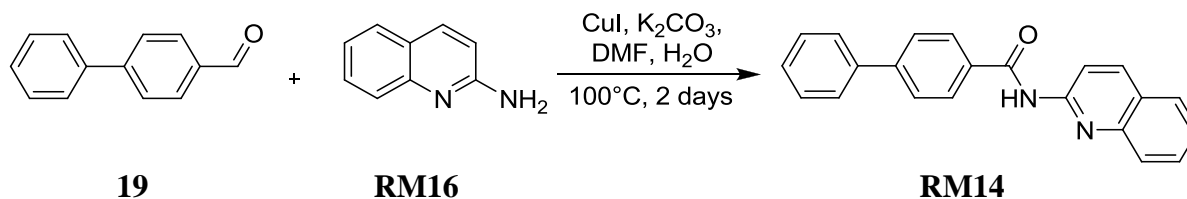
The two starting reagents **RM16** and **19** were dissolved in *N,N*-dimethylformamide, whereupon the base in a trace amount of water, and copper iodide were added. The reaction mixture was heated to 100 °C for a period of two days.

Finally, the reaction was quenched with water and the product was extracted with ethyl acetate. Upon purification by means of column chromatography, the product was isolated in a low 32% yield.

Unfortunately, the reaction did not proceed to completion, and by allowing the reaction to reflux for a longer period of time, or by adding more reagents, a higher yield was not achieved.
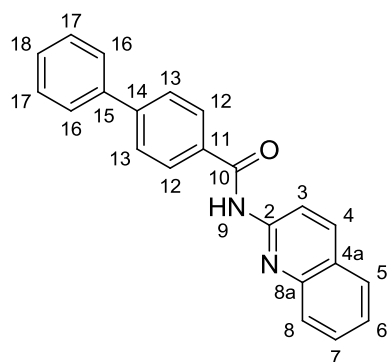
RM14

A singlet integrating for 1 at 11.15 ppm in the ^{1}H NMR for H_9, together with the peaks at 166.11 and 151.91 ppm for C_{10} and C_2 respectively, is indicative of the formation of the amide group. Moreover, the result of the mass spectral analysis of 325.1357 amu correlated well with the expected mass of 325.1341 amu.

Having successfully performed the Ullman-type coupling between the aldehyde **19** and the amine **RM16** to form the amide product **RM14**, this reaction could be used for the synthesis of the remaining target compounds.

4.2.4.3 Synthesis pertaining to compound RM10

4.2.4.3.1 Attempted synthesis of 4-(7-chloroquinolin-2-yl)benzaldehyde - 21

With the successful synthesis of compound **19** and finally **RM14**, the synthesis of compound **21** from previously synthesised **S2** and commercially available boronic acid **20**, was attempted (Scheme 27).

Scheme 27
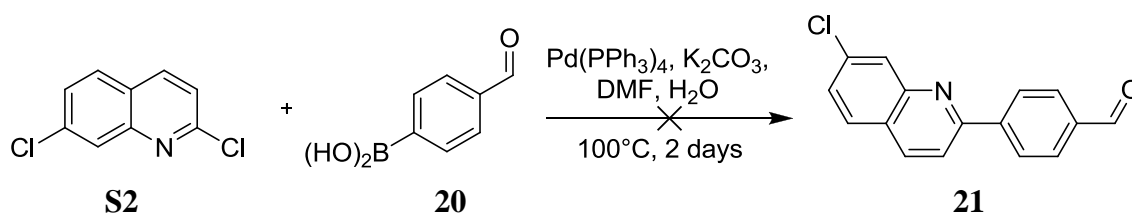
The same Suzuki coupling procedure for the synthesis of compound **19** from **15** and **18** was used, where the reaction mixture was allowed to reflux for two days until the full consumption of the starting material **S2** was obtained.

Unfortunately, the Suzuki coupling occurred at both the 2-position, as well as at the 7-position of the quinoline **S2**. This resulted in the formation of two inseparable products, which had the same R_f values (R_f = 0.50, 10% EtOAc/Hexane), in a low 5% yield.

21
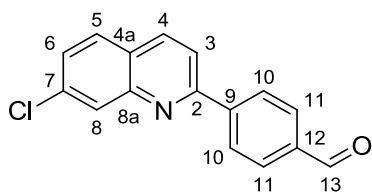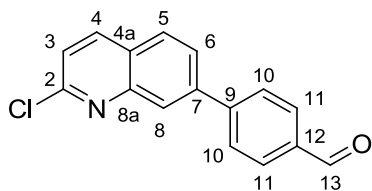
While it was not possible to unambiguously determine which compound (**21** or **22**) was favoured, the ^{1}H NMR spectrum showed a singlet integrating for 1 at 10.08 ppm, as well as a singlet integrating for 2 at 10.07 ppm. This indicated that a 1:2 mixture of two aldehyde compounds was obtained.

22

It is expected that the coupling reaction would have been preferred at the more reactive 2-position of the quinoline. However, this was not the case. The coupling reaction occurred on both ends of the quinoline **S2**.

Unfortunately, even by performing the coupling reaction at lower temperature (60 °C) or for a shorter time period, these methods still did not overcome the problem of separating the two products that were isolated, and once again, a low yield was obtained. Therefore, with compound **21** not being successfully isolated, the synthesis of compound **RM10** was not pursued.

4.2.4.4 Synthesis pertaining to compounds RM12 and RM15

4.2.4.4.1 Attempted synthesis of N-(quinolin-2-yl)-4-(quinolin-2-ylamino)benzamide -

RM12

and the synthesis of 4-bromo-N-(quinolin-2-yl)benzamide - RM15

A one-pot synthesis was attempted for the synthesis of compound **RM12** from **RM16** and **15** (Scheme 28). By performing the first part of the reaction under inert reaction conditions, the amine bond would be introduced between **RM16** and **15**, where in the presence of oxygen and a trace amount of water, the amide bond would be introduced between the amine of **RM16** and the aldehyde intermediate.

Scheme 28
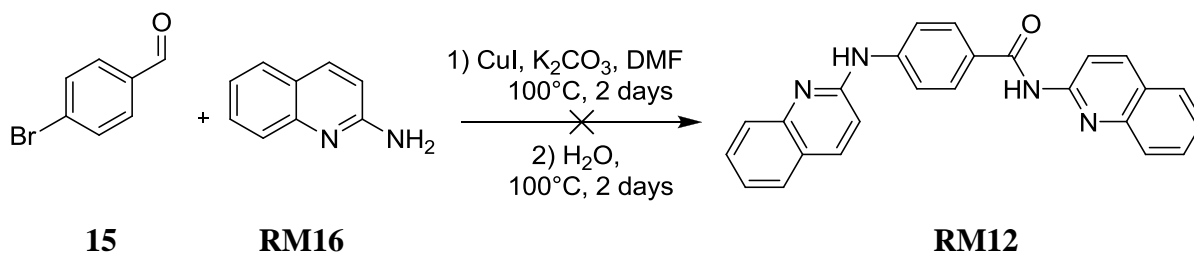
Therefore, **15** and **RM16** were dissolved in dry *N*,*N*-dimethylformamide. Copper iodide and base were added and the reaction was refluxed under a positive pressure of nitrogen gas at 100 °C. Unfortunately, after 2 days, the reaction did not proceed and only the starting reagents were present, as determined by means of thin layer chromatography. The reaction was gradually heated to 160 °C. Unfortunately, the amination reaction did not occur.

The reaction was repeated, open to atmospheric oxygen, whereupon a trace amount of water was added and the reaction was allowed to reflux for 2 days. Only the formation of product **RM15** was observed, as determined by means of thin layer chromatography (Scheme 29).

Scheme 29
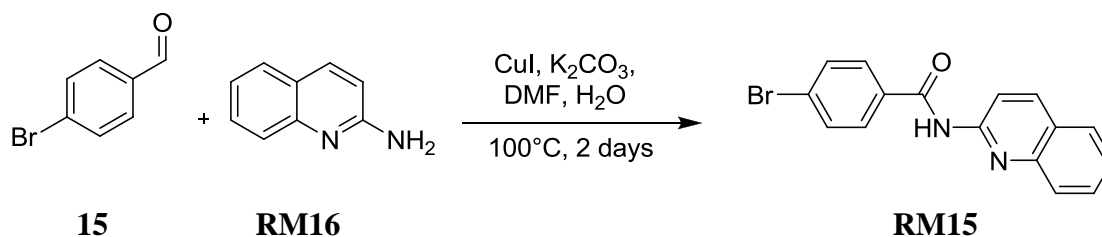
Unfortunately, the reaction did not proceed to completion, and the starting reagents remained in the reaction mixture. The reaction mixture was quenched with water and the product was extracted with ethyl acetate. Afterwards, product **RM15** was purified by means of column chromatography, upon which it was recovered in a low 19% yield.

RM15
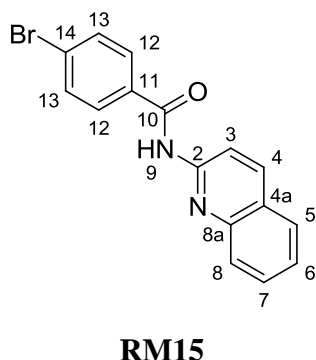
A singlet integrating for 1 at 11.23 ppm in the ^{1}H NMR for H$_9$, together with the peaks at 165.73 ppm for C$_{10}$, is indicative of the formation of the amide group. Moreover, the result of the mass spectral analysis of 327.0133 amu and 329.0116 amu correlated exactly with the expected mass of 327.0133 amu and 329.0114amu.

From these reactions (synthesis of **RM14** and **RM15**), it was apparent that the Ullmann-type coupling did not provide high yields when a 2-aminoquinoline **RM16** was used to form the amide bond, as opposed to 2-aminopyridines that were originally used by

221

Yang *et al.*[169] It is suspected that the 2-aminoquinoline was not a strong enough nucleophile to bring about the formation of the desired secondary amine for the formation of compound **RM12**.

Therefore, another synthesis approach was needed for the synthesis of these compounds, or different molecules had to be considered to evaluate the adsorption into the two neighbouring primary adsorption sites.

Peng *et al*. reported the formation of the amine bond at the 2-position of a quinoline by means of an amination reaction, thereby treating substituted amino benzene rings with 2-chloroquinoline.[170] In proceeding with this alternative approach to form the amine bond, the quinoline moiety needs to act as an electrophile and would require a halogen in the 2-position of the quinoline. However, in order to obtain compound **24**, an extremely expensive reagent, 4-aminobenzaldehyde **23**, is needed to act as the nucleophile (Scheme 30).

Scheme 30
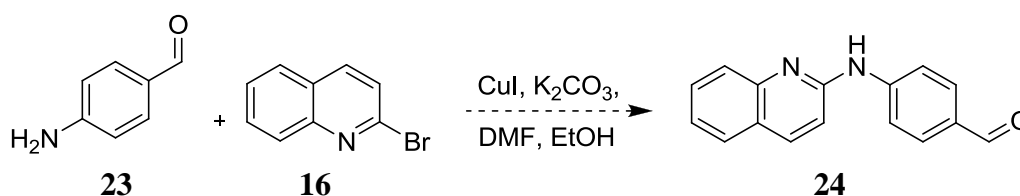
Another approach could be used, where 4-aminobenzoic acid **25** is rather used to form the amine bond of compound **26** (Scheme 31). The benzoic acid **26** could be treated with thionyl chloride to obtain the acid chloride **27**, which could again be reacted with 2-aminoquinoline **RM16** to obtain the desired final product **RM12**.

_____

Scheme 31
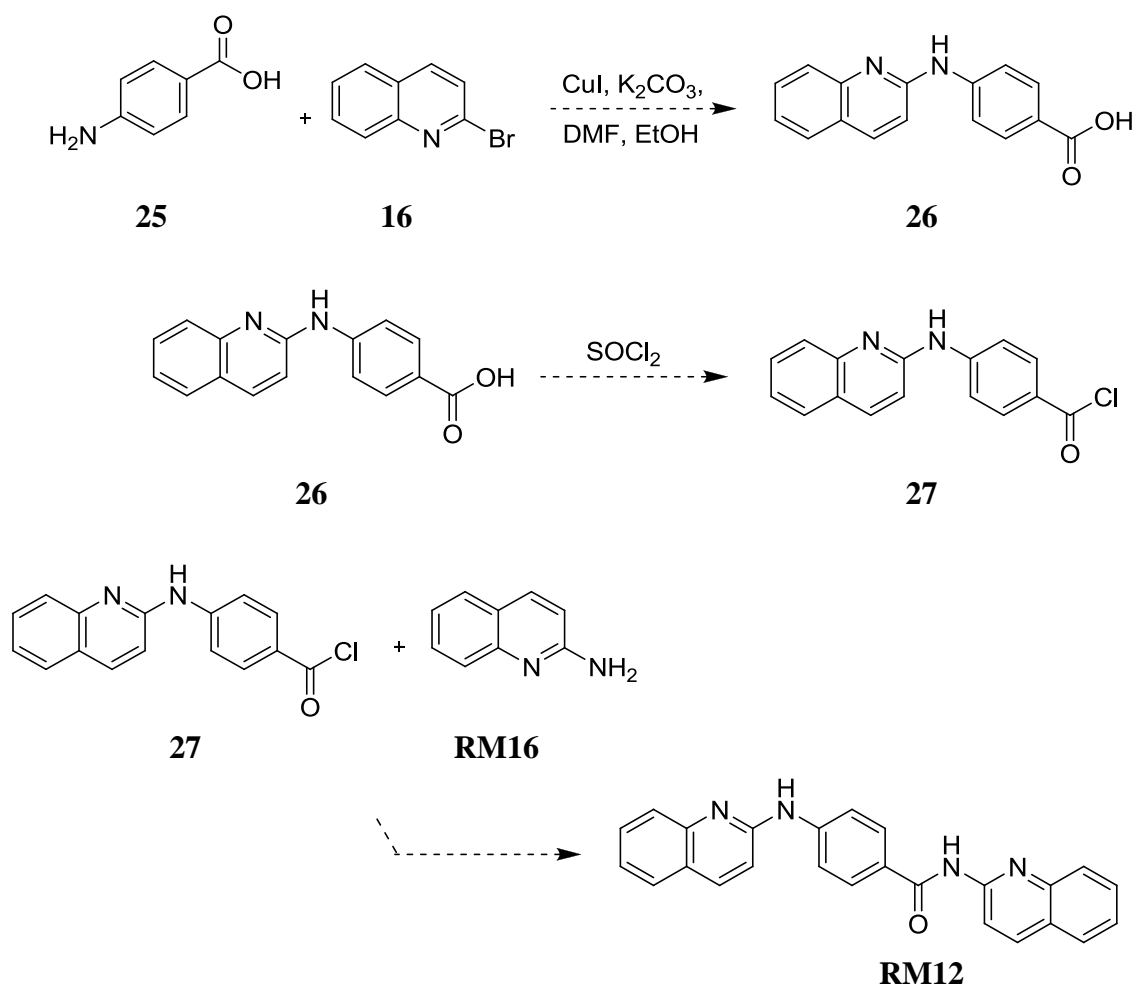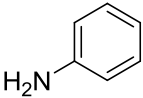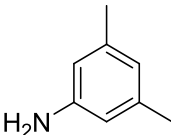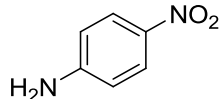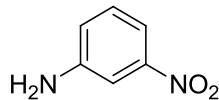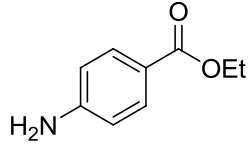
Even though this suggested synthetic route is viable, the execution of the overall synthesis would depend on the initial amine formation, where 2-bromoquinoline **16** would be treated with the amine **25**. With the carboxylic acid being a strong electron withdrawing group, it might cause the amine in the 4-position of compound **25** to be less nucleophilic. Therefore, it is less likely that the amination reaction would proceed.

_____

The same trend in reactivity is observed in the results published by Peng *et al*., where slightly lower yields were reported when anilines, with electron withdrawing groups on the benzene ring were used.[170]

Table 39: Reaction yields reported by Peng *et al*.[170]

Benzo -aniline	% Yield
	95
	86
	68
	61
	72

The aim of this study is to evaluate the adsorption of compounds that would contribute in gaining a greater understanding of the adsorption of inhibitors into two neighbouring primary adsorption sites. Therefore, it was deemed more efficient to spend time and resources on obtaining such compounds, rather than to concentrate on the synthesis of specific compounds. To this end, with the amination reaction posing potential difficulties, the synthesis of new compounds was rather pursued, and the alternative synthesis of compound **RM12** was set aside.

4.2.5 Introducing two new linear compounds for the adsorption onto face {001}

With compounds **RM14**-**16** in hand, the emphasis was set on designing molecules that would extend this data set, thereby contributing in gaining a greater understanding of the adsorption of these into the two neighbouring primary pockets.
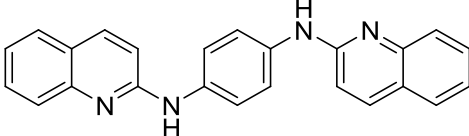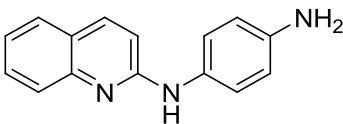
As mentioned above, compound **RM14** adsorbs with one phenyl ring into the second primary adsorption site, where for compound **RM15**, only one bromine atom could form interactions at this position in the second primary adsorption site. Moreover, compound **RM16** was only able to adsorb into a single primary adsorption site. For these compounds, the formation of hydrogen bonding interactions is not seen. Building on the structure-activity relationships that could be determined for these two compounds, compound **RM17** and **RM18** would also contribute to this study (Table 40).

Upon evaluating the adsorption of these two compounds into the crevice on face {001}, it is found that compound **RM17** adsorbs in a similar conformation as compound **RM10** and **RM12** investigated above, where the molecule is able to occupy both primary adsorption sites completely (Figure 92). Compound **RM18** is not able to extend into a second primary adsorption site to form π-π interactions to the porphyrin structure, where the formation of a hydrogen bond between the primary amine and a carbonyl group on the crystal surface is seen, with a measured interaction distance of 2.7 Å.

By synthesising these two compounds and by determining the NP40 $BHIC_{50}$ activities thereof, structure-activity correlations could be evaluated. Moreover, the activity data of these two compounds could be compared to that of compounds **RM14-16**, where the extent of adsorption into the crevice on face {001} could be evaluated.

Table 40: The chemical structures of compounds RM17 and RM18.

Compound	Chemical structure	% Diprotic	% Monoprotic	% Neutral
RM17		22	50	28
RM18		16	62	22
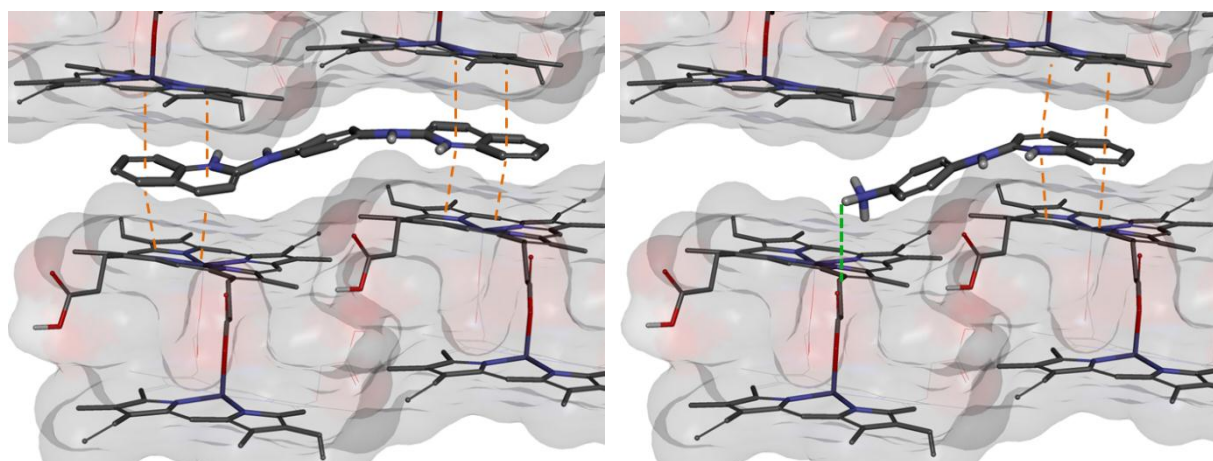
Figure 92: Adsorption of compounds RM17 and RM18 onto face {001}

*The adsorption of compounds **RM17** (left) and **RM18** (right) in the diprotic form onto face {001}, is shown, as viewed from above. The hydrogen bonding interaction, with a measured interaction distance of 2.7 Å, is indicated by ▪ ▪, and π-π interaction, with measured interaction distances between 3.5 and 3.8 Å, are indicated by ▪ ▪ .*

_____

4.2.5.1. Towards the synthesis of compounds RM17 and RM18

With the 2-aminoquinoline **RM16** not being a strong nucleophile, the synthetic procedure for the formation of the amine bond that was attempted before, was not pursued. Instead, the amination reaction reported by Peng *et al*. was rather considered.[171]

By heating an excess amount of **16** with **28** in dry ethanol, under a positive pressure of nitrogen gas, both compounds **RM17** and **RM18** would be obtained (Scheme 32). The formation of **RM18** would be observed with the addition of 1 equivalent of **16**. By allowing the reaction to proceed for a longer period of time, and by adding 2 equivalents of **16**, a higher yield for **RM17** would be obtained.

Scheme 32
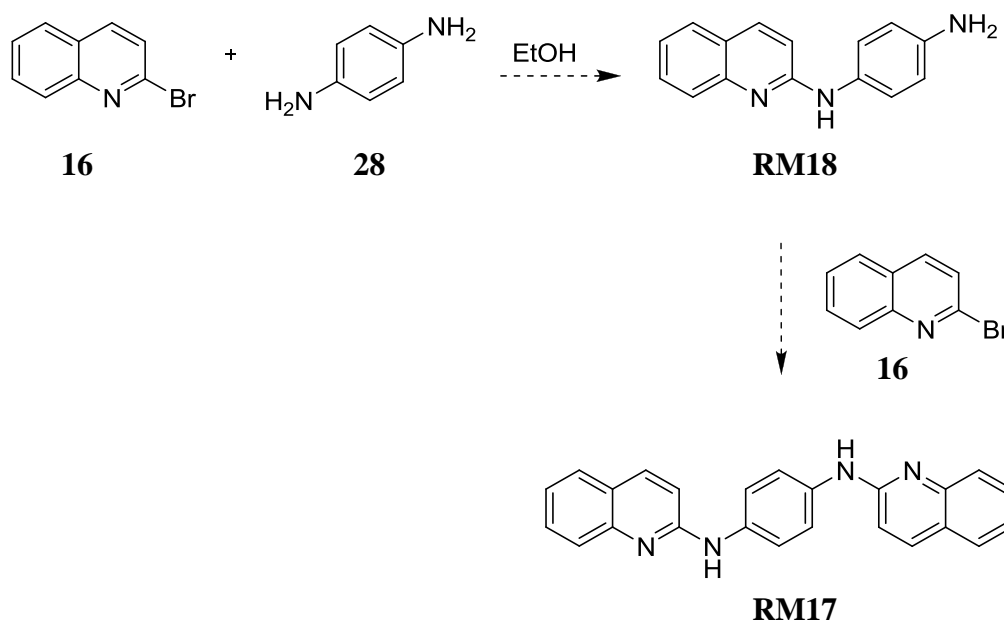
4.2.5.2 Synthesis of the two new quinoline compounds

4.2.5.2.1 Synthesis of N^1,N^4-di(quinolin-2-yl)benzene-1,4-diamine -RM17

and N^1-(quinolin-2-yl)benzene-1,4-diamine - RM18

For synthesising compounds **RM17** and **RM18** from **16** and **28**, the reagents were added to dry ethanol, where a small amount of *N*,*N*-dimethylformamide was added to ensure the solubility of reagent **16** (Scheme 33).[171]

The reaction mixture was allowed to reflux under a positive pressure of nitrogen for three days. Unfortunately the reaction did not proceed to completion and a vast amount of starting reagent **16** was still present. Product formation was not seen at lower temperatures, and simultaneous formation of both products **RM17** and **RM18** was observed after refluxing the reaction mixture for 6 hours, as determined by means of thin layer chromatography analysis.

Scheme 33
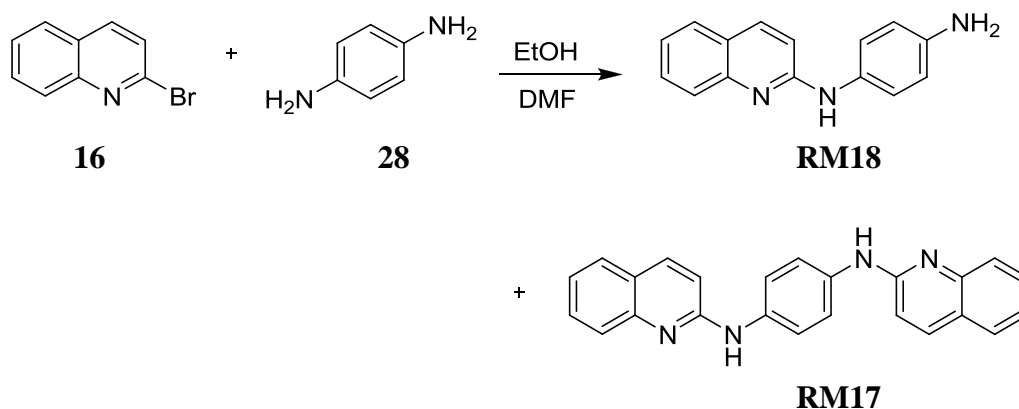
Nevertheless, after the three day time period, the reaction mixture was allowed to cool to room temperature, whereafter the excess solvent was removed *in vacuo*. The desired products were purified by means of column chromatography.

228

Compound **RM17** was obtained in a low 3% yield, and compound **RM18** in a low 19% yield, where 30% of the starting reagent **16** was recovered.
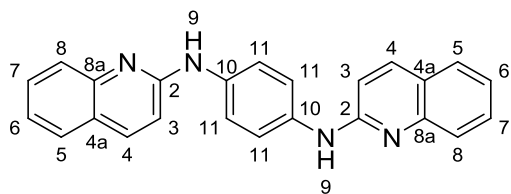
RM17
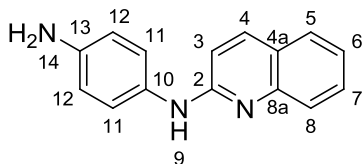
RM18

For compound **RM17**, the ^{1}H NMR spectrum served as a confirmation of the successful synthesis of a symmetrical molecule with two identical secondary amines, where a peak integrating for 1 at 9.33 ppm for H_9, was observed. Furthermore, the result of the mass spectral analysis of 363.1610 amu correlated exactly with the expected mass of 363.1613. For compound **RM18**, a peak integrating for 1 at 8.89 ppm for H_9, and a peak integrating for 2 at 4.76 ppm for H_{14} were observed in the ^{1}H NMR spectrum, which indicated that the reaction only occurred once, where both a primary and a secondary amine are present.

Unfortunately, these low yields could not be improved by allowing the reaction to proceed for longer, by adding more of compound **16**, or with the addition of a strong base. By performing the reaction on a larger scale, the reaction did not proceed at all. However, a sufficient amount of product **RM17** and **RM18** was obtained in order to achieve full characterisation, and to determine the NP40 BHIC$_{50}$ activities thereof. Furthermore, considering that a low yield was obtained for this reaction, the synthesis of compound **RM12** was not pursued.

In retrospect, a more selective synthesis could have been achieved. By reacting compound **16** with 2-nitroaniline **29**, the nitro intermediate **30** could have been isolated, which could

subsequently have been reduced to obtain compound **RM18**. Upon the further treatment of

compound **RM18** with **16**, compound **RM17** could have been isolated.

Scheme 34
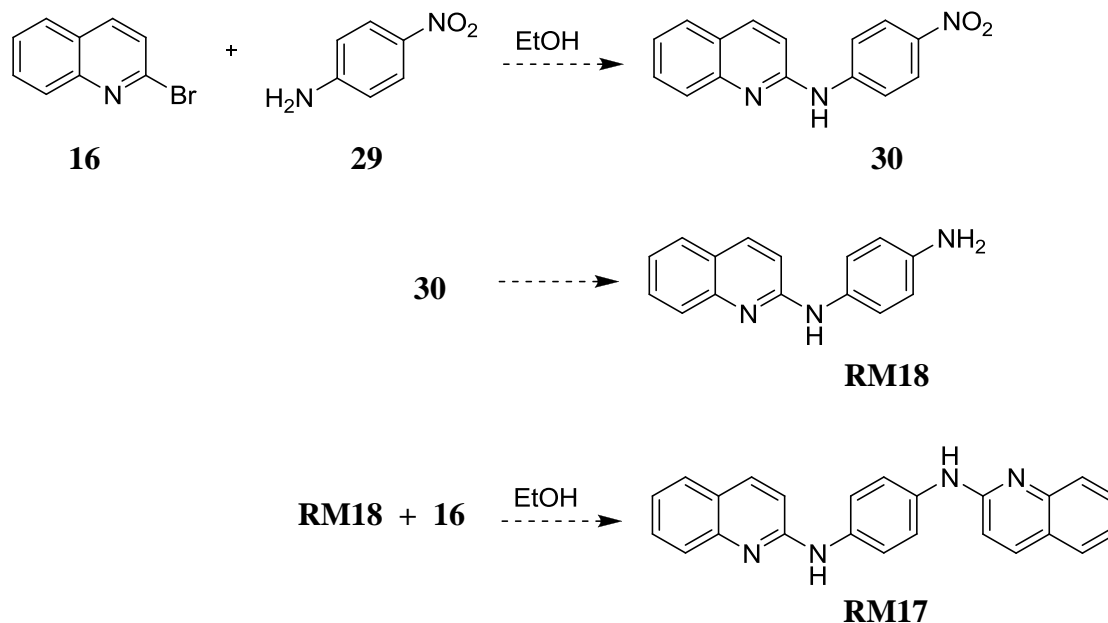
Even though compound **RM17** was obtained in a low yield, it is an ideal target molecule for

this study, as it is able to adsorb in such a geometry where the two quinoline moieties occupy

two neighbouring primary adsorption sites simultaneously. Furthermore, with compound

RM18 only being one quinoline moiety smaller than **RM17**, and with compound **RM16** only

comprising of one quinoline structure, the obtained structure-activity relationships would

provide valuable insight as to whether the adsorbed geometry of compound **RM17** is truly

more favoured.
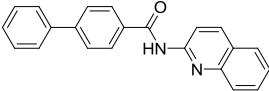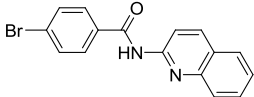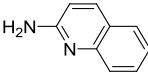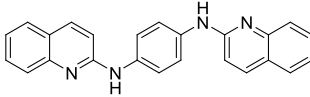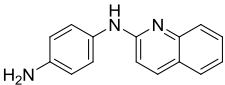
Therefore, with five final compounds in hand that were each observed to occupy the crevice in a different manner, the NP40 $BHIC_{50}$ activities were determined in order to evaluate the structure-activity relationships of these compounds.

4.2.6 Investigating structure-activity relationships for the synthesised quinoline compounds

For the clinically-relevant quinoline, as well as for the non-quinoline compounds, a linear correlation was found between the calculated adsorption energies (E_{ads}), and the NP40 $BHIC_{50}$ activities (Chapter 2 and 3). Furthermore, two main adsorbed geometries were found to be preferred for the adsorption onto face {001}. The molecules preferred adsorption into one primary adsorption site with the side-chains forming interactions on the crystal surface outside of the crevice, or an adsorption geometry is preferred where the compounds adsorb entirely into two neighbouring adsorption sites.

In this Chapter, five final compounds with a novel structure were synthesised for the purpose of further evaluating structure-activity relationships for the adsorption into two neighbouring primary adsorption sites. The calculated E_{ads} values for the adsorption onto face {001} are compared to the determined NP40 $BHIC_{50}$ activities (Table 41, and Figure 93), and a linear correlation was found, with an R^2 value of 0.87 and a P value of 0.02, when only taking into account the percentage speciation at pH 4.8.

Table 41: The determined NP40 BHIC$_{50}$ activity of the synthesised compounds, as well as the calculated E$_{ads}$ values for the adsorption onto face {001}, taking into account the percentage speciation.

	Compound	E$_{ads}$ Diprotic (kcal.mol^{-1})			E$_{ads}$ Monoprotic (kcal.mol^{-1})			E$_{ads}$ Neutral (kcal.mol^{-1})			% Diprotic	% Monoprotic	% Neutral	E$_{ads}$ face {001} (kcal.mol^{-1})	NP40 BHIC$_{50}$ (µM)		
	RM14	–			–			-73.5	±	0.5	0	0	100	-73.5	148	±	16
	RM15	–			–			-62.3	±	1.5	0	0	100	-62.3	318	±	0.4
	RM16	-46.8	±	0.01	–			–			100	0	0	-46.8	453	±	2.7
	RM17	-99.4	±	0.2	-99.8	±	4.2	-90.8	±	0.5	22	50	28	-97.2	10.5	±	0.02
	RM18	-66.4	±	0.6	-65.5	±	0.1	-66.0	±	0.5	16	61	22	-65.8	155	±	0.01

232

_____
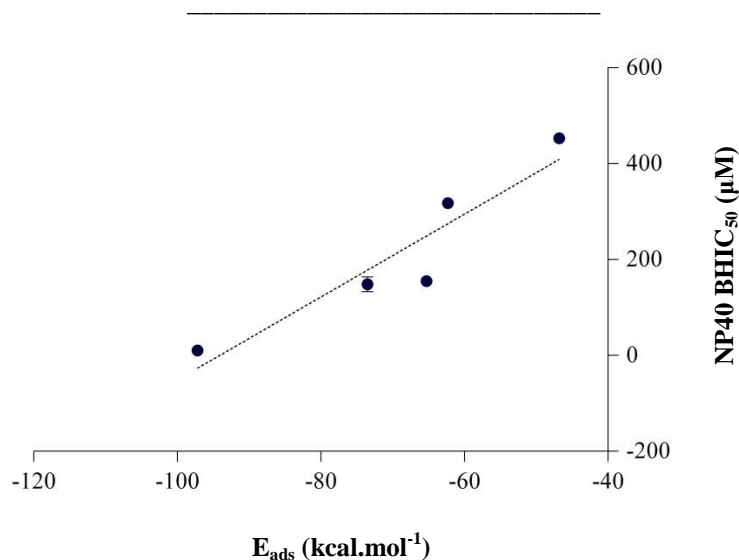
Figure 93: The calculated E_{ads} values for the adsorption onto face {001}, by also taking into account the percentage speciation, is compared to the determined NP40 BHIC$_{50}$ activity of the synthesised compounds.

An R^2 value of 0.87 and a P value of 0.02 are obtained.

This was indeed a pleasing result, which confirmed that the activities of new β-haematin inhibitors were successfully predicted by using the molecular modelling approach. Furthermore, this result has demonstrated that a greater NP40 BHIC$_{50}$ activity is indeed obtained when an inhibitor is able to adsorb into two neighbouring primary adsorption sites, as opposed to adsorbing into a single primary adsorption site.

Compound **RM14** is able to adsorb with a phenyl ring into the second primary adsorption site, where compound **RM15** only has a halogen atom adsorbed in this position, therefore it is expected for compound **RM14** to be a significantly more active β-haematin inhibitor. This result is indeed found when comparing the determined NP40 BHIC$_{50}$ activities, where compound **RM14**, with a NP40 BHIC$_{50}$ activity of 148 ± 16 μM, is twice as active as compound **RM15**, with a NP40 BHIC$_{50}$ activity of 318 ± 0.4 μM.

Furthermore, for compound **RM16**, which is only able to adsorb into one primary adsorption site, a significantly less favoured NP40 BHIC$_{50}$ activity of 453 ± 2.7 μM is determined. Therefore, this result indicates that either the bromine atom or the benzene ring on compound **RM15** might give rise to additional hydrophobic interactions (halogen-π, or alkyne-π interactions) to the porphyrin structures in the crevice, which results in an improved NP40 BHIC$_{50}$ activity, compared to that of compound **RM16**.

In contributing to this argument, compound **RM16** only adsorbed into one primary adsorption site, where compound **RM18** has one more benzene ring that forms alkyne-π interactions in the second primary adsorption site. As a result, a more favoured NP40 BHIC$_{50}$ activity of 155 ± 0.01 μM is determined for compound **RM18**.

The second quinoline of compound **RM17** is able to extend further into the second primary adsorption site, forming additional π-π interactions to the porphyrin structure. Therefore, a considerably improved NP40 BHIC$_{50}$ activity of 10.5 ± 0.02 μM is determined for this compound.

This result adds merit to the argument that when two neighbouring primary adsorption sites are occupied simultaneously, enhanced adsorption (E$_{ads}$), and more importantly, enhanced β-haematin growth inhibition (NP40 BHIC$_{50}$ activity), is achieved. Furthermore, considering that the NP40 BHIC$_{50}$ activity of AQ is 7.2 ± 0.05 μM, and that of CQ is 31.5 ± 2.0 μM, compound **RM17** is regarded as an active β-haematin growth inhibitor.

In reviewing the structure-activity relationships more closely, a more in-depth understanding is obtained with regards to the intermolecular interactions that form between the inhibitor and the crystal surface. According to computational results, compounds **RM15** and **RM18** are

predicted to be equally active β-haematin inhibitors, with calculated E_{ads} values of -62.3 and -65.2 kcal.mol^{-1}, respectively. However, when comparing the determined NP40 BHIC$_{50}$ activities of these two compounds, it is found that compound **RM18** is twice as active as compound **RM15**. Upon inspecting the visual results more closely, compound **RM18** only adsorbed into one primary adsorption site, where the protonated primary amine N-H was able to form a hydrogen bonding interaction to the carbonyl group on the crystal surface. Compound **RM15** has a bromine atom extending into the second primary adsorption site. Therefore, it is suggested that the formation of a hydrogen bonding interaction to the carbonyl group on the outside of the crevice contributes significantly in promoting β-haematin growth inhibition.

Additionally, compounds **RM14** and **RM18** are found to be equally active β-haematin growth inhibitors, even though the calculated E_{ads} value of compound **RM14** indicates a more favoured adsorption onto face {001}. Compound **RM14** is able to adsorb with an additional phenyl ring into the second primary adsorption site, where compound **RM18** only adsorbs into one primary adsorption site, forming a hydrogen bonding interaction to the crystal surface. With the NP40 BHIC$_{50}$ activities of these two compounds being similar, this outcome indicates that the hydrogen bonding interaction and a π-π interaction in the primary adsorption site contributes equally in promoting β-haematin inhibition. Therefore, with compound **RM17** being significantly more active than compounds **RM14** and **RM18**, this result indicates that the additional π-π interactions formed between the quinoline ring and the porphyrin in the primary adsorption site, promotes β-haematin growth inhibition even more.

This finding coincides with the notion that the formation of an increased number of interactions results in an improved adsorption, and thus enhanced β-haematin growth

_____

inhibition. Therefore, it is suggested that both the visual results, as well as the calculated E_{ads} values should be applied when predicting the β-haematin growth inhibition activity of a molecule.

Overall, it could be concluded that the computational adsorption model for evaluating the adsorption of small inhibitors onto the fastest growing face of β-haematin, and thereby calculating the E_{ads} values, is suitable for predicting the β-haematin inhibition activities of small compounds, as well as for the design of new antimalarial compounds.

4.3 INVESTIGATING STRUCTURE-ACTIVITY RELATIONSHIPS FOR ALL COMPOUNDS EXAMINED

With the NP40 $BHIC_{50}$ activities obtained in this chapter being more widespread, the results were combined with those obtained in the previous two chapters (non-quinoline and clinically-relevant quinoline inhibitors), in order to attain a more representative data set (Table 42). By performing the same multiple correlation calculation as in the end of the previous chapter, the final variables v_1 to v_6 are obtained (Table 43), which were consistent with the overall speciation distribution of the inhibitors at pH 4.8, where a slight preference for the adsorption onto face {011} in the diprotic form is found.

When comparing the optimised E_{ads} values for the adsorption onto β-haematin against the determined NP40 $BHIC_{50}$ activities of all compounds investigated, an R^2 value of 0.63 and a P value of <0.0001 are obtained for a significant linear correlation (Figure 94). However, with this data set also including the less active compounds synthesised in this chapter, it is apparent that the correlation that is obtained, is not strictly linear, and an exponential correlation is rather found. Therefore, by comparing the log of the NP40 $BHIC_{50}$ activity against the log of the absolute value of the optimised E_{ads}, for all compounds investigated (Table 44), an improved linear correlation is found, with an R^2 value of 0.75 and a P value of <0.0001 (Figure 95).

Table 42: The determined NP40 BHIC$_{50}$ activity and the calculated E$_{ads}$ values for the adsorption onto β-haematin for all compounds investigated

Compounds	E$_{ads}$ Diprotic face {001} (kcal.mol^{-1})	E$_{ads}$ Monoprotic face {001} (kcal.mol^{-1})	E$_{ads}$ Neutral face {001} (kcal.mol^{-1})	E$_{ads}$ Diprotic face {011} (kcal.mol^{-1})	E$_{ads}$ Monoprotic face {011} (kcal.mol^{-1})	E$_{ads}$ Neutral face {011} (kcal.mol^{-1})	% Diprotic	% Monoprotic	% Neutral	E$_{ads}$ (kcal.mol^{-1})	NP40 BHIC$_{50}$ (μM)
KN6	−66.5 ± 0.3	−	−	−46.4 ± 0.1	−	−	100	0	0	**−79.5**	58.8 ± 3.8
KN7	−51.5 ± 0.01	−	−	−53.1 ± 0.0	−	−	100	0	0	**−81.4**	135 ± 10.4
KW1	−	−80.1 ± 0.0	−82.9 ± 0.2	−	−56.0 ± 0.8	−55.7 ± 0.0	0	59	41	**−81.9**	18.7 ± 0.1
KW2	−	−70.0 ± 0.7	−74.5 ± 0.5	−	−57.4 ± 0.1	−53.3 ± 0.2	0	54	48	**−102.5**	14.6 ± 0.2
KW3	−	−77.4 ± 0.9	−82.9 ± 0.1	−	−65.5 ± 0.7	−66.8 ± 0.7	0	52	46	**−98.5**	13.8 ± 0.4
KW4	−71.7 ± 0.2	−86.6 ± 0.8	−	−63.6 ± 0.1	−63.9 ± 0.4	−	75	23	0	**−101.1**	13.3 ± 0.7
KW5	−93.6 ± 0.1	−96.1 ± 0.0	−96.4 ± 0.0	−61.1 ± 0.2	−63.3 ± 0.3	−63.1 ± 0.4	7	39	53	**−81.5**	9.1 ± 0.7
KW6	−	−72.5 ± 0.0	−73.2 ± 1.0	−	−59.8 ± 0.0	−62.0 ± 0.0	0	27	73	**−88.1**	12.7 ± 1.4
KW7	−78.7 ± 0.1	−84.5 ± 0.0	−	−64.6 ± 0.1	−65.5 ± 0.1	−	75	23	0	**−88.6**	22.2 ± 1.4
FL1	−	−67.3 ± 0.0	−90.6 ± 0.0	−	−61.8 ± 0.8	−58.4 ± 0.8	0	70	30	**−84.6**	38.2 ± 1.4
FL2	−	−72.0 ± 0.0	−99.1 ± 0.0	−	−62.7 ± 0.9	−63.6 ± 0.0	0	70	30	**−90.0**	24.5 ± 4.2
FL3	−	−68.9 ± 0.3	−89.8 ± 0.4	−	−61.9 ± 0.0	−65.1 ± 0.0	0	70	30	**−86.1**	32.0 ± 1.4
S11	−49.4 ± 0.5	−	−	−39.4 ± 0.03	−	−	100	0	0	**−64.6**	100.3 ± 2.0
RM14	−	−	−73.5 ± 0.5	−	−	−57.7 ± 0.1	0	0	100	**−79.1**	148 ± 15.8
RM15	−	−	−62.3 ± 1.5	−	−	−51.0 ± 0.0	0	0	100	**−67.8**	318 ± 0.4
RM16	−46.8 ± 0.01	−	−	−28.5 ± 0.2	−	−	100	0	0	**−52.2**	453 ± 2.7
RM17	−99.4 ± 0.2	−99.8 ± 4.2	−90.8 ± 0.5	−61.4 ± 0.5	−63.1 ± 0.0	−62.3 ± 0.1	22	50	28	**−106.3**	10.5 ± 0.02
RM18	−66.4 ± 0.6	−65.5 ± 0.1	−66.0 ± 0.5	−43.0 ± 0.0	−44.0 ± 0.0	−43.8 ± 0.4	16	61	22	**−71.8**	155 ± 0.01

AQ	-69.8	±	0.2	-70.5	±	0.0	–	-59.1	±	0.0	-58.9	±	0.0	–	98	2	0	**-94.5**	7.2	±	0.5
CQ	-67.0	±	0.0		–		–	-48.3	±	0.0		–		–	100	0	0	**-81.7**	31.5	±	2.0
MQ-*S*		–		-55.7	±	0.0	–		–		-48.8	±	0.0	–	0	100	0	**-66.3**	304.8	±	9.2
MQ-*R*		–		-61.6	±	0.0	–		–		-55.3	±	0.5	–	0	100	0	**-73.9**	304.8	±	9.2
QD	-80.8	±	0.0	-73.6	±	0.0	–	-57.3	±	0.1	-56.3	±	0.0	–	14	86	0	**-86.4**	25.6	±	2.0
QN	-66.2	±	0.0	-65.4	±	0.0	–	-48.5	±	0.0	-49.3	±	0.0	–	14	86	0	**-75.8**	61.8	±	1.8
QC	-75.1	±	0.0		–		–	-59.6	±	0.8		–		–	100	0	0	**-97.5**	6.3	±	0.5

Table 43: Final variables calculated for all compounds investigated

Variable	Value	Crystal face	Speciation form
v_1	0.17	{001}	Monoprotic
v_2	0.14	{011}	Monoprotic
v_3	0.13	{001}	Diprotic
v_4	0.26	{011}	Diprotic
v_5	0.15	{001}	Neutral
v_6	0.15	{011}	Neutral
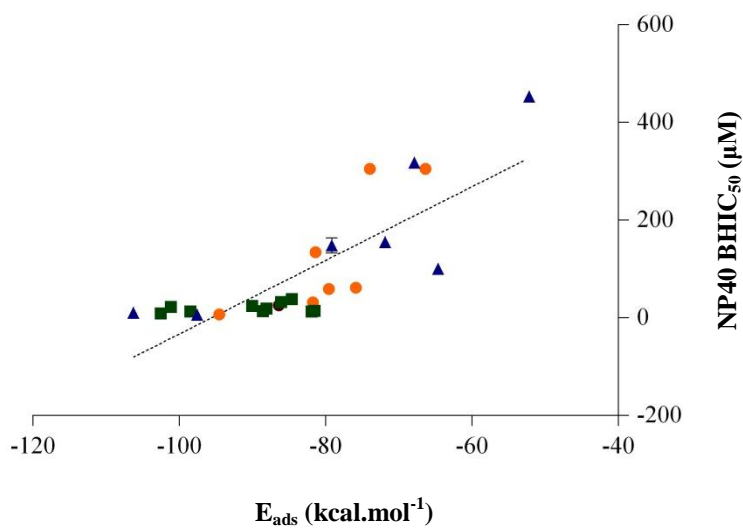
Figure 94: The best-fit E_{ads} values for the adsorption onto β-haematin are compared to the determined

NP40 BHIC$_{50}$ activity of all compounds investigated.

An R^2 value of 0.63 with a P value of <0.0001 are obtained for a linear graph.

The quinoline inhibitors are indicated in orange, the non-quinoline inhibitors are indicated in green, and the

synthesised compounds and QC are indicated in blue.

240

Table 44: The log of the NP40 BHIC$_{50}$ activities and the log of the absolute value of the optimised E$_{ads}$ values for the adsorption onto β-haematin for all compounds investigated.

Compounds	Log |E$_{ads}$|	Log NP40 BHIC$_{50}$
KN6	1.901	1.769
KN7	1.910	2.129
KW1	1.913	1.105
KW2	2.011	0.957
KW3	1.933	1.122
KW4	2.005	1.346
KW5	1.911	1.164
KW6	1.945	1.273
KW7	1.947	1.141
FL1	1.927	1.582
FL2	1.954	1.390
FL3	1.935	1.505
S11	1.810	2.001
RM14	1.898	2.171
RM15	1.832	2.502
RM16	1.717	2.656
RM17	2.026	1.021
RM18	1.856	2.189
AQ	1.976	0.859
CQ	1.912	1.498
MQ-*S*	1.822	2.484
MQ-*R*	1.869	2.484
QD	1.937	1.409
QN	1.880	1.791
QC	1.989	0.798
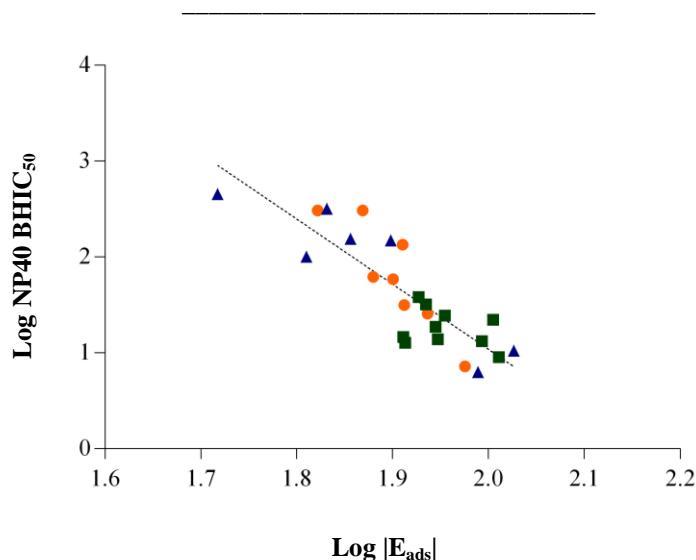
Figure 95: The log of the NP40 BHIC$_{50}$ activity is compared to the log of the absolute value of E$_{ads}$ for all compounds investigated.

An R^2 value of 0.73 with a P value of <0.0001 are obtained.

The quinoline inhibitors are indicated in orange, the non-quinoline inhibitors are indicated in green, and the synthesised compounds and QC are indicated in blue.

Now that an exponential correlation is obtained, it is clear why MQ and other less active β-haematin inhibitors were considered as outliers in a linear correlation (Section 3.2.2). With fewer data points, the correlations were thus incorrectly found to be linear. This outcome thus highlights the importance of evaluating a fully representative data set.

However, with the new structure-activity evidence obtained, and with a greater understanding of the preferred intermolecular interactions formed between the inhibitor and the crystal surface, this information could be combined and used in future antimalarial drug development.

_____

4.4 CONCLUDING REMARKS PERTAINING TO CHAPTER 4

4.4.1 The significance of this chapter

Chapter 4 mainly focused on obtaining a greater understanding of β-haematin growth inhibition by adsorption of inhibitors onto the fastest growing face, and more specifically the adsorption of inhibitors into the primary adsorption site.

For investigating the small molecular scaffolds for the adsorption into a single primary adsorption site computationally, it is observed that the best adsorption is found for the carbazole and benzo(b)(1-5)napthyridine scaffolds. Unfortunately, as these compounds are not particularly soluble in the NP40 BHIC$_{50}$ assay buffer solution, structure-activity relationships were not investigated for these compounds.

However, upon evaluating the adsorption of these small molecular fractions into the primary adsorption site, the adsorption of CQ was compared to that of QC. As both of these active inhibitors have the same side-chain, and as these compounds adsorb in a similar geometry onto face {001}, it can be concluded that the greater β-haematin activity of QC is owing to the more favoured adsorption of its benzo(b)(1-5)napthyridine moiety into the primary adsorption site, as opposed to the quinoline moiety of CQ. Therefore, with an increased number of π-π interactions formed between the inhibitor and the porphyrin structures in the crevice, an improved adsorption is obtained (E$_{ads}$ value), which results in an improved β-haematin growth inhibition activity (NP40 BHIC$_{50}$).

The second part of this chapter was dedicated to the design and synthesis of compounds that would contribute in a greater understanding of the inhibition of β-haematin growth by adsorption onto face {001}, and more specifically, the adsorption into two neighbouring

primary adsorption sites. In the end, five molecules that were able to adsorb into the crevice were successfully synthesised, of which the NP40 BHIC$_{50}$ activities were determined.

It was found that both the formation of hydrogen bonding interactions, as well as π-π interactions between the inhibitor and the crystal surface are of great importance for enhanced adsorption, and thus β-haematin growth inhibition. It has been demonstrated that an increase in the number of these intermolecular interactions that form between the inhibitor and the crystal surface, results in an increase in the β-haematin growth inhibition activity (NP40 BHIC$_{50}$). Consequently, it was demonstrated that a more favoured adsorption (E$_{ads}$), and an improved β-haematin growth inhibition activity (NP40 BHIC$_{50}$) is obtained when a molecule is able to adsorb entirely into two neighbouring primary adsorption sites.

In the third and final part of this chapter, the results of the synthesised compounds were combined with that of the clinically-relevant quinoline inhibitors and the non-quinoline inhibitors, in order to evaluate structure-activity relationships. By applying the multiple correlation calculation, a significant linear correlation, with an R^2 value of 0.63 and a P value of <0.0001, was obtained. However, by including less active β-haematin inhibitors into the data set, an exponential correlation is obtained when comparing the optimised E$_{ads}$ values for the adsorption of inhibitors onto β-haematin, and the determined NP40 BHIC$_{50}$ activities. By comparing the absolute values of the log of the E$_{ads}$ to the log of the NP40 BHIC$_{50}$ activity, an improved linear correlation with an R^2 value of 0.73 and a P value of 0.0001 is found, which is considered to be significant.

It can be concluded that more active β-haematin growth inhibitors would adsorb more favourably onto the fastest and second fastest growth faces of β-haematin.

_____

4.4.2 Final conclusion

In performing a more in-depth study of the adsorption of inhibitors into the primary adsorption site, it was concluded that with the formation of a larger number of intermolecular π-π or hydrogen bonding interactions between the inhibitor and the crystal surface, a subsequent improved adsorption and thus an enhanced β-haematin growth inhibition activity was obtained.

Furthermore, by including additional less active β-haematin growth inhibitors into the overall data set of quinoline and non-quinoline inhibitors, an exponential correlation is found when the NP40 $BHIC_{50}$ activities were compared to the adsorption onto β-haematin (E_{ads}), thereby taking into account the adsorption of these inhibitors onto both the fastest and the second fastest growth faces, and the speciation at pH 4.8.

_____

CHAPTER 5

OVERALL CONCLUSION AND FUTURE WORK

5.1 CONCLUDING REMARKS PERTAINING TO THIS DISSERTATION

As malaria is one of the most prevalent diseases known to mankind, this project was inspired to contribute towards the global fight against this epidemic. A substantial amount of research has been performed on gaining a more in-depth understanding of the mechanism of action of quinoline antimalarial drugs, where it is hypothesised that these drugs adsorb onto the crystal surface of β-haematin, thereby impeding further crystal growth.

In preceding work, Solomonov *et al.* reported physical evidence for this phenomenon,[73] and Buller *et al.* proposed adsorbed geometries in which the clinically-relevant inhibitors adsorb onto the fastest growing crystal face.[54] For this, a universal force field was used, and the molecules were manually fitted onto the fastest growing face of β-haematin, followed by a geometry optimisation. Therefore, in the absence of a thorough computational investigation for the adsorption of clinically-relevant inhibitors onto β-haematin, a more in-depth study was needed.

Upon parameterising a force field that is able to accommodate the high-spin Fe(III)-porphyrin complex, the adsorption of inhibitors onto both the fastest and the second fastest growth faces, was evaluated computationally. For the adsorption onto face {001}, similar adsorption geometries were obtained as previously reported by Buller *et al.*, where less favoured adsorbed geometries were obtained for the adsorption of inhibitors onto the second fastest growth face.

By evaluating structure-activity relationships, it was demonstrated that multiple parameters need to be taken into account when assessing the adsorption of the clinically-relevant inhibitors onto β-haematin. Therefore, by taking into account the adsorption onto the fastest and the second fastest growth faces ({001} and {011}, respectively), as well as the percentage speciation at pH 4.8, a significant linear correlation is obtained when the adsorption of the inhibitors (E_{ads} values) was compared to the determined lipid $BHIC_{50}$ activities. This result supports our research hypothesis that quinoline antimalarial drugs inhibit β-haematin formation by adsorbing onto the fastest growing faces of the crystal. In the absence of antimalarial activity data, this evidence does not point necessarily to the mechanism of action of quinoline antimalarial drugs.

This adsorption study was subsequently further extended to evaluate the adsorption of non-quinoline inhibitors onto the two fastest growing crystal surfaces, where a new adsorption geometry was observed. For example, for the adsorption onto the second fastest growth face, the molecules were able to adsorb over two unit cells, thereby forming intermolecular interactions to two adjacent porphyrin structures. Furthermore, for the adsorption onto the fastest growing crystal face, these molecules were able to occupy two neighbouring primary adsorption sites.

A linear correlation was found when comparing the adsorption of the non-quinoline inhibitors onto β-haematin (E_{ads} values) to the determined NP40 $BHIC_{50}$ activities. Moreover, by combining the two data sets of the clinically-relevant and the non-quinoline inhibitors, a linear correlation was again found. This result was indicative that these compounds adsorb onto the fastest growing crystal faces of β-haematin, and thereby inhibit further crystal growth.

To this end, it was concluded that two adsorption geometries are preferred for the adsorption of inhibitors on the fastest growing crystal face. The one adsorption geometry has previously been reported by Buller *et al.*, where the inhibitor (QN and QD) was able to adsorb in such a manner that the formation of π-π interactions between the inhibitor and the porphyrin structures inside the primary adsorption site is observed, as well as the formation of a hydrogen bonding interaction between a hydrogen donor atom on the inhibitor and a free carbonyl group outside of the crevice. The second adsorption geometry was observed for the adsorption of the linear non-quinoline inhibitors, where the formation of multiple π-π interactions between the inhibitor and the porphyrin structures inside two neighbouring primary adsorption sites is observed, as well as the formation of a hydrogen bonding interaction between a hydrogen donor atom on the inhibitor and a free carbonyl group outside of the crevice.

With a new adsorption geometry identified, which has not yet been reported in literature, the intermolecular interactions that form inside the two neighbouring primary adsorption sites, were evaluated more closely. It was found that an inhibitor which is able to fully occupy the two neighbouring primary adsorption sites, would be able to form a greater number of π-π interactions to the porphyrin structures, and would therefore be a more likely active β-haematin inhibitor than a compound that is only able to occupy one adsorption site. Consequently, it was demonstrated that a more favoured adsorption (E_{ads} value) and also a greater inhibition activity (NP40 $BHIC_{50}$) is obtained with the formation of an increased number of intermolecular interactions.

In the end, all of the adsorption and activity data determined in this project were combined and the adsorption onto β-haematin (E_{ads}) was compared to the determined β-haematin

growth inhibition (NP40 BHIC$_{50}$). With this combined data set also including less active inhibitors, when once again considering adsorption onto both the fastest and the second fastest growth faces, and by taking into account the percentage speciation at pH 4.8, an improved exponential correlation was obtained.

Overall, it has been demonstrated that the mechanism by which inhibitors cause β-haematin growth inhibition by adsorbing onto the β-haematin crystal, is a complex process. For crystal growth in the *c* direction, adsorption onto both the fastest and the second fastest growing faces needs to be accounted for, as well as the percentage speciation at pH 4.8. It has been demonstrated that a greater inhibition activity results from the formation of an improved number of intermolecular interactions between the inhibitor and the crystal surface, and that an exponential correlation exists between the modelled adsorption (E$_{ads}$ values) and the determined β-haematin inhibition activity (NP40 BHIC$_{50}$), when taking into account the above mentioned parameters.

The results obtained in this study strongly support, and greatly contribute to the understanding that clinically-relevant inhibitors execute their mechanism of action by adsorbing onto the fastest growing crystal faces of β-haematin, which brings about crystal growth inhibition and the subsequent accumulation of toxic free haem in the parasitic food vacuole.

5.2 FUTURE WORK

In this project, the adsorption of clinically-relevant quinoline inhibitors and a set of more rigid and linear non-quinoline inhibitors onto the fastest growing crystal faces of β-haematin, was evaluated. Considering that these inhibitors are not the only non-artemisinin compounds found to be active against malaria, this study could be extended to evaluate the adsorption of a significantly larger library of compounds onto β-haematin. By doing so, the following research outputs could be achieved:

- The adsorption of a greater variety of molecular scaffolds onto β-haematin could be evaluated. Thereby, the preferred adsorption geometry for each class of molecular scaffold investigated could be identified.

- This study could also be extended to evaluate whether a more flexible, as opposed to a more rigid scaffold, would contribute to an improved adsorbed geometry, and thus an enhanced inhibition activity.

- Considering that the duration of a single adsorption simulation could extend up to 5 days, a more high-throughput adsorption protocol would be needed to study a larger compound library. However, by knowing the preferred adsorption site on each of the two fastest growing crystal faces, the target sites could be specified prior to the simulation. This could, for example be achieved by applying a more selective grid-based docking simulation, or by using a smaller crystal surface.

In Chapter 4, it has been demonstrated that for the adsorption to the primary adsorption site, the formation of an increased number of intermolecular interactions between the inhibitor and the crystal surface results in an enhanced β-haematin inhibition activity. Therefore, upon

identifying two preferred adsorption geometries for the adsorption of inhibitors onto the fastest growing crystal face, this combined information could be utilised to design novel and more active β-haematin growth inhibiting antimalarial drugs, with the required ADME properties (adsorption, digestion, metabolism, and excretion). In doing so, the following could also be considered:

- For the adsorption geometry occupying the two neighbouring primary adsorption sites, enhanced activity could be obtained by the formation of the necessary π-π interactions, hydrogen bonding interactions, as well as possible C-H···X halogen bonding interactions, between the inhibitor and the crystal surface.

- Also, for the adsorption geometry occupying both the primary and the secondary adsorption sites, improved activity could be obtained by the formation of the necessary π-π interactions and possible C-H···X halogen bonding interactions between the inhibitor and the crystal surface in the primary adsorption site, as well as hydrogen bonding interactions outside of the crevice. Furthermore, the molecule could be optimised to such an extent that the formation of π-π interactions between the inhibitor and the porphyrin structure in the secondary adsorption site could be achieved.

A final challenge to consider is to design a more flexible molecule that is able to adsorb into both of these adsorption geometries, or which is able to occupy two neighbouring primary adsorption sites while being able to form a hydrogen bonding interaction outside of the crevice.

CHAPTER 6 – EXPERIMENTAL

6.1 MOLECULAR MODELLING

6.1.1 Theory of molecular modelling techniques used

6.1.1 Density Functional Theory (DFT)

Density Functional Theory (DFT) is one of the most widely used methods in quantum mechanics and calculates properties of molecules based on the three dimensional electronic density thereof.[172] This method is preferred to wave function theory (WFT) due to its better performance-to-time ratio. Wave function theory uses a wave function approximation to solve the Schrödinger equation in order to calculate the energy. Thus, as the number of electrons increases, the complexity of the wave function increases tremendously. By using the electron density, the calculation is less complex, resulting in a faster simulation.[172]

DFT is a general, multi-purpose method, which is not only used for organic molecules, but is also optimised to apply to transition metals.[172] Here, the functional and the basis set for representing the atomic orbitals would be chosen to represent the particular system on which the DFT calculation is performed. Local density approximation (LDA) functionals include PWC and VWN functionals,[173,174] whereas generalised gradient approximations (GGA) includes, for instance, PW91, BP, PBE, BLYP, BOP, VWN-BP, RPBE and HCTH functionals.[173,175–179] More recently, hybrid functionals were introduced, which are optimised for specific organic systems. These include functionals such as B3LYP. However, these are not optimal for the use on periodic systems.[172]

_____

With such a vast range of DFT approximations available, it is thus important to use a functional and a basis set that would most accurately represent the system on which the DFT calculation is performed. For the purposes of this project, a simple GGA PW91 functional was used, with a DNP basis set, in order to accommodate the Fe(III) metal centre in the porphyrin.

The DFT calculation was applied to optimise hydrogen atoms in crystal structures obtained from the Cambridge Structural Database (CSD).[180] These optimised crystal structures were subsequently used to parameterise a force field, which was applied in molecular mechanics calculations.

6.1.2 Molecular mechanics

Molecular mechanics (MM) is an empirical model of molecular structure, where the nuclear coordinates are generated by internal variables that are defined within a force field. Each force field is specially parameterised for a specific system and is carefully chosen for each molecular calculation.[181] Therefore, unlike quantum mechanical models, which use electrons in the calculations, parameterised molecular models cannot be used to calculate the energy distribution within any system.

However, by choosing the appropriate force field, molecular mechanics is a significantly faster and more robust method for modelling the motion of larger molecules within sound accuracy.[181] It is therefore the method of choice when performing molecular modelling calculations on large systems, such as protein-protein interactions, and protein-ligand interactions.

_____

6.1.2.1 Force fields and the parameterisation thereof

The force field, also known as the energy expression, is a sum of the potential energy terms, and specifies how the atoms within a molecule will behave in the presence of other atoms.[181] The internal variables that are defined within a force field consist of bonding and non-bonding interactions, where these are combined with energy terms to form the potential energy terms.

The bonding interactions, are treated as a harmonic "ball-and-spring" model, where the molecular vibrations are derived from Hooke's law (Displacement or extension is directly proportional to the force applied to bring about the change) and Newton's second law (For a constant mass, the force applied is equal to the product of the mass and the acceleration of an object).[182,183] Here, the atoms (represented as balls) are connected by bonds (represented as springs), where the size of the atoms and the rigidity of the bonds are defined by the force field. These internal variables taken into account are: bond lengths (r_{ij}), bond angles (θ_{ijk}), torsion angles (τ_{ijkl}), and inversion angles (γ_{ijkl}), as shown in Figure 96.
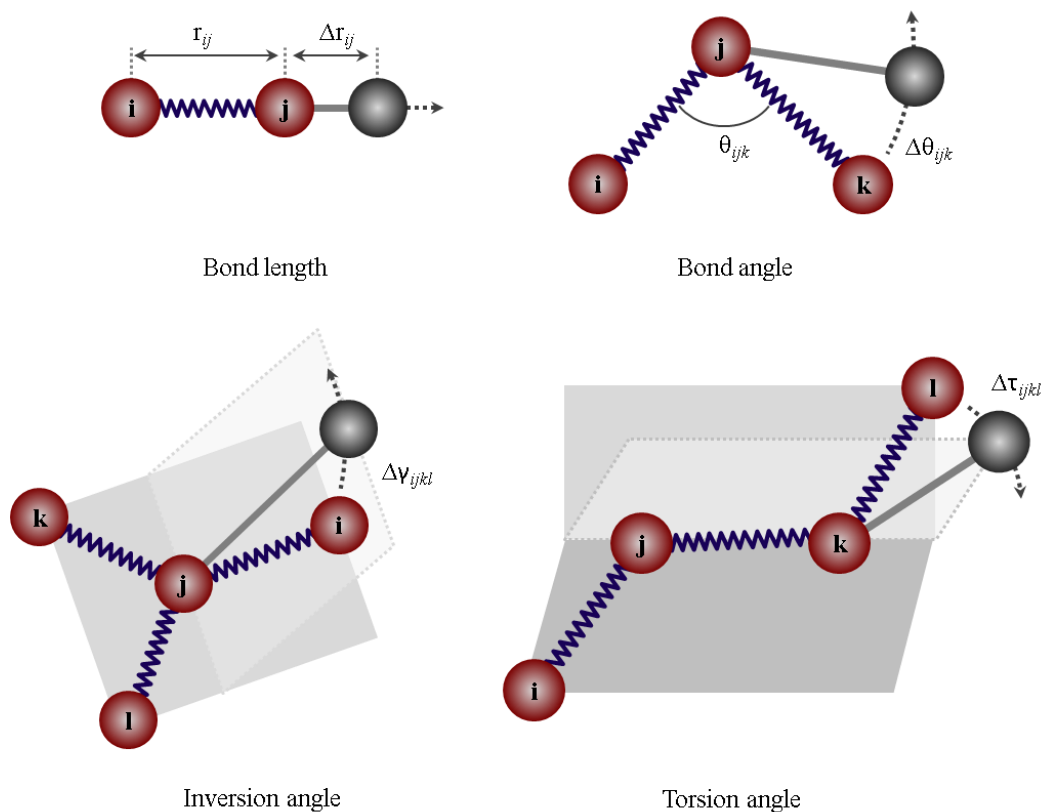
Figure 96: Internal variables commonly examined during a force field optimisation

This image was created with information obtained from images published by Machida,[183] and Rappé and

Casewit.[181] The internal variables taken into account during a force field optimisation are: bond lengths (rij),

bond angles (θijk), torsion angles (τijkl), and inversion angles (γijkl). Atoms are represented as red balls and

bonds are represented as springs. Movement is represented by a grey ball for each variable.

Chapter 6 – Experimental

_____

The non-bonding interactions in the force field extend over the entire system, where these include van der Waals and electrostatic interactions. Van der Waals interactions involve polar or induced polar interactions between molecules, such as dipole-dipole, dipole-induced dipole, and induced dipole-induced dipole (London dispersion forces) interactions.[184,185] Non-bonded van der Waals interactions are generally included using Lennard-Jones 6-12 potentials,[186,187] exponential repulsions,[188] or a Buckingham exponential-6 potential.[189,190] For the Lennard-Jones 6-12 potential (V_{LJ}) used in this project, this potential takes into account the non-bonded distance (ρ), the inner-wall repulsion (A), and the van der Waals attraction (B), between atoms (Equation 6.6).[181]

$$V_{LJ} = \frac{A}{\rho^{12}} - \frac{B}{\rho^6} \tag{6.6}$$

In earlier force fields, which were designed for modelling hydrocarbons, electrostatic interactions were ignored. Kitaygorodsky first introduced the use of partial point charges or bond dipoles in 1960.[191,192] Even though the benefit of applying these charges is still under debate, it is still largely considered to be more beneficial to include these charges.[193] Resultantly, modern force fields are rather parameterised to compensate for the limitations presented by applying partial point charges or bond dipoles.[194]

Force fields are typically parameterised based on available experimental data. For this, information obtained from X-ray diffraction, electron diffraction, microwave spectroscopy, NMR spectroscopy, and IR vibrational frequencies, are frequently used.[181] In the absence of physical experimental data, results from quantum mechanical calculations are applied, where these are also preferred to obtain more detailed potential energy curves.

Chapter 6 – Experimental

_____

With the force field being applied to represent molecules in a system, it has to be parameterised to fully mimic the natural state of the molecules investigated. For example, in parameterising the bond stretch harmonic potential (V_r in Equation 6.7), and the harmonic angle bend potential (V_θ in Equation 6.8), the representing force constants (k_{ij} and k_{ijk}, respectively) could be altered by means of an iterative process to represent the natural bond distance (r_{ij}) and bond angle (θ_{ijk}).[181] The optimisation of a force field is deemed adequate when the smallest root square deviation between the estimated and the natural bond angles and distances, is obtained.

$$V_r = \frac{1}{2} k_{ij}(r \,-\, r_{ij})^2 \tag{6.7}$$

$$V_\theta = \frac{1}{2} k_{ijk}(\theta \,-\, \theta_{ijk})^2 \tag{6.8}$$

Other terms that could be optimised, include the bond energy, the torsional potential, as well as the van der Waals potential terms. However, for the purposes of this project, only the above-mentioned force constants (k_{ij} and k_{ijk}) were optimised to account for the high-spin Fe(III) atom in the β-haematin porphyrin structure.

6.1.2.2 Molecular modelling of Fe porphyrin structures and related transition metal complexes.

A significant amount of work has been performed in parameterising force fields for high-spin Co(III) complexes, Cu(I) and Cu(II) complexes, as well as for high and low-spin Ni(II) complexes.[195] In general, transition metal complexes are best modelled using quantum mechanical methods. However, with these methods being more time consuming, it has been

demonstrated that by knowing the spin state of the complex, the correct parameters could be applied to model these complexes using molecular mechanical methods.

Unfortunately, this does not apply for porphyrin complexes containing high-spin Fe(III) or low-spin Fe(II) atoms. Marques *et al.* compared crystal structures obtained from the Cambridge Structural Database (CSD),[180] upon which it was established that the N-Fe bond distances and angles depended upon the overall coordination geometry, and the oxidation and spin state of the Fe atom.[132] In general, it was observed that the Fe-N bond lengths of low-spin complexes were slightly shorter $(2.001 \pm 0.015$ Å) than for high-spin complexes $(2.046 \pm 0.013$ Å). Moreover, the coordination geometries varied depending on the coordinated ligands. Evidently, it was stated that separate force fields are required to efficiently model each of the different types of Fe(II) and Fe(III) porphyrin complexes.

By separately defining the four nitrogen atoms in the *cis* and *trans* N-Fe-N angles in the porphyrin structure, a force field for Fe-containing complexes was optimised using structures obtained from the CSD, where the smallest allowed deviations between the natural and the modelled bond lengths, bond angles, and torsion angles, were 0.015 Å, 1.5°, and 4.0°, respectively.[132] In the end, by comparing the modelling results to the original crystal structures, it was demonstrated that this force field is ideal for modelling hexa-coordinate low-spin Fe(III) porphyrin structures with imidazoles and pyridines as axial ligands. In addition to this work, Munro *et al.* ensued further refinement of this force field in order evaluate the structure of ruffled low-spin Fe(III) porphyrin complexes in more detail.[131]

One challenge in modelling transition metal complexes, as opposed to performing quantum mechanical calculations, is to accurately mimic the electrostatic interactions between the

metal and the ligand. An argument was raised as to whether these interactions could be best described as covalent bonding or non-bonding interactions.[196] However, by evaluating the total energies, the binding energies, and the molecular structures of octahedral coordination complexes of glyoxal diimine ligands of the ten first row transition metals, Xiong *et al.* was able to demonstrate that by using a suitable parameterised force field, this limitation could be overcome.[197] The energy properties of these complexes were determined by means of DFT calculations, where after these results were compared to that of the parameterised force field. Resultantly, it was concluded that by treating the metal-ligand interactions as covalent bonding interactions, molecular mechanics studies were effectively able to mimic the energy results obtained from the DFT calculations.

More recently, in relation to the Fe(III)-oxygen bond in β-haematin, Yapo-Kicho *et al.* reported the successful development of a force field to evaluate high-spin Fe(III)/Fe(II)-oxygen interactions specifically occurring between non-haemic iron and polyphenols found in tannins.[198] Four model complexes containing Fe-water and Fe-catechol complexation, were evaluated by means of DFT calculations. The calculated geometry and vibrational results were combined with parameters previously reported in literature, upon which these results were applied to successfully parameterise the SPASIBA force field. Yapo-Kicho *et al.* demonstrated that high-spin Fe(III)-oxygen interactions could successfully be modelled by means of molecular mechanical calculations.

With this relevant research performed on optimising force fields for high-spin Fe(III)-oxygen and low-spin Fe(II)-porphyrin complexes, the same procedure for optimising these force fields was applied in this project. Furthermore, the reported parameters were used as initial

guides for optimising a force field that is able to adequately model high-spin Fe(III)-porphyrin complexes, such as β-haematin.

6.1.2 Software packages used

6.1.2.1 Cambridge Crystallographic Data Centre

The Cambridge Structural Database (CSD) is an online structural database that contains published single-crystal and powder X-ray refraction data of small organic and metal-organic molecules. This database was accessed through the Cambridge Crystallographic Data Centre (CCDC), by means of the Con Quest v1.16 software package.[180] The crystal structures used in this project were obtained from this database.

6.1.2.2 Marvin Sketch

Marvin Sketch (version 6.3.1),[143] a Java-based chemical drawing program, was utilised for the theoretical calculation of the pK_a values of the molecules used in the computational studies. The pK_a values gave a theoretical indication of the speciation of these molecules at pH 4.8.

6.1.2.3 Accelrys Discovery Studio

Accelrys Discovery Studio is a full comprehensive molecular modelling software package, specifically developed for protein-based drug discovery and ligand design.[144] It includes software applications such as molecular mechanics, molecular dynamics and quantum mechanical simulations, as well as quantitative structure–activity relationship (QSAR) and

pharmacophore modelling. In this project Discovery Studio was primarily used to generate conformations of molecules, and for visualisation and image generation.

6.1.2.3.1 Generate conformations

The Generate conformations protocol in Discovery studio was used to generate conformations of the inhibitors used in this study.[144] The default settings allow for a maximum number of conformations to be determined. However, for a more thorough search, the allowed degrees of rotation around bonds could be defined.

6.1.2.4 Accelrys Materials Studio

Accelrys Materials Studio is a software package specifically developed for materials science research in order to better understand the relationship between the molecular composition and the properties of the material.[123] These include materials such as metallic and organic surfaces, polymers, crystals and mesoscale structures. As with Discovery Studio, various molecular mechanics, molecular dynamics and quantum mechanical tools are available for these larger material systems. For this reason, Materials Studio was largely used for the computational studies.

6.1.2.4.1 DMol ^{3}

DMol^3 is a module in Materials Studio that allows the modulation of the electronic structure and energetics of a system using Density Functional Theory (DFT).[123] This module was utilised for the evaluation of a set of crystal structures, which was later used during the optimisation of the force field. The parameters that were applied are tabulated in Table 45.

_____

Table 45: Energy parameters used for the DMol^3 quantum mechanics calculations.

Electronic	
SCF tolerance	1×10^{-6}
Maximum SCF cycles	50 000
Core treatment	DFT Semi-core Pseudopots
Basis set	DNP
Geometry optimisation	
Quality	2×10^{-5} Ha
Maximum iterations	1 000
Functional	GGA PW91
Use symmetry	No
Metal	Yes

6.1.2.4.2 Perl scripting

Materials Studio allows for Perl scripting, an open source scripting language, by means of a script viewer.[123] Here, new scripts could be written, or scripts generated from modules, could be edited. Not only does this allow for versatility within the software package, but it also simplifies the operation thereof, since simulations could be automated, or even be sequentially combined. Moreover, especially within the Adsorption locater and Forcite, scripting was mainly used to ensure consistency during iterative or repeated simulations.

Chapter 6 – Experimental

_____

6.1.2.4.3 Force field viewer

The force field viewer within Materials studio is designed to edit and view force fields for the use in molecular mechanics calculations.[123] For this project, the cvff force field (version 2.4) was parameterised to accommodate the β-haematin porphyrin structure with a Fe(III) centre.[125] In order to optimise the force field, the crystal structure of β-haematin, as well as a training set of eight similar published crystal structures, was used.[40,108,133–137,199] The initial parameters that were applied, were obtained from literature, as published by Munro and co-workers.[131]

With the parameterised force field, a new atom type was defined for Fe (III). Special care was taken in the manual typing of the carbon atoms within the porphyrin structures, as these were incorrectly typed with the automatic typing in the Forcite module. The force field types used in the porphyrin are tabulated in Table 46.

Table 46: Force field types used in the parameterised force field

Types	Description
Fe3	Fe^{III}
n	nitrogen, SP2, connected to heavy atoms
np	nitrogen, SP2, aromatic
o	oxygen, SP3, in ether or ester groups
c	carbon, SP3, aliphatic
c1	carbon, SP3, bonded to 1H and heavy atoms
c3	carbon, SP3, in methyl group
c=	carbon, non-aromatic, doubly bonded
c=1	carbon, non-aromatic, doubly bonded, next to end
cp	carbon, SP2, aromatic

Chapter 6 – Experimental

_____

6.1.2.4.4 Forcite

Forcite is a module in Materials Studio that holds a collection of molecular mechanics tools.[123] This module was initially used for the parameterisation of the cvff force field, which was specifically optimised for the β-haematin crystal. Ligands were prepared for succeeding simulations, where the molecules were typed with the force field, the geometries were optimised, and the initial energies calculated. Most of these processes for large batches of molecules were automated by generated scripts. The final parameters used for the energy calculations and geometry optimisations are tabulated in Table 47 and Table 48, respectively.

Table 47: Energy parameters used for the Forcite energy calculations.

Energy	
Force field	cvff (parameterised for β-haematin)
Charges	Charge using QEq
Quality	2×10^{-5} kcal.mol^{-1}
Summation method – electrostatics	Ewald
Summation method – van der Waals	Group based

Table 48: Energy parameters used for the Forcite geometry optimisation calculations.

Energy	
Force field	cvff (parameterised for β-haematin)
Charges	Charge using QEq
Quality	2×10^{-5} kcal.mol^{-1}
Summation method – electrostatics	Group based
Summation method – van der Waals	Group based
Geometry optimisation	
Algorithm	Conjugate gradient
Quality	2×10^{-5} kcal.mol^{-1}
Maximum iterations	20 000

6.1.2.4.6 Morphology

The Morphology module within Materials Studio allows for the determination of the overall morphology of crystalline materials, as well as the investigation of the growth of the faces.[123] In this project, the morphology tool was utilised to determine the theoretical growth morphology of β-haematin and to locate the fastest and second-fastest growing faces. The parameters used are tabulated in Table 49.

Table 49: Energy parameters used for the growth morphology calculations.

Energy	
Force field	cvff (parameterised for β-haematin)
Charges	Charge using QEq
Quality	2×10^{-5} kcal.mol^{-1}
Summation method – electrostatics	Ewald
Summation method – van der Waals	Group based

6.1.2.4.7 The adsorption locator

The Adsorption locator module in Materials studio is designed to find low energy adsorption sites on substrates, or to investigate the preferential adsorbed geometries of compounds.[123] Either single molecules or mixtures could be adsorbed onto a substrate. Possible adsorption geometries were determined by means of Monte Carlo simulations, while the temperature was slowly decreased. This process was then repeated several times in order to obtain the lowest energy adsorbed geometry.

In order to obtain the best adsorption results, the ligands adsorbed and the substrate were prepared by means of a Forcite geometry optimisation, at the same quality as required in the adsorption calculation. Moreover, the calculation was optimised to obtain the best time

efficiency, and output quality. The results were deemed optimised, when a standard deviation of 1 kcal.mol^{-1} was obtained over three calculations, and when a higher quality and more timely calculation produced the same result. The final parameters used are tabulated in Table 50.

Table 50: Energy parameters used for the adsorption molecular mechanics calculations.

Energy	
Force field	cvff (parameterised for β-haematin)
Charges	Charge using QEq
Quality	2×10^{-5} kcal.mol^{-1}
Summation method – electrostatics	Ewald
Summation method – van der Waals	Group based
Simulated annealing	
Number of cycles	5
Steps per cycle	500 000*
Geometry optimisation	
Algorithm	Conjugate gradient
Quality	2×10^{-5} kcal.mol^{-1}
Maximum iterations	20 000

* *For larger molecules, 700 000 steps per cycle was used.*

_____

6.1.2.4.8 The Forcite Anneal Dynamics protocol

The Forcite Anneal Dynamics protocol is designed to overcome energy barriers in a computational system.[123] For this protocol a specified number of annealing cycles was performed where the temperature was increased to a chosen mid-cycle temperature and then slowly decreased back to the chosen initial temperature (Table 51). For each of these temperature steps, a specified number of dynamics steps were performed. In the end, an ultra-fine geometry optimisation was applied in order to refine the final output geometry.

Table 51: Annealing parameters used for the final adsorption minimisation calculations.

Annealing	
annealing cycles	100
Initial temperature	300 K
Mid-cycle temperature	500 K
Heating ramps per cycle	5
Dynamics steps per ramp	100
Dynamics	
Ensemble	NVE
Initial velocities	random
Time step	1.5 fs
Integration tolerance	50 000 kcal.mol^{-1}
Geometry optimisation	
Algorithm	Conjugate gradient
Quality	2×10^{-5} kcal.mol^{-1}
Maximum iterations	20 000

_____

6.2 SYNTHESIS

6.2.1 General procedures

6.2.1.1 Purification of solvents and reagents.

All chemicals used in these experiments were purchased from Merck, Kimmix Chemicals, or Sigma Aldrich. Solvents used for thin layer and column chromatographic purposes were distilled by means of conventional distillation procedures. Tetrahydrofuran was distilled from sodium metal, using benzophenone as indicator, and ethanol was distilled from magnesium turnings and iodine. Both of these solvents were distilled under a positive pressure of nitrogen gas. All other solvents used were pre-dried over molecular sieves (pore diameter 4 Å) for a minimum of three days.

6.2.1.2 Chromatography

The chromatography techniques utilised in this project are tabulated in Table 52, where compounds on the TLC plates were viewed under UV light and if necessary stained using prepared solutions of $KMnO_4$, or ninhydrin, followed by heating.

Table 52: Chromatography techniques utilised

Chromatography	Materials used
Thin layer chromatography	Merck silica gel 60 F254 coated on aluminium sheets.
Column chromatography	Merck silica gel (particle size 0.063-0.200 mm, 60 Å)

_____

6.2.1.3 Spectroscopic and physical data

The relevant techniques applied to achieve full characterisation of synthesised compounds, are tabulated in Table 53.

Table 53: Techniques applied to achieve full characterisation of synthesised compounds

Techniques applied	Instruments
Spectroscopy analysis	
NMR spectroscopy	300 MHz Varian VNMRS (75 MHz for ^{13}C)
(^{1}H, ^{13}C, COSY and gHSQC)	400 MHz Varian Unity Inova (101 MHz for ^{13}C)
	600 MHz Varian Unity Inova (150 MHz for ^{13}C)
Infrared spectroscopy (FTIR)	Thermo Nicolet Nexus 470,
	Attenuated Total Reflectance (ART) mode
Spectrometry analysis	
Mass spectrometry (MS)	Waters SYNAPT G2
	(Includes reverse phase liquid chromatography, LC-MS)
Physical analysis	
Melting points	Gallenkamp Melting Point Apparatus

6.2.1.4 Other general procedures

Reactions were performed under a positive pressure of nitrogen gas, unless water was used as a solvent, or when atmospheric oxygen was needed as an oxidant. The glassware was pre-dried at 120 °C for a minimum of two hours.

Solvents were removed *in vacuo*, where the bulk of the solvent was removed by using a rotary evaporator, followed by removal of trace amounts of solvent using a high vacuum pump at ca. 0.08 mm Hg.

6.2.2 Experimental work pertaining to Chapter 4.1

6.2.2.1 Towards the small quinoline inhibitor -S2

6.2.2.1.1 3,3-Diethoxypropanoic acid - 2

A 250 mL two-neck round bottom flask was fitted with a reflux condenser. This was charged with sodium hydroxide (1.5 equivalents, 1.58 g, 39.4 mmol), which was dissolved in water (20 mL). Ethyl 3,3-diethoxypropanoate (4.90 mL, 5.00 g, 26.3 mmol) was added to this, whereupon the reaction mixture was refluxed at 110 °C for 4 hours.

Upon completion, the reaction was allowed to cool to room temperature, where after the starting material was extracted with ethyl acetate (3 x 30 mL). The basic water layer was neutralised with a 2M solution of hydrochloric acid, whereupon the product was extracted with ethyl acetate (3 x 30 mL). The organic layer was washed with brine, dried over magnesium sulphate and filtered. The filtrate was concentrated *in vacuo* to yield the crude polar title compound **2** (3.65 g, 22.4 mmol, 85%), as a light yellow oil. This was used without further purification.
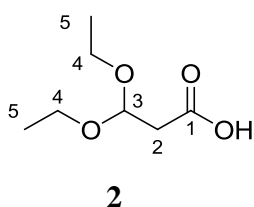
IR (ATR, cm^{-1}): 3427 (O-H str), 3090 - 2563 (C-H str), 1667 (C=O str), 1601 (C=C str), 1426, 1305, 1211. **^{1}H NMR (300 MHz, CDCl$_3$)** **δ** 7.69 (m, J = 12.5, 4.5 Hz, 1H, H$_3$), 5.18 (d, *J* = 12.6 Hz, 2H, H$_2$), 3.95 (q, *J* = 7.0 Hz, 4H, H$_4$), 1.36 (t, *J* = 7.1 Hz, 6H, H$_5$). **^{13}C NMR (75 MHz, CDCl$_3$) δ** 173.5 (C$_1$), 164.6 (C$_3$), 95.7 (C$_4$), 67.3 (C$_2$), 14.5 (C$_5$). **HRMS:** The molecular ion was not found.

_____

6.2.2.1.2 (E)-N-(3-Chlorophenyl)-3-ethoxyacrylamide - 5

3,3-Diethoxypropanoic acid (10.0 g, 61.7 mmol) was dissolved in dichloromethane (5 mL) and added to a 250 mL two-neck flask, fitted with a reflux condenser. Thionyl chloride (30 mL) was slowly added to this, whereupon the reaction mixture was heated to 80 °C overnight.

After 18 h, the thionyl chloride was evaporated off and the crude product ($R_f = 0.36$, 10% EtOAc/Hexane) was dissolved in dichloromethane (10 mL), whereafter this mixture was transferred into a dropping funnel. A 250 mL two-neck flask was fitted with the dropping funnel and was charged with 3-chloroaniline (0.6 equivalents, 3.9 mL, 4.74 g, 37.2 mmol), dichloromethane (10 mL), and pyridine (10 mL). The crude product obtained above was then added drop-wise to the 3-chloroanaline mixture, where after the reaction mixture was heated to 40 °C overnight.

Upon completion, the reaction was quenched with water and slowly acidified with a 2M hydrochloric acid solution. The product was extracted with dichloromethane (3 x 100 mL) and the organic layer was washed with brine, dried over magnesium sulphate and filtered. The filtrate was concentrated *in vacuo* to yield the residue that was further purified by column chromatography (5% EtOAc/Hexane). The product was recrystallised from hot ethyl acetate, to afford the title compound **5** (3.47 g, 15.4 mmol, 41% (crude)) ($R_f = 0.29$, 20% EtOAc/Hexane), as white needles.

_____

5
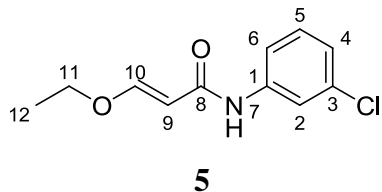
Mp 75-80 °C. **IR (ATR, cm^{-1}):** 3281 (C-H str), 2978 (C-H str), 1658 (C=O str), 1589 (C=C str), 1525, 1406, 1342, 1281. **^{1}H NMR (600 MHz, DMSO-d$_6$)**

δ 9.90 (s, 1H, H$_7$), 7.85 (t, *J* = 2.0 Hz, 1H, ArH), 7.50 (d, *J* = 12.3 Hz, 1H, H$_{10}$), 7.42 (ddd, *J* = 8.3, 2.0, 0.9 Hz, 1H, ArH), 7.30 (t, *J* = 8.1 Hz, 1H, ArH), 7.06 (ddd, *J* = 7.9, 2.2, 0.9 Hz, 1H, ArH), 5.49 (d, *J* = 12.3 Hz, 1H, H$_9$), 3.96 (d, *J* = 7.0 Hz, 2H, H$_{11}$), 1.27 (t, *J* = 7.1 Hz, 3H, H$_{12}$). **^{13}C NMR (150 MHz, CDCl$_3$) δ** 165.4 (C$_8$), 161.8 (C$_{10}$), 139.6, 134.7, 130.1, 124.1, 120.13, 118.0, 98.8 (C$_9$), 67.7 (C$_{11}$), 14.8 (C$_{12}$). **HRMS:** calcd for C$_{11}$H$_{13}$NO$_2$Cl [M+H]$^+$, 226.0635 and 228.0608, found 226.0606 and 228.0608. (100 and 33% MS peak ratio)

6.2.2.1.2 2,7-Dichloroquinoline - S2

(E)-N-(3-Chlorophenyl)-3-ethoxyacrylamide (3.27 g, 14.5 mmol) was dissolved in 10 mL dichloromethane in a 250 mL two-neck round bottom flask. The reaction mixture was cooled to 0 °C by means of an ice bath, whereupon concentrated sulphuric acid (21 mL) was slowly added over a period of 15 minutes. This was allowed to slowly heat to room temperature overnight.

The resulting mixture was quenched with aqueous ammonium chloride and filtered, whereupon the resulting residue was washed with hexane. The water layer was extracted with ethyl acetate (3 x 80 mL). The organic layer was washed with brine, dried over magnesium sulphate and filtered. The filtrate was combined with the previously obtained residue and concentrated *in vacuo* to afford a waxy orange residue.

A 250 mL two-neck flask was fitted with a reflux condenser, and was charged with the waxy orange residue and phosphorus oxychloride (10 mL). The reaction mixture was refluxed at 110 °C overnight.

After the 18 h time period, the reaction was quenched on ice and the product was extracted with ethyl acetate (3 x 80 mL). The organic layer was washed with brine, dried over magnesium sulphate and filtered. The filtrate was concentrated *in vacuo* to yield the residue that was purified by column chromatography (2% EtOAc/Hexane) to afford compound **S3** (80 mg, 0.404 mmol, 3%) (R_f = 0.75, 20% EtOAc/Hexane), as a white solid, and the title compound **S2** (887 mg, 4.48 mmol, 31%) (R_f = 0.83, 20% EtOAc/Hexane), as a white solid with a purity of 98.4% as determined by means of LC-MS.
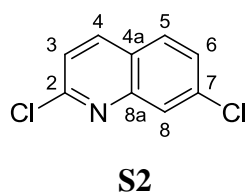
Mp 98-101 °C. **IR (ATR, cm^{-1}):** 3050 (C-H str), 1605 (C=C str), 1580, 1479 (C=C str), 1412, 1328, 1281. **^{1}H NMR (400 MHz, CDCl$_3$) δ** 8.53 (d, *J* = 8.8 Hz, 1H, H$_4$), 7.96 (dd, *J* = 7.5, 2.0 Hz, 1H, H$_5$), 7.69 − 7.61 (m, 2H, H$_8$ and H$_6$), 7.50 (d, *J* = 8.8 Hz, 1H, H$_3$). **^{13}C NMR (101 MHz, CDCl$_3$) δ** 151.8, 148.7, 136.1 (C$_4$), 131.6 (C$_8$), 130.6 (C$_5$), 127.9(C$_6$), 127.3, 125.3 (C$_3$), 123.4. **HRMS:** calcd for C$_9$H$_6$NCl$_2$ [M+H]$^+$, 197.9877 and 199.9848, found 197.9875 and 199.9847. (100 and 64% MS peak ratio).
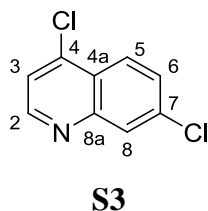
Mp 81-83 °C. **IR (ATR, cm^{-1}):** 3081 (C=C), 1581, 1558, 1490, 1454, 1388, 1289. **^{1}H NMR (400 MHz, DMSO-d$_6$) δ** 8.08 (d, *J* = 8.6 Hz, 1H, H$_2$), 8.02 (d, *J* = 1.9 Hz, 1H, H$_8$), 7.76 (d, *J* = 8.7 Hz, 1H, H$_5$), 7.52 (dd, *J* = 8.6, 2.0 Hz, 1H, H$_6$), 7.39 (d, *J* = 8.5 Hz, 1H, H$_3$). **^{13}C NMR (101 MHz, CDCl$_3$) δ** 152.0, 148.3, 138.7 (C$_2$), 136.8, 128.9 (C$_6$), 128.2 (C$_5$), 127.8 (C$_8$), 125.3 (C$_3$), 122.7.

The ^{1}H NMR and the IR characterisation of compound **S3** are in agreement with that reported by Theeraladanon *et al.* and Cui *et al.*[200,201]

6.2.2.2 The synthesis of the carbazole compounds

6.2.2.2.1 2-Nitrobiphenyl - 10

A 50 mL two-neck round bottom flask, fitted with a reflux condenser, was charged with *N,N*-dimethylformamide (20 mL) and water (4 mL). To this was added 1-bromo-2-nitrobenzene (300 mg, 1.49 mmol), phenylboronic acid (1.5 equivalents, 272 mg, 2.23 mmol), potassium carbonate (2 equivalents, 410 mg, 2.97 mmol), and palladium-tetrakis(triphenylphosphine) (5 mol %, 85.5 mg, 0.0743 mmol). The reaction mixture was heated to 80 °C for 5 hours under a positive pressure of nitrogen gas.

Upon completion, the reaction was quenched with water and the product was extracted with ethyl acetate (3 x 30 mL). The organic layer was washed with brine, dried over magnesium sulphate and filtered. The filtrate was concentrated *in vacuo* to yield the residue that was purified by column chromatography (5% EtOAc/Hexane) to afford the title compound **10** (248 mg, 1.35 mmol, 91%) (R$_f$ = 0.63, 10% EtOAc/Hexane), as yellow crystals.
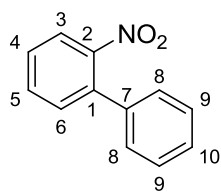
Mp 40-45 °C. **IR (ATR, cm^{-1}):** 2922 (C-H str), 2853 (C-H str), 1519 (C=C str), 1470 (C=C str), 1354 (N=O str). **^{1}H NMR (300 MHz, CDCl$_3$) δ** 7.89 – 7.83 (m, 1H, H$_3$), 7.65 – 7.59 (m, 1H, H$_4$), 7.52 – 7.40 (m, 5H, ArH), 7.36 – 7.31 (m, 2H, ArH). **^{13}C NMR (101 MHz, CDCl$_3$) δ** 149.4 (C$_2$), 137.5, 136.4, 132.4, 132.1, 128.8, 128.3, 128.3, 128.0, 124.2. **HRMS:** calcd for C$_{12}$H$_{10}$NO$_2$ [M+H]$^+$, 200.0712, found 200.0717.

6.2.2.2.2 9-H Carbazole - S6

A 50 mL round bottom flask was charged with dry tetrahydrofuran (15 mL) and 2-nitrobiphenyl (200 mg, 1.09 mmol) under a positive pressure of nitrogen gas. The reaction mixture was cooled to 0 °C by means of an ice bath. Phenylmagnesium bromide (1M in tetrahydrofuran) (4.5 equivalents, 6,0 mL, 5.90 mmol) was slowly added to the reaction mixture over a period of 20 minutes.

The reaction mixture was allowed to stir for another 10 minutes, whereupon it was quenched with aqueous ammonium chloride. Subsequently, the product was extracted with ethyl acetate (3 x 30 mL), where after the organic layer was washed with brine, dried over magnesium sulphate and filtered. The filtrate was concentrated *in vacuo* to yield the residue that was purified by column chromatography (5% EtOAc/Hexane) to afford the title compound **S6** (157 mg, 0.939 mmol, 86%) (R$_f$ = 0.17, 2% EtOAc/Hexane), as light brown crystals with a purity of 99.8% as determined by means of LC-MS.
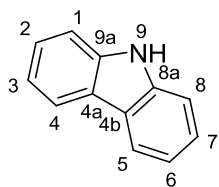
Mp 235-239 °C. **IR (ATR, cm^{-1}):** 3416 (N-H str), 3048 (C-H str), 1596, 1449, 1323. **^{1}H NMR (600 MHz, DMSO-d$_6$) δ** 11.22 (s, 1H, H$_9$), 8.10 (d, *J* = 7.8 Hz, 2H, H$_4$ and H$_5$), 7.48 (d, *J* = 8.1 Hz, 2H, H$_2$ and H$_7$), 7.37 (ddd, *J* = 8.2, 7.1, 1.2 Hz, 2H, H$_3$ and H$_6$), 7.19 − 7.05 (m, 2H, H$_1$ and H$_8$). **^{13}C NMR (150 MHz, CDCl$_3$) δ** 139.6, 126.0, 123.5, 120.5, 119.6, 110.7. **HRMS:** calcd for C$_{12}$H$_{10}$N [M+H]$^+$, 168.0813, found 168.0816.

6.2.2.2.3 Attempted synthesis of 4-chloro-2-nitrobiphenyl - 12

The same procedure was used as for preparing compound **10** in Section 6.2.2.2.1.

The equivalents used were as follows: *N*,*N*-dimethylformamide (20 mL), water (4 mL), 1-bromo-4-chloro-2-nitrobenzene (350 mg, 1.49 mmol), phenylboronic acid (1.5 equivalents, 272 mg, 2.23 mmol), potassium carbonate (2 equivalents, 410 mg, 2.97 mmol), and palladium-tetrakis(triphenylphosphine) (5 mol %, 85.5 mg, 0.0743 mmol).

Upon completion, the reaction was quenched with water and the product was extracted with ethyl acetate (3 x 30 mL). The organic layer was washed with brine, dried over magnesium sulphate and filtered. The filtrate was concentrated *in vacuo* to yield the residue that was purified by column chromatography (5% EtOAc/Hexane). Unfortunately, the title compound was not isolated, as another product co-eluted with the final compound. This additional product might have been 4-bromo-3-nitrobiphenyl, where the coupling reaction occurred at the 3-position of the benzene ring. This mixture of compounds was isolated (269 mg) (R$_f$ = 0.44, 2% EtOAc/Hexane) as a yellow powder.
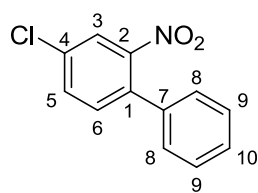
12 (crude)

Mp 95-98 °C. **IR (ATR, cm^{-1}):** 2924 (C-H str), 1527 (C=C str), 1474 (C=C str), 1358 (N=O str). **HRMS:** calcd for $C_{12}H_9ClNO_2$ [M+H]$^+$, 234.0322 and 236.0296, found 234.0968 and 236.1191. (100 and 33% MS peak ratio)

6.2.2.2.4 Attempted synthesis of 2-chloro-9H-carbazole - S7

The same procedure was used as for preparing compound **S6** in Section 6.2.2.2.2.

The equivalents used were as follows: dry tetrahydrofuran (15 mL), 4-chloro-2-nitrobiphenyl (297 mg, 1.27 mmol), and phenylmagnesium bromide (1M in tetrahydrofuran) (4.5 equivalents, 5.7 mL, 5.72 mmol).

The reaction was quenched with aqueous ammonium chloride. The product was extracted with ethyl acetate (3 x 30 mL), whereupon the organic layer was washed with brine, dried over magnesium sulphate and filtered. The filtrate was concentrated *in vacuo* to yield the residue that was purified by column chromatography (5% EtOAc/Hexane).

This product decomposed from white crystals, in the presence of light within a time period of 30 minutes, to a light blue powder. Unfortunately, the formation of multiple compounds was observed when analysed by means of thin layer chromatography.

_____

6.2.2.3 Towards the 4-amino-7-chloroquinoline - S11

6.2.2.3.1 4-Azido-7-chloroquinoline - 14

A 50 mL two neck round bottom flask, fitted with a reflux condenser, was charged with dimethylsulfoxide (10 mL), sodium azide (1.2 equivalents, 790 mg, 12.2 mmol), and 4,7-dichloroquinoline (2.0 g, 10.1 mmol). The reaction was heated to 60 °C for 18 hours, under a positive pressure of nitrogen.

Upon completion, the reaction was quenched with water and the product was extracted with ethyl acetate (3 x 30 mL). The organic layer was washed with brine, dried over magnesium sulphate and filtered. Afterwards, the filtrate was concentrated *in vacuo* to yield the residue that was purified by column chromatography (10% EtOAc/Hexane) to afford the title compound **14** (1.9 g, 9.43 mmol, 93%) (Rf = 0.74, 40% EtOAc/Hexane), as a white powder.

14
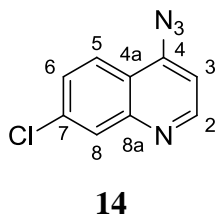
Mp 92-95 °C. **IR (ATR, cm^{-1}):** 3070 (C-H str), 2325, 2250 (N$_3$ str), 1612 (C=C bend), 1560, 1535, 1447, 1322. **^{1}H NMR (300 MHz, DMSO-d$_6$) δ** 8.85 (d, *J* = 5.0 Hz, 1H, H$_3$), 8.07 − 8.03 (m, 1H, H$_6$), 7.99 (dd, *J* = 8.6, 5.5 Hz, 1H, H$_8$), 7.63 (dd, *J* = 8.9, 2.2 Hz, 1H, H$_5$), 7.48 (d, *J* = 5.0 Hz, 1H, H$_2$). **^{13}C NMR (75MHz, DMSO-d$_6$) δ** 152.0, 148.9, 145.7, 135.1, 127.6, 127.3, 124.1, 119.4, 110.3.

The ^{1}H NMR and the IR characterisation are in agreement with that reported by Pereira *et al.* and Hollywood *et al.*[166,167]

_____

6.2.2.3.2 4-Amino-7-chloroquinoline - S11

A 50 mL round bottom flask, fitted with a rubber septum, was charged with dimethyl sulphoxide (2 mL), dry ethanol (10 mL), and 4-azido-7-chloroquinoline (1.9 g, 9.43 mmol). To this was added one table spoon of activated Raney®-Nickel, three times, at 4 hour intervals (12 hours in total), while the reaction was kept under a positive pressure of hydrogen gas. After the last addition of Raney®-Nickel, the reaction was left to stir overnight.

Upon the full consumption of the starting material, the reaction mixture was filtered through celite, and washed with ethyl acetate. The filtrate was concentrated *in vacuo* to yield the residue that was purified by column chromatography (40% EtOAc/Hexane) to afford the title compound **S11** (1.3 g, 7.23 mmol, 77%) (R_f = 0.00, 40% EtOAc/Hexane), as a yellow solid with a purity of 92.0% as determined by means of LC-MS.

S11
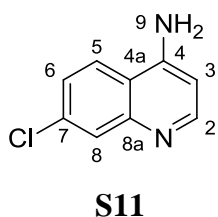
Mp 70-75 °C. **IR (ATR, cm^{-1}):** 3422 (C-N str), 3255 (C-H str), 1644 (N-H bend), 1562, 1507, 1481, 1430, 1288. **^{1}H NMR (400 MHz, DMSO-d$_6$) δ** 8.30 (d, *J* = 5.2 Hz, 1H), 8.18 (d, *J* = 9.0 Hz, 1H), 7.76 (d, *J* = 2.2 Hz, 1H), 7.39 (m, 1H), 6.93 (s, 2H, H$_9$), 6.52 (dd, *J* = 19.9, 5.3 Hz, 1H, H$_3$). **^{13}C NMR (101 MHz, DMSO-d$_6$) δ** 151.7, 151.6, 149.5, 133.5, 127.4, 124.7, 123.8, 117.1, 102.7. **HRMS:** calcd for C$_9$H$_8$N$_2$Cl [M+H]$^+$, 179.0376 and 181.0348, found 179.0381 and 181.0342 (100 and 33% MS peak ratio)

_____

6.2.3 Experimental work pertaining to Chapter 4.2

6.2.3.1 Towards the 2-aminoindole

The synthesis of the 2-aminoindole was briefly mentioned in Chapter 4.2. Unfortunately, this compound was not successfully isolated and the quinoline scaffold was rather used in this project. Therefore, this section is only included for the curious reader.

6.2.3.1.1 Attempted synthesis of 2,6-dichloro-1H-indole

A 250 mL two-neck flask was fitted with a reflux condenser, and charged with 6-chloroindolin-2-one (500 mg, 2.98 mmol) and phosphorus oxychloride (10 mL). The reaction mixture was refluxed at 110 °C and monitored over a period of 5 hours.

Upon completion, the reaction was quenched on ice and the product was extracted with ethyl acetate (3 x 80 mL). The organic layer was washed with brine, dried over magnesium sulphate and filtered. The filtrate was concentrated *in vacuo* to yield the residue that was purified by column chromatography (5% EtOAc/Hexane) to afford a compound (R_f = 0.69, 20% EtOAc/Hexane), as white crystals. Unfortunately, this compound turned dark of colour within 30 minutes, and decomposed into multiple compounds as determined by means of thin layer chromatography analysis.

Therefore, the desired product was not isolated and the compound that formed was used immediately for the subsequent reactions without purification.

6.2.3.1.2 Attempted synthesis of 6-chloro-1H-indol-2-amine

A 50 mL two-neck round bottom flask, fitted with a reflux condenser, was charged with *N*,*N*-dimethylformamide (10 mL). To this was added the crude 2,6-dichloro-1*H*-indole product obtained in Section 6.2.3.1.1, ammonium hydroxide (10 mL), potassium carbonate (2 equivalents, 824 mg, 5.97 mmol), and copper (I) iodide (10 mol%, 56.8 mg, 0.298 mmol). The reaction was heated to 110 °C, and monitored over a period of 5-24 hours.

Unfortunately, by monitoring the reaction by means of thin layer chromatography, the formation of multiple compounds was observed, and neither the final amine product, nor the starting indole reagent, were isolated.

The reaction conditions were considered to be too harsh, and a milder synthesis route was considered *via* the formation of the azide intermediate, with the azide in the 2-position of the indole.

A 50 mL two neck round bottom flask, fitted with a reflux condenser, was charged with dimethylsulfoxide (10 mL), sodium azide (1.2 equivalents, 233 mg, 3.58 mmol), and the crude 2,6-dichloro-1*H*-indole product obtained in Section 6.2.3.1.1. The reaction was heated to 100 °C under a positive pressure of nitrogen, whereupon it was monitored over a period of 5- 24 hours.

To our dismay, by monitoring the reaction by means of thin layer chromatography, the formation of multiple compounds was observed, and as before, neither the final amine product nor the starting reagent were isolated.

6.2.3.1.3 Attempted synthesis of tert-butyl 2,6-dichloro-1H-indole-1-carboxylate

The crude 2,6-dichloro-1*H*-indole product obtained in Section 6.2.3.1.1 and di-*tert*-butyl dicarbonate (1.3 equivalents, 0.9 mL, 3.87 mmol) were added to 20 mL anhydrous tetrahydrofuran in a 50 mL two-neck round bottom flask at 30 °C. A catalytic amount of 4-dimethylaminopyridine was added and the reaction mixture was left to stir for 30 minutes.

The decomposition of the 2,6-dichloro-1*H*-indole compound was observed, as monitored by means of thin layer chromatography. The desired Boc-protected indole product was thus not obtained.

By performing these reactions, especially by attempting a Boc protection, it was clear that this 2,6-dichloro-1*H*-indole product was too unstable to use as the primary aromatic scaffold in this project.

6.2.3.2 Towards the amide target compounds

6.2.3.2.1 Attempted synthesis 2-aminoquinoline - RM16

A 50 mL two-neck round bottom flask, fitted with a reflux condenser, was charged with *N*,*N*-dimethylformamide (10 mL). To this was added 2-bromoquinoline (200 mg, 0.961 mmol), ammonium hydroxide (10 mL), and copper (I) iodide (10 mol%, 18.3 mg, 0.0961 mmol). The reaction was heated to 110 °C, and monitored over a period of 5-24 hours. Upon full consumption of the starting material, the reaction was quenched on ice, and the reaction mixture was neutralised with 2M hydrochloric acid.

Unfortunately, the product was not extracted, as it was found to be water soluble.

6.2.3.2.2 2-Azidoquinoline - 17

A 50 mL two neck round bottom flask, fitted with a reflux condenser, was charged with dimethyl sulphoxide (10 mL), sodium azide (1.2 equivalents, 113 mg, 1.73 mmol), and 2-bromoquinoline (300 mg, 1.44 mmol). The reaction was heated to 100 °C for 2 days, under a positive pressure of nitrogen gas.

Upon completion, the reaction was quenched with water and the product was extracted with ethyl acetate (3 x 30 mL). The organic layer was washed with brine, dried over magnesium sulphate and filtered. The filtrate was concentrated *in vacuo* to yield the residue that was purified by column chromatography (10% EtOAc/Hexane) to afford the title compound **17** (183 mg, 1.07 mmol, 75%) (R$_f$ = 0.21, 20% EtOAc/Hexane), as a white powder.
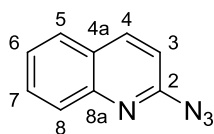
Mp 130-134 °C. **IR (ATR, cm^{-1}):** 3070 (C-H str), 2325, 2250 (N$_3$ str), 1612 (C=C bend), 1560, 1535, 1447, 1322. **^{1}H NMR (300 MHz, DMSO-d$_6$) δ** 8.64 (d, J = 8.3 Hz, 1H), 8.28 (dd, J = 15.3, 8.7 Hz, 2H), 8.10 (d, J = 9.4 Hz, 1H), 8.00 (m, 1H), 7.83 (dd, J = 8.0, 7.3 Hz, 1H). **^{13}C NMR (75 MHz, DMSO-d$_6$) δ** 134.1, 131.5, 129.5, 128.2, 123.8, 116.2, 112.4. **HRMS:** calcd for C$_9$H$_7$N$_4$ [M+H]$^+$, 171.0671, found 171.0652.

Not all of the ^{13}C peaks are accounted for. However, the mass spectrometry and infrared spectroscopy results indicate that compound **17** was indeed isolated.

6.2.3.2.3 2-Aminoquinoline - RM16

A 50 mL round bottom flask, fitted with a rubber septum, was charged with dimethyl sulphoxide (2 mL), dry ethanol (10 mL), and 2-azidoquinoline (1.2 g, 7.21 mmol). To this

was added one table spoon of activated Raney®-Nickel, twice a day for 3 days. The reaction was kept under a positive pressure of hydrogen gas.

Upon full consumption of the quinoline starting material, the reaction mixture was filtered through celite, and washed with ethyl acetate. The filtrate was concentrated *in vacuo* to yield the residue that was purified by column chromatography (40% EtOAc/Hexane) to afford the title compound **RM16** (977 mg, 6.78 mmol, 94%) (R_f = 0.10, 40% EtOAc/Hexane), as a yellow powder with a purity of 91.3% as determined by means of LC-MS.
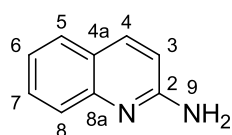
Mp 70-74 °C. **IR (ATR, cm^{-1}):** 3422 (C-N str), 3255 (C-H str), 1644 (N-H bend), 1562, 1507, 1481, 1430, 1288. **^{1}H NMR (400 MHz, DMSO-d$_6$) δ** 7.87 (d, *J* = 8.8 Hz, 1H, H$_4$), 7.61 (d, *J* = 7.8 Hz, 1H), 7.48 – 7.42 (m, 2H), 7.17 – 7.08 (m, 1H), 6.75 (d, *J* = 8.8 Hz, 1H, H$_3$), 6.41 (s, 2H, H$_9$). **^{13}C NMR (75 MHz, DMSO-d$_6$) δ** 158.2 (C$_2$), 148.0, 136.8, 129.0, 127.5, 125.1, 122.7, 121.1, 112.4. **HRMS:** calcd for C$_9$H$_9$N$_2$ [M+H]$^+$, 145.0759, found 145.0766.

RM16

6.2.3.2.4 Biphenyl-4-carbaldehyde - 19

A 50 mL two-neck round bottom flask, fitted with a reflux condenser, was charged with *N,N*-dimethylformamide (20 mL) and water (4 mL). To this was added 4-bromobenzaldehyde (300 mg, 1.62 mmol), phenylboronic acid (1.2 equivalents, 237 mg, 1.95 mmol), potassium carbonate (2 equivalents, 447 mg, 3.24 mmol), and palladium-tetrakis(triphenylphosphine) (5 mol%, 112 mg, 0.0810 mmol). The reaction mixture was heated to 100 °C for 2 days under a positive pressure of nitrogen gas.

The reaction was quenched with water and the product was extracted with ethyl acetate (3 x 30 mL). The organic layer was washed with brine, dried over magnesium sulphate and

filtered. The filtrate was concentrated *in vacuo* to yield the residue that was purified by column chromatography (5% EtOAc/Hexane) to afford the title compound **19** (175 mg, 0.960 mmol, 59%) (R$_f$ = 0.43, 5% EtOAc/Hexane), as a white powder.
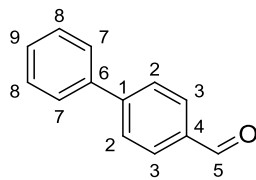
Mp 65-70 °C. **IR (ATR, cm^{-1}):** 3030-2737 (C-H str), 1695 (C=O str), 1601 (C=C str), 1562, 1484, 1450, 1412, 1288. **^{1}H NMR (300 MHz, CDCl$_3$) δ** 10.06 (d, *J* = 0.6 Hz, 1H, H$_5$), 8.03 − 7.88 (m, 2H, C$_3$), 7.74 (ddd, *J* = 7.7, 4.6, 2.2 Hz, 2H, C$_2$), 7.66 − 7.59 (m, 2H, C$_7$), 7.52 − 7.35 (m, 3H, C$_8$ and C$_9$). **^{13}C NMR (75 MHz, CDCl$_3$) δ** 192.1 (C$_5$), 147.3, 139.9, 135.3, 130.4, 129.1, 128.6, 127.8, 127.5. **HRMS:** calcd for C$_{13}$H$_{11}$O [M+H]$^+$, 283.0810, found 283.2805.

6.2.3.2.5 N-(Quinolin-2-yl) biphenyl-4-carboxamide - RM14

A 50 mL two-neck round bottom flask, fitted with a reflux condenser, was charged with *N*,*N*-dimethylformamide (10 mL) and water (0.5 mL). To this was added biphenyl-4-carbaldehyde (150 mg, 0.823 mmol), 2-aminoquinoline (1.2 equivalents, 142 mg, 0.988 mmol), potassium carbonate (2 equivalents, 302 mg, 1.65 mmol), and copper (I) iodide (10 mol%, 15.7 mg, 0.0823 mmol). The reaction was heated to 100 °C, for 2 days.

Once the aldehyde starting material was consumed, the reaction was quenched with water and the product was extracted with ethyl acetate (3 x 30 mL). The organic layer was washed with brine, dried over magnesium sulphate and filtered. The filtrate was concentrated *in vacuo* to yield the residue that was purified by column chromatography (10% EtOAc/Hexane) to afford the title compound **RM14** (86.7 mg, 0.267 mmol, 32%) (R$_f$ = 0.43, 20% EtOAc/Hexane), as a yellow powder with a purity of 99.4% as determined by means of LC-MS.

_____
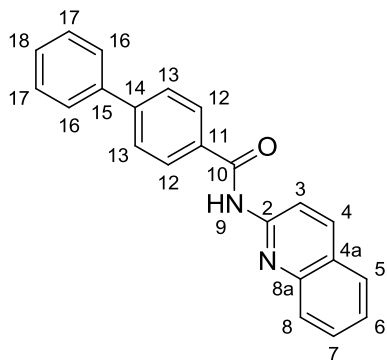
RM14

Mp 135-140 °C. **IR (ATR, cm^{-1}):** 3350-3330 (N-H str), 2831-2733 (C-H str), 1680-1695 (C=O str, N-H bend), 1596 (C=C str), 1567, 1492, 1423, 1315. **^{1}H NMR (300 MHz, DMSO-d$_6$) δ** 11.15 (s, J = 19.5 Hz, 1H, H$_9$), 8.40 (m, 2H), 8.23 – 8.17 (m, 2H), 7.96 (dd, J = 8.1, 1.1 Hz, 1H), 7.90 (d, J = 8.1 Hz, 1H), 7.87 – 7.81 (m, 2H), 7.81 – 7.73 (m, 3H), 7.57 – 7.48 (m, 3H), 7.46 – 7.40 (m, 1H). **^{13}C NMR (75 MHz, DMSO-d$_6$) δ** 166.1 (C$_{10}$), 151.9, 146.4, 143.6, 139.0, 138.1, 132.7, 130.0, 129.1, 128.9, 128.2, 127.8, 127.1, 126.9, 126.6, 125.8, 125.2, 115.5. **HRMS:** calcd for C$_{22}$H$_{16}$N$_2$O [M+H]$^+$, 325.1341, found 325.1357.

6.2.3.2.6 Attempted synthesis of 4-(7-chloroquinolin-2-yl) benzaldehyde - 21

The same procedure was used as for preparing compound **19** in Section 6.2.3.2.4.

The equivalents used were as follows: *N,N*-dimethylformamide (20 mL), water (4 mL), 4-formylphenylboronic acid (1.2 equivalents, 540 mg, 2.92 mmol), 2,7-dichloroquinoline (482 mg, 2.44 mmol), potassium carbonate (2 equivalents, 673 mg, 4.87 mmol), and palladium-tetrakis(triphenylphosphine) (5 mol %, 141 mg, 0.122 mmol).

Upon completion, the reaction was quenched with water and the product was extracted with ethyl acetate (3 x 30 mL). The organic layer was washed with brine, dried over magnesium sulphate and filtered. The filtrate was concentrated *in vacuo* to yield the residue that was purified by column chromatography (10% EtOAc/Hexane) to afford a mixture of compounds **21** and **22** (32.0 mg, 0.120 mmol, 5%) (R$_f$ = 0.50, 10% EtOAc/Hexane), as a white powder.

The reaction was repeated at 60 °C, but the formation of the same products was observed, as determined by means of thin layer chromatography analysis.

When integrating the two aldehyde protons in the ^{1}H NMR (10.08 and 10.07 ppm), a 2:1 ratio is obtained. It is most likely that compound **21** is the major product, since the 2-position of the quinoline is deemed more reactive than the 7-position. However, without separating these two compounds, this could not be resolved.
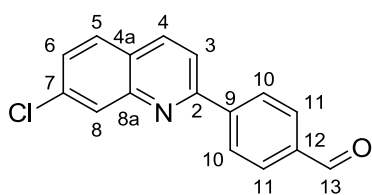
21
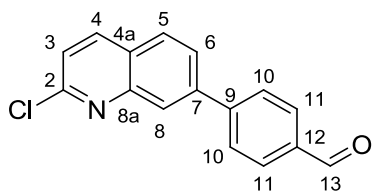
22

Mp 58-62 °C. **IR (ATR, cm^{-1}):** 3029-2731 (C-H str), 1696 (C=O str), 1591 (C=C str), 1211. **^{1}H NMR (300 MHz, DMSO-d$_6$) δ** 10.08 (s, *J* = 2.4 Hz, 1H), 10.07 (s, 2H), 8.01 − 7.93 (m, 7H), 7.81 − 7.63 (m, 12H), 7.60 − 7.37 (m, 12H), 7.34 − 7.27 (m, 7H).

6.2.3.2.7 Attempted synthesis of N-(quinolin-2-yl)-4-(quinolin-2-ylamino) benzamide -

RM12,

and synthesis of 4-bromo-N-(quinolin-2-yl) benzamide - RM15

A 50 mL two-neck round bottom flask was fitted with a reflux condenser and charged with *N,N*-dimethylformamide (10 mL). To this was added 4-bromobenzaldehyde (96.3 mg, 0.520 mmol), 2-aminoquinoline (2 equivalents, 150 mg, 1.04 mmol), potassium carbonate (2 equivalents, 193 mg, 1.40 mmol), and copper (I) iodide (10 mol%, 19.8 mg, 0.104 mmol). The reaction was heated to 100 °C, for 2 days under a positive pressure of nitrogen gas.

Unfortunately, the reaction did not proceed and the starting material was isolated. The reaction was repeated whereupon water (0.5 mL) was added, and the reaction was heated to 100 °C. This reaction mixture was left open to the atmosphere.

Upon completion, the reaction was quenched with water and the product was extracted with ethyl acetate (3 x 30 mL). The organic layer was washed with brine, dried over magnesium sulphate and filtered. The filtrate was concentrated *in vacuo* and the compounds that had formed were separated by column chromatography (40% EtOAc/Hexane). The title compound was not obtained. The intermediate, compound **RM15** (32.0mg, 0.0978 mmol, 19%) (Rf = 0.57, 80% EtOAc/Hexane), was however isolated as orange crystals with a purity of 92.0% as determined by means of LC-MS.
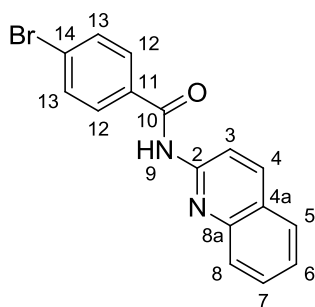
RM15

Mp 133-135 °C. **IR (ATR, cm^{-1}):** 3345 (N-H str), 3133-2852 (C-H str), 1692 (C=O str), 1598 (C=C str), 1537 (N-H bend), 1499 (N-H bend), 1426, 1333. **^{1}H NMR (600 MHz, DMSO-d$_6$)** **δ** 11.23 (s, 1H), 8.37 (dd, *J* = 52.6, 8.9 Hz, 2H), 8.06 − 7.82 (m, 4H, H$_{12}$ and H$_{13}$), 7.74 (m, 3H), 7.53 (dd, *J* = 11.0, 3.9 Hz, 1H).

^{13}C NMR (150 MHz, DMSO-d$_6$) δ 165.7, (C$_{10}$), 151.8, 146.4, 138.2, 137.3, 133.2, 131.4, 130.3, 130.1, 130.1, 127.9, 127.1, 126.0, 125.9, 125.3, 115.5.

HRMS: calcd for C$_{16}$H$_{11}$BrN$_2$O [M+H]$^+$, 327.0133 and 329.0114, found 327.0133 and 329.0116. (100 and 99% MS peak ratio).

Chapter 6 – Experimental

_____

6.2.3.2.8 N^1,N^4-di(quinolin-2-yl)benzene-1,4-diamine - RM17

### and N^1-(quinolin-2-yl)benzene-1,4-diamine - RM18

A 50 mL two-neck round bottom flask was fitted with a reflux condenser and charged with dry ethanol (15 mL), *N,N*-dimethylformamide (2 mL), 2-bromoquinoline (2.2 equivalents, 250 mg, 1.20 mmol), and benzene-1,4-diamine (59.0 mg, 0.546 mmol), whereupon the reaction was refluxed at 80 °C for 3 days under a positive pressure of nitrogen.

Upon completion, the solvent was removed *in vacuo* and the compounds that formed were purified by column chromatography (20% EtOAc/Hexane) to afford the title compound **RM17** (5 mg, 0.0138 mmol, 3%) (R_f = 0.57, 40% EtOAc/Hexane), as a light brown powder with a purity of 98.7 %, and compound **RM18** (25 mg, 0.106 mmol, 19%) (R_f = 0.37, 40% EtOAc/Hexane), as a light brown powder with a purity of 97.8% as determined by means of LC-MS. The remaining starting material, 2-bromoquinoline (74.0 mg, 0.356 mmol, 30%), was recovered.

In several attempts to improve the product yield, the reaction was allowed to proceed for a longer time period, more of compound **RM16** was added (3 equivalents), and potassium carbonate was added (1.3 equivalents, 100 mg, 0.724 mmol). Unfortunately, a higher product yield was not obtained.
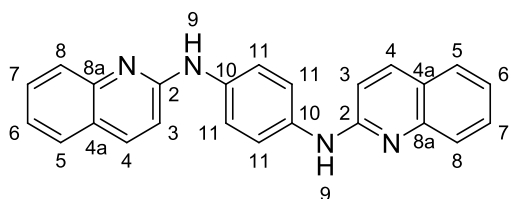
RM17

Mp 210-213 °C. **IR (ATR, cm^{-1}):** 3411-3390 (N-H str), 3045 (C-H str), 1619 (C=C str), 1538, 1509, 1392. **^{1}H NMR (300 MHz, DMSO-d$_6$) δ** 9.33 – 9.27 (m, 1H, H$_9$), 8.04 – 7.97 (m, 1H), 7.95 – 7.90 (m, 2H), 7.73 – 7.64 (m, 2H), 7.60 – 7.51 (m, 1H), 7.30 – 7.21 (m, 1H), 7.06 – 7.00 (m, 1H). **^{13}C NMR (75 MHz, DMSO-d$_6$) δ** 154.8, 147.4, 143.6, 136.4, 130.6,

129.2, 127.4, 125.9, 123.2, 121.7, 121.0, 114.2, 113.6. **HRMS:** calcd for $C_{24}H_{19}N_4$ [M+H]$^+$,

363.1613, found 363.1610.
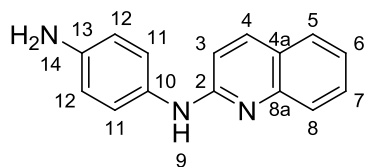
RM18

Mp 150-155 °C. **IR (ATR, cm^{-1}):** 3404-3331 (N-H str),

3045-3195 (C-H str), 1608 (C=C str), 1538, 1510, 1475,

1400, 1249. **^{1}H NMR (300 MHz, DMSO-d$_6$) δ** 8.89 (s,

1H, H$_9$), 7.99 − 7.82 (m, 1H), 7.64 (d, *J* = 7.8 Hz, 1H),

7.52 (ddd, *J* = 6.7, 3.6, 1.5 Hz, 4H), 7.23 − 7.14 (m, 1H), 6.91 (d, *J* = 9.0 Hz, 1H),

6.60 − 6.53 (m, 2H), 4.76 (s, 2H, H$_{14}$). **^{13}C NMR (75 MHz, DMSO-d$_6$) δ** 155.2, 147.9,

144.0, 136.8, 131.0, 129.5, 127.8, 126.3, 123.6, 122.2, 121.4, 114.6, 114.0. **HRMS:** calcd for

$C_{15}H_{14}N_3$ [M+H]$^+$, 236.1188, found 236.1184.

_____

6.3 β -HAEMATIN INHIBITION ASSAYS

6.3.1 General procedures

6.3.1.1 Solvents and reagents used

Chemicals used in these assays were purchased from Sigma Aldrich, where the solvents were either purchased from Sigma Aldrich or Kimix Chemicals.

6.3.1.1.1 General procedure for converting inhibitors into the free base form

Amodiaquine dihydrochloride dihydrate (300 mg, 0.645 mmol)(Table 54) was dissolved in hot distilled water (6 mL). This was slowly added to a 6M sodium hydroxide solution (20 mL) and heated for 2 min in a boiling water bath. This was allowed to cool to room temperature for the product to precipitate out, and left to stand for an additional 2 hours.

The precipitate was filtered, washed with a cold 1M sodium hydroxide solution (2 x 5 mL), and dried over phosphorus pentoxide (5.00 g, 17.7 mmol) in a desiccator for 3 days.

Table 54: Inhibitors converted into the free base form and the yields obtained

Inhibitor	Amount used	Free base obtained	% Yield
Amodiaquine dihydrochloride dihydrate	300 mg, 0.645 mmol	216 mg, 0.606 mmol	94%
Chloroquine diphosphate salt	300 mg, 0.582 mmol	169 mg, 0.530 mmol	91%

6.3.1.2 Spectroscopic data

UV-visible single wavelength readings (405 nm), were collected on a Thermo Scientific Mulitskan^{TM} GO UV-visible spectrophotometer.

6.3.1.3 Measuring pH

A Mettler Toledo FE20 pH meter was used to measure the pH of buffer solutions. The electrode was calibrated using pH buffer solutions (pH 4.0 and pH 7.0) purchased from Crison Instruments.

6.3.1.4 Temperature regulated incubation

The experiments were performed in a temperature regulated laboratory at 23 °C. The samples were incubated in a fan-assisted oven at 37 °C.

6.3.1.5 IC$_{50}$ determination

The data that were obtained were analysed using the GraphPad Prism v.6.0 software package.[202] A sigmoidal dose response curve was obtained by plotting the measured absorbance (nm) against the log of the concentration (μM). The required IC$_{50}$ data with the standard deviations from three replicate experiments were determined.

_____

6.3.2 Lipid β-haematin inhibition IC$_{50}$

6.3.2.1 Stock solutions prepared

6.3.2.1.1 50 Stock solution of citrate buffer (50 mM), pH4.8

Citric acid monohydrate (5.26 g, 25.0 mmol) was dissolved in distilled water (450 mL) in a 600 mL beaker. The pH was adjusted to 4.8 by the slow addition of a 6M sodium hydroxide solution. The solution was transferred to a 500 mL volumetric flask, where it was made to volume with distilled water.

6.3.2.2 Solubility testing

3,6-Dibromocarbazole (1.63 g, 0.500 mmol) and 4,7-dichloroquinoline (0.990 g, 0.500 mmol) were dissolved separately in various mixtures of the 50 mM citrate buffer stock solution (Section 6.3.2.1.1) and dimethyl sulfoxide, in 12 mL polytop glass vials (Table 55). The samples were incubated at 37 °C and monitored for 6 hours, where after it was left overnight.

Table 55: The time to precipitation of 0.5 mM drug solution in mixtures of acetate buffer and dimethyl sulfoxide were investigated.

Time to precipitation (h):	Ratio of dimethyl sulfoxide to acetate buffer				
	0:10	**1:9**	**2:8**	**3:7**	**4:6**
3,6-dibromocarbazole (0.5 mM)	0	0	0	0.5	>24
4,7-dichloroquinoline (0.5 mM)	0	4	>24	>24	>24

_____

6.3.3 NP40 β-haematin inhibition IC$_{50}$

6.3.3.1 Stock solutions prepared

6.3.3.1.1 NP40 solution

Distilled water (7.00 mL), dimethyl sulfoxide (1.00 mL), and NP40 (306 μM, 2.00 mL) were added to a 15 mL Falcon conical centrifuge tube. This was vortexed for 30 seconds. This solution was stored in the refrigerator.

6.3.3.1.2. Acetate buffer (1.0M), pH 4.8

Sodium acetate (8.20 g, 0.0100 mmol) was dissolved in distilled water (10.0 mL) in a 100 mL volumetric flask. Glacial acetic acid was added (2.40 mL), and the solution was made to volume with distilled water.

6.3.3.1.3 Haemin solution

Haemin (10.0 mg, 0.0153 mmol)) was dissolved in dimethyl sulfoxide (613 μL) in a 5 mL polytop glass vial and vortexed for 1 minute. This solution was freshly prepared daily.

6.3.3.1.4 Haemin in acetate buffer solution

The sodium acetate buffer (Section 6.3.3.1.2)(10.0 mL) was added to a 15 mL Falcon conical centrifuge tube. The haemin solution (Section 6.3.3.1.3)(72.0 μL) was added to this and the solution was vortexed for 1 minute. This was used without further delay.

_____

6.3.3.1.5 2M HEPES and pyridine solution

HEPES (4-(2-hydroxyethyl)-1-piperazineethanesulfonic acid) (4.77 g, 20 mmol) was dissolved in water (30.0 mL) in a 100 mL volumetric flask. Acetone (20.0 mL) was added and the solution was made to volume with pyridine.

6.3.3.1.6 Inhibitor stock solution

In order to prepare an inhibitor stock solution, the inhibitor was dissolved in dimethyl sulfoxide. The concentration used for each inhibitor varied (Table 56).

_____

Table 56: Inhibitor concentrations prepared for the NP40 assay.

Inhibitor	Concentration (mM)	Mass (mg)	Dimethyl sulfoxide (µL)
CQ free base	10.0	2.5	782
AQ free base	10.0	2.5	703
QC	10.0	2.5	529
KN6	10.0	2.5	900
KN7	10.0	2.5	805
S1	180	10	340
S2	180	7.0	196
S3	180	10	366
S4	180	10	281
S5	180	15	393
S6	180	6.0	199
S9	180	15	273
S10	180	15	300
S11	20	2.0	559
S12	180	15	339
S13	180	20	342
RM14	20	1.0	161
RM15	20	1.0	153
RM16	20	2.0	812
RM17	20	1.0	138
RM18	20	1.0	213

6.3.3.2 Determining the NP40 β-haematin inhibition IC$_{50}$

6.3.3.2.1 General procedure for performing the NP40 assay

This general procedure was reported by Dr Kathryn Wight.[122]

A 96-well plate was prepared by adding inhibitor stock solution (20.0 µL)(Section 6.3.3.1.6), NP40 solution (40.0 µL) (Section 6.3.3.1.1), and distilled water (140 µL) to 4 of the wells in the 12th column (Figure 97). NP40 solution (100 µL) (Section 6.3.3.1.1) was added to the remaining wells in the 4 rows.
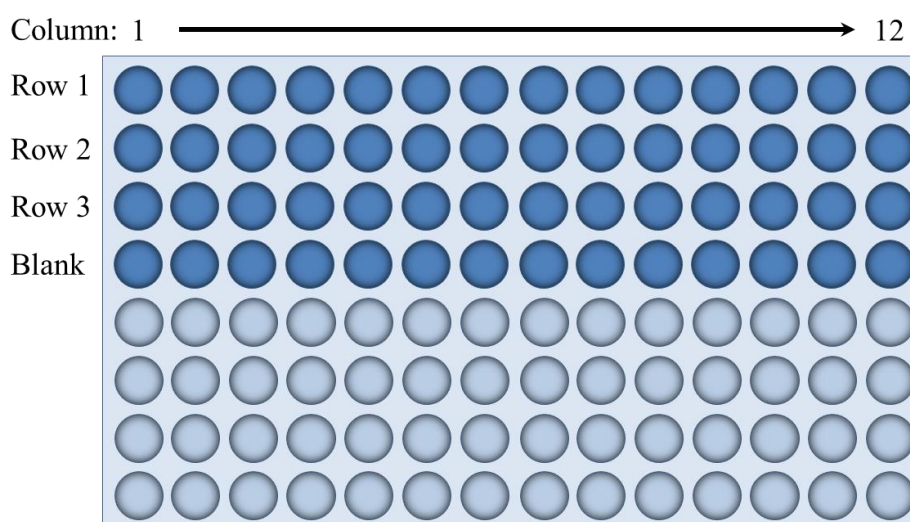
Figure 97: An illustration of the 96-well plate

A serial dilution was performed by transferring 100 µL of the mixture in the 12th column to the 11th column in the same row, halving the concentration. This was repeated down till the 2nd column, from which the 100 µL was discarded and not added to the 1st column.

A fresh solution of haemin (Section 6.3.3.1.4) was prepared and 100 µL was added to each of the wells of the first three rows. The 96-well plate was incubated with a lid for 5 hours.

After the 5 hour incubation period, 2M HEPES and pyridine solution was added (32.0 µL) (Section 6.3.3.1.5), followed by the addition of acetone (60.0 µL). This was allowed to stand for 5 minutes, where after the absorbance was measured at 405nm.

6.3.3.2.2 Determining the NP40 β-haematin inhibition IC$_{50}$

Using the GraphPad Prism 6.0 software package, the measured absorbance at 405 nm was plotted against the log of the concentration (µM). A sigmoidal dose response curve was fitted to the graph, from which the IC$_{50}$ value (µM) was readily determined. This value is reported as the EC$_{50}$ value in the software.

The standard deviation was calculated from the reported standard deviation log EC$_{50}$ and standard deviation EC$_{50}$ values by using Equation 6.3

$$SD = 0.434(SD\ EC_{50})(SD \log EC_{50})^{-1} \tag{6.3}$$

_____

CHAPTER 7 – REFERENCES

(1)   Cox, F. E. G. *Paristes & Vectors* **2010**, *3* (5), 1–9.

(2)   World Health Organisation. *World Malaria Report 2015*; France, 2015.

(3)   World Health Organisation. *Reversing the Incidence of Malaria 2000–2015*; France, 2015.

(4)   Sherman, I. W. *Malaria: Parasite Biology, Pathogenesis, and Protection*; American Society for Microbiology: Washington, 1998.

(5)   Jones, W. H. S.; Ross, R.; Ellett, G. G. *Malaria: A Neglected Factor in the History of Greece and Rome*; Macmillan & Co., Ltd.: London, 1907.

(6)   Phillips, R. S. *Malaria*; Edward Arnold Publishers, Ltd.: London, 1983.

(7)   Chandler, A. C.; Read, C. P. *Introduction to Parasitology*, 10th ed.; John Wiley & Sons, Inc.: New York, 1961.

(8)   Krafts, K.; Hempelmann, E. *Parasitol. Res.* **2012**, *111*, 1–6.

(9)   Flannery, E. L.; Chatterjee, A. K.; Winzeler, E. A. *Nat. Rev. Microbiol.* **2013**, *11* (12), 849–862.

(10)   Cone, M. Should DDT be used to combat Malaria? http://www.scientificamerican.com/article/ddt-use-to-combat-malaria/ (accessed Sep 19, 2016).

(11)   Laveran, C. L. A. *Rev. Infect. Dis.* **1982**, *4* (4), 908–911.

(12)   Weissbuch, I.; Leiserowitz, L. *Chem. Rev.* **2008**, *108* (11), 4899–4914.

(13)   Singh, B.; Daneshvar, C. *Clin. Microbiol. Rev.* **2013**, *26* (2), 165–184.

(14)   Florens, L.; Washburn, M. P.; Raine, J. D.; Anthony, R. M.; Grainger, M.; Haynes, J. D.; Moch, J. K.; Muster, N.; Sacci, J. B.; Tabb, D. L.; Witney, A. A.; Wolters, D.; Wu,

Y.; Gardner, M. J.; Holder, A. A.; Sinden, R. E.; Yates, J. R.; Carucci, D. J. *Nature* **2002**, *419* (6906), 520–526.

(15)   Bautista, J. M.; Marín-García, P.; Diez, A.; Azcárate, I. G.; Puyet, A. *J. Proteomics* **2014**, *97*, 107–125.

(16)   Sherman, I. W. *Microbiol. Rev.* **1979**, *43* (4), 453–495.

(17)   McNamara, C. W.; Lee, M. C. S.; Lim, C. S.; Lim, S. H.; Roland, J.; Nagle, A.; Simon, O.; Yeung, B. K. S.; Chatterjee, A. K.; McCormack, S. L.; Manary, M. J.; Zeeman, A.-M.; Dechering, K. J.; Kumar, T. R. S.; Henrich, P. P.; Gagaring, K.; Ibanez, M.; Kato, N.; Kuhen, K. L.; Fischli, C.; Rottmann, M.; Plouffe, D. M.; Bursulaya, B.; Meister, S.; Rameh, L.; Trappe, J.; Haasen, D.; Timmerman, M.; Sauerwein, R. W.; Suwanarusk, R.; Russell, B.; Renia, L.; Nosten, F.; Tully, D. C.; Kocken, C. H. M.; Glynne, R. J.; Bodenreider, C.; Fidock, D. A.; Diagana, T. T.; Winzeler, E. A. *Nature* **2013**, *504* (7479), 248–253.

(18)   Sherman, I. W. *Bull. World Health Organ.* **1977**, *55*, 211–225.

(19)   Goldberg, D. E.; Slater, A. F. G.; Cerami, A.; Henderson, G. B. *Proc. Natl. Acad. Sci.* **1990**, *871*, 2931–2935.

(20)   Ziegler, J.; Linck, R.; Wright, D. W. *Curr. Med. Chem.* **2001**, *8*, 171–189.

(21)   Rosenthal, P. J.; McKerrow, J. H.; Aikawa, M.; Nagasawa, H.; Leech, J. H. *J. Clin. Invest.* **1988**, *82* (5), 1560–1566.

(22)   Vander Jagt, D. L.; Hunsaker, L. A.; Campos, N. M. *Mol. Biochem. Parasitol.* **1986**, *18*, 389–400.

(23)   Scherman, I. W.; Tanigoshi, L. *Mol. Biochem. Parasitol.* **1983**, *8*, 207–226.

(24)   Aissi, E.; Bouquelet, S.; Biguet, J. *Comp. Biochem. Physiol. Part B* **1983**, *74* (3), 559–566.

(25)   Groman, N. B. *J. Infect. Dis.* **2016**, *88* (2), 126–150.

_____

(26)   Morrison, D. B.; Jeskey, H. A. *J. Natl. Malar. Soc.* **1948**, *7* (4), 259–264.

(27)   Ball, E. G.; McKee, R. W.; Anfinsen, C. B.; Cruz, W. O.; Geiman, Q. M. *J. Biol. Chem.* **1948**, *175*, 547–571.

(28)   Aikawa, M. H.; Sprinz, P.; Pathology, E. *J. Cell Biol.* **1966**, *28*, 355–373.

(29)   Olliaro, P. L.; Goldberg, D. E. *Parasitol. Today* **1995**, *11* (8), 294–297.

(30)   Fitch, C. D.; Kanjananggulpan, P. *J. Biol. Chem.* **1987**, *262* (32), 15552–15555.

(31)   Slater, A. F.; Swiggard, W. J.; Orton, B. R.; Flitter, W. D.; Goldberg, D. E.; Cerami, A.; Henderson, G. B. *Proc. Natl. Acad. Sci. U. S. A.* **1991**, *88* (2), 325–329.

(32)   Slater, A. F.; Cerami, A. *Nature* **1992**, *355* (6356), 167–169.

(33)   Sullivan, D. J.; Matile, H.; Ridley, R. G.; Goldberg, D. E. *J. Biol. Chem.* **1998**, *273* (47), 31103–31107.

(34)   Sullivan, D. J.; Gluzman, I. Y.; Russell, D. G.; Goldberg, D. E. *Proc. Natl. Acad. Sci. U. S. A.* **1996**, *93* (21), 11865–11870.

(35)   Papalexis, V.; Siomos, M. A.; Campanale, N.; Guo, X. G.; Kocak, G.; Foley, M.; Tilley, L. *Mol. Biochem. Parasitol.* **2001**, *115* (1), 77–86.

(36)   Akompong, T.; Kadekoppala, M.; Harrison, T.; Oksman, A.; Goldberg, D. E.; Fujioka, H.; Samuel, B. U.; Sullivan, D.; Haldar, K. *J. Biol. Chem.* **2002**, *277* (32), 28923–28933.

(37)   Noland, G. S.; Briones, N.; Sullivan, D. J. *Mol. Biochem. Parasitol.* **2003**, *130* (2), 91–99.

(38)   Dorn, A.; Stoffel, R.; Matile, H.; Bubendorf, A.; Ridley, R. G. *Nature* **1995**, *374* (6519), 269–271.

(39)   Egan, T. J.; Tshivhase, M. G. *Dalton Trans.* **2006**, *42*, 5024–5032.

(40)   Pagola, S.; Stephens, P. W.; Bohle, D. S.; Kosar, A. D.; Madsen, S. K. *Nature* **2000**,

404 (6775), 307–310.

(41)   Jackson, K. E.; Klonis, N.; Ferguson, D. J. P.; Adisa, A.; Dogovski, C.; Tilley, L. *Mol. Microbiol.* **2004**, *54* (1), 109–122.

(42)   Coppens, I.; Vielemeyer, O. *Int. J. Parasitol.* **2005**, *35* (6), 597–615.

(43)   Pisciotta, J. M.; Coppens, I.; Tripathi, A. K.; Scholl, P. F.; Shuman, J.; Bajad, S.; Shulaev, V.; Sullivan, D. J. *Biochem. J.* **2007**, *402*, 197–204.

(44)   Ambele, M. A.; Sewell, B. T.; Cummings, F. R.; Smith, P. J.; Egan, T. J. *Cryst. Growth Des.* **2013**, *13* (10), 4442–4452.

(45)   Bendrat, K; Berger, B.; Cerami, A. *Nature* **1995**, *378* (6553), 138–139.

(46)   Beaumelle, B. D.; Vial, H. J. *Vitr. Cell. Dev. Biol.* **2016**, *24* (7), 711–718.

(47)   Vial, H. J.; Ancelin, M. L. *Subcell. Biochem.* **1992**, *18*, 259–306.

(48)   Vial, H. J.; Eldin, P.; Tielens, A. G. M.; Hellemond, J. J. Van. *Mol. Biochem. Parasitol.* **2003**, *126*, 143–154.

(49)   Olafson, K. N.; Ketchum, M. A.; Rimer, J. D.; Vekilov, P. G. *Proc. Natl. Acad. Sci. U. S. A.* **2015**, *112* (16), 4946–4951.

(50)   de Villiers, K. A.; Osipova, M.; Mabotha, T. E.; Solomonov, I.; Feldman, Y.; Kjaer, K.; Weissbuch, I.; Egan, T. J.; Leiserowitz, L. *Cryst. Growth Des.* **2009**, *9* (1), 626–632.

(51)   Bohle, D. S.; Dinnebier, R. E.; Madsen, S. K.; Stephens, P. W. *J. Biol. Chem.* **1997**, *272* (2), 713–716.

(52)   Bominaar, E. L.; Ding, X.; Gismelseed, A.; Bill, E.; Winkler, H.; Trautwein, A. X.; Nasri, H.; Fischer, J.; Weiss, R. *Inorg. Chem.* **1992**, *31*, 1845–1854.

(53)   Gildenhuys, J.; le Roex, T.; Egan, T. J.; de Villiers, K. A. *Am. Chem. Soc.* **2013**, *135*, 1037–1047.

(54)   Buller, R.; Peterson, M. L.; Almarsson, Ö.; Leiserowitz, L. *Cryst. Growth Des.* **2002**, *2* (6), 553–562.

(55)   Hartman, P., Perdok, W. G. *Acta Crystallogr.* **1955**, *8*, 525–529.

(56)   Hartman, P., Perdok, W. G. *Acta Crystallogr.* **1955**, *8*, 521–524.

(57)   Hartman, P.; Perdok, W. G. *Acta Crystallogr.* **1955**, *8* (1), 49–52.

(58)   Hartman, P.; Bennema, P. *J. Cryst. Growth* **1980**, *49*, 145–156.

(59)   Bennema, P. *Cryst. Growth Des.* **2004**, *4* (5), 905–913.

(60)   Straasø, T.; Kapishnikov, S.; Kato, K.; Takata, M.; Als-Nielsen, J.; Leiserowitz, L. *Cryst. Growth Des.* **2011**, *11*, 3342–3350.

(61)   Marom, N.; Tkatchenko, A.; Kapishnikov, S.; Kronik, L.; Leiserowitz, L. *Cryst. Growth Des.* **2011**, *11* (8), 3342–3350.

(62)   World Health Organization. *Treatment of Severe Malaria*; Italy, 2015.

(63)   Morris, C. A.; Duparc, S.; Borghini-Fuhrer, I.; Jung, D.; Shin, C.; Fleckenstein, L. *Malar. J.* **2011**, *10* (1), 263.

(64)   U.S. Food and Drug Administration. FDA Approves Coartem Tablets to Treat Malaria http://www.fda.gov/NewsEvents/Newsroom/PressAnnouncements/ucm149559.htm (accessed Mar 14, 2016).

(65)   Drugs for Neglected Diseases initiative. Coarsucam[TM] (artesunate/amodiaquine) first fixed-dose antimalarial combination to receive WHO Prequalification http://www.dndi.org/2008/media-centre/press-releases/coarsucam-artesunateamodiaquine-first-fixed-dose-antimalarial-combination-to-receive-who-prequalification/ (accessed Mar 14, 2016).

(66)   Drugs for Neglected Diseases initiative. Cipla-DNDi Press Release: WHO Prequalifies A New Artemisinin-Based Combination Treatment (ACT) for Malaria. Artesunate-Mefloquine Fixed-Dose Combination (ASMQ FDC) to be rolled out throughout Asia

http://www.dndi.org/2012/media-centre/press-releases/asmqprequal/ (accessed Mar 14, 2016).

(67) Medicines for Malaria Venture. Eurartesim® (dihydroartemisinin-piperaquine) receives WHO prequalification http://www.mmv.org/newsroom/news/eurartesim-dihydroartemisinin-piperaquine-receives-who-prequalification (accessed Mar 14, 2016).

(68) BBC News. Malaria vaccine gets "green light" http://www.bbc.com/news/health-33641939 (accessed Mar 16, 2016).

(69) Medscape Medical News. First Malaria Vaccine Approved by EU Regulators http://www.medscape.com/viewarticle/848608 (accessed Mar 16, 2016).

(70) Nature. Malaria vaccine cautiously recommended for use in Africa http://www.nature.com/news/malaria-vaccine-cautiously-recommended-for-use-in-africa-1.18638 (accessed Mar 16, 2016).

(71) Krogstad, D. J.; Schlesinger, P. H.; Gluzman, I. Y. *J. Cell Biol.* **2016**, *101* (6), 2302–2309.

(72) Fitch, C. D.; Yunis, N. G.; Chevli, R.; Gonzalez, Y. *J. Clin. Invest.* **1974**, *54* (1), 24–33.

(73) Solomonov, I.; Osipova, M.; Feldman, Y.; Baehtz, C.; Kjaer, K.; Robinson, I. K.; Webster, G. T.; McNaughton, D.; Wood, B. R.; Weissbuch, I.; Leiserowitz, L. *J. Am. Chem. Soc.* **2007**, *129* (9), 2615–2627.

(74) de Villiers, K. A.; Marques, H. M.; Egan, T. J. *J. Inorg. Biochem.* **2008**, *102* (8), 1660–1667.

(75) de Villiers, K. A.; Gildenhuys, J.; le Roex, T. *ACS Chem. Biol.* **2012**, *7* (4), 666–671.

(76) Foley, M. *Pharmacol. Ther.* **1998**, *79* (1), 55–87.

(77) Su, X.; Kirkman, L. A.; Fujioka, H.; Wellems, T. E. *Cell* **1997**, *91* (5), 593–603.

_____

(78) Sidhu, A. B. S.; Verdier-Pinard, D.; Fidock, D. A. *Science.* **2002**, *298* (5591), 210–213.

(79) Fidock, D. A.; Nomura, T.; Talley, A. K.; Cooper, R. A.; Dzekunov, S. M.; Ferdig, M. T.; Ursos, L. M. B.; Sidhu, A. S.; Naudé, B.; Deitsch, K. W.; Su, X.; Wootton, J. C.; Roepe, P. D.; Wiellems, T. E. *Mol. Cell* **2000**, *6* (4), 861–871.

(80) Maeno, Y.; Toyoshima, T.; Fujioka, H.; Ito, Y.; Meshnick, S.; Benakis, A.; Milhous, W.; Aikawa, M. *Am. J. Trop. Med. Hyg.* **1993**, *49*, 485–4891.

(81) Dutta, G. P.; Bajpai, R.; Vishwakarma, R. A. *Chemotherapy* **1989**, *35*, 200–207.

(82) Skinner, T. S.; Manning, L. S.; Johnston, W. A.; Davis, T. M. E. *Int. J. Parasitol.* **1996**, *26* (5), 519–525.

(83) Terkuile, F.; White, N. J.; Holloway, P.; Pasvol, G.; Krishna, S. *Exp. Parasitol.* **1993**, *76*, 85–95.

(84) Meshnick, S. R. *Int. J. Parasitol.* **2002**, *32* (13), 1655–1660.

(85) Meshnick, S. R.; Yang, Y.; Lima, V.; Kuypers, F.; Kamchonwongpaisan, S.; Yuthavong, Y. *Antimicrob. Agents Chemother.* **1993**, *37* (5), 1108–1114.

(86) Meshnick, S. R.; Thomas, A.; Ranz, A.; Xu, C. M.; Pan, H. Z. *Mol. Biochem. Parasitol.* **1991**, *49*, 181–189.

(87) Hopkins Sibley, C. *BMC Med.* **2015**, *13* (1), 67.

(88) Noedl, H.; Se, Y.; Schaecher, K.; Smith, B. L.; Socheat, D.; Fukuda, M. M. *N. Engl. J. Med.* **2008**, *359* (24), 2619–2620.

(89) Ariey, F.; Witkowski, B.; Amaratunga, C.; Beghain, J.; Langlois, A. C.; Khim, N.; Kim, S. *Curr. Sci.* **2014**, *106* (3), 345.

(90) Mohon, A. N.; Alam, M. S.; Bayih, A. G.; Folefoc, A.; Shahinas, D.; Haque, R.; Pillai, D. R. *Malar. J.* **2014**, *13* (1), 431.

(91) Ayad, F.; Tilley, L.; Deady, L. W. *Bioorg. Med. Chem. Lett.* **2001**, *11*, 2075–2077.

_____

(92)   Hrycyna, C. A.; Summers, R. L.; Lehane, A. M.; Pires, M. M.; Namanja, H.; Bohn, K.; Kuriakose, J.; Ferdig, M.; Henrich, P. P.; Fidock, D. A.; Kirk, K.; Chmielewski, J.; Martin, R. E. *ACS Chem. Biol.* **2014**, *9*, 722–730.

(93)   Raynes, K. *Int. J. Parasitol.* **1999**, *29*, 367–379.

(94)   Kakuru, A.; Jagannathan, P.; Muhindo, M. K.; Natureeba, P.; Awori, P.; Nakalembe, M.; Opira, B.; Olwoch, P.; Ategeka, J.; Nayebare, P.; Clark, T. D.; Feeney, M. E.; Charlebois, E. D.; Rizzuto, G.; Muehlenbachs, A.; Havlir, D. V. *N. Engl. J. Med.* **2016**, *374* (10), 928–939.

(95)   Davis, T. M. E.; Hung, T.; Sim, I.; Karunajeewa, H. A.; Ilett, K. F. *Drugs* **2005**, *65* (1), 75–87.

(96)   Oliveira, R.; Miranda, D.; Magalhães, J.; Capela, R.; Perry, M. J.; Neill, P. M. O.; Moreira, R.; Lopes, F. *Bioorg. Med. Chem.* **2015**, *23* (16), 5120–5130.

(97)   Peyton, D. H. *Curr. Top. Med. Chem.* **2012**, *12*, 400–407.

(98)   Burgess, S. J.; Kelly, J. X.; Shomloo, S.; Wittlin, S.; Peyton, D. H. *J. Med. Chem.* **2010**, *53*, 6477–6489.

(99)   Musonda, C. C.; Whitlock, G. A.; Witty, M. J.; Brun, R.; Kaiser, M. *Bioorg. Med. Chem. Lett.* **2009**, *19* (2), 481–484.

(100)   Chong, C. R.; Chen, X.; Shi, L.; Liu, J. O.; Sullivan, D. J. *Nat. Chem. Biol.* **2006**, *2* (8), 415–417.

(101)   Walsh, J. J.; Coughlan, D.; Heneghan, N.; Bell, A. *Bioorg. Med. Chem. Lett.* **2007**, *17*, 3599–3602.

(102)   Grellepois, F.; Grellier, P. *ChemBioChem* **2005**, *6*, 648–652.

(103)   Miller, L. H.; Ackerman, H. C.; Su, X.; Wellems, T. E. *Nat Med* **2013**, *19* (2), 156–167.

(104)   de Villiers, K. A.; Egan, T. J. *Molecules* **2009**, *14* (8), 2868–2887.

_____

(105) Drinkwater, N.; Mcgowan, S. *Biochem. J.* **2014**, *461* (3), 349–369.

(106) Egan, T. J. *Targets* **2003**, *2* (3), 115–124.

(107) Ncokazi, K. K.; Egan, T. J. *Anal. Biochem.* **2005**, *338* (2), 306–319.

(108) Gildenhuys, J.; le Roex, T.; Egan, T. J.; de Villiers, K. A. *J. Am. Chem. Soc.* **2013**, *135* (3), 1037–1047.

(109) Webster, G. T.; Tilley, L.; Deed, S.; Mcnaughton, D.; Wood, B. R. *FEBS Lett.* **2008**, *582* (582), 1087–1092.

(110) Ginsburg, H.; Nissani, E.; Krugliak, M. *Biochem. Pharmacol.* **1989**, *38* (16), 2645–2654.

(111) Dubar, F.; Egan, T. J.; Pradines, B.; Kuter, D.; Ncokazi, K. K.; Forge, D.; Pierrot, C.; Kalamou, H.; Khalife, J.; Buisine, E.; Rogier, C.; Forfar, I.; Slomianny, C.; Trivelli, O. X.; Kapishnikov, S.; Leiserowitz, L.; Dive, D.; Biot, C. *ACS Chem. Biol.* **2011**, *6*, 275–287.

(112) Chavain, N.; Dive, D.; Touati, N.; Buisine, E.; Biot, C. *Mol. Pharm.* **2008**, *4*, 239–244.

(113) Dorn, A.; Vippagunta, S. R.; Matile, H.; Jaquet, C.; Vennerstrom, J. L.; Ridley, R. G. *Biochem. Pharmacol.* **1998**, *55* (6), 727–736.

(114) Gildenhuys, J.; Sammy, C. J.; Müller, R.; Streltsov, V. A.; le Roex, T.; Kuter, D.; de Villiers, K. A. *Dalton. Trans.* **2015**, *44*, 16767–16777.

(115) Parapini, S.; Basilico, N.; Pasini, E.; Egan, T. J.; Olliaro, P.; Taramelli, D.; Monti, D. *Exp. Parasitol.* **2000**, *96* (4), 249–256.

(116) Huy, N. T.; Maeda, A.; Uyen, D. T.; Trang, D. T. X.; Sasai, M.; Shiono, T.; Oida, T.; Harada, S.; Kamei, K. *Acta Trop.* **2007**, *101*, 130–138.

(117) Sandlin, R. D.; Carter, M. D.; Lee, P. J.; Auschwitz, J. M.; Leed, S. E.; Johnson, J. D.; Wright, D. W. *Antimicrob. Agents Chemother.* **2011**, *55* (7), 3363–3369.

(118) Carter, M. D.; Phelan, V. V; Sandlin, R. D.; Bachmann, B. O.; David, W. *Comb.*

_____

Chem. High Throughput Screen. **2011**, *13* (3), 285–292.

(119) Fitzroy, S. Towards the Development of a Medium-Throughput Assay to Investigate the Kinetics of β-Haematin Formation in the Presence of Diverse Inhibitors, Stellenbosch University, Stellenbosch, South Africa, 2015.

(120) Kaschula, C. H.; Egan, T. J.; Hunter, R.; Basilico, N.; Parapini, S.; Taramelli, D.; Pasini, E.; Monti, D. *J. Med. Chem.* **2002**, *45* (16), 3531–3539.

(121) Wicht, K. J.; Combrinck, J. M.; Smith, P. J.; Hunter, R.; Egan, T. J. *J. Med. Chem.* **2016**, *59*, 6512–6530.

(122) Wicht, K. Discovery of Benzamides and Triarylimidazoles Active against Plasmodium falciparum via Haemozoin Inhibition: High Throughput Screening, Synthesis and Structure-Activity Relationships, University of Cape Town, Cape Town, South Africa, **2015.**

(123) Materials Studio v.7.0, Accelrys Software Inc.: San Diego, CA. 2013.

(124) Brooks, B. R.; Bruccoleri, R. E.; Olafson, B. D.; States, D. J.; Swaminathan, S.; Karplus, M. *J. Comput. Chem.* **1983**, *4* (2), 187–217.

(125) Dauber-Osguthorpe, P.; Roberts, V. A.; Osguthorpe, D. J.; Wolff, J.; Genest, M.; Hagler, A. T. *Proteins Struct. Funct. Bioinformtics* **1988**, *4*, 31–47.

(126) Mayo, S. L. .; Olafson, B. D. .; Goddard, W. A. *J. Phys. Chem.* **1990**, *94*, 8897–8909.

(127) Sun, H. *J. Comput. Chem.* **1994**, *15*, 752.

(128) Sun, H.; Mumby, S. J.; Maple, J. R.; Hagler, A. T. *J. Am. Chem. Soc.* **1994**, *116*, 2978–2987.

(129) Sun, H. *Macromolecules* **1995**, *28*, 701.

(130) Hill, J. R.; Sauer, J. *J. Phys. Chem.* **1994**, *98*, 1238–1244.

(131) Munro, O. Q.; Marques, H. M.; Debrunner, P. G.; Mohanrao, K.; Scheidt, W. R. *J. Am. Chem. Soc.* **1995**, *17*, 935–954.

Chapter 7 – References

_____

(132) Marques, H. M.; Munro, O. Q.; Grimmer, N. E.; Levendis, D. C.; Marsicano, F.; Pattrick, G.; Markoulides, T. *J. Chem. Soc. Faraday Trans.* **1995**, *1* (12), 1741–1749.

(133) Prevot, L.; Jaquinod, L.; Fischer, J.; Weiss, R. *Inorganica Chim. Acta* **1998**, *283*, 98–104.

(134) Lecomte, C.; Chadwick, D. L.; Coppens, P.; Stevens, E. D. *Inorg. Chem.* **1983**, *22*, 2982–2992.

(135) Johnson, M. R.; Seok, W. K.; Ma, W.; Slebodnick, C.; Wilcoxen, K. M.; Ibers, J. A. *J. Org. Chem.* **1996**, *61* (10), 3298–3303.

(136) Hoard, J. L., Hamor, M. J., Hamor, T. A., Caughey, W. S. *J. Am. Chem. Soc.* **1965**, *87* (11), 2312–2319.

(137) Hatano, K.; Uno, T. *Bull. Chem. Soc. Jpn* **1990**, *63*, 1825–1827.

(138) Perdew, J. P.; Wang, Y. *J. Chem. Inf. Model.* **1992**, *45* (23), 13244–13249.

(139) Perdew, J. P.; Wang, Y. *Phys. Rev. B* **1986**, *33* (12), 8800–8802.

(140) Delley, B. *J. Chem. Phys* **1990**, *92*, 50–517.

(141) Rappé, A. K.; Goddard, W. A. *J. Phys. Chem.* **1991**, *95* (8340), 3358–3363.

(142) Nsumiwa, S.; Kuter, D.; Wittlin, S.; Chibale, K.; Egan, T. J. *Bioorg. Med. Chem.* **2013**, *21* (13), 3738–3748.

(143) Marvin Sketch v6.3.1, Chem Axon Ltd.: Budapest. 1998.

(144) Discovery Studio v.4.1, Accelrys Software Inc.: San Diego, CA. 2015.

(145) Hunter, C. A.; Sanders, J. K. M. *J. Am. Chem. Soc.* **1990**, *112* (14), 5525–5534.

(146) Janiak, C. *J. Chem. Soc. Dalt. Trans.* **2000**, No. 21, 3885–3896.

(147) Hawley, S. R.; Bray, P. G.; O'Neill, P. M.; Park, B. K.; Ward, S. A. *Biochem. Pharmacol.* **1996**, *52* (5), 723–733.

(148) Zhou, P.; Zou, J.; Tian, F.; Shang, Z. *J. Chem. Inf. Model.* **2009**, *49*, 2344–2355.

(149) Voth, A. R.; Khuu, P.; Oishi, K.; Ho, P. S. *Nat. Chem.* **2009**, *1* (1), 74–79.

(150) Patrick, G. L. *An introduction to medicinal chemistry*, 4th ed.; Oxford University Press Inc.: New York, 2009.

(151) Hay, J. B. Design and Synthesis of Dual-active Heterocyclic Hybrid Inhibitors for β-Hematin and Plasmodium falciparum N-Myristoyltransferase, Stellenbosch University, Stellenbosch, South Africa, **2016.**

(152) Ongarora, D. S. B.; Strydom, N.; Wicht, K.; Njoroge, M.; Wiesner, L.; Egan, T. J.; Wittlin, S.; Jurva, U.; Masimirembwa, C. M.; Chibale, K. *Bioorganic Med. Chem.* **2015**, *23* (17), 5419–5432.

(153) Kuter, D.; Mohunlal, R.; Fitzroy, S.; Asher, C.; Smith, P. J.; Egan, J.; de Villiers, K. A. *CrystEngComm* **2016**, *18*, 5177–5187.

(154) Bissantz, C.; Kuhn, B.; Stahl, M. *J. Med. Chem.* **2010**, *53*, 5061–5084.

(155) Webster, R. V.; Craio, J. C.; Shyamala, V.; Kirby, G. C.; Warhurst, D. C. *Biochem. Pharmacol.* **1991**, *42*, C225-S227.

(156) Zaragoza, F.; Stephensen, H.; Peschke, B.; Rimvall, K. *J. Med. Chem.* **2005**, *48* (1), 306–311.

(157) Gao, H.; Xu, Q. L.; Yousufuddin, M.; Ess, D. H.; Kürti, L. *Angew. Chemie - Int. Ed.* **2014**, *53* (10), 2701–2705.

(158) Miyaura, N.; Yamada, K.; Suzuki, A. *Tetrahedron Lett.* **1979**, No. 36, 3437–3440.

(159) Nobelprize.org. Nobel Media AB. The Nobel Prize in Chemistry 2010 http://www.nobelprize.org/nobel_prizes/chemistry/laureates/2010/ (accessed Sep 4, 2016).

(160) Maluenda, I.; Navarro, O. *Molecules* **2015**, *20*, 7528–7557.

(161) Kotha, S.; Lahiri, K.; Kashinath, D. **2002**, *58* (625), 9633–9695.

_____

(162)   Han, F. *Chem. Soc. Rev.* **2013**, *42*, 5270–5298.

(163)   Gujral, S. S.; Khatri, S.; Riyal, P. *Indo Glob. J. Pharm. Sci.* **2012**, *2* (4), 351–367.

(164)   Lennox, A. J. J.; Lloyd-Jones, G. C. *Chem. Soc. Rev.* **2014**, *43*, 412–443.

(165)   Erba, E.; Gelmi, M. L.; Poca, D. *Tetrahedron* **2000**, *56* (51), 9991–9997.

(166)   Pereira, G. R.; Célio, G.; Arantes, L. M.; de Oliveira, H. A.; de Paula, R. C.; do Nascimento, M. F.; dos Santos, F. M.; da Rocha, R. K.; Lopes, J. C.; de Oliveira, A. B. *Eur. J. Med. Chem.* **2014**, *73*, 295–309.

(167)   Hollywood, B. F.; Scriven, E. F. V; Suschitzky, H.; Thomas, R.; Laboratories, T. R.; Chemistry, A. *J. Chem. Soc. Perkin Trans. 1* **1982**, 431–433.

(168)   Ribas, J.; Cubero, E.; Luque, F. J.; Orozco, M. *J. Org. Chem.* **2002**, No. 67, 7057–7065.

(169)   Yang, S.; Yan, H.; Ren, X.; Shi, X.; Li, J.; Wang, Y.; Huang, G. *Tetrahedron* **2013**, *69* (31), 6431–6435.

(170)   Peng, H.; Lin, C.; Yang, S.; Tseng, C.; Tzeng, C.; Lee, J.; Yang, S. *Bioorganic Med. Chem. Lett.* **2012**, *22*, 1107–1110.

(171)   Peng, H.; Lin, C.; Yang, S.; Tseng, C.; Tzeng, C.; Lee, J.; Yang, S. *Bioorganic Med. Chem. Lett.* **2012**, *22*, 1107–1110.

(172)   Cramer, C. J.; Truhlar, D. G. *Phys. Chem. Chem. Phys.* **2009**, *11*, 10757–10816.

(173)   Perdew, J. P.; Yue, W. *Phys. Rev. B* **1986**, *33* (12), 8800–8802.

(174)   Vosko, S. H.; Wilk, L.; Nusair, M. *Can. J. Phys.* **1980**, *58*, 1200–1211.

(175)   Perdew, J. P.; Wang, Y. *Phys. Rev. B* **1992**, *45* (23), 244–249.

(176)   Becke, A. D. J. *J. Chem. Phys.* **1988**, *88*, 2547–2553.

(177)   Lee, C.; Yang, W.; Parr, R. G. *Phys. Rev. B* **1988**, *37*, 2785–2789.

(178)   Boese, A. D. *J. Chem. Phys.* **2001**, *114*, 5497–5503.

(179)   Hammer, B.; Hansen, L. B.; Norskov, J. K. *Phys. Rev. B* **1999**, *59*, 7413–7421.

(180)   ConQuest v.1.16, The Cambridge Crystallographic Data Centre.: Cambridge. 2013.

(181)   Rappé, A. K.; Casewit, C. J. *Molecular Mechanics across Chemistry*; University Science Books: Sausalito, CA., 1997.

(182)   Young, H. D.; Freedman, R. A. *Sears and Zemansky's University Physics with Modern Physics*, 11th ed.; Pearson Education, Inc.: San Francisco, 2004.

(183)   Machida, K. *Principles of Molecular Mechanics*; Kodansha Ltd., and John Wiley and Sons, Inc.: Tokyo, 1999.

(184)   Kotz, J. C.; Treichel, P. M.; Weaver, G. C. *Chemistry and Chemical reactivity*, 6th ed.; Thomson Brooks/Cole: Belmont, USA, 2006.

(185)   McNaught, A. D.; Wilkinson, A.; Nic, M.; Jirat, J.; Kosata, B.; Jenkins, A. IUPAC. Compendium of Chemical Terminology, 2nd ed. (the "Gold Book") http://goldbook.iupac.org/V06597.html (accessed Sep 5, 2016).

(186)   Jones, J. E. *Proc. R. Soc. London, A.* **1924**, *106* (738), 463–477.

(187)   Hill, T. L. *J. Chem. Phys.* **1946**, *4* (7), 465.

(188)   Westheimer, F. H.; Mayer, J. E. *J. Chem. Phys.* **1946**, *4* (12), 733–738.

(189)   Buckingham, R. A. *Proc. R. Soc. A.* **1938**, *168* (933), 264–283.

(190)   Hill, T. L. *J. Chem. Phys.* **1948**, *16* (4), 394–399.

(191)   Kitaygorodsky, A. I. *Tetrahedron* **1961**, *14*, 230–236.

(192)   Kitaygorodsky, A. I. *Tetrahedron* **1960**, *9*, 183–193.

(193)   Vinter, J. G.; Gardner, M. *Molecular modelling and drug design*; CRC Press Inc.: Boca Raton, 1994.

_____

(194) Hagler, A. T.; Lifson, S.; Dauber, P. *J. Am. Chem. Soc.* **1979**, *101* (18), 5122–5130.

(195) Deeth, R. J.; Anastasi, A.; Diedrich, C.; Randell, K. *Coord. Chem. Rev.* **2009**, *253*, 795–816.

(196) Munro, O. Q.; Bradley, J. C.; Hancock, R. D.; Marques, H. M.; Marsicano, F.; Wade, P. W. *J. Am. Chem. Soc.* **1992**, *114*, 7218–7230.

(197) Xiong, Z.; Liu, Y.; Sun, H. *J. Phys. Chem.* **2008**, *112*, 2469–2476.

(198) Yapo-Kicho, D.; Lagant, P.; Vergoten, G. *Int. J. Mol. Sci.* **2007**, *8*, 259–272.

(199) de Villiers, K. A.; Marques, H. M.; Egan, T. J. *J. Inorg. Biochem.* **2008**, *102* (8), 1660–1667.

(200) Theeraladanon, C.; Arisawa, M.; Nishida, A.; Nakagawa, M. *Tetrahedron* **2004**, *60*, 3017–3035.

(201) Cui, X.; Li, Y.; Bachmann, S.; Scalone, M.; Surkus, A. *J. Am. Chem. Soc.* **2015**, *137*, 10652–10658.

(202) Prism v.6.0, GraphPad Software Inc.: La Jolla, CA. 2012.